Mirror Suspensions for the Glasgow Sagnac Speed Meter

Jan-Simon Hennig

MSc

Submitted in fulfilment of the requirements for the degree of

Doctor of Philosophy

School of Physics and Astronomy
College of Science and Engineering
University of Glasgow

April 2018

Abstract

A new era of gravitational wave astronomy has begun with the first direct detections of gravitational waves from the collision of binary black holes and a binary neutron star system. The scientific outcomes from these detections have been magnificent, however in order to increase the event rates for known sources, to be sensitive to new sources, to detect sources at greater distances, and to increase the signal to noise ratio for better extraction of source parameters, further research is required to increase the detectors sensitivity. The Advanced LIGO and Advanced Virgo detectors that enabled these first detections will ultimately be limited in their sensitivity by reaching the *standard quantum limit* (SQL). One novel technique to reduce the influence of quantum radiation pressure noise in a measurement of strain between two test masses is the *speed meter* topology. As a proof of concept experiment the Glasgow Sagnac speed meter experiment aims to show a reduction in quantum radiation pressure noise compared to an equivalent Michelson interferometer at audioband frequencies. Two triangular cavities are the core of the experiment and consist of two *100 g end test masses* and one *1 g input test masses* per cavity, all suspended from multistage pendulums. In this combination the whole Sagnac speed meter experiment should be limited by quantum radiation pressure noise from about 100 Hz to 1 kHz and it is expected to achieve a reduction of quantum radiation pressure noise by a factor of 3-5 compared to an equivalent Michelson interferometer.

This thesis presents the development, design, commissioning and testing of the three main types of suspensions in the Sagnac speed meter experiment. The longitudinal displacement noise requirement for both cavity suspension types is $<1.5 \times 10^{-18}\,\mathrm{m}/\sqrt{\mathrm{Hz}}$ over the measurement band between 100 Hz and about 1 kHz. In order to isolate the mirrors from seismic ground motion in the Sagnac speed meter experiment, they are suspended from multistage pendulums, resulting ideally in a $1/f^{2n}$ response for n pendulum stages above the pendulums rigid body modes. Reduction of thermal noise in the suspension elements (suspension thermal noise) is achieved by the introduction of high quality-factor materials in the lowest pendulum stage, making it fully monolithic. The *100 g end test mass suspension* is based on an existing design, originally developed for the AEI 10 m prototype, as a triple suspension with two stages of vertical blade springs and a fully monolithic lowest pendulum stage. The *1 g input test mass suspension*, designed as a quadruple pendulum with a fully monolithic lowest pendulum stage, utilises the same vertical blade springs and top mass as the 100 g end test mass suspension. The quadruple pendulum design enables passive damping of test mass motion at the penultimate stage. As passive damping introduces force noise due to thermal noise, a switchable passive damping system was developed and tested to mitigate limitation by this force noise. The *auxiliary suspension*, a double pendulum, serves to suspend the mirrors in the experiment that guide the beam towards the Sagnac speed

meter, in between the cavities, and towards the *balanced homodyne detector*. As these are not part of the cavities, the longitudinal displacement noise requirement can be relaxed to $<8 \times 10^{-15}\,\mathrm{m}/\sqrt{\mathrm{Hz}}$ at 100 Hz.

The pendulum dynamics of the auxiliary and 100 g end test mass suspension were measured in an optical lever set up and, in case of the auxiliary suspension, additionally with a vibrometer. With these measurements, the models were adjusted and could be used to estimate the longitudinal displacement noise due to coupling from seismic ground motion and thus verify the required performance of the suspensions. The research conducted in this thesis is an important step towards establishing the speed meter topology for consideration in future gravitational wave detectors. The developments in the scope of the monolithic assembly for the 100 g end test masses will be applied to the AEI 10 m prototype in order to enable sub-SQL measurements.

Table of contents

List of tables

List of figures

Acknowledgements

This thesis would not have been possible without the many people around me that helped me to keep my head above water and made the last four years some of the most enjoyable in my life. Please forgive me if I miss out on the one or other name.

Firstly, I want to thank my supervisors, Stefan Hild and Ken Strain. To Stefan, for his endless enthusiasm and ideas pushing me always in the right direction and for always having an open ear, may it be for work-related or personal matters. To Ken, whose wisdom helped in numerous situations to find the right answer to a problem. To both of you, thank you for teaching me and shaping my knowledge up to this point.

Secondly, I want to thank all the people that made my personal life a joy in Glasgow...and Stirling. To the IGR colleagues at coffee, lunch or curry nights out, you have enriched every day with some social banter, discussions or just a nice chat. In particular, to Gail, who always made sure that I would get enough fresh air and walked with me (and others) up the several hills. Thank you for driving us everywhere and being a good friend over the whole time. To Russell, who helped in countless discussions to make all my ideas work and transfer them into Solidworks. Thank you for taking me to the football matches, discussing the particularities of scottish football and having an open ear, whenever it was needed. To Mike (MPL), for helping in many situations with Solidworks questions and for all the nice pub evenings. To Alasdair Grant, your crosswords and puzzles at lunch have extended my vocabulary beyond my expectations and made every lunch break special. To Sebastian, who always helped with great enthusiasm in the lab and made things magically work. Thank you for your friendship and the chocolate supply while writing this thesis. To Stefan Danilishin, for all the discussions in our office, for the constant supply of small treats, and for constant wisdom on any matters starting with the word “quantum”. Thanks to Daniela, whom I have spend many hours with in the cleanroom cleaning and preparing our mirrors and ears, before bonding them. To Marielle, who showed us how to properly mix bonding solution with a little dance. To Iain, thank you for hosting me for the summer-project in 2012 and teaching me about mechanical loss. Thank you for remembering me and inviting me back to Glasgow to choose my PhD. To Raymond and Mallory, for all the cinema, hillwalking and beer halle trips, for always putting effort in their halloween costumes, for all the board-game nights and the beer-pong playing, and to Raymond for the short episode of snooker. Thank you for being my friends. To the whole of the speed meter and interferometry group, for always having an open ear for problems and helping to solve them.

Thirdly, I want to thank all the people proof-reading this piece and helping to make it at least readable. Thank you, Kay, Bryan, Stefan, Ken and Margot for all the very useful comments. You have been a great help over the last four months.

Lastly, I want to thank my family. To my mom and dad, thank you for your constant support and love. To my brothers, thank you for always being there for me and helping me whenever I need it. To my second family, Mariela and Stuart, you have made the last four years the most enjoyable time of my life. Your constant support and generosity is special and rare, I am glad to call you my friends. To my fiancèe, Margot, meeting you has been the best thing in my life and I am looking forward to sharing the rest of my life with you. Thank you for your constant support and love and thank you for all the awesome travel experiences, and the many more to follow. I love you.

Preface

This thesis is an account of the work carried out between February 2014 and October 2017 towards the development of suspensions for the Glasgow Sagnac speed meter experiment.

Chapter 1 presents a short introduction to the topic of gravitational waves and possible sources as well as the direct detections over the last two years on the basis of published literature. The data for the event GW150914 was provided by the LIGO open science centre from the LIGO scientific collaboration.

Chapter 2 discusses limitations to gravitational wave detectors. The measurements of the seismic noise in the Glasgow lab were taken together with Matthew Marwick and were used in Chapter 5, Chapter 6, Chapter 7 and Chapter 9. Other material presented in this chapter originates from published literature.

Chapter 3 highlights the speed meter topology and introduces the Glasgow Sagnac speed meter experiment as part of which this thesis was carried out. The optical layout was developed by the author in collaboration with Roland Schilling. Roland provided the initial formulation of the central Sagnac and the arm cavities after which the author further developed solutions for the local oscillator. The geometry of the bridge structure followed a Solidworks model from Russell Jones. The theoretical foundations on speed meters were derived from published literature.

Chapter 4 presents the modelling of mirror suspensions in two approaches and gives an overview on tools used throughout this thesis. The examples and theoretical methods are derived from published literature. The equations for the analytical approach closely follow the calculations in the PhD thesis from Calum Torrie.

Chapter 5 introduces the auxiliary suspension. Highlighted are the mechanical design, simulations, estimation of longitudinal displacement noise, and testing. The design of the auxiliary suspensions was developed together with Russell Jones. The ANSYS® simulations on eddy current damping were performed together with Liam Cunningham. The experimental work was conducted together with Conner Gettings, with input from Bryan Barr, Christian Gräf and Sebastian Steinlechner. The assembly of the several auxiliary suspensions was done together with Conner Gettings, Daniela Pascucci, Teng Zhang, Stefan Hild and Christian Gräf. Many mechanical parts were created by Colin Craig and Steven Craig.

Chapter 6 contains the development of the 100 g end test mass suspension. The mechani-

cal design is based on an earlier design of this suspension for the AEI 10 m prototype. The existing Mathematica® model was altered by the author to accommodate other wire orientations and to allow lateral and rotational compliance of the vertical blade springs. The final development of the monolithic assembly was led by the author, planning and performing a chain of actions in order to repeatedly build monolithic assemblies. The dynamics of the first monolithic 100 g end test mass suspension were measured by the author and the model adjusted correspondingly to fit the measurement. The initial design of the 100 g suspension for the AEI 10 m prototype was developed by Kenneth Strain, Giles Hammond, Liam Cunningham and Russell Jones. The changes to the design were developed together with Russell Jones, together with whom designs for jigs, holders and auxiliary parts were developed. The initial Mathematica® model was compiled by Giles Hammond and the corresponding Simulink® model was created by Conor Mow-Lowry. The eddy-current simulations in ANSYS® were performed by Liam Cunningham. Preparation of all parts for ultra-high vacuum was done together with Jessi Duncan. The 100 g end test mass suspension cages were pre-assembled together with Honi Gulliver. The simulations in ANSYS® for the electro-static drives were performed by Christian Gräf and Christopher Mullen. Flatness measurements of the ears were done together with Daniela Pascucci, who also measured the roughness of these ears and derived the mirror specifications. Cleaning and bonding of the masses and ears was performed together with Marielle Van-Veggel and Daniela Pascucci. The bonding template and mass caps were a design from Liam Cunningham. The small fibre puller as well as profiler were developed by Karl Toland and Alan Cumming. Karl Toland also provided the first iteration of velocity profiles for the puller. The pulled fibres were characterised together with Margot Phelps. Welding of the fibres was done by Alan Cumming with support from Stefan Hild, Angus Bell and Sean Leavey. The installation of the measured monolithic assembly was performed with Stefan Hild, after Sean Leavey prepared a full 100 g end test mass suspension. Many mechanical parts were created by Colin Craig, Steven Craig and the mechanical workshop at the Albert Einstein Institute in Hannover.

Chapter 7 presents the development of the 1 g input test mass suspension. Full models of the suspension in Mathematica® as well as in Simulink® were written by the author. The mechanical designs of the masses were developed by the author and transferred into drawings together with Russell Jones. The cage structure was developed together with Russell Jones. The ANSYS® simulations were carried out together with Liam Cunningham. The mirror specifications were derived by Daniela Pascucci. Cleaning and bonding of the test masses was done together with Marielle Van Veggel and Daniela Pascucci. The 1 g suspension cages were pre-assembled with help from Teng Zhang and Sean Leavey. The fibre puller and profiler were developed by Karl Toland and Alan Cumming. The initial velocity

profile for the puller was provided by Karl Toland. Suspension thermal noise modelling was done together with Andrew Spencer and Sean Leavey, who wrote the MATLAB® code to utilise the speed meter parameter list for this modelling. This script was also applied in Chapter 6 and Chapter 9. Several mechanical parts were created or altered by Colin Craig and Steven Craig. The 1 g input test mass suspension development greatly benefited from input during a weekly author-led meeting with participants Jim Hough, Sheila Rowan, Giles Hammond, Alan Cumming, Marielle Van Veggel, Liam Cunningham, Daniela Pascucci, Ken Strain, Stefan Hild, Angus Bell and Russell Jones. Many mechanical parts were created by Colin Craig and Steven Craig.

Chapter 8 is based on the publication led by the author on switchable eddy-current damping. The idea of switchable eddy-current damping originated from Ken Strain. The polyether ether ketone coil former for the test were modified by Steven Craig.

Chapter 9 presents a four fibre design for the 1 g ITM suspension in order to gain static pitch adjustment of the 1 g mirror.

Chapter 10 summarises the work conducted in the scope of this thesis and gives a short outlook on future steps to be taken for the Sagnac speed meter experiment.

Appendix A explains the effect of phase shifting and phase wrapping that has been used in order to improve the representation of phase from the measurements of linear response functions.

Appendix B shows and example for the Lagrangian approach for modelling and how state space matrices are derived from it. Additionally, a list of the design parameters for the auxiliary suspension is presented.

Appendix C lists all necessary procedures for the 100 g and 1 g suspensions. The bonding procedures were developed together with Marielle Van Veggel. The welding procedure was developed by Alan Cumming, Angus Bell and Stefan Hild.

Chapter 1

The new era of gravitational wave astronomy

1.1 Gravitational waves

Gravitational waves (GWs) are a direct prediction of Albert Einstein's theory of general relativity, published in 1916 [1]. They are created due to changes in the quadrupole moment of mass distributions and travel at the speed of light. The effect of gravitational waves is orthogonal to their direction of travel. They stretch and squeeze space time, which is called *strain*. The strain of a gravitational wave can be decomposed into two distinct polarisations, "plus" h_+ and "cross" $h_\times$. The effect of a passing gravitational wave in both polarisations on a ring of free falling test masses with diameter L can be seen in Figure 1.1. A gravitational wave in this figure would be incident to the plane of the paper and stretches the test mass ring by an amount of ΔL in one direction while squeezing it by the same amount ΔL in the orthogonal direction. The strain of the gravitational wave can be expressed as

$$h = \frac{2\Delta L}{L}. \tag{1.1}$$

The gravitational force is the weakest of the four fundamental forces in nature. A binary neutron star system with equal masses of $M = 1.4 M_\odot$, an orbital frequency of $f_{\mathrm{orb}} \approx 400\,\mathrm{Hz}$ and in which the neutron stars get close enough to almost touch ($r_0 \approx 20\,\mathrm{km}$), located about 15 Mpc away from the earth in the Virgo Cluster, would create a strain of about $h = 1 \times 10^{-21}$ [2].

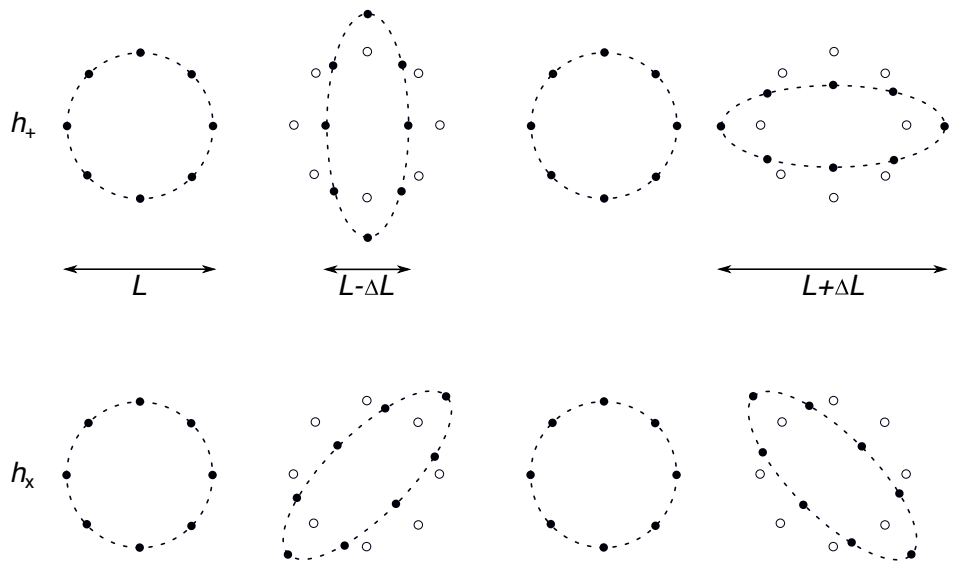

Figure 1.1: Influence of a gravitational wave incident to the plane of paper on a ring of free falling test masses for both possible polarisations. The ring is squeezed in one direction and stretched in the orthogonal direction by ΔL.

1.2 Sources of gravitational waves

A whole spectrum of gravitational radiation exists composed of numerous sources over a wide frequency band [2]. Ground based detectors aim to operate at a frequency band between about 10 Hz and 7000 Hz in order to be sensitive to gravitational waves from sources such as binary neutron stars and stellar mass black holes. More massive objects, such as supermassive black holes, emit gravitational radiation at lower frequencies and will be observable with detectors in space that are designed to operate at lower frequencies, such as LISA [3, 4]. Generally, sources of gravitational waves can be placed in two main categories, continuous and transient. In the following, a small subset of possible sources is briefly described; a more comprehensive list can be found in Reference [5].

As the name suggests, *continuous sources* emit gravitational radiation at a continuous rate, however, their strain amplitude is believed to be low and very difficult to detect with current ground-based gravitational wave observatories [2]. One example of a continuous source are *pulsars* [2]. Pulsars, discovered by Bell in 1967 [6], are neutron stars that rotate around their magnetic poles and can be observed due to emission of electromagnetic radiation. Asymmetries in their rotation releases energy in form of a mix of gravitational and electromagnetic radiation. It is an active area of research to find upper limits for the amount of energy that is released as gravitational waves [7]. Strain amplitudes of up to $h \approx 10^{-25}$ could be expected for this type of continuous source [8].

Transient sources emit gravitational waves of short bursts with high peak energy and include the most violent events in the universe, such as supernovae, coalescing compact binary

systems and possibly other exotic sources. At the end of the life of a massive star (larger than 10 solar masses), its core collapses and a huge amount of energy is expelled by the explosion that follows. This event is referred to as a *supernova* [9] and non-axisymmetric supernovae could generate a strain amplitude of $h \approx 10^{-21}$ [10]. If the core of this dying star survives this explosion, and is above the Chandrasekhar limit of 1.4 solar masses, then it will survive as a neutron star; if it is above 3 solar masses it will survive as a black hole. For these dense objects it is possible to form binary systems that ultimately collide to form a bigger object while radiating away energy in form of gravitational waves. However, as these compact binary systems are made up of two of the most massive and dense objects in our universe, the inspiral and collapse of such a system can produce gravitational waves with strain amplitudes of $h \approx 10^{-19}$ [2].

1.3 Discoveries

100 years after Albert Einstein published his theory of general relativity in 1916 [1] and gravitational waves were derived from it [11], the first direct detection of gravitational waves from two colliding black holes by the two Advanced LIGO detectors in the United States was announced [12]. With the implications from this and following detections the new era of gravitational astronomy had begun.

1.3.1 Binary black holes

On September 14$^{\text{th}}$, 2015 the two Advanced LIGO detectors picked up a signal from two colliding black holes and was labelled GW150914 [12]. The signal was first picked up by the detector in Livingston at 09:50:45 UTC and 7 ms later by the detector in Hanford. The signal, matched to template waveforms in an automated search, originated from two colliding black holes, one with 36 solar masses and the other with 29 solar masses. The single black hole, generated by this merger, had a mass of 62 solar masses. About 3 solar masses were radiated away in form of gravitational waves that were lastly detected here on Earth. The signal was identified in the data in a search for coincident signals that could be overlapped with modelled templates. The signal of the first ever detection of gravitational waves was so strong that it was far above the noise level of the detector and it became clear very quickly that it was real. The detected waveform can be seen in Figure 1.2, where the Hanford data has been shifted in time to overlap the two detected signals and reveal the astonishing similarity of both.

The very first direct detection of gravitational waves was followed by further detections of signals from binary black holes in the first and second observation run O1 and O2, with

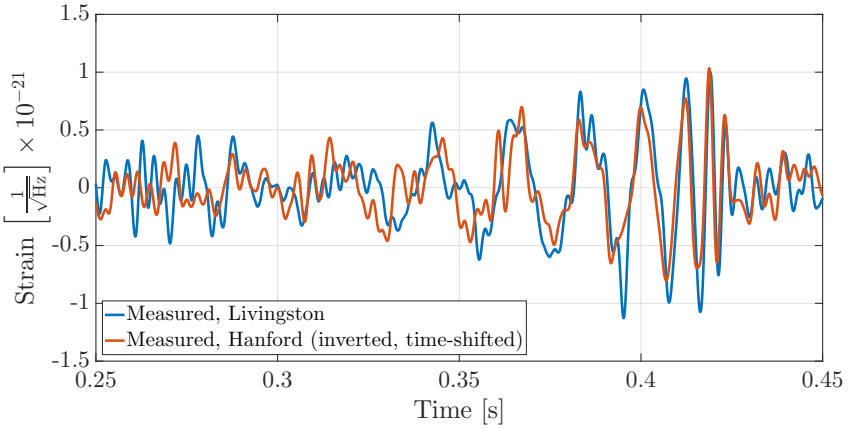

Figure 1.2: Gravitational wave data from GW150914 for both Advanced LIGO detectors. The Hanford data has been shifted in time and inverted to overlap both signals.

names GW151226 [13], GW170104 [14], GW170608 [15], GW170814 [16] and a less significant candidate LVT151012. GW170814 had some special significance due to the fact that it was the first detection with a three detector network, two weeks after Advanced Virgo joined the Advanced LIGO detectors in their 2$^{\text{nd}}$ observation run. Some of the many scientific outcomes from the first and following detections are that the black holes observed were likely formed in a low-metallicity environment [17], that tests of strong gravitational fields present during the events are still consistent with general relativity [18] and that the rate of black hole mergers in the universe could be constrained to $12 - 213\,\text{Gpc}^{-3}\,\text{yr}^{-1}$ [14][1]. Keeping this number in mind, it is expected that many more binary black hole mergers will be detected in the coming observation runs.

1.3.2 Binary neutron stars

On August 18$^{\text{th}}$, 2017 the signal from two colliding neutron stars was detected by the two Advanced LIGO detectors as well as the Advanced Virgo detector in Italy [19]. The signal first arrived at the Advanced Virgo detector at 12:41:04.4 UTC, then 22 ms later at the Advanced LIGO detector in Livingston, Louisiana, and another 3 ms later at the Advanced LIGO detector in Hanford, Washington. An automated template search through the Hanford detector data-stream triggered an alert for a binary system that occurred at 12:41:04 UTC, about 6 min after the event. By the time the LIGO trigger was issued, the satellite mission Fermi had already triggered an alert for an observed gamma-ray-burst, later labelled GRB 170818A, 16 s after the event. The GRB was detected 1.7 s later than the event suggested by the gravitational wave data from the collision of the two neutron stars [20] and was later confirmed by INTEGRAL [21]. The data from the Advanced LIGO detectors

[1]This estimate was calculated on basis of O1 data together with the first announced detection of O2 GW170104. The full analysis of all the data from O2 is yet to be published.

as well as the data from the Advanced Virgo detector helped to narrow down the location of the source in the sky from initially ∼1100 $\deg^2$, based on only the GRB data from Fermi, to 28 $\deg^2$ [20]. This precise sky localisation allowed a multitude of about 70 telescopes to point their instruments at the location of the source, after it was optically localised in galaxy NGC 4993. Over the following days the signal was measured through a large part of the electromagnetic spectrum, as can be seen in Figure 1.3. From the gravitational wave data it is possible to estimate the masses of the two neutron stars to a range of $m_1 = 1.36$–$1.60 M_\odot$ and $m_2 = 1.17$–$1.36 M_\odot$ and a total mass estimate of $m_{\text{total}} = 2.74^{+0.04}_{-0.01} M_\odot$ for the assumption of low spins [19]. The neutron star merger rate could be calculated to be $R = 1540^{+3200}_{-1220}\,\text{Gpc}^{-3}\,\text{yr}^{-1}$ using the upper limit from the data in O1.

Some of the scientific outcomes are that the gravitational wave data from GW170818 can solely be used as a standard siren to independently estimate the Hubble constant to $H_0 = 70^{+12.0}_{-8.0}\,\text{km}\,\text{s}^{-1}\,\text{Mpc}^{-3}$ [22], that the observed electromagnetic counterpart indicated a signature of a kilonova, labelled AT 2017gfo [23, 24] and that AT 2017gfo produced and ejected about 0.5 solar masses of heavy elements, such as gold and platinum [23].

With this joint observation of a single event the door to a bright future of multi-messenger astronomy has been widely opened!

1.4 Structure of this thesis

In this thesis the development, design, construction and testing of suitable mirror suspensions for the Glasgow Sagnac speed meter experiment is described. The goal of the Sagnac speed meter experiment is to show a reduction of quantum radiation pressure noise at audio-band frequencies compared to an equivalent Michelson interferometer in an attempt to establish the speed meter configuration for consideration in future generations of gravitational wave detectors.

Chapter 2 outlines limitations of current ground-based gravitational wave detectors. In Chapter 3 the speed meter topology is introduced and the experiment highlighted in the scope of which this work was conducted. Chapter 4 gives an overview on the topic of suspension modelling and presents tools that were used in this thesis. Chapters 5 to 9 build the main body of this work and explain the different types of suspensions for the Sagnac speed meter experiment, the auxiliary suspension in Chapter 5, the 100 g end test mass suspension in Chapter 6 and the 1 g input test mass suspension in Chapter 7 as well as a switchable damping system for the 1 g input test mass suspension in Chapter 8 and an alternative four fibre solution for the 1 g input test mass suspension in Chapter 9. A conclusion and outlook of the work can be found in Chapter 10.

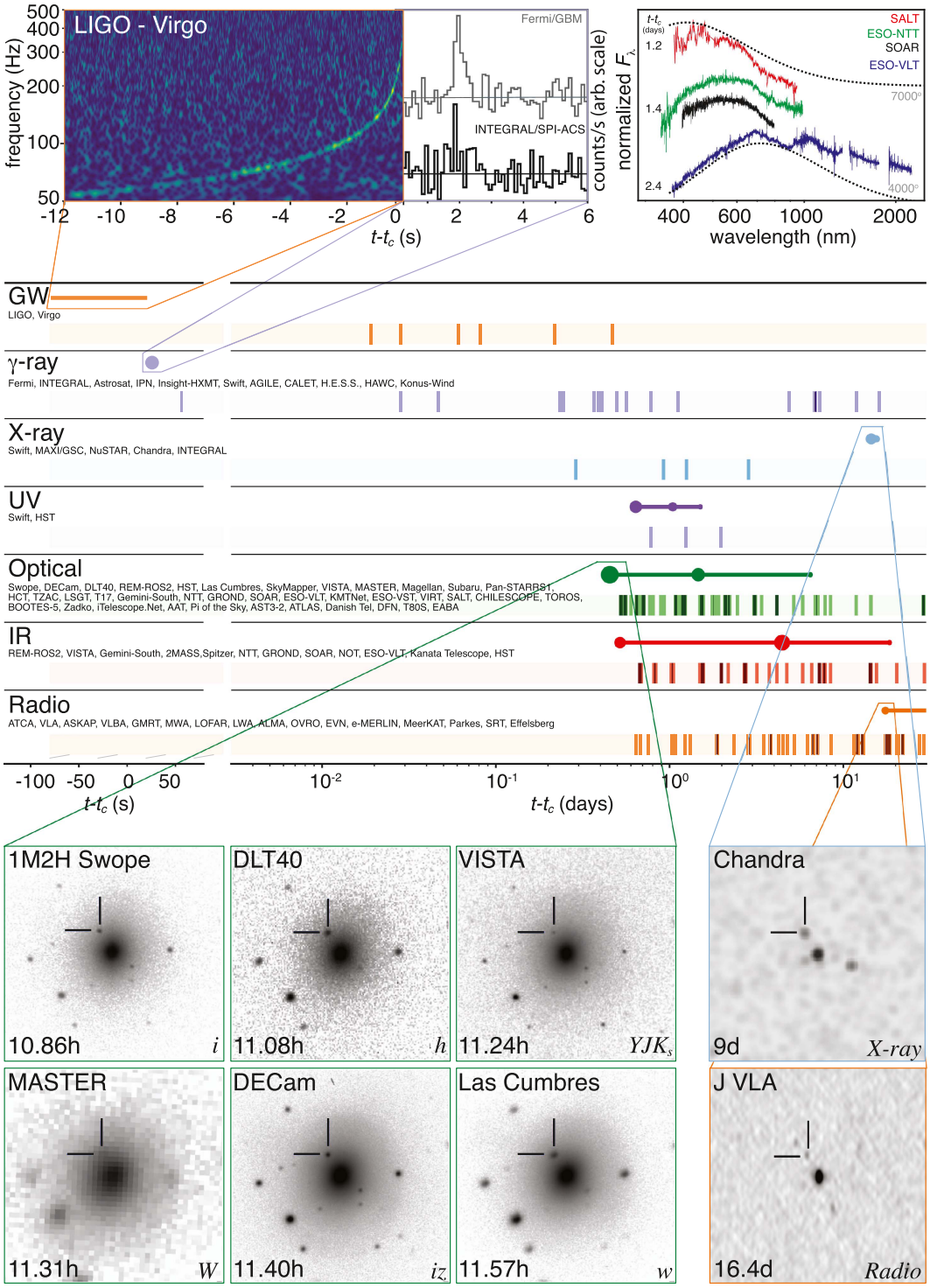

Figure 1.3: Multi-messenger astronomy with GW170818. Depicted are the different areas of the electromagnetic and gravitational spectrum with selected results showing a timeline for GW170818 and its electromagnetic counterpart. It can be seen that the event was observable through many different areas of the electromagnetic spectrum over a period of about two weeks after the event happened [20].

Chapter 2

Limitations of ground based gravitational wave detectors

This chapter discusses the limitations of GW detectors. In their current design, GW detectors operate interferometrically as position meters in a Michelson scheme, continuously sensing the positions of an ensemble of mirrors. Several techniques have been implemented over the course of the last decades to improve the sensitivity of these detectors; however, they are limited by noise sources that can only be reduced to a certain level. In the first part of this chapter the general principle of interferometric GW detection will be explained and the Michelson interferometer will be introduced. In the second part the several limiting noise sources will be named and quantified.

2.1 Gravitational wave detection

2.1.1 A brief history

In the 1960s, the hunt for gravitational waves via direct detection was pioneered by Joseph Weber with a resonant bar detector [25]. This type of detector is based on the excitation of internal modes of a aluminium bar that is resonant over a few tens of hertz to a passing GW. A trade-off has to be made between high sensitivity which can be achieved by a high quality factor Q of the bars material and bandwidth of the detector which increases with decreasing Q. In order to reach strain sensitivities at which it could be expected to sense a passing GW (about $10^{-21}/\sqrt{\mathrm{Hz}}$), most bar detectors chose high-Q materials and further upgrades focussed on higher sensitivity of the bar detectors including cold upgrades in which the bars are operated at cryogenic temperatures to reduce noise from thermal fluctuations [26].

In the beginning of the 21$^{\mathrm{st}}$ century bar detectors were superseded by interferometric systems due to their higher attainable sensitivities over a much broader bandwidth [27]. It

was found that advanced interferometric schemes would generate higher signal-to-noise ratios for GW sources [28]. The ultimate goal was to build a network of gravitational wave detectors allowing triangulation for sky localisation of sources. Over the years several detectors were built including GEO 600, a British-German detector in Ruthe near Hanover in Germany with 600 m long arms [29], TAMA 300, a Japanese detector near Tokyo in Japan with 300 m long arms, Initial Virgo, a French-Italian detector in Cascina, Italy with 3 km long arms and the Initial LIGO detectors (H1 and L1 located in Hanford, Washington and Livingston, Louisiana in the United States each with 4 km long arms, and an additional detector (H2) located in the facilities in Hanford with 2 km arm length [30]. With their initial designs not sensitive enough to detect gravitational waves, the Initial Virgo and Initial LIGO detectors went through an upgrade phase lasting about five years between 2010 and 2015, resulting in Advanced Virgo [31] and Advanced LIGO [32], the latter detecting gravitational waves for the first time [12] in 2015. With KAGRA, a novel Japanese cryogenic detector with 3 km long arms, coming online in 2019 [33] and LIGO India, a replica of the Advanced LIGO detectors build in India, the 2nd generation network of GW detectors will be complete and even a 3rd generation is already in planning stage with the Einstein Telescope [34] and Cosmic Explorer [35].

2.1.2 The Michelson Interferometer

All current GW detectors operate interferometrically in a Michelson configuration in which a laser beam is split at a beam splitter. The two beams travel then orthogonally to two end mirrors where they are reflected. At the beam splitter (BS) the beams are re-combined and the resulting signal depends on the differential length change between the two arms. This Michelson configuration is depicted in Figure 2.1. The position of the mirrors is measured continuously and influenced by the GW.

In order to increase the detector's sensitivity, the length of the north and east arm could be increased. However, the increase in length is constrained by geological, financial and political aspects. In order to overcome these constraints, *Fabry-Pérot cavities* are implemented in the two interferometer arms consisting of an *input test mass* (ITM) and an *end test mass* (ETM). The light that enters these cavities undergoes multiple reflections between the ITM and ETM and will leave the cavity towards the main beam splitter after the characteristic cavity storage time. This interferometer configuration is depicted in Figure 2.2.

The light power per differential change in arm length in a Michelson interferometer is largest *mid-fringe* where equal amounts of light are reflected and transmitted by the interferometer. For practicality Michelson interferometers are operated at or near the *dark-fringe* at which most or all of the light is reflected off the interferometer back towards the laser. The apparent benefit of this configuration is that the light power on the photo-detector

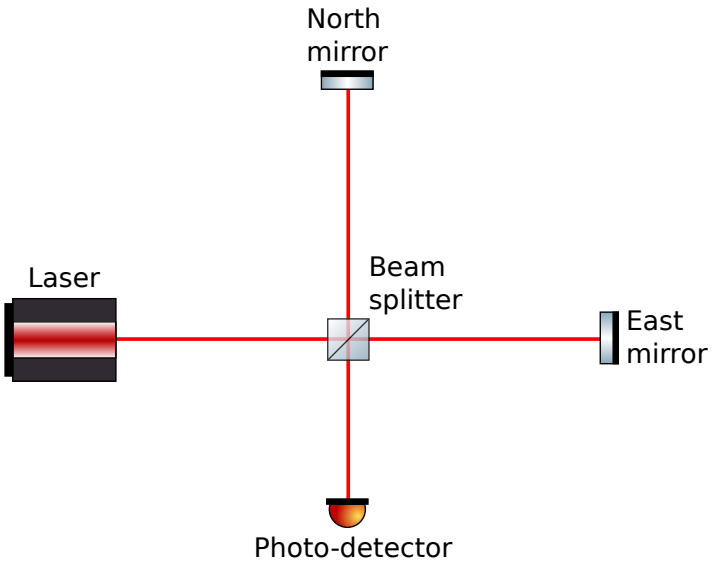

Figure 2.1: Schematic layout of a simple Michelson interferometer. The light of a laser is split by the beam splitter and reflected off end mirror defining the *east* and *north* arms in this schematic. The reflected light is re-combined at the beam splitter and leaves the interferometer through the output port towards the photo-detector in case of fully constructive interference. In case of fully destructive interference all light is reflected back to the laser.

(PD) is kept at very low levels, allowing the light power inside the interferometer to be increased which, as will be discussed in Section 2.2.4, reduces quantum shot noise. Operating at destructive interference at the output a passing GW or any other differential length change in the interferometer causes partial constructive interference and thus a signal on the PD.

Two additional optical elements can be implemented in this Fabry-Perot Michelson interferometer as shown in Figure 2.2 to make use of the light in the input and output port of the interferometer. *Power-recycling mirror* (PRM) and *signal-recycling mirror* (SRM) are used to create additional auxiliary cavities with the interferometer arms. Operating the interferometer at or near the *dark-fringe* means that all or most of the light is reflected off the interferometer back into the input port and would be lost. The PRM allows recycling of this light back into the Fabry-Perot cavities, enhancing the light power inside the interferometer without the need of a more powerful laser.

The SRM, located at the output port of the interferometer, creates another cavity with the two interferometer arms. Depending on the chosen parameters of the mirror and its precise location, the SRM enhances the imprinted signal side-bands due to a passing wave, whereby the transmission of the SRM determines quality-factor (Q-factor) and thus bandwidth of the resonant enhancement. More general this means that a low transmission allows a high resonant enhancement at the cost of a small detection bandwidth.

In case of Advanced LIGO the SRM is used as a *signal extraction mirror* (SEM) for a scheme referred to as *resonant sideband extraction* (RSE) [36, 37]. In this case the SEM creates small

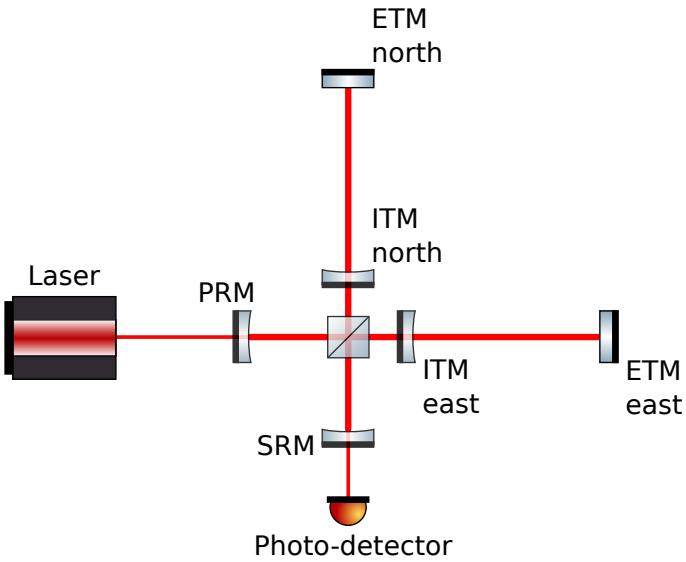

Figure 2.2: Schematic of a dual-recycled Fabry-Perot Michelson interferometer. The introduction of semi-transmissive *input test masses* (ITM) in the arms creates two *Fabry-Pérot cavities* in which photons are reflected multiple times before leaving the cavity. The *power-recycling mirror* (PRM) and *signal-recycling mirror* are used for creating additional cavities in which laser power and signal side-bands can be resonantly enhanced.

cavities with the input test masses of the Fabry-Perot arm cavities. The choice of reflectance of the SEM allows to effectively decrease the reflectivity of the input test masses of the arm cavities for the signal sidebands and thus their average storage time. This effect broadens the response function of the Fabry-Perot Michelson interferometer for the interferometer output and yields, at the cost of decreased resonant enhancement, an increase in detection bandwidth.

2.2 Noise sources

Gravitational wave detectors are limited in their sensitivity by a multitude of noise sources. In order to reach sensitivities at which GW sources can be measured on Earth, these noise sources need to be reduced to a small level. The Advanced LIGO detectors are designed to achieve strain sensitivities of $h \sim 10^{-23}/\sqrt{\text{Hz}}$ using several complex techniques and sophisticated mechanical and optical designs. The current GW detectors are expected to be ultimately limited by quantum noise of the laser light and thermal noise of the optics and their suspensions. In this section the three most important noise sources for the scope of this thesis, namely seismic noise, thermal noise as well as quantum noise, will be introduced. Other limiting noise sources will be named and briefly highlighted before a full noise budget (of the Advanced LIGO detectors) will be explained.

2.2.1 Seismic noise

Seismic noise can be divided into two categories of sources, one being of natural origin at low frequencies and the other of anthropogenic origin at higher frequencies. An example of a vertical and horizontal seismic displacement spectrum from the lab in Glasgow can be found in Figure 2.3. Above about 2 Hz the vertical seismic noise can be approximated by

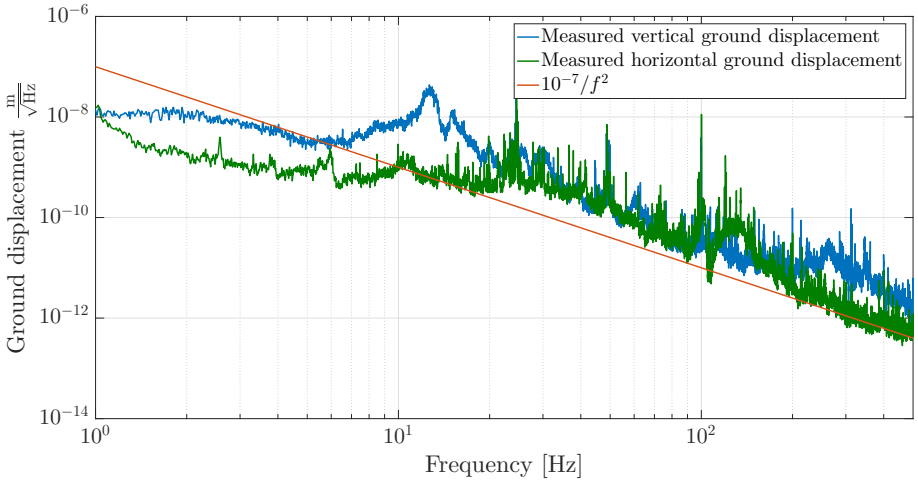

Figure 2.3: Seismic displacement spectra measured in the lab in Glasgow. Above about 2 Hz both vertical and horizontal seismic can roughly be approximated by $10^{-7}\,\mathrm{m}/\sqrt{\mathrm{Hz}}\cdot\,[1\,\mathrm{Hz}/f]^2$.

$10^{-7}\,\mathrm{m}/\sqrt{\mathrm{Hz}}\cdot\,[1\,\mathrm{Hz}/f]^2$. The seismic motion in the lab is about 6 to 7 orders of magnitude above the experimental requirement throughout the measurement band between 100 Hz and 1 kHz for the Sagnac speed meter experiment which will be introduced in Section 3.3.

In order to achieve attenuation of seismic ground motion, the mirrors in the Advanced LIGO detectors are suspended from a quadruple pendulum system [38] and the suspension point is fixed to sophisticated seismic pre-isolation tables. These consist of an external "Hydraulic External Pre-Isolator" on which an in-vacuum two stage seismic isolator, called the "Basic Symmetric Chamber", is mounted [39]. The underlying physics of how the attenuation works for the pendulum will be explained in more detail in Chapter 4, however, every pendulum stage introduces a $1/f^2$ response above its highest resonance frequency. In the case of Advanced LIGO seismic ground motion is attenuated by 10 orders of magnitude at about 10 Hz [38]. In Advanced Virgo the mirrors are suspended from the so-called "super-attenuator" that consists of three main parts, the inverted pendulum, the chain of six seismic filters, and the mirror suspension at a total height of 8 m - 9 m [31]. In this final stage, the mirror is suspended by four fused silica fibres to reduce thermal noise. The super-attenuator provides isolation of the test masses from seismic motion in all six degrees of freedom by 10 orders of magnitude above a few Hz [40]. In the case of KAGRA the input and end test masses are suspended from a 14 m high, eight stage pendulum called

Type-A [41]. At the top a seismic filter is mounted on an inverted pendulum table. From the top seismic filter the pendulum chain is suspended with three standard seismic filters, one bottom filter, the platform, the marionette, an intermediate mass and the test mass [42]. The four lowest stages are cryogenic and operating at 20 K with the test mass and the fibres made from sapphire [43]. With this system it is planned to achieve an attenuation of seismic noise of 10 orders of magnitude at 10 Hz [41].

Due to imperfections in a real suspension, e.g. non-symmetric attachment points at the masses due to manufacturing tolerances, vertical seismic motion can couple into longitudinal motion of the test mass mirror. For large detectors the local gravitational fields for ITMs and ETMs differ due to the curvature of the earth and cause further coupling of vertical seismic motion. For a 4 km detector as Advanced LIGO the coupling is estimated to be about 0.1 % [38]. In this thesis a more conservative estimate of 1 % will be used.

2.2.2 Newtonian noise

Newtonian noise—also often referred to as *gravity gradient noise*—is a consequence of density fluctuations in the proximity of the test masses which includes density changes of the ground or motion of walls and equipment. Generated by Rayleigh-, S-, and P-waves, it has been shown in simulations that Newtonian noise can be subtracted with a series of witness sensors [44] or reduced by shaping of the ground near the test mass suspensions [45]. A full description of seismic effects on GW detectors can be found in Reference [44].

2.2.3 Thermal noise

Thermal noise in GW detectors can be calculated based on the *Fluctuation-Dissipation-Theorem* (FDT) originally formulated in the 1950s [46–48] which relates thermal fluctuations in a system to the dissipation of energy; without a dissipation channel there can not be thermal fluctuations. Dissipation channels can be of various origins, including viscous damping, internal friction, and thermoelastic damping. In the Sagnac speed meter experiment for instance, viscous damping is introduced by passive eddy-current dampers on the suspension systems that will be highlighted throughout Chapter 5, Chapter 6, and Chapter 7. Chapter 8 will present a switchable passive damping system that allows the reduction of force noise arising due to thermal noise in the eddy-current damper. The most significant thermal noise contributors in current GW detectors are thermal fluctuations associated with damping in the mirrors and suspension systems material.

Suspension thermal noise

The suspension elements (wires or fibres) and their attachments are one source of thermal noise that can couple into the interferometric measurement. Thermal noise of these elements excites the pendulum modes and their internal, so called violin modes. For suspension thermal noise it is valid to only treat the lowest pendulum stage as the noise source, since the loss in the upper stage will be filtered by the second pendulum stage [49]. Following the fluctuation dissipation theorem [46], the displacement noise of such a system can be described by [50]

$$\tilde{x}^2(\omega) = \frac{4k_B T}{m\omega} \frac{\phi_{\text{total}}\omega_{\text{p}}^2}{(\omega_{\text{p}}^2 - \omega^2)^2 + \phi_{\text{total}}^2\omega_{\text{p}}^4}, \tag{2.1}$$

where m is the mass of the mirror, ω is the angular frequency, $\omega_{\text{p}} = 2\pi f_{\text{p}}$ is the fundamental pendulum angular frequency, k_B is the Boltzmann constant, T is the temperature, and ϕ_{total} is the total mechanical loss of the system. The total loss is the weighted sum over all loss mechanisms that dissipate energy in the system

$$\phi_{\text{total}} = \frac{\phi_{\text{weld}} + \phi_{\text{thermoelastic}} + \phi_{\text{surface}} + \phi_{\text{bulk}}}{D}, \tag{2.2}$$

where the loss terms are weld loss of the connection between fibre and mirror, thermoelastic loss of the bending of the fibre, surface loss of the fibres surface and bulk loss which is negligible in case of thin fibres. These terms are weighted by the dilution factor D

$$D = \frac{2l}{N}\sqrt{\frac{mg}{YI}}, \tag{2.3}$$

where l is the fibre length, N is the number of fibres, Y is Young's modulus of the fibre material and I denotes the moment of area of the fibre shape (for spherical cross section $I = \frac{\pi d^4}{64}$). In other words, the dilution factor is the ratio of the total energy (elastic, E_{elastic} and gravity, E_{gravity}) stored in the suspension to the elastic energy in the system [50]. The loss terms can be described [50] as

$$\phi_{\text{weld}} \approx 5.8 \times 10^{-7}, \tag{2.4}$$

$$\phi_{\text{surface}} \approx \frac{8h\phi_{\text{s}}}{d}, \tag{2.5}$$

$$\phi_{\text{thermoelastic}}(f) = \frac{YT}{\rho C}\left(\alpha - \sigma_0 \frac{\beta}{Y}\right)^2 \left(\frac{2\pi f \tau}{1 + (2\pi f \tau)^2}\right) \tag{2.6}$$

with

$$\tau = \frac{1}{4.32\pi} \frac{\rho C d^2}{\kappa}, \tag{2.7}$$

where Y is Young's modulus of the fibre, ρ is the density of the material, C is the specific heat capacity, α is the linear thermal expansion coefficient, σ_0 is the static stress in the fibre, $\beta = \frac{1}{Y}\left[\frac{dY}{dT}\right]^{-1}$ is the thermoelastic coefficient, ϕ_s is the mechanical loss of the material surface, h is the depth over which surface loss takes place and d is the diameter of the fibre. τ is the characteristic time in which heat flows across the fibre and κ denotes the thermal conductivity of the fibre.

Figure 2.4 shows the thermal noise plotted for the longitudinal pendulum mode with a fundamental pendulum frequency $f_p = 1.11$ Hz for different total loss factors. The trace in

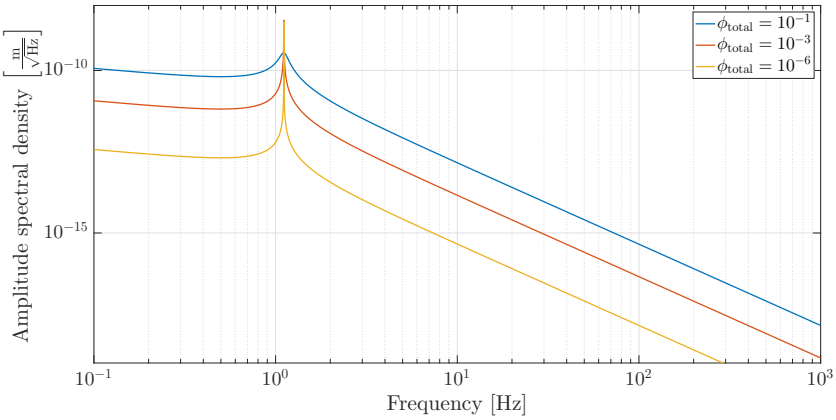

Figure 2.4: Suspension thermal noise of the pendulum mode with varying loss factors. The blue trace is calculated with a loss factor of 10^{-1}, whereas red and yellow traces are calculated for loss factors of 10^{-3} and 10^{-6} respectively. The area underneath the curves is equal for all traces storing more energy in the fundamental pendulum mode for the lower-loss cases.

blue shows the suspension thermal noise of the pendulum mode for a loss factor of 10^{-1}. The red and yellow trace depict the suspension thermal noise for loss factors of 10^{-3} and 10^{-6} respectively. The overall level of noise decreases with decreasing total loss factor, however, as the quality-factor of the fundamental pendulum resonance is the inverse of the loss factor, more energy is stored in the resonance. The larger motion at the pendulum resonance can become an issue and can be counteracted with additional damping systems.

As will be explained in Chapter 4 the modes of the six degrees of freedom are determined for straight fibres, but the fibres themselves can be excited by thermal fluctuation and start

to oscillate. The oscillations are called violin modes of the fibre and can be imagined as the vibrations of a violin string playing a tune. The resonant frequency of the violin modes is given [51] by

$$f_{\text{violin}} = \frac{n}{ld}\sqrt{\frac{T}{\pi\rho}}, \tag{2.8}$$

where n denotes the nth mode of resonant frequency, l and d the fibre length and diameter[1], T the tension in the thin section of the fibre and ρ the density of the fibre material. Knowing the resonant frequencies of the violin modes it is possible to calculate the total thermal noise of the suspension [51] by

$$\tilde{x}^2(f) = \tilde{x}^2_{\text{pend}}(f) + \sum_{\text{N wires}} \left(\sum_{\text{n modes}} \tilde{x}^2_{\text{violin}}(f) \right), \tag{2.9}$$

with

$$\tilde{x}^2_{\text{violin}}(\omega) = \sum_{\text{n}} \frac{4k_B T}{\mu_{\text{n}}\omega} \frac{\phi_{\text{total}}\omega^2_{\text{violin}}}{(\omega^2_{\text{violin}} - \omega^2)^2 + \phi^2_{\text{total}}\omega^4_{\text{violin}}}, \tag{2.10}$$

where μ_{n} is the reduced mass that is given by

$$\mu_{\text{n}} = \begin{cases} m & \text{if } n = 0 \\ \frac{1}{2}m\left(\frac{\omega_{\text{violin}}}{\omega_{\text{pend}}}\right)^2 & \text{if } n > 0. \end{cases} \tag{2.11}$$

To get a complete estimate for suspension thermal noise it is important to know which degrees of freedom (DOF) can couple into longitudinal motion of the test mass. A physical pendulum has six rigid body modes (compare Section 4.2.1), namely longitudinal, sideways, vertical, roll, pitch and yaw. For four DOFs (pitch, yaw, sideways and vertical) coupling factors into longitudinal motion can be found. For the vertical and sideways movement as mentioned before we assume conservatively 1:100, whereas for yaw and pitch the coupling is a little more complicated. If the laser beam is aligned perfectly to the centre of the mirror and the rotation point is on the front surface of the mirror, no coupling will take place. Due to a finite thickness t of the mirror and slight misalignments δ of the beam, a coupling to longitudinal motion will be introduced. Following the notation of Section 4.2.1 for the

[1] Length and diameter to be used are in respect to the thin section of the fibre. Stock and neck section are not taken into account.

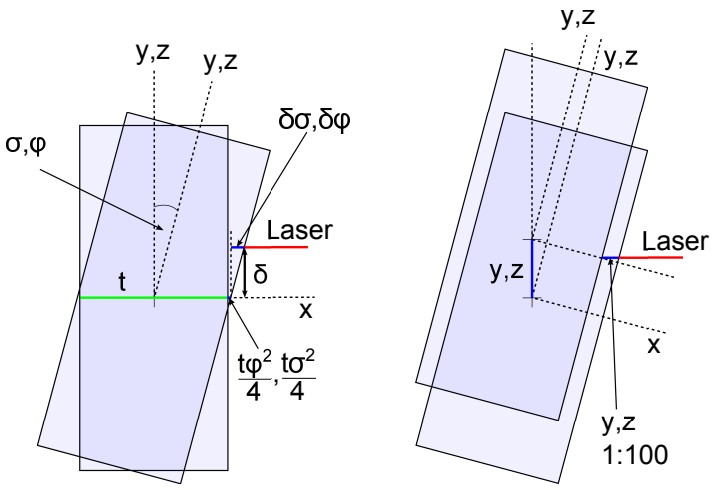

Figure 2.5: Left: Coupling from pitch motion to longitudinal motion. Right: Coupling from vertical/sideways motion to longitudinal motion.

angles for yaw and pitch the coupling is given by (see Figure 2.5)

$$\tilde{x}_{\text{pitch}} = \delta\tilde{\varphi} + \frac{t\tilde{\varphi}^2}{4}, \tag{2.12}$$

$$\tilde{x}_{\text{yaw}} = \delta\tilde{\sigma} + \frac{t\tilde{\sigma}^2}{4}. \tag{2.13}$$

For the following example, the misalignment δ of the laser beam is assumed to be 500 µm.

Figure 2.6 shows an example for the total suspension thermal noise of a 10 cm long pendulum with 10 µm diameter fused silica fibres and a weight of 1 g. The fundamental longitudi-

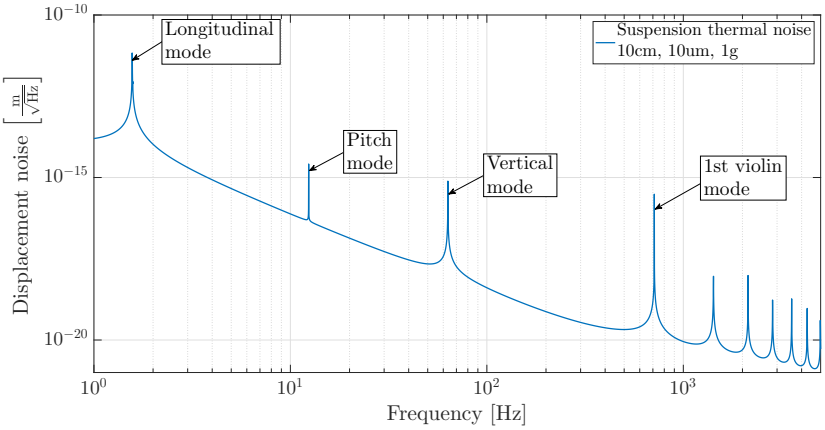

Figure 2.6: Total suspension thermal noise for a 1 g mirror suspended from two 10 cm long, 10 µm diameter fused silica fibres. The beam offset is assumed as 500 µm and longitudinal, pitch, vertical and violin modes can be easily identified.

nal pendulum mode can be seen at about 1.6 Hz. The first violin mode and higher harmonics can be seen starting at about 700 Hz and coupling from pitch and vertical motion can be spotted in between at about 12 Hz and 62 Hz.

Coating Brownian noise

Another limiting thermal noise source is Brownian noise of the optical coatings on the mirrors in GW detectors [52]. Optical coatings are made from alternating layers of high and low index materials where the number of layers depends on the choice of material and reflectivity specification. Brownian noise is calculated in a direct approach following a method first introduced by Levin [53] and later by Lui and Thorne [54], in which a hypothetical pressure is applied to the coated mirror surface resembling the incident laser beam. From this the dissipated power can be calculated. The power spectral density of coating Brownian noise can then be quantified, in the approximation where the mechanical loss of bulk material, surface and coating are equal ($\phi_B = \phi_S = \phi_C$), by [55]

$$S_{\text{Coating}}(f) = \frac{4k_B T}{\pi^2 f} \frac{(1+\sigma_S)(1-2\sigma_S)}{E_S} \frac{d}{w} \phi_C, \tag{2.14}$$

for Boltzmann constant k_B, temperature T, frequency f, with Possion ratio σ_S and Young's modulus E_S of the substrate, coating thickness d and beam diameter w. From Equation 2.14 it becomes clear that coating Brownian noise can be reduced by increasing the beam size on the mirror, minimising the coating thickness or reducing the mechanical dissipation of the coating material.

2.2.4 Quantum noise

From quantum theory it is understood that vacuum fluctuations are existing throughout time and space anywhere in the universe. By spontaneously creating and annihilating photons, a spectrum of different modes exists and ensembles of mirrors can allow certain vacuum modes to circulate. Virtual photons in these vacuum modes follow the same Poissonian statistics as are known for the laser light in GW detectors and enter through open ports or loss points into the interferometer. The resulting fluctuations in phase that appear at the sensor in the output port of the interferometer cause *quantum shot noise* and the fluctuations in amplitude that interact with the test masses create *quantum radiation pressure noise*. Together these effects build the fundamental limit for a GW detector: the *standard quantum limit* (SQL). A more complete description on quantum noise and quantum measurement can be found in Reference [56].

Quantum shot noise

The stochastic arrival of photons at the photo-detector is the cause for *quantum shot noise*. As a statistical random process this kind of noise is *white*: it has the same power density at

all frequencies. The amplitude spectral density, equivalent to strain, and normalised to the arm length L is given by

$$\tilde{h}_{\mathrm{SN}} = \frac{1}{L}\sqrt{\frac{\hbar c \lambda}{2\pi P}}, \tag{2.15}$$

where L is the cavity length, λ is the wavelength of the laser and P is power. It can be seen that an increase in either length or power will reduce the contribution to strain sensitivity.

Quantum radiation pressure noise

The Poissonian statistics of photons in laser light also causes *quantum radiation pressure noise* as the photons transfer momentum to the freely suspended test masses upon reflection. The contribution to strain sensitivity is given by

$$\tilde{h}_{\mathrm{RPN}} = \frac{1}{\mu f^2 L}\sqrt{\frac{\hbar P}{2\pi^3 c \lambda}}, \tag{2.16}$$

where $\mu = \frac{m_1 m_2}{m_1 + m_2}$ is the reduced mass of the cavity mirrors and f is frequency. Increasing the length again reduces the contribution, however an increase in power leads to a higher contribution of this noise which is not white as it drops as $1/f^2$.

The Standard Quantum Limit

With quantum shot noise being inversely proportional and quantum radiation pressure noise being proportional to power, a lower bound of these combined noises exist. This lower bound is called the *standard quantum limit* (SQL) and can be derived as the uncorrelated sum of quantum shot and radiation pressure noise. For each specific light power, one frequency exists where the contributions of both noises is equal, defining the SQL. For two free test masses the SQL can be expressed by

$$\tilde{h}_{\mathrm{SQL}} = \frac{1}{2\pi f L}\sqrt{\frac{8\hbar}{\mu}}. \tag{2.17}$$

One apparent way of reducing the fundamental SQL and thus gaining low frequency sensitivity is to increase the mirror mass; however, this can only be done to a certain degree as availability and quality of suitable test masses becomes an issue. In order to increase the high frequency sensitivity the laser power could be further increased, however, this leads to new challenges due to stability requirements for the laser source.

There are some techniques that can be employed and are under active study to surpass the SQL and reach better sensitivity; these are known as *quantum non-demolition* (QND) tech-

niques [57] throughout the literature; the most prominent are squeezing [58], variational readout [59, 60], optical springs [61–65] and speed meters [66].

2.3 Current status and future upgrades

The Advanced LIGO detectors successfully completed their second observation run (O2) and were for the last weeks joined by Advanced Virgo. As highlighted in the previous chapter, this network of 2nd generation GW detectors detected GWs from a binary black hole system [16] as well as from a binary neutron star system [19] for the first time ever. The next joint observation run (O3) is planned to begin in autumn 2018 and these detectors together with KAGRA will reach their ultimate design sensitivities over the coming few years by implementing further upgrades [67]. Figure 2.7 presents the noise budget for Advanced LIGO. The multitude of noise sources can be identified which, as an uncorrelated sum, make

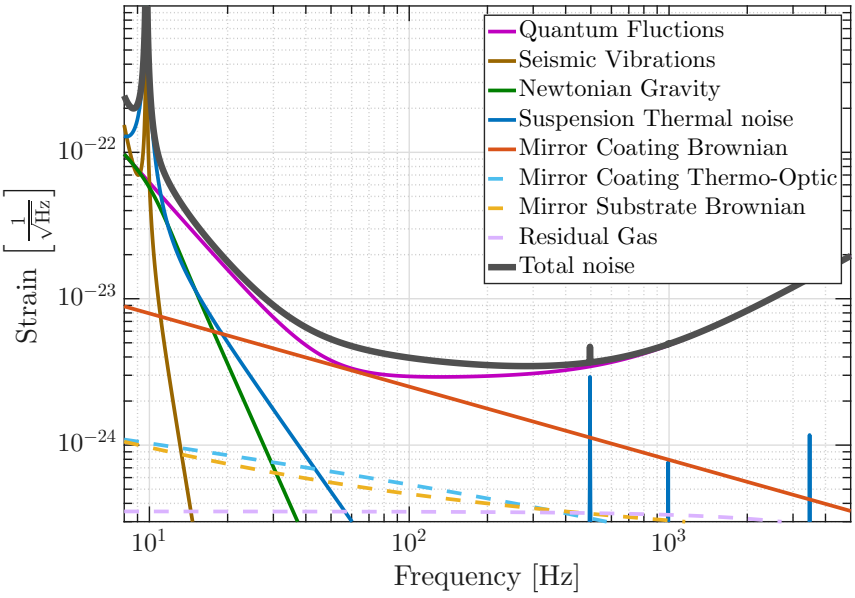

Figure 2.7: Noise budget and design sensitivity curve for the two Advanced LIGO detectors in Hanford, WA and Livingston, LA created with GWINC [68]. The total noise is calculated as the uncorrelated sum of all noise contributors. At low frequencies below 10 Hz seismic noise dominates. For most of the remaining measurement band quantum noise dominates and at about 70 Hz coating Brownian noise jointly limits the sensitivity.

up the total noise of the detector. Quantum noise limits the sensitivity at high frequencies and at low frequencies until the seismic wall at about 10 Hz becomes limiting. At about 70 Hz coating thermal noise jointly limits the detectors sensitivity.

In the mid term it is planned to upgrade the Advanced LIGO detectors to cryogenic temperatures following the example of KAGRA, however, both Advanced LIGO and Advanced

Virgo are already now pushing the limits of their facilities. In an approach to develop a 3rd generation of GW detectors bigger detectors in new facilities are being investigated such as Einstein Telescope with 10 km arms in a triangular configuration [69] and Cosmic Explorer with 40 km arm length [35, 70].

Chapter 3

Speed meters

This chapter describes one *quantum non-demolition* (QND) technique, namely the *speed meter*. The speed meter is expected to outperform an equivalent Michelson interferometer or position meter at low frequencies due to reduced quantum radiation pressure noise. The first half of this chapter will explain the speed meter effect and its historical development before presenting different topologies that act as speed meters. In the second half of this chapter the Sagnac speed meter experiment, currently being in its final commissioning step in Glasgow, is highlighted. In the course of this thesis, an optical layout for the Sagnac speed meter experiment was developed together with all suspensions that were needed to isolate the mirrors of the experiment from seismic ground motion.

3.1 The speed meter concept

The idea of measuring speed and with it momentum, a QND-variable, of a test mass rather than continuously monitoring its position in GW detectors dates back to 1990 [71]. Measurement of momentum at an earlier time does not influence the result of its measurement at a later time, in contrast to position measurement, and thus it should be theoretically possible to measure momentum to arbitrary precision. In an interferometric topology, radiation pressure noise is imparted on the light due to interaction with the mirrors of the experiment and the fact that the classical carrier amplitude beats with the vacuum fields that are entering through the dark port of the interferometer. In order to reduce radiation pressure noise in a speed meter, the light field has to coherently interact with the test masses twice and subtraction of the two back-action kicks occurs when a π-phase shift is imparted on one of the light fields upon re-combination.

Intensive theoretical studies were undertaken to find suitable topologies that could be implemented in GW detectors, such as *sloshing speed meters* [72, 73], *polarisation speed meters* [74, 75], and *Sagnac speed meters* [76, 77].

3.2 Speed meter configurations

Over the years, many different speed meter configurations were investigated [75, 77, 78]. In the following two subsections a Michelson-like speed meter configuration as well as a Sagnac speed meter will be highlighted.

3.2.1 Michelson-like speed meter

In an approach to make use of the well-known and well-studied Michelson configuration a speed meter can be realised with the layout shown in Figure 3.1. In the top part the

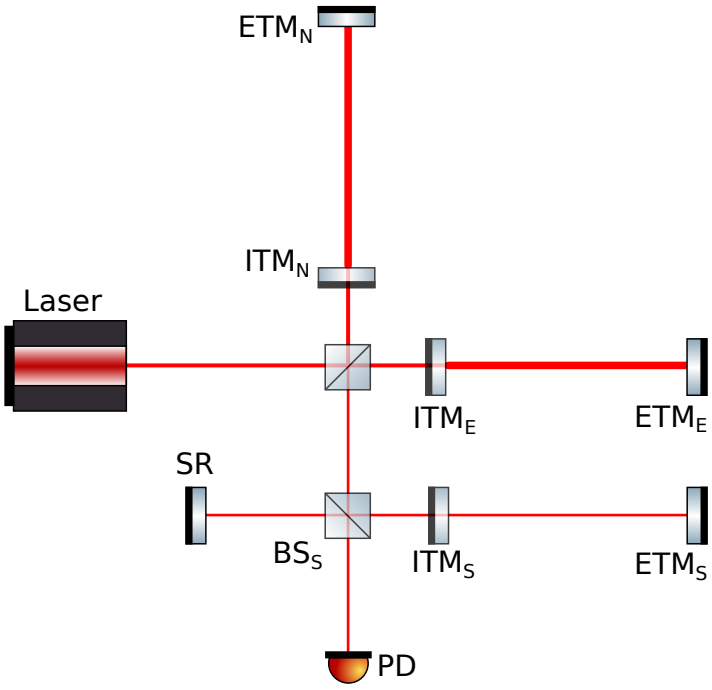

Figure 3.1: Schematic layout of a sloshing speed meter. An additional sloshing cavity in the output port of the Michelson interferometer stores the dark port light field and sends it back to the Fabry-Perot Michelson interferometer with a π-phase shift.

regular Michelson topology with Fabry-Perot arm cavities can be seen. In order to convert it into a speed meter, an additional *sloshing cavity* is implemented, in which the dark port field is stored. The required π-phase shift is realised by an additional reflection of the dark port field [72, 73]. The light leaving this *sloshing cavity* is either reflected at the additional beam splitter BS_S and probes the mirrors again, or is transmitted and reflected off a signal recycling mirror for the sloshing cavity. The signal registered at the interferometer output on the photo-detector contains the superposition of out-of-phase radiation pressure noise components and shows reduced noise due to the subtraction.

3.2.2 Sagnac speed meter

The Sagnac interferometer was invented in 1913 as a device to sense rotational motion [79] and it was investigated in the 1990s—as a *zero-area* Sagnac interferometer[1]—for use in GW detectors [80]. About a decade later it was found that the Sagnac interferometer is automatically a speed meter and that it, theoretically, can be used to perform sub-SQL measurements of GWs [81]. The light of a laser is split by a beam splitter and the transmitted and reflected fields travel through a central Sagnac interferometer with triangular Fabry-Perot cavities in opposite direction, gathering phase along their way. *Counter-clockwise* (ccw) propagation will be defined for the input light transmitted through the beam splitter, and *clockwise* (cw) for the input light initially reflected off the main beam splitter. The required π-phase shift in this configuration naturally comes from the reflection of the vacuum field at the main beam splitter upon entering from the dark port. Asymmetries of the beam splitter and unequal light power in the arms can introduce additional radiation pressure noise components in the readout port of the Sagnac speed meter [82]. Figure 3.2 shows a schematic layout for a Sagnac speed meter with triangular arm cavities and a central Sagnac interferometer. De-

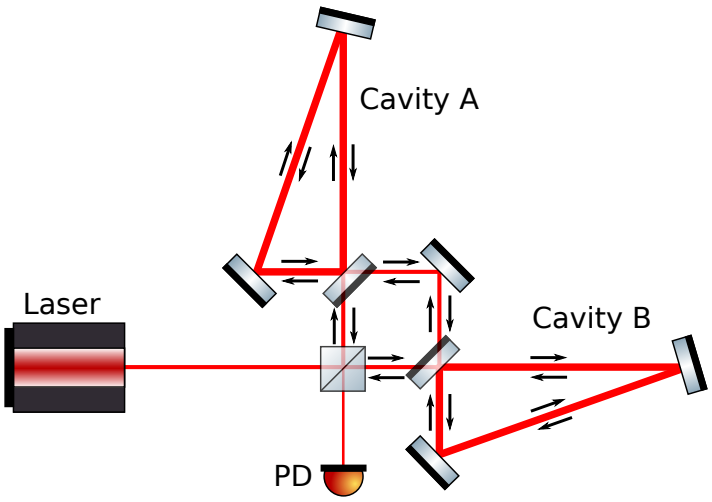

Figure 3.2: Schematic layout of a zero-area Sagnac speed meter with triangular arm cavities. The light from the laser is split at the main beam splitter and the black arrows mark the two counter-propagating modes that travel through the inner Sagnac and the arm cavities. The two modes are re-combined at the main beam splitter with the resulting signal containing the relative test mass velocity.

noting the positions of the cavity end mirrors x_1 and x_2 for cavities A and B respectively, the phase change for the light fields propagating ccw and cw can be expressed as [83]

$$\phi_{\mathrm{ccw}} \sim x_2(t) + x_1(t + \tau_{\mathrm{ccw}}), \tag{3.1}$$

$$\phi_{\mathrm{cw}} \sim x_1(t) + x_2(t + \tau_{\mathrm{cw}}), \tag{3.2}$$

[1] In the zero-area configuration the rotational signal is cancelled by circulating light around equally sized areas in opposing orientation.

with time t and travel time between the end mirrors in ccw and cw direction τ_{ccw} and τ_{cw}. For ($\tau_{ccw} = \tau_{cw} = \tau$) the differential phase change can be derived as

$$\begin{aligned}\Delta\phi &\sim \phi_{ccw} - \phi_{ccw}, \\ &\sim \left[x_2(t) - x_2(t+\tau)\right] - \left[x_1(t) - x_1(t+\tau)\right], \\ &\approx \dot{x}_2(t) - \dot{x}_1(t). \end{aligned} \tag{3.3}$$

As can be seen in Equation 3.3 the differential phase only depends on the *time-dependent* part and thus the speed of the test masses is measured for frequencies much smaller than $1/\tau$, whereas a mix of speed and its time derivatives is measured for higher frequencies.

3.2.3 Quantum noise limited sensitivity

A visualisation of the speed meter effect compared to a position meter or Michelson interferometer can be realised by plotting the interferometer response function. Calculated with the *two-photon formalism* [84, 85], following a derivation outlined in [86] for *input-output relations* of a Michelson interferometer and implementing modified *round-trip phase* and *optomechanical coupling factor* for the Sagnac speed meter topology [83], Figure 3.3 shows a comparison of the response functions for a Sagnac speed meter and a Michelson position meter. This example is calculated for reduced mass $\mu = 50\,\mathrm{kg}$, laser wavelength $\lambda = 1064\,\mathrm{nm}$, arm length $L = 1\,\mathrm{km}$, cavity half-bandwidth of $\gamma = 250\,\mathrm{Hz}$ and laser power equivalent to the laser power required to reach the SQL $P_{SQL} = 173\,\mathrm{W}$. In this plot it can be seen that the response towards low frequencies is flat for the position meter in blue and falls off with f for the speed meter in red, resulting in the loss of position information. The

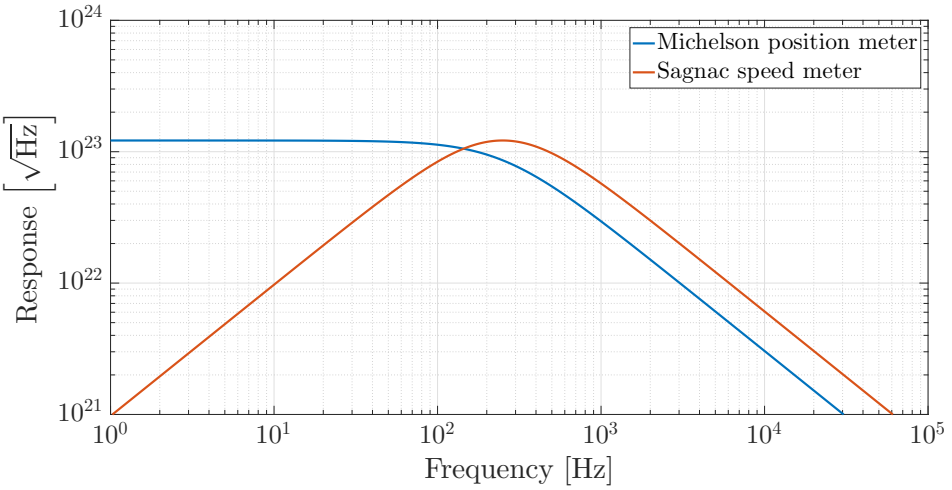

Figure 3.3: Comparison of response functions for Michelson position meter and Sagnac speed meter. Towards low frequencies and below the cavity pole the Sagnac speed meter has vanishing response with f whereas the Michelson position meter has constant response.

$1/f$ slope above about 250 Hz for both meters is due to arm cavity characteristics.

The normalised (to shot noise) quantum noise contribution for both meters is plotted in Figure 3.4. At high frequencies both meters are limited by quantum shot noise as discussed

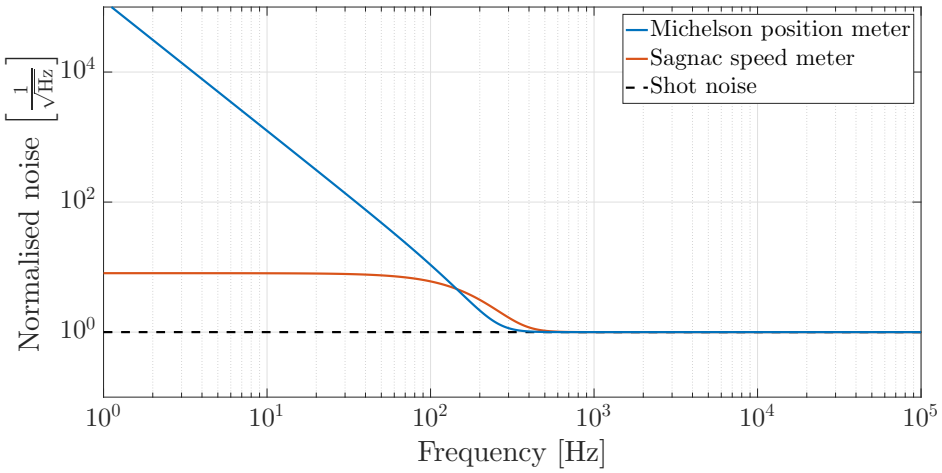

Figure 3.4: Comparison of quantum noise for Michelson position meter in blue and Sagnac speed meter in red. The quantum noise in this plot is normalised to quantum shot noise. Both meters are limited by shot noise at high frequencies, however, at low frequencies the Sagnac speed meter noise is flat due to reduced radiation pressure noise where the Michelson position meter noise raises due to radiation pressure noise.

in Section 2.2.4, however as shown by the red trace, at low frequencies the quantum noise is flat for the speed meter, after a short transition stage, due to the reduction in quantum radiation pressure noise. For the Michelson position meter, as shown in blue, the quantum noise rises as $1/f^2$ towards low frequencies.

The quantum noise limited sensitivity of speed and position meters is given by the ratio of quantum noise and the response function of each meter. Figure 3.5 depicts the quantum noise limited sensitivity of both meters in comparison to the SQL. The Michelson position meter (blue trace) has a slope of $1/f^2$ at low frequencies due to the dominating radiation pressure noise and flat response of the interferometer. The Sagnac speed meter (red trace) in contrast follows the SQL with the same $1/f$ trend.

3.3 The Glasgow Sagnac speed meter

Up to the current date the direct measurement, not to mention reduction, of quantum radiation pressure noise due to the QND behaviour of a speed meter has not been shown in an experiment. However investigations on the use of a Sagnac topology were conducted in [87–89] and their application in a GW detector investigated [80].

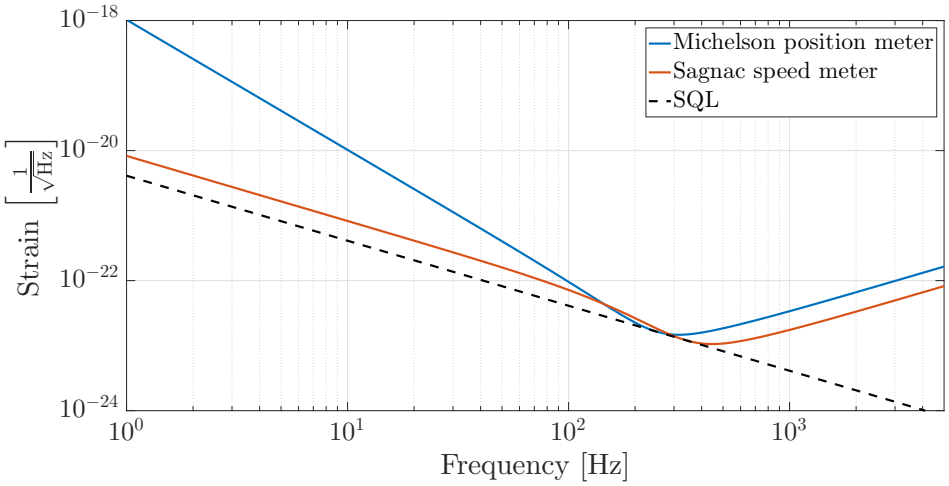

Figure 3.5: Comparison of quantum noise limited sensitivity for Michelson position meter in blue and Sagnac speed meter in red. Due to the reduction in quantum radiation pressure noise the sensitivity of the Sagnac speed meter follows the SQL at low frequencies. The quantum noise limited sensitivity is calculated as the ratio of quantum noise and interferometer response function.

In an approach to measure the reduction of quantum radiation pressure noise in a Sagnac speed meter topology compared to a Michelson topology with equivalent parameters, the *ERC Sagnac speed meter*[2] is currently in the commissioning stage at the University of Glasgow. The desired operating band, in which a reduction of quantum radiation pressure noise is anticipated and could be measured, is between 100 Hz to 1 kHz and thus in the audioband. The main characteristic of the experiment are triangular arm cavities with a Finesse of about 8900, which utilise a 1 g ITM in combination with two 100 g ETMs. This choice of mass distribution concentrates radiation pressure effects on the 1 g ITM, that will be displaced by about 4.8 kW of intra-cavity power and makes radiation pressure dominate the design sensitivity of the Sagnac speed meter experiment between about 100 Hz and about 1 kHz. For readout of the Sagnac speed meter experiment a suspended balanced homodyne detector is planned to be used that allows choosing of the readout quadrature.

The total noise together with the quantum noise limited sensitivity of the Sagnac speed meter is shown in Figure 3.6 in comparison to a Michelson interferometer with equivalent parameters. The total noise of the Michelson interferometer is plotted in blue together with the quantum noise limited sensitivity in green. For the Sagnac speed meter the same curves are plotted in red and purple. The SQL is plotted in black as a reference for the quantum noise curves. It can be seen that the total noise curve for the Sagnac speed meter is below the total noise curve of the Michelson for frequencies below about 1 kHz. The greatest reduction in quantum noise is expected between about 100 Hz to about 1 kHz with a factor of 3-5.

[2]Further information and updates on the status of the experiment available at `www.speed-meter.eu`

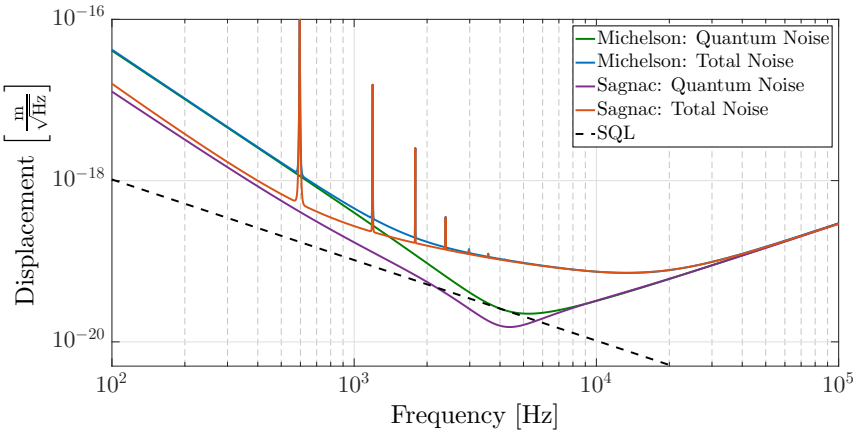

Figure 3.6: Design sensitivity of the ERC Sagnac speed meter experiment. The Michelson quantum and total noise curves are plotted in green and blue respectively. The Sagnac speed meter quantum and total noise curves are shown in purple and red respectively and it can be seen that the total noise of the Sagnac speed meter is about a factor 3-5 below the total noise of the Michelson interferometer between about 100 Hz and about 1 kHz. The SQL is plotted in black in this figure as reference.

3.3.1 Vacuum system

The experiment will be built on two 90 cm diameter breadboards that are connected by a rigid bridge structure to avoid differential motion of the two boards at low frequencies. The breadboards are isolated from seismic ground motion with a set of passive pre-isolation stacks, consisting of three alternating layers of 60 kg steel plates of the same diameter as the breadboards and fluorel rubber springs. The stacks were designed to have a vertical resonance frequency of about 18 Hz and it is expected that they work the same way for horizontal and vertical motion (with a slightly lower resonance frequency in the horizontal direction). The seismic pre-isolation stacks together with the breadboards are installed in two connected circular vacuum tanks with inner diameter of 1 m. A computer-aided-design model of the tank with the pre-isolation stacks and the connected breadboards can be seen in Figure 3.7. The diameter of the breadboards as well as inner diameter of the tanks are highlighted in this figure. The Sagnac speed meter experiment is going to be operated under ultra-high vacuum at pressures below 10^{-6} mbar.

3.3.2 Balanced homodyne detector

The readout for the Glasgow Sagnac speed meter experiment is realised with a balanced homodyne detector (BHD) [90]. The output port of the Sagnac interferometer is at the dark-fringe at all times; even small offsets of arm length mismatch are cancelled as the light accumulates phase in opposite directions before re-combination at the main beam splitter. The BHD is realised by overlapping the dark port signal beam with a local oscillator beam with which it is possible to chose arbitrary readout angles by shifting the phase of the *local*

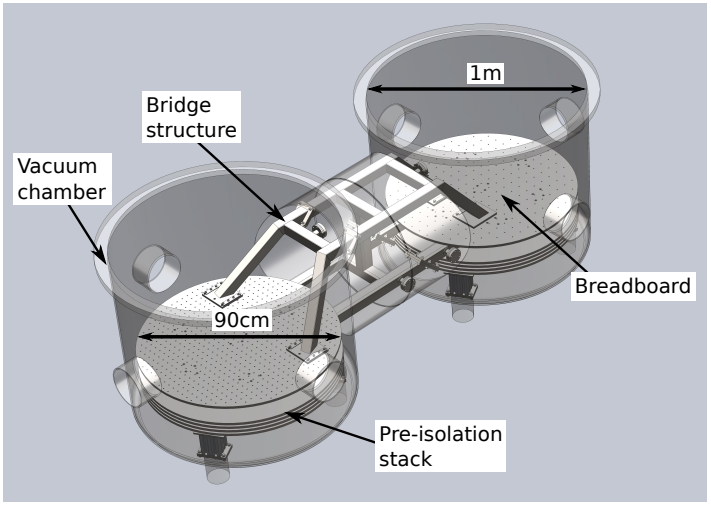

Figure 3.7: Computer-aided-design model of the vacuum system for the Sagnac speed meter experiment. Inside two circular tanks with 1 m diameter, two rigidly connected breadboards of 90 cm diameter are mounted on passive seismic pre-isolation stacks.

oscillator (LO) beam relative to the signal beam.

A schematic of a BHD can be found in Figure 3.8. At the beam splitter the signal and LO

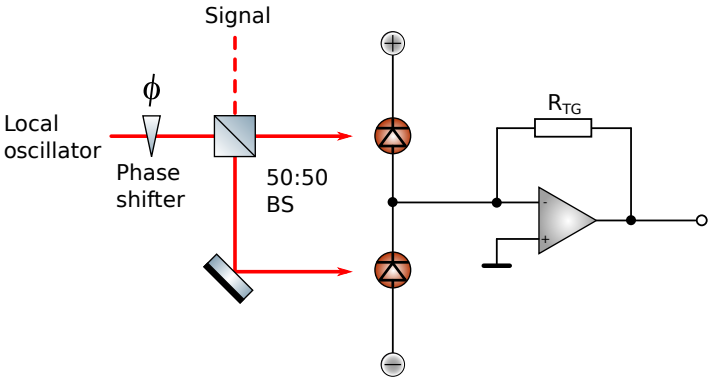

Figure 3.8: Schematic layout of the balanced homodyne detector. The dark port signal beam is overlapped with a local oscillator beam and both output ports of the beam splitter are measured and subtracted. The phase shifter in the LO path allows choice of arbitrary readout angles. The subtracted signal is amplified proportional to the transimpedance-gain resistor R_{TG}.

beam are overlapped. Denoting the corresponding light fields a and b for LO and signal beam respectively, the fields in the output ports c and d can be calculated as [90]

$$c^\dagger c = \frac{1}{2}\left[a^\dagger a + a^\dagger b e^{-i\phi} + a b^\dagger e^{i\phi} + b^\dagger b\right], \tag{3.4}$$

$$d^\dagger d = \frac{1}{2}\left[a^\dagger a - a^\dagger b e^{-i\phi} - a b^\dagger e^{i\phi} + b^\dagger b\right], \tag{3.5}$$

with phase shift ϕ equivalent to the homodyne readout angle. For a perfect splitting ratio of the beam splitter of 50:50, the difference in photo-current of the two output ports can be

derived as

$$i_{-} = c^{\dagger}c - d^{\dagger}d = a^{\dagger}be^{-i\phi} + ab^{\dagger}e^{i\phi}, \tag{3.6}$$

cancelling the dc-part and thus yielding common-mode suppression of noise that is imprinted on the LO beam.

3.4 Optical layout for the Sagnac speed meter experiment

Over the course of this thesis the optical layout for the Glasgow Sagnac speed meter experiment was developed starting from an initial design in which solely the arm cavities as well as the central Sagnac were defined. The first iteration of an optical layout was done in 2013 with OptoCAD. OptoCAD is a Fortran based program to trace Gaussian beams (TEM_{00}) through optical set-ups [91].

The ground-zero state can be seen in Figure 3.9 which was based on the original proposal for the Sagnac speed meter experiment. The input light enters the optical layout from the

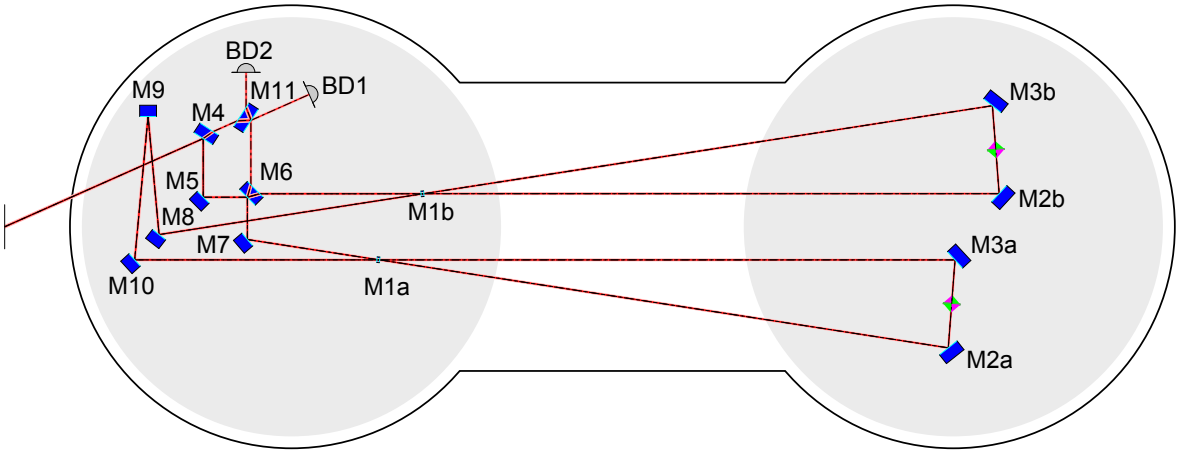

Figure 3.9: Initial optical layout of the Sagnac speed meter experiment in OptoCAD. Starting from the definition of the arm cavities and the inner Sagnac interferometer, a suitable local oscillator for the BHD as well as realistic optics and space for suspensions had to be found.

left side in this figure. Utilising mirrors M_4 and M_5 the beam is guided towards the main beam splitter M_6 where it is partially reflected towards M_7 and the first triangular cavity comprised of M_1^A, M_2^A and M_3^A and partially transmitted towards the second triangular cavity comprised of M_1^B, M_2^B and M_3^B. The beam from the second cavity then passes the central Sagnac interferometer via M_8, M_9 and M_{10} before entering the first cavity, after which the beam is guided back to the main beam splitter. The beam initially reflected off the main beam splitter beam passes the central Sagnac and the second cavity in the opposite

direction. After re-combination at the main beam splitter M_6 the (dark) signal beam is overlapped with a partial transmission from the input beam through M_4 at the BHD beam splitter M_{11}. This optical layout works in theory, however, for practical implementation further development of the layout was required.

In the initial optical layout only the cavity mirrors M_1, M_2 and M_3 of each cavity were chosen in their final or very close to final specifications. All other components required further work to attain realistic sizes and geometries. The orientation of the input beam also had to be changed, due to the limiting size of the viewport by which it enters the vacuum system. The main addition to the optical layout was a suitable LO beam for the BHD and to allow enough space for a sophisticated BHD platform on which the beam splitter as well as the photo-detectors could be mounted. It was decided that all auxiliary optics—that is the mirrors and beam splitters guiding the beam through the setup—would be of 30 mm diameter and 6 mm thickness. The main beam splitter was later chosen to be of 50 mm diameter and 12.5 mm thickness and the beam splitter for the BHD was chosen as a component of 25 mm diameter and 6 mm thickness.

3.4.1 Local oscillator options

The choice of a suitable LO for the BHD was driven by the demand of mode-matched beams at the BHD beam splitter. In order to maximise the detected signal, both beams, LO and signal beam, need to have identical parameters at the BHD beam splitter, that is equal size of beam waist w and wavefront curvature $R(x)$. Three implementations for a LO were initially considered, which are all shown in Figure 3.10 as Images A, B, and C respectively.

Image A presents the case in which the input beam is used as LO. This situation is in principle identical to the initial design in Figure 3.9, with the small difference that here the

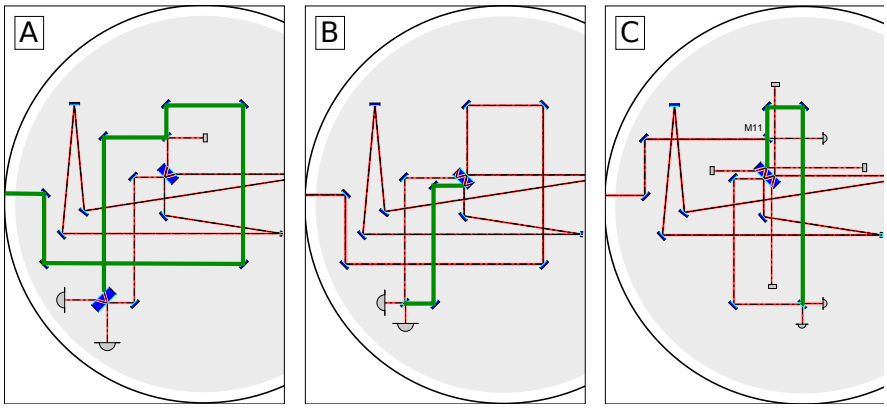

Figure 3.10: The figure shows three different implementations of a LO beam for the BHD in the OptoCAD model. In Image A the input beam is taken as a LO beam, in Image B the AR reflection of the main beam splitter is used as a LO beam and in Image C the bright port of the interferometer is used as a LO beam for the BHD.

reflection of the input beam is used as the LO. However, this solution is not suited to practical implementation due to opposite wavefront curvature compared to the signal beam. The input beam is mode-matched to the two triangular cavities in which the waist of the beam is between the two 100 g ETMs. This means the output beam of the interferometer is diverging, whereas the input beam is converging and thus has the opposite wavefront curvature, which will result in loss of signal at the beam splitter due to non perfect beam overlap.

In Image B the LO beam is realised as a reflection off the anti-reflective coating of the main beam splitter. In this case the waist and divergence angle of the signal and LO beam are close to being matched, however, it becomes technically difficult to separate the reflection from the signal beam (which is dark) without using a wedged beam splitter or a very thick beam splitter substrate.

Image C depicts a third solution in which the bright port of the interferometer is used as the LO for the BHD. Similar to Image A the input beam is guided towards the main beam splitter being reflected off an additional partially reflective mirror/BS. The transmitted input beam can be used with an additional in-vacuum photo-detector for power stabilisation of the laser. The light leaving the central Sagnac through the bright port of the main beam splitter can be used in transmission of the partially reflecting mirror as the LO for the BHD. By matching the optical path lengths of signal and LO beams, both waist and radius of curvature become matched. In addition, it is possible to modify the LO power by swapping to mirrors or beam splitters with different reflectivity.

3.4.2 Optical layout

In the baseline optical layout, the third option (interferometer bright port as LO) was chosen to be implemented. After further minor changes, in which sizes of components were slightly altered and the constraints arising from the bridge structure were implemented, the current version of the optical layout for the Glasgow Sagnac speed meter experiment was created and is shown here in Figure 3.11. In this view, as in Figure 3.9, the input beam enters the optical layout from the left hand side and is steered with M_4, M_5, and with the partially transmissive M_{11} towards the main beam splitter M_6. Here the beam is split, and the reflected, as well as transmitted, parts pass through both arm cavities as well as the central Sagnac interferometer in two counter-propagating modes before they are recombined at M_6. The signal beam is guided with M_{14} and M_{15} towards the BHD. The light from the bright port is partially transmitted through M_{11} and then guided towards the BHD with M_{12} and M_{13}. Recent investigations show that the use of the interferometer bright port as the LO can reduce noise due to asymmetries in the Sagnac speed meter [92].

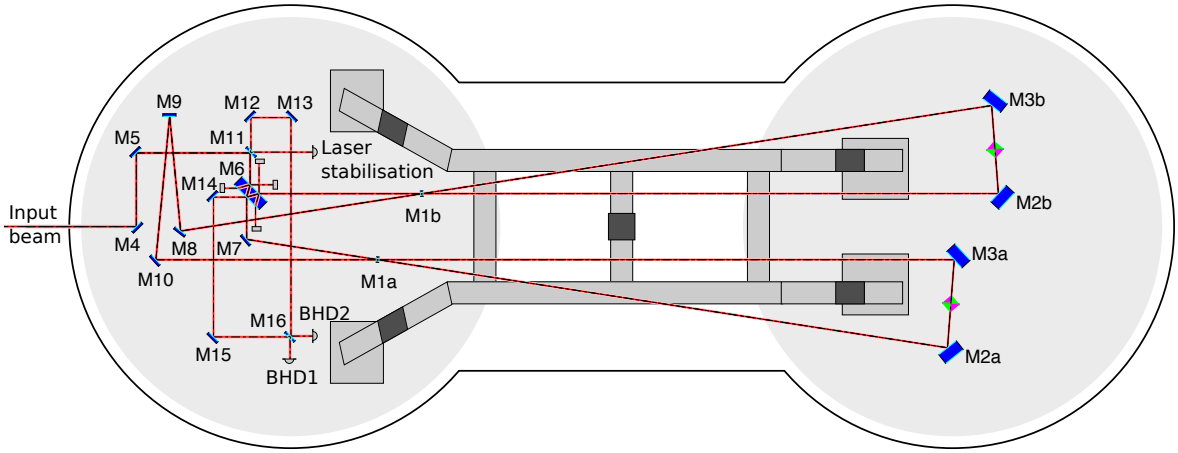

Figure 3.11: Final optical layout of the Sagnac speed meter experiment in OptoCAD. All optics are to scale and the local oscillator for the balanced homodyne detector is realised with the bright port of the interferometer. In the figure M_{12} and M_{13} are used to guide the LO and M_{14} and M_{15} guide the signal beam to the BHD.

3.5 Displacement requirements for different suspension types

In order to achieve the required sensitivity and not be limited by displacement noise due to seismic noise, the mirrors of the Sagnac speed meter experiment need to be further isolated from motion on the breadboards inside the vacuum chamber. The level of required attenuation depends on where the mirror is used. As part of a cavity the displacement noise of the cavity mirrors M_1, M_2 and M_3 is required to be a safety factor 10 below design sensitivity of the Sagnac speed meter experiment which is equivalent to $<1.5 \times 10^{-18}\,\mathrm{m}/\sqrt{\mathrm{Hz}}$ at 100 Hz. For the auxiliary mirrors—mainly used for beam steering—this requirement is relaxed by the *cavity factor*, that can be calculated from the *finesse* of the cavity

$$F_{\mathrm{cavity}} = \frac{2\mathcal{F}}{\pi}, \tag{3.7}$$

with *finesse* $\mathcal{F}$ for a triangular cavity defined as

$$\mathcal{F} = \pi \frac{\left(R_1 R_2 R_3\right)^{\frac{1}{4}}}{1 - \left(R_1 R_2 R_3\right)^{\frac{1}{2}}}, \tag{3.8}$$

with power reflectivity of the cavity mirrors R_1, R_2 and R_3. Considering an ITM with 700 ppm transmission and perfect ETMs with $R_2 = R_3 = 1$, the Finesse $\mathcal{F}$ can be calculated to be about 8900 and the cavity factor F_{cavity} can be calculated to be about 5650. Relaxing the requirement of the cavity mirrors for the auxiliary mirrors with this factor yields a displacement requirement of about $8 \times 10^{-15}\,\mathrm{m}/\sqrt{\mathrm{Hz}}$ at 100 Hz.

The estimated filtering effect of the passive seismic pre-isolation stacks together with the seismic approximation for the lab in Glasgow in Figure 2.3 of $10^{-7}\,\mathrm{m}/\sqrt{\mathrm{Hz}} \cdot [1\,\mathrm{Hz}/f]^2$ can be used to estimate the residual seismic motion on the breadboard inside the vacuum system at 100 Hz to be about $2.8 \times 10^{-14}\,\mathrm{m}/\sqrt{\mathrm{Hz}}$.

In order to sufficiently isolate the mirrors to the requirements, they are suspended from multistage pendulums. The auxiliary mirrors are suspended from (two-stage) double pendulums which will be referred to as *Auxiliary Suspension* throughout this thesis. The *100 g ETM suspensions* are designed as a triple pendulum to achieve the required isolation and are based on a Glasgow-design for the AEI 10 m prototype [93]. In order to allow damping of the 1 g mirror and to utilise critical components from the 100 g ETM suspension the *1 g ITM suspensions* are designed as a quadruple pendulum. The development, design, commissioning and partial performance testing of all required suspensions for the Sagnac speed meter experiment are presented in the main body of this thesis in the following chapters.

Chapter 4

Modelling of mirror suspensions

In this chapter modelling of mirror suspensions is discussed. One of the limiting noise sources in gravitational wave detectors is seismic noise. As was briefly noted in Chapter 2, to counteract the influence of seismic noise the mirrors of GW detectors are suspended from multistage pendulums. In the following sections, the underlying principles behind multistage pendulums are discussed in an analytical and Lagrangian approach. The benefits of both methods will be highlighted together with other useful tools for this kind of modelling.

4.1 Mirror suspensions

In order to overcome limitation by seismic ground motion, the mirrors in interferometric GW detectors and related prototypes (such as the Sagnac speed meter experiment) are suspended from (multi-stage) pendulums. A single pendulum can be seen as a harmonic oscillator with longitudinal resonance frequency ω_0 given by

$$\omega_0 = \sqrt{\frac{\kappa}{m}} = \sqrt{\frac{g}{l}}, \tag{4.1}$$

where κ is the spring constant, m denotes the mass, g is the acceleration due to gravity and l is the length of the pendulum. As an example, a single pendulum suspended by one wire with a length of 20 cm results in a resonance frequency f_0 of 1.11 Hz, as $f_0 = \frac{1}{2\pi}\omega_0$. Driving the suspension point, or the attachment point of the pendulum, below this resonance frequency causes an in-phase unitary response where the pendulum directly follows the motion of the suspension point. At the resonance frequency of the pendulum the phase between ground motion and motion of the suspended mass is 90°. This phase lag results in resonant enhancement of pendulum motion to a magnitude where the energy introduced by suspension point motion is in equilibrium with the energy dissipated during the

oscillation. At frequencies above the highest pendulum resonance the phase lag between excitation at the suspension point and motion of the mass is 180°. As a result of this phase lag, the magnitude response of the pendulum decays with $1/f^2$.

It is possible to visualise these three cases by plotting the dimensionless transfer function of a suspended mass x_{TM} due to motion of the suspension point x_{SP}. The transfer function of the suspended mass is given by

$$x(\omega) = \left|\frac{x_{\mathrm{TM}}}{x_{\mathrm{SP}}}\right| = \sqrt{\frac{\left(1+\phi^2\right)\omega_0^4}{\left(\omega_0^2-\omega^2\right)^2+\phi^2\omega_0^4}}, \tag{4.2}$$

with corresponding phase

$$\varphi = \arctan\frac{\phi\omega^2}{\omega^2-\omega_0^2\left(1+\phi^2\right)} \tag{4.3}$$

where ϕ denotes the damping factor in the system and ω is the angular frequency. Figure 4.1 shows the transfer function of a single pendulum with length $l = 20\,\mathrm{cm}$ and a damping factor $\phi = 10^{-3}$. The three cases mentioned can be identified in this figure. Below the

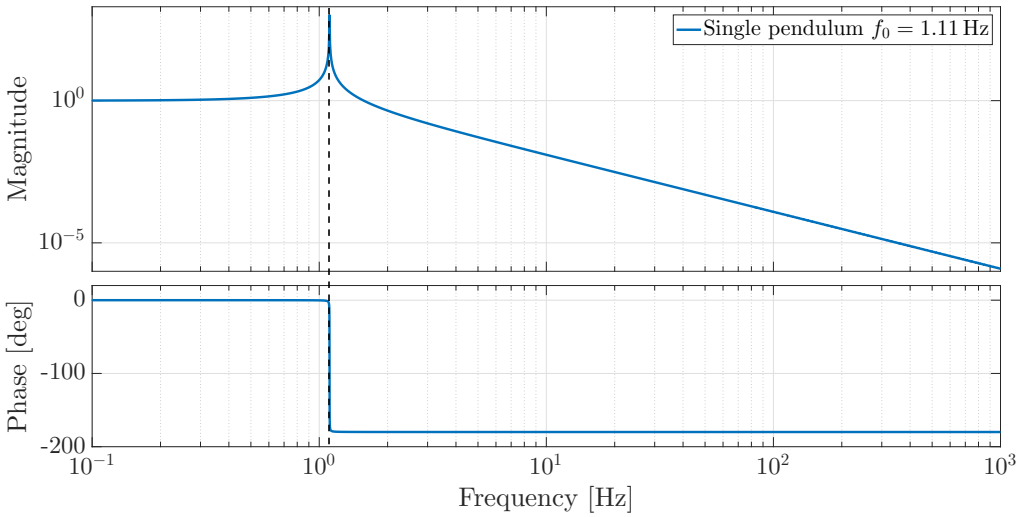

Figure 4.1: Transfer function of a single pendulum with a damping factor of $\phi = 10^{-3}$.

pendulums resonance frequency with in-phase unitary response, at resonance where the phase lag is 90° and the area in which the response decays with $1/f^2$ due to the phase lag of 180°. The resonance frequency is calculated as at 1.11 Hz. The damping factor ϕ can be considered frequency independent[1] for the materials usually used in suspension design and

[1]The damping factor is frequency dependent due to the thermoelastic peak.

is inversely equal to the mechanical quality factor $Q = \frac{1}{\phi}$ of the system,

$$Q = 2\pi \frac{\text{Energy stored in the system}}{\text{Energy dissipated per cycle}}. \tag{4.4}$$

The benefits of high-Q materials in terms of thermal noise have already been highlighted in Section 2.2.3. A trade-off has to be made as high-Q factors can result in extreme motion of the pendulum at the resonance frequency.

4.1.1 Damping

For operation of a pendulum in a GW detector, these resonances need to be damped. As will be highlighted throughout this thesis, different damping mechanisms can be employed. Two mechanisms of particular interest are active and passive damping. Active damping, as described in Reference [94, 95] for Advanced LIGO, can be realised with a coil-magnet actuator and a shadow sensor. The shadow sensor senses motion of the pendulum and provides a phase lead for actuation on the pendulum with the coil-magnet actuator. With active damping it is possible to damp selected mode frequencies resonantly. Passive damping, as described in Reference [96], can be achieved with eddy-current damping and allows damping of motion over the whole band. This type of damping is velocity dependent, thus viscous, and is based on loss due to Joule heating in a conductive material due to induced eddy currents. In the mirror suspensions for the Sagnac speed meter experiment this is achieved with magnets on the pendulum mass that interact with copper coil-formers on which conductive wire coils are wound that are used for actuation on the pendulum.

4.1.2 Multi-stage pendulums

In theory a coupled system of multiple pendulum stages would result in a response of $1/f^{2n}$ from the suspension point, where n denotes the number of stages. This response occurs above the rigid body modes of the pendulum and excludes internal modes such as violin modes, blade spring modes and internal mirror modes. The mirrors in GW detectors or suspended masses can thus be isolated from seismic ground motion to a large degree by adding multiple pendulum stages, however, other noise sources, intrinsic to the pendulum and the materials from which it is made, become limiting. One example was explained as suspension thermal noise in Section 2.2.3. A real mirror suspension as used in the Sagnac speed meter experiment or any GW detector is also much more complex than a single mass suspended by a single wire. With multiple wires (two or four wires are generally used) and attachment points away from the centre of mass (COM) of the suspended mass, all six degrees of freedom (DOF) of the rigid mass need to be taken into account (see Section 4.2.1),

and even couplings between different DOFs occur. Some can be coupled in asymmetric pendulums (e.g. one fixed suspension point) while some will occur due to mechanical inaccuracy or machining tolerances which results in non symmetric attachment points of wires or fibres on the masses. More generally a transfer function for a multi-stage pendulum looks much more complex than the single pendulum in Figure 4.1, showing common and differential mode frequencies of the pendulum masses. As an example of a double stage pendulum, Figure 4.2 shows the longitudinal displacement transfer function for the auxiliary suspension of the Sagnac speed meter experiment which will be discussed in detail in Chapter 5. Depicted is the displacement transfer function from longitudinal top suspen-

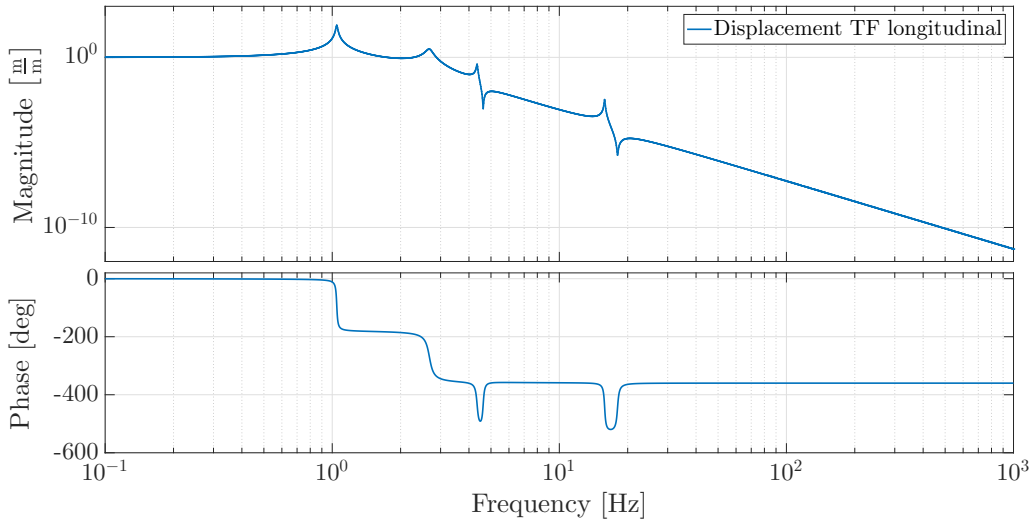

Figure 4.2: Displacement transfer function from longitudinal top suspension point excitation to test mass motion for a double stage mirror suspension, the auxiliary suspension. First and second resonance peak are common and differential longitudinal modes. The two resonance anti-resonance pairs are cross coupling from pitch motion due to coupling between the DOFs. Each resonance can be identified in the phase of the transfer function with a 180° phase lag.

sion point excitation to longitudinal test mass motion. The two resonance peaks at about 1 Hz and 2.7 Hz are the common and differential longitudinal mode frequencies. The two resonance anti-resonance pairs are due to coupling from pitch motion into the longitudinal DOF. This coupling occurs since four wires are used to suspend the test mass from the top mass in the design of this suspension. The expected $1/f^4$ response can be seen to start above the highest mode frequency of the primary DOF, however, cross coupling from different DOFs can introduce resonances that can contaminate the frequency region of interest (here above 3 Hz).

Actuators in multistage pendulum suspensions are used to impose forces onto masses in the pendulum stages in order to statically shift mirror positions or dynamically actuate on the mirror. In contrast to a transfer function, which is dimensionless as defined in Section 4.1, the transfer of imposed force to mirror or test mass motion is referred to as linear response

function. It is common practice to refer to the linear response function as force transfer function. In the following and throughout this thesis, linear response functions will be referred to as "force-displacement" and "torque-angle" transfer functions depending on the kind of input, linear force or torque, respectively. Phase responses will only be shown for measurements. For all other linear response and transfer functions only the magnitude response is presented.

4.2 Modelling of pendulum dynamics

In order to design a mirror suspension that can fulfil given requirements in terms of displacement noise and to gain knowledge about the location of mode frequencies, modelling of the pendulum dynamics is required. The modelling is done by defining all pendulum parameters such as attachment points, materials, shape and weight of suspended masses and finding the equations of motion of the pendulum. This can be done in an analytical approach where the equations of motion are directly found from the pendulum geometry or in a Lagrangian approach where kinetic and potential energy of the system are defined in terms of generalised coordinates and the equations of motion are derived from the Lagrangian equation. Both approaches are presented below and have been used in the course of this PhD thesis.

4.2.1 Direct analytical approach

The simplest model of a suspension is a single stage pendulum moving in one plane only. Considering a point mass (mass m) suspended from a massless wire of length l, as can be seen in Figure 4.3, the pendulum dynamics can be easily found by writing down the angular

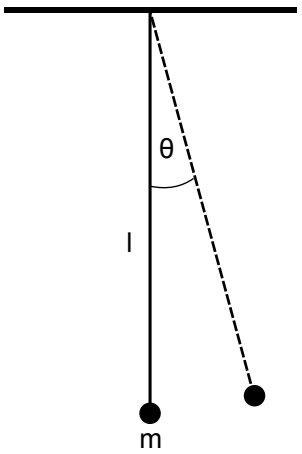

Figure 4.3: Point mass suspended by a massless wire of length l. The dashed wire pictures the same system with a displacement angle of θ.

equation of motion for this system

$$I\ddot{\theta} = M, \tag{4.5}$$

where I is the moment of inertia of the point mass ($I = ml^2$), θ is the angle between the wire in vertical equilibrium and deflected position and M is the torque acting. Whenever the pendulum is displaced slightly the restoring torque is

$$M = -mgl \sin\theta. \tag{4.6}$$

Substituting M in Equation 4.5 the equation of motion becomes

$$l\ddot{\theta} = -g \sin\theta. \tag{4.7}$$

For small angles $\sin\theta \approx \theta$ and thus

$$l\ddot{\theta} = -g\theta, \tag{4.8}$$

which has the form of a simple harmonic motion. As a solution the longitudinal mode frequency of this system becomes

$$f_{\text{long}} = \frac{1}{2\pi}\sqrt{\frac{g}{l}}. \tag{4.9}$$

Before the calculation of a more realistic physical pendulum is started, it is necessary to consider the relevant DOFs of a pendulum. An ideal pendulum has 6n modes, namely the longitudinal mode along the x-axis, the sideways mode along the y-axis, the vertical mode along the z-axis, roll ψ of the mass around the the x-axis, tilt ϕ of the mass around the y-axis (pitch), and rotation σ of the mass around the z-axis (yaw). For the calculation of the mode frequencies for each DOF it is required to know the moments of inertia MOI of the mass I_{x}, I_{y} and I_{z}, the number of wires N used for suspending this mass and their attachment points relative to the centre of mass (COM) described by $\vec{r} = (s_{\text{i}}, n_{\text{i}}, d_{\text{i}})$, where index i denotes the stage number. The analytical calculations and equations, as well as notation, closely follows Reference [97]. Figure 4.4 shows the front and side view of a realistic pendulum mass suspended by four wires. The tension T in each wire can now be described with

$$T = \frac{mg}{N}, \tag{4.10}$$

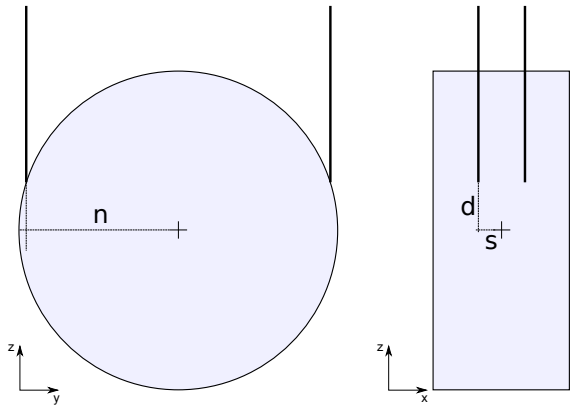

Figure 4.4: Physical pendulum in which the attachment points at the test mass are defined by $\vec{r} = (s, n, d)$. In the picture s is half the wire separation in x-direction, n denotes half the wire separation in y-direction and d defines the distance of the wire attachment point above centre of mass.

where N is the number of wires. Under the assumption of massless wires, each wire acts as a spring with spring constant

$$k_{\text{vertical}} = \frac{AY}{l}, \tag{4.11}$$

where A denotes the cross section of the wire, Y the Young's modulus of the wire material and l the wire length. In the following calculations the mass is assumed to be rigid and all wires to be vertical as is usually the case.

Vertical (bounce) modes

Considering the same pendulum as shown in Figure 4.4 with wire length l on which a force acts in the z-direction, this pendulum mass will be displaced by a small amount z from its equilibrium position z_0. The new wire length is then

$$l' = l + z. \tag{4.12}$$

Treating every wire as an ideal spring the equation of motion can be described with Hooke's law (mass suspended by four equal springs)

$$m\ddot{z} = -4k_{\text{vertical}}z. \tag{4.13}$$

Again this is simple harmonic motion in which $\ddot{z} = -(2\pi f)^2 z$. Thus the vertical mode frequency of a single pendulum is

$$f_{\text{vertical}} = \frac{1}{2\pi}\sqrt{\frac{4k_{\text{vertical}}}{m}}. \tag{4.14}$$

Longitudinal and pitch modes

If the pendulum as in Figure 4.4 is displaced in x-direction, the mass is not only displaced in that direction but the mass is also rotated through an angle ϕ to the vertical. Figure 4.5 shows the situation. The angle of the wires to the vertical is denoted as θ. The COM is linearly displaced by x_n, the crossing point of the line joining the wires to the mass by x_1 and the line joining the wires at the suspension point by x_0. For simplicity it is assumed that the mass is suspended by two wires of length l at a distance d above the line through the COM. The restoring force for tilting the mass is related to the tension in the wires as

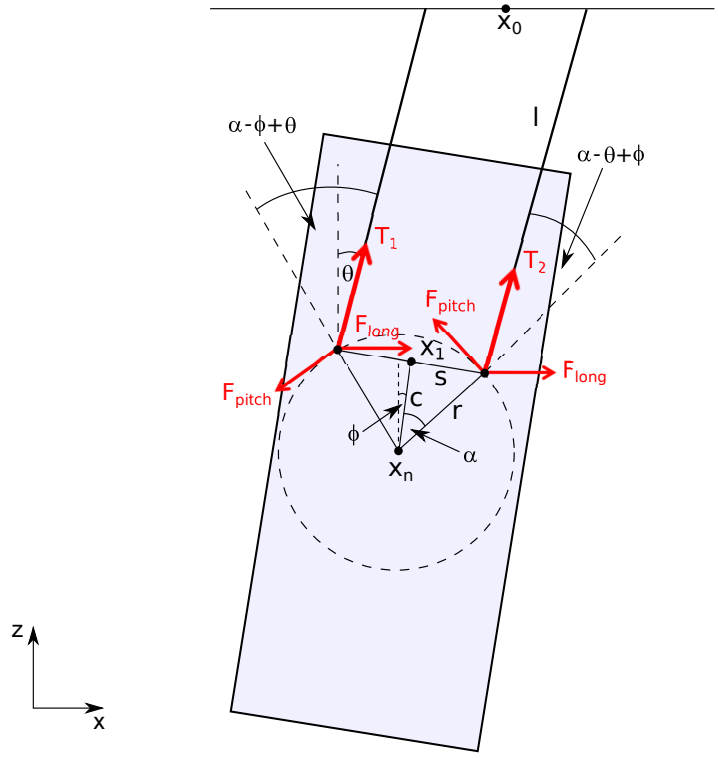

Figure 4.5: Coupled longitudinal and pitch motion of a physical pendulum. The coupling vanishes when the attachment point lies on the line through the COM. The two wires are of the same length, but shown here differently to clarify the coupled motion.

$$F_{1,2} = T_{1,2} \sin(\alpha \mp \phi \pm \theta), \tag{4.15}$$

where the force of the two front wires is equal as is the case for the two rear wires. For small angles ϕ and θ can be defined as

$$\phi = \frac{x_n - x_1}{d}, \tag{4.16}$$

and

$$\theta = \frac{x_1 - x_0}{l}. \tag{4.17}$$

The tension in each wire can be described as

$$T_{1,2} = \frac{mg}{2} \mp kz, \tag{4.18}$$

where z is the change in vertical height as the mass tilts. The restoring torque on the mass can be described as

$$\vec{M} = \vec{r} \times \vec{F}, \tag{4.19}$$

where $\vec{r}$ is the distance to the attachment point and $\vec{F}$ is the perpendicular component of force and thus

$$I_{\mathrm{y}}\ddot{\phi} = -T_2 r \sin(\phi - \theta + \alpha) - T_1 r \sin(\phi - \theta - \alpha), \tag{4.20}$$

where I_{y} is the MOI about the y-axis. Expanding this equation for small $(\phi - \theta)$ and using $z = s\phi$ (with small angle ϕ) gives

$$I_{\mathrm{y}}\ddot{\phi} = mgd(\phi - \theta) - 2ks^2, \tag{4.21}$$

where $d = r\cos\alpha$ and $s = r\sin\alpha$. Solving Equation 4.16 for x_1, substituting in Equation 4.17 and inserting derived θ in Equation 4.21 yields

$$I_{\mathrm{y}}\ddot{\phi} = \frac{mgd}{l}(x_{\mathrm{n}} - x_0) + \left(-mgd - \frac{mgd^2}{l} - 2ks^2\right)\phi. \tag{4.22}$$

For the longitudinal motion the equation of motion is much simpler and given by

$$m\ddot{x}_{\mathrm{n}} = -mg\theta. \tag{4.23}$$

Again substituting θ gives

$$m\ddot{x}_{\mathrm{n}} = -\frac{mg}{l}(x_{\mathrm{n}} - x_0) + \frac{mgd}{l}\phi. \tag{4.24}$$

It is important to note that from Equations 4.22 and 4.24 it is directly visible that longitudinal and pitch motion are coupled whenever the attachment point of the fibres is not on the line of the COM ($d \neq 0$). In case of four wires the k in the above equations needs to be substituted by $2k$. To get the mode frequencies associated with the coupled longitudinal and pitch motion it is necessary to calculate the eigenvalues from the matrix of the coupled

equations. Equation 4.22 and Equation 4.24 can be represented in matrix form

$$\frac{\mathrm{d}^2}{\mathrm{d}t^2}\begin{pmatrix}\phi\\ x_\mathrm{n}\end{pmatrix} = \begin{pmatrix}k_{11} & k_{12}\\ k_{21} & k_{22}\end{pmatrix}\begin{pmatrix}\phi\\ x_\mathrm{n}\end{pmatrix} = \mathbf{A}\begin{pmatrix}\phi\\ x_\mathrm{n}\end{pmatrix}, \tag{4.25}$$

with

$$\begin{aligned} k_{11} &= -\frac{mgd}{I_\mathrm{y}} - \frac{mgd^2}{I_\mathrm{y} l} - \frac{2ks^2}{I_\mathrm{y}},\\ k_{12} &= \frac{mgd}{I_\mathrm{y} l},\\ k_{21} &= \frac{gd}{l},\\ k_{22} &= -\frac{g}{l}. \end{aligned}$$

The coupled mode frequencies can be obtained from the absolute value of the eigenvalues of $\mathbf{A}$

$$f_\mathrm{pitch/long} = \frac{1}{2\pi}\sqrt{(|\mathrm{eig}[\mathbf{A}]|)}. \tag{4.26}$$

Yaw, sideways and roll modes

The mode frequencies for yaw, sideways and roll motion can be obtained in a similar fashion. For brevity only the results are given here and the interested reader can find all calculation steps in [97].

Yaw modes

For yaw the according equation of motion becomes

$$I_\mathrm{z}\ddot{\sigma} = -\frac{mg}{l}(s^2 + n^2)\sigma, \tag{4.27}$$

with the angle of rotation around the z-axis σ and half the wire separation in y-direction n (compare Figure 4.4). Once more this is a simple harmonic motion and the obtained mode frequency for yaw motion can be written as

$$f_\mathrm{yaw} = \frac{1}{2\pi}\sqrt{\frac{mg}{I_\mathrm{z} l}(s^2 + n^2)}. \tag{4.28}$$

Sideways and roll modes

For sideways and roll motion the equations of motion are coupled in a similar way as with the coupling between the longitudinal and pitch motion. The coupling vanishes whenever the wires are attached on the line of the COM of the mass ($d = 0$). The equations of motion can be written as

$$m\ddot{y}_\mathrm{n} = -\frac{mg}{l}(y_\mathrm{n} - y_0) - \frac{mgd}{l}\psi, \tag{4.29}$$

and

$$I_\mathrm{x}\ddot{\psi} = \left(-mgd - \frac{mgd^2}{l} - 2k_\mathrm{roll}n^2\right)\psi + \frac{mgd}{l}(y_\mathrm{n} - y_0), \tag{4.30}$$

where y_0 and y_n denote positions along the y-axis at the top suspension point and in the COM of the suspended mass respectively, and ψ is the rotation angle around the x-axis. Again these coupled equations can be written in matrix form and the mode frequencies can be calculated from the eigenvalue of this matrix. In the case of four wires the k_roll in the above equations needs to be substituted by $2k_\mathrm{roll}$. Equations 4.29 and 4.30 can again be represented in matrix form

$$\frac{\mathrm{d}^2}{\mathrm{dt}^2}\begin{pmatrix}\psi\\ y_\mathrm{n}\end{pmatrix} = \begin{pmatrix}s_{11} & s_{12}\\ s_{21} & s_{22}\end{pmatrix}\begin{pmatrix}\psi\\ y_\mathrm{n}\end{pmatrix} = \mathbf{A}\begin{pmatrix}\psi\\ y_\mathrm{n}\end{pmatrix}, \tag{4.31}$$

with

$$\begin{aligned}
s_{11} &= -\frac{mgd}{I_\mathrm{x}} - \frac{mgd^2}{I_\mathrm{x}l} - \frac{2k_\mathrm{roll}n^2}{I_\mathrm{x}},\\
s_{12} &= \frac{mgd}{I_\mathrm{x}l},\\
s_{21} &= -\frac{gd}{l},\\
s_{22} &= -\frac{g}{l},
\end{aligned}$$

and

$$f_\mathrm{roll,sideways} = \frac{1}{2\pi}\sqrt{(|\mathrm{eig}[\mathbf{A}]|)}. \tag{4.32}$$

This is the full analytical description of the pendulum dynamics in all DOF for a single stage pendulum. The dynamics of multi stage pendulums become somewhat more complicated and involve the inclusion of coupled terms for two or more pendulum masses. The

uncoupled motions (vertical and yaw) become coupling terms between the masses. A detailed description of how this extension is done can again be found in [97] and will not be included here. In [97] the scope was to find the equations of motion for a triple stage pendulum suspension for the GW detector GEO 600 [98], but this model can be reduced to a double stage pendulum as will be used for the auxiliary suspension in the Sagnac speed meter experiment as presented in Chapter 5.

4.2.2 A Lagrangian approach

An alternative approach in finding the equations of motion for a multi-stage pendulum system is using Lagrangian mechanics [99]. The description presented here follows Reference [100] and Reference [101] closely. Instead of finding the equations of motion analytically the Lagrangian approach uses the description of kinetic and potential energies in that system in terms of generalised coordinates q_i. The Lagrangian, often simply named L is defined as kinetic minus potential energy of the system

$$L = E_\mathrm{kin} - E_\mathrm{pot}. \tag{4.33}$$

When the Lagrangian is found it is possible to directly write down the equations of motion for every coordinate by

$$\frac{\mathrm{d}}{\mathrm{dt}}\left(\frac{\partial L}{\partial \dot{q}_\mathrm{i}}\right) = \frac{\partial L}{\partial q_\mathrm{i}}. \tag{4.34}$$

The main challenge is thus to find expressions for the kinetic and potential energies of the system.

Kinetic energy

The kinetic energy of the pendulum system is composed of the translational and rotational energy of the masses. The notation of the coordinates is equal to the one in the analytical approach, thus kinetic energy becomes

$$E_\mathrm{kin} = \frac{1}{2}m_\mathrm{i}(\dot{x}_\mathrm{i}^2 + \dot{y}_\mathrm{i}^2 + \dot{z}_\mathrm{i}^2) + \frac{1}{2}I_\mathrm{x}\dot{\psi}_\mathrm{i}^{\,2} + \frac{1}{2}I_\mathrm{y}\dot{\phi}_\mathrm{i}^{\,2} + \frac{1}{2}I_\mathrm{z}\dot{\sigma}_\mathrm{i}^{\,2}. \tag{4.35}$$

The main assumption again is that the masses are treated as rigid and are the only elements in the system with mass and kinetic energy.

Potential energy

The potential energy in the Lagrangian is a little bit more complex. This is because of different terms contributing. The first term to mention is *gravity*. The potential energy due to the gravitational field can be described as

$$E_{\mathrm{p,grav}} = m_{\mathrm{i}} z_{\mathrm{i}} g. \tag{4.36}$$

The other potential energy terms that play a role are more complicated to describe and will not be derived or shown here but can be found in [100] and [101]. These terms are namely *twisting*, *bending* and *stretching* of the suspension wires and additionally the *cantilever springs*. Cantilever springs are blade springs that act mainly vertically to isolate the suspended masses from vertical ground motion. Additional information can be found in [101]. The sum of all potential energy terms gives the total potential energy for the system

$$E_{\mathrm{p,total}} = E_{\mathrm{p,grav}} + E_{\mathrm{p,twisting}} + E_{\mathrm{p,bending}} + E_{\mathrm{p,stretching}} + E_{\mathrm{p,cantilever}}. \tag{4.37}$$

For determining the dynamics of the system the equilibrium position of the pendulum needs to be found. This can be done by finding the minimum in the potential energy. In the case of the pendulum system this problem can be simplified since the equilibrium is given by the balancing of the tension in the wires to the force of gravity acting on the mass. After that the equilibrium lengths of all wires can be calculated and the state variables can be replaced by

$$q_{\mathrm{i}} \rightarrow q_{\mathrm{i}} + q_{\mathrm{i0}}, \tag{4.38}$$

where q_{i0} are the variables for the equilibrium position. By introducing small perturbations to this equilibrium position the dynamics can now be calculated using the Lagrangian Equation 4.34:

$$\frac{\mathrm{d}}{\mathrm{dt}}\left(\frac{\partial L}{\partial \dot{q}_{\mathrm{i}}}\right) - \frac{\partial L}{\partial q_{\mathrm{i}}} = 0. \tag{4.39}$$

This equation can be re-written in terms of the kinetic and potential energies since the kinetic energy only depends on the $\dot{q}_{\mathrm{i}}$ and the potential energy only depends on the q_{i}

$$\frac{\mathrm{d}}{\mathrm{dt}}\left(\frac{\partial E_{\mathrm{kin}}}{\partial \dot{q}_{\mathrm{i}}}\right) = -\frac{\partial E_{\mathrm{pot}}}{\partial q_{\mathrm{i}}}, \tag{4.40}$$

or in matrix form

$$\frac{\mathrm{d}}{\mathrm{dt}}\left(\mathbf{M}\dot{\vec{q}}\right) = -\mathbf{K}\vec{q}, \tag{4.41}$$

where $\mathbf{M}$ denotes the mass matrix and $\mathbf{K}$ the stiffness matrix of the system. In general the mass matrix only contains constant coefficients, which leads to

$$\mathbf{M}\ddot{\vec{q}} = -\mathbf{K}\vec{q}. \tag{4.42}$$

Assuming a sinusoidal solution the equations of motion become

$$\mathbf{K}\vec{e}_{\mathrm{i}} = \omega_{\mathrm{i}}^2\mathbf{M}\vec{e}_{\mathrm{i}}. \tag{4.43}$$

Diagonalisation of both matrices gives the eigenfrequencies $f_{\mathrm{i}} = \omega_{\mathrm{i}}/2\pi$ and eigenmodes $\mathbf{e}_{\mathrm{i}}$ of the system:

$$q_{\mathrm{i}}(t) = q_{\mathrm{i}} + \mathbf{e}_{\mathrm{i}}e^{\omega_{\mathrm{i}}t}. \tag{4.44}$$

4.3 State space formalism

The description of the dynamical response of a pendulum system (or more general linear time-invariant [LTI] systems) can be done with a state space model. The system can be described with the first order linear differential equation

$$\dot{\mathbf{x}} = \mathbf{A}\mathbf{x} + \mathbf{B}\mathbf{u}, \tag{4.45}$$

$$\mathbf{y} = \mathbf{C}\mathbf{x} + \mathbf{D}\mathbf{u}, \tag{4.46}$$

in which $\mathbf{x}$ describes the state vector (in the case of a simple pendulum $\mathbf{x} = (\phi, x, \dot{\phi}, \dot{x})^{\mathrm{T}}$), $\mathbf{u}$ and $\mathbf{y}$ describe the input and output vectors, $\mathbf{A}$ describes the internal dynamics of the system, $\mathbf{B}$ the inputs, $\mathbf{C}$ the outputs and $\mathbf{D}$ allows so called "pass-through" variables. In case of a pendulum these will not be allowed and thus $\mathbf{D}$ is set equal to zero.

A simple example will demonstrate this modelling. Consider a damped harmonic oscillator with an external driving force F_{ext}. It can be imagined as a mass hanging from a spring k with an additional damping γ implemented in direction of the spring, as can be seen in Figure 4.6. The equation of motion becomes

$$m\ddot{x} = F_{\mathrm{ext}} - kx - \gamma\dot{x} \tag{4.47}$$

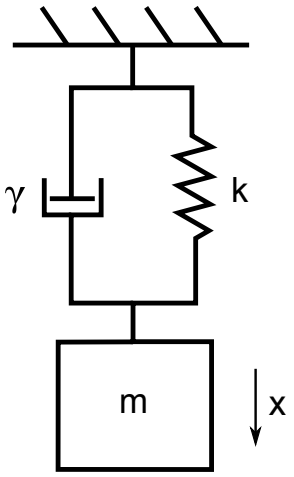

Figure 4.6: Damped harmonic oscillator. A mass m is suspended by an ideal spring k and additional damping γ is implemented parallel to the spring.

The state space equation then become

$$A = \begin{pmatrix} 0 & 1 \\ -\frac{k}{m} & -\frac{\gamma}{m} \end{pmatrix}, \qquad B = \begin{pmatrix} 0 \\ \frac{1}{m} \end{pmatrix}, \tag{4.48}$$

$$C = \begin{pmatrix} 1 & 0 \end{pmatrix}, \qquad D = \begin{pmatrix} 0 \end{pmatrix}, \tag{4.49}$$

and thus

$$\begin{pmatrix} \dot{x} \\ \ddot{x} \end{pmatrix} = \begin{pmatrix} 0 & 1 \\ -\frac{k}{m} & -\frac{\gamma}{m} \end{pmatrix} \begin{pmatrix} x \\ \dot{x} \end{pmatrix} + \begin{pmatrix} 0 \\ \frac{1}{m} \end{pmatrix} F_{\text{ext}}, \tag{4.50}$$

$$\begin{pmatrix} y \end{pmatrix} = \begin{pmatrix} 1 & 0 \end{pmatrix} \begin{pmatrix} x \\ \dot{x} \end{pmatrix} + \begin{pmatrix} 0 \end{pmatrix} F_{\text{ext}}. \tag{4.51}$$

4.4 Useful tools

The tools used for modelling the different types of suspensions throughout this thesis were implemented in MATLAB® [102], Simulink® [102], and Mathematica® [103]. Derivation of the pendulum dynamics was performed in either MATLAB® or Mathematica® from which it was possible to derive the corresponding state space matrices. Modelling of transfer functions functions as well as the implementation of passive velocity-dependent damping was performed in Simulink®. The damping constants for the passive eddy-current dampers were derived from finite element simulations in ANSYS® [104].

4.4.1 Reduced GEO 600 MATLAB® model

The initial modelling followed the analytical approach in a MATLAB® script which was formulated by Callum Torrie in Reference [97] for the GEO 600 triple stage test mass suspension [29]. This particular type of suspension pioneered several techniques that led to a monolithic lowest stage, with hydroxide catalysis bonded ears and fused silica fibres, that ultimately lead to the first ever detection of GWs with Advanced LIGO [12]. John Robert Taylor, a previous PhD-student in Glasgow, reduced this model to cover a double suspension case. This model, together with a custom written Simulink® model, was used for the initial modelling of the auxiliary suspension presented in Chapter 5. In the course of study a major weakness became apparent. The MATLAB® model does not allow the introduction of non-vertical wires that would reduce stress within them and result in very different pendulum dynamics. The implementation of non-vertical wires was considered unnecessary, as a Mathematica model, and in fact a whole toolbox around it, would cover this and all other possible cases. In the most general case, however, the MATLAB® model convinces by ease of use and simplicity. As the auxiliary suspension ended up being designed with vertical wires, this model was used for the parameter study presented in Section 5.6.

4.4.2 The suspension toolbox in Mathematica®

In contrast to the analytical MATLAB® model, the Mathematica® model follows the Lagrangian approach as described above. Initially formulated by Matthew Husman in Reference [100] and directly compared to Reference [97], the Lagrangian approach was transferred and implemented into Mathematica® by Mark Barton [101] for Advanced LIGO. In order to allow for all possible cases a whole toolbox was developed making it possible to model any kind of pendulum up to a 4-stage (quadruple) pendulum. The example in Appendix B.1 shows the basic principle from which the model works for a mass suspended by two coupled springs and how state space matrices are derived from the resulting matrices. The Mathematica® model not only allows all required cases of wire orientation but also enables the implementation of further elastic objects such as vertical blade springs and takes elasticity of wires and fibres into account. The initial model for the 100 g AEI 10 m prototype suspension [93] was formulated in Mathematica®. In this 3-stage or triple pendulum, two stages of vertical isolation blade springs are implemented. The 100 g ETM suspension for the Sagnac speed meter experiment as presented in Chapter 6 is based on a very similar suspended chain, with the same top mass as well as the same vertical blade springs. In the course of this thesis the model was further developed to allow compliance in other DOFs than only vertical to better reflect the transfer function measurements with this suspension.

4.4.3 Simulink® model

In order to implement velocity dependent damping and to allow plotting of transfer functions of the pendulum in MATLAB®, the previously generated state space matrices are fed into a Simulink® model. In the model the inputs and outputs of interest can be defined and perturbations as well as measurement points can be set. During this thesis Simulink® models for each type of pendulum have been written and used for the modelling of transfer functions. The degree of complexity directly depends on the amount of pendulum stages as every additional pendulum stage adds six DOFs for a newly introduced mass.

4.5 Conclusion

In this chapter the modelling of mirror suspensions was described. Starting with the $1/f^2$ response of a pendulum above its fundamental mode frequency, which is basis for attenuating seismic noise, two different approaches to derive the equations of motion were described; the first being an analytical approach in MATLAB® and the second being a Lagrangian formulation in Mathematica®. Both approaches ultimately allow the derivation of state space matrices to describe the full pendulum. In the last section of this chapter the different tools with their advantages and disadvantages for modelling mirror suspensions were presented. This chapter is the basis for all modelling of the dynamics and transfer functions of all suspensions designed in the following chapters.

Chapter 5

The auxiliary suspension

The auxiliary suspension was the first type of suspension to be developed during the course of this PhD work. In the optical layout of the Sagnac speed meter experiment (see Chapter 3.4), most suspended optics are used to align the laser beam, and a total of eleven auxiliary suspensions are required to steer the beam through the set-up. These suspensions are located on one 0.9 m breadboard along with a beam splitter suspension, a suspension for the balanced homodyne readout and two 1 g input test mass (ITM) suspensions. The auxiliary suspensions are not part of the triangular cavities their displacement noise requirement is relaxed compared to the input and end test masses due to the reduced coupling of noise from these suspensions into the readout channel of the Sagnac speed meter experiment compared to the cavity suspensions. The goal was to design a suspension with a compact footprint of no larger than 5 cm × 8 cm and a modelled displacement noise due to coupling from seismic ground motion below the design sensitivity of the Sagnac speed meter experiment, meaning below about 8×10^{-15} m/$\sqrt{\text{Hz}}$ at 100 Hz.

5.1 Mechanical design

The auxiliary suspension is designed as a double pendulum. A schematic of the auxiliary suspension can be seen in Figure 5.1. The design requirements for the auxiliary suspension are summarised in Table 5.1. The optic used in the auxiliary suspension is a 30 mm diameter mirror mounted in a test mass ring-holder made from stainless steel, where the size of the optic was chosen to allow the use of large laser beams while keeping clipping losses of the beam at a minimum. The test mass ring has an outer diameter of 41 mm and leaves a clear aperture of 26 mm for beams to pass through or to be reflected. The sides of the test mass rings are flat and are used as attachment points for wire clamps.

The total weight of the test mass is 75 g and it is suspended by four stainless steel wires of 50 µm diameter from the top mass. Locating two wires on either side of the test mass

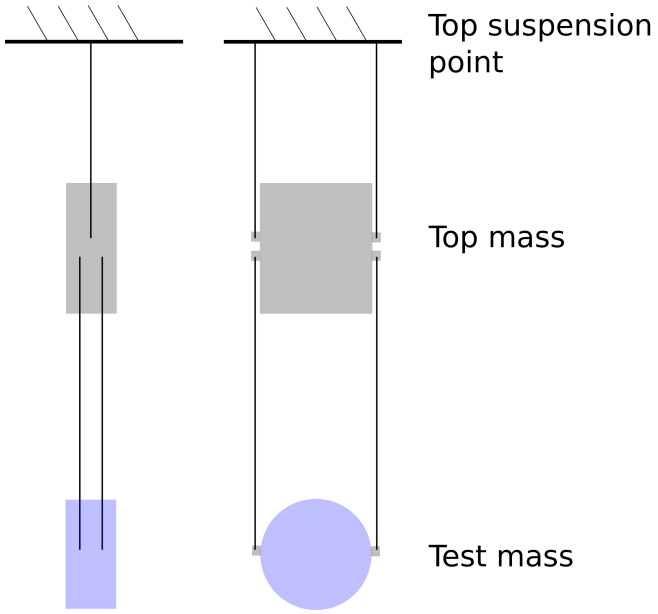

Figure 5.1: Schematic of the double pendulum for the auxiliary suspension. The left hand side shows a side- the right hand side a front view of the double pendulum. The top mass (grey) is made from aluminium and the test mass is a ring made from stainless steel holding a 30 mm diameter optic (blue).

Design requirements
Displacement noise below 8×10^{-15} m/$\sqrt{\text{Hz}}$ at 100 Hz
Highest pitch mode of pendulum below 20 Hz
Control of test mass pitch and yaw
Large clear aperture of test mass
Compact footprint no larger than 5 cm × 8 cm

Table 5.1: Design requirements for the auxiliary suspension.

allows for rotational alignment from the top mass stage. The top mass is designed as a square aluminium block. In order to allow damping of test mass motion at the top mass stage, the top mass was designed to have the same weight and moments of inertia as close as possible to the test mass, while the dimensions were chosen to allow mounting of four 3 mm × 6 mm (diameter × length) magnets. Together with coils wound on copper formers these give rise to passive eddy-current damping and actuation at the top mass stage to align longitudinal, yaw and pitch of the test mass. The top mass is suspended by two 50 µm diameter wires from the top suspension point. The top mass will not be actively controlled as there are no further actuators at the top suspension point. The use of four wires between the top and test mass allows adjusting pitch of the test mass from the top mass, but comes with strong coupling between longitudinal and pitch motion. Due to the $1/f^2$ response of a single pendulum stage, where f denotes frequency, it is optimal to keep all pendulum

resonance frequencies as low as possible. For the auxiliary suspension a pitch mode below 20 Hz was targeted, which could be achieved by placing the wire break-off points on the test mass at 2.5 mm above the centre-of-mass, setting the wire separation on the test and top mass sides to 4 mm.

Figure 5.2 shows a computer-aided-design (CAD) model of the full suspension on the left, parametric and side view of the first assembled real suspension and three close-up pictures showing details of the top mass, the local control assembly, and the test mass holder. The

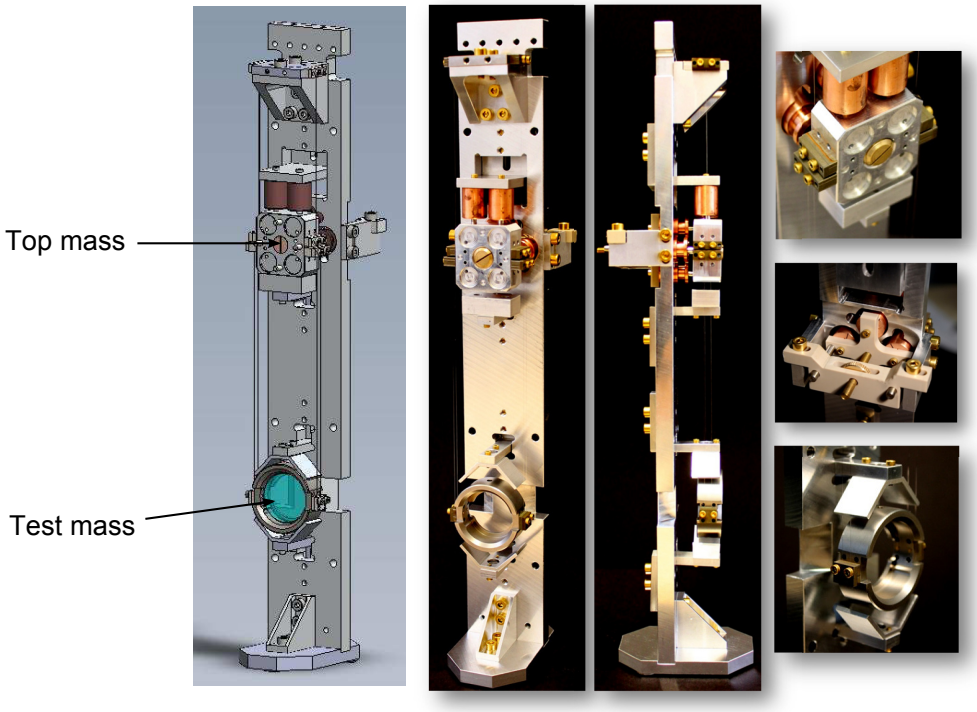

Figure 5.2: Left: Computer aided design model of the assembled auxiliary suspension. Centre: Isometric and side view taken of the auxiliary suspension after test assembling. Right from top to bottom: Close up pictures of top mass, local control assembly and test mass. The local control assembly can be adjusted relative to the top mass in the horizontal and vertical direction. Top and test masses can be clamped in place with mass catchers as can be seen in the CAD model on the left. The suspension frame and local control assembly are described in the main body of this chapter.

suspension was designed to suspend the double pendulum from a top plate that could be mounted to a backboard, thus eliminating the need of a full suspension cage with several feet. The drawback of a single backboard is decreased stability of the suspension, but this can be counteracted by cross-bracing multiple suspensions, thus creating a cage from which several optics are suspended. As can be seen in the figure, additional damping of vertical motion in the suspension is achieved by the use of two additional eddy-current dampers on the top surface of the top mass. These consist of solid copper cups and the same 3 mm×6 mm magnets used in the four coil-magnet actuators for local control.

5.2 Local control and damping

The local control assembly on the auxiliary suspension is mainly used for alignment of the laser beam in the Sagnac speed meter experiment set-up and consists of four coil-magnet actuators in which coils are wound on copper formers. The coils for the auxiliary suspension are made from 150 µm Kapton-enamelled copper wire with 200 turns and are wound on copper coil-formers for a coil length of 4 mm and an inner diameter of 9 mm. As mentioned, 3 mm × 6 mm magnets were used. The response of these coil-magnet actuators can be calculated with a Mathematica® script written by Mark Barton. Figure 5.3 shows the response of the actuator varying with the distance between centre of the coil and centre of the magnet. The point of maximum response (at about 3.9 mm) is often referred to as the

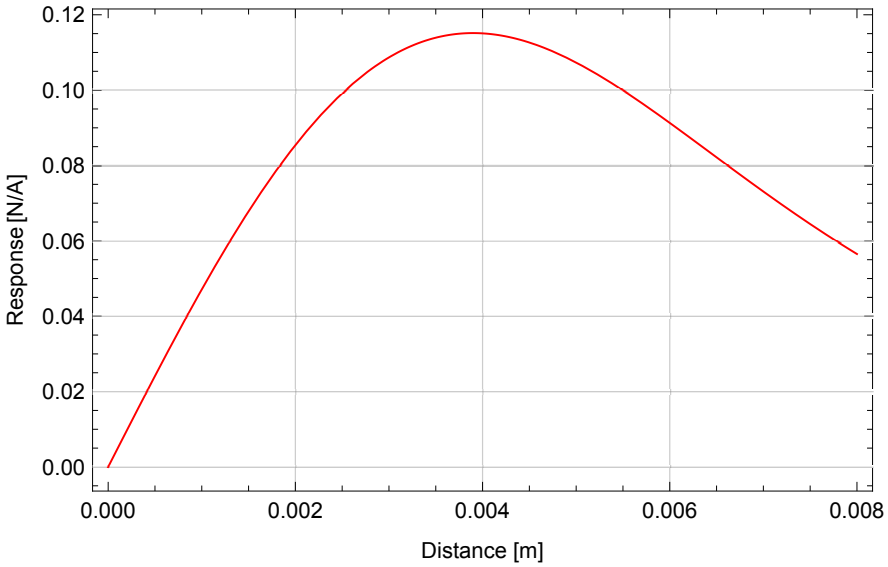

Figure 5.3: The response of the auxiliary suspension coil-magnet actuators is plotted as a function the distance between the centre of the coil and the centre of the magnet.

"sweet-spot" of the coil-magnet actuator in which the coupling from external motion on to the mass is at a minimum. Misalignments from this sweet-spot result in lower response of the coil-magnet actuator and thus in smaller angular and longitudinal range. From this figure it can be seen that the response in the sweet-spot of the actuator is 0.115 N A^{-1}. With a maximum current from the coil-driver electronics of 10 mA, a force of 1.15 mN per coil can be imposed on the top mass, equivalent to approximately 340 µm of longitudinal range using all four coils.

The use of the conductive material copper for the coil former gives rise to passive eddy-current damping. The motion of a 3 mm × 6 mm magnet relative to the coil former creates eddy-currents in the conductive material that represent power loss due to Joule heating. The damping constant, which relates power loss and relative velocity between conductive material and magnet, can be estimated from simulations in ANSYS® Maxwell® [105], in

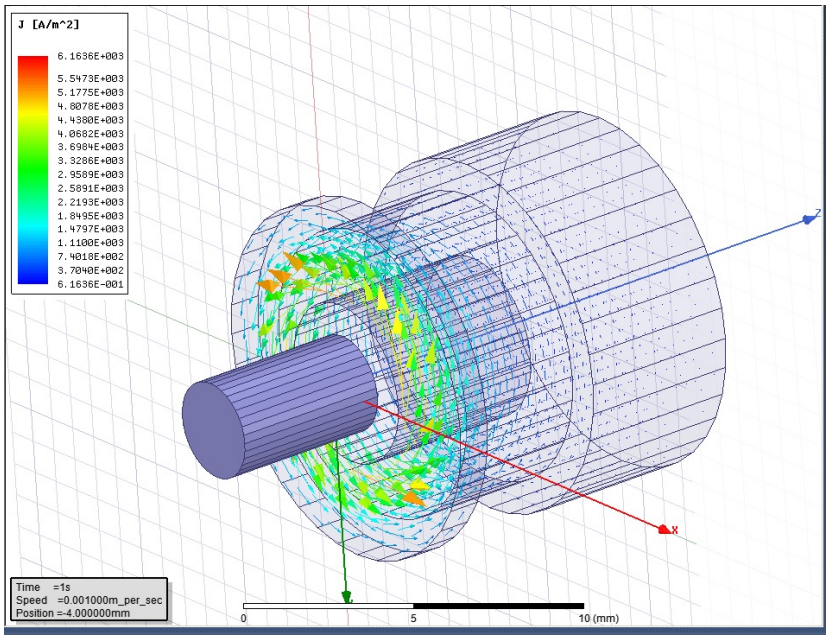

Figure 5.4: A simulation of a coil-magnet actuator in ANSYS® Maxwell® [105]. In this figure the induced Eddy currents from motion of the magnet relative to the coil can be seen as small vectors.

which the power loss in the coil former is simulated. Figure 5.4 shows a screenshot of this simulation. In this figure the induced eddy-currents are made visible. From the simulated motion of the magnet inside the copper former the power-loss per cycle can be estimated and the damping constant deduced to be about $22\,\mathrm{g\,s^{-1}}$ per coil-magnet actuator.

5.3 Modelling

The different modelling tools for suspensions were discussed in Chapter 4. For the initial auxiliary suspension model the analytical approach in MATLAB® was used. During the investigation of parameter influences for the pitch mode, a weakness of the model was identified whereby the analytical model did not accurately represent the case of non-vertical wires. In order to allow all possible cases of wire orientation, the Mathematica® toolbox from Mark Barton [101] was used. In addition, a model-definition for a double pendulum without further isolation objects, such as vertical blade springs, was written for the auxiliary suspension. The modelled pendulum mode-frequencies for the auxiliary suspension are summarised in Table 5.2. From this table it is clear that the initial requirement of the highest pitch mode below 20 Hz is fulfilled. The Mathematica® model also allows the user to export the pendulum dynamics into MATLAB® in the form of state space matrices. These exported state space matrices can be fed into a custom written Simulink® model in which inputs and outputs can be defined. It also allows velocity outputs to be fed back to their corresponding inputs to implement damping into the model. The first six inputs

Frequency in [Hz]		Pendulum mode
1.05	2.68	longitudinal
4.35	15.8	pitch
1.7	4.28	yaw
1.08	2.68	sideways
38.2	123.3	roll
32.0	90.3	vertical

Table 5.2: Simulated resonance mode-frequencies of the auxiliary suspension.

were defined as displacement and rotation of the top suspension point and used for modelling displacement noise due to seismic ground motion in Section 5.4. A linearisation of the Simulink® model allows estimation of corresponding transfer functions from selected inputs to outputs. These are displacement transfer functions in $\frac{\mathrm{m}}{\mathrm{m}}$ and linear response functions from longitudinal or rotational excitation to test mass motion in $\frac{\mathrm{m}}{\mathrm{N}}$ (longitudinal) and $\frac{\mathrm{rad}}{\mathrm{N\,m}}$ (rotation). Even though these are not dimensionless, as a transfer function would be, it is common practice to refer to them as "force transfer functions". In the remainder of this thesis they will be referred to as "force-displacement" transfer function and "torque-angle" transfer function, respectively, depending on the kind of excitation.

The transfer functions of primary interest are two displacement transfer functions from longitudinal and vertical displacement of the top suspension point to test mass motion and the force-displacement and torque-angle transfer functions (longitudinal, yaw and pitch) that can be directly measured. Figure 5.5 shows the displacement transfer functions from longitudinal and vertical motion of the suspension point to corresponding motion of the test mass. The force-displacement and torque-angle transfer functions are depicted in Figure 5.6. It is easy to identify the resonance mode-frequencies from Table 5.2 in these plots.

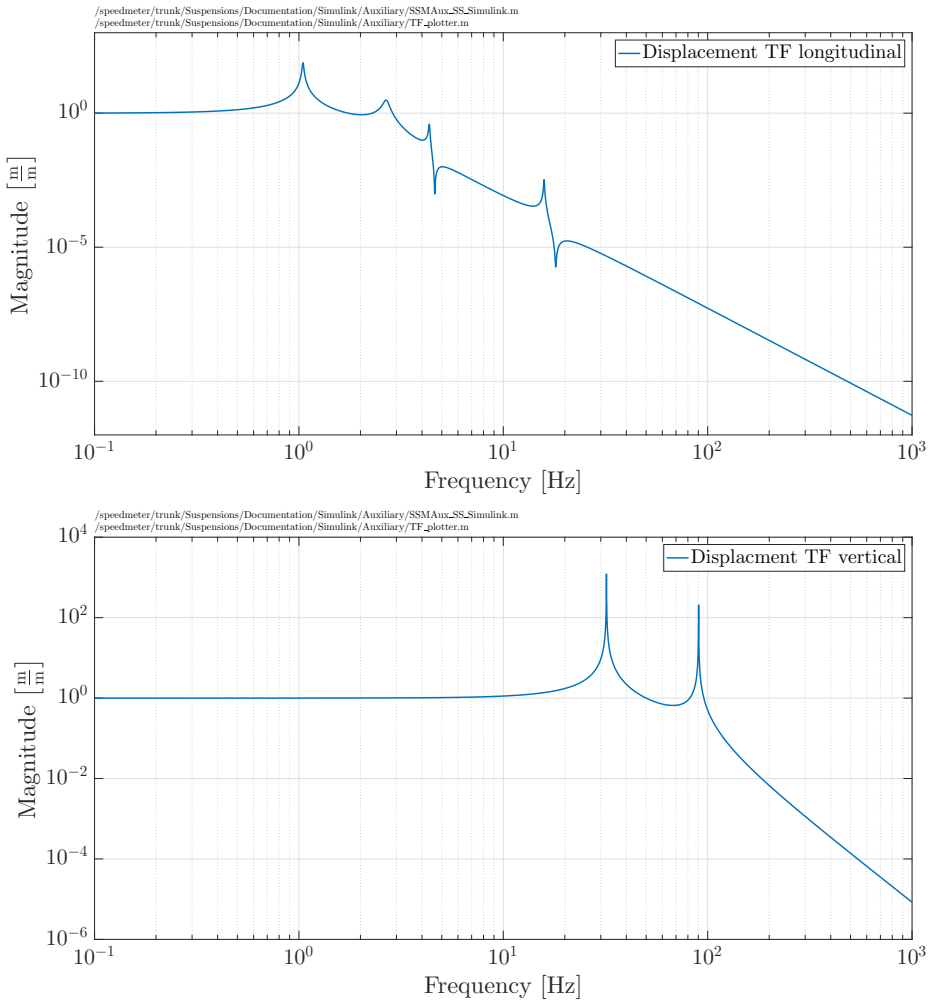

Figure 5.5: Displacement transfer functions from the top suspension point to displacement of the test mass of the auxiliary suspension. Top: Longitudinal transfer function. Bottom: Vertical transfer function.

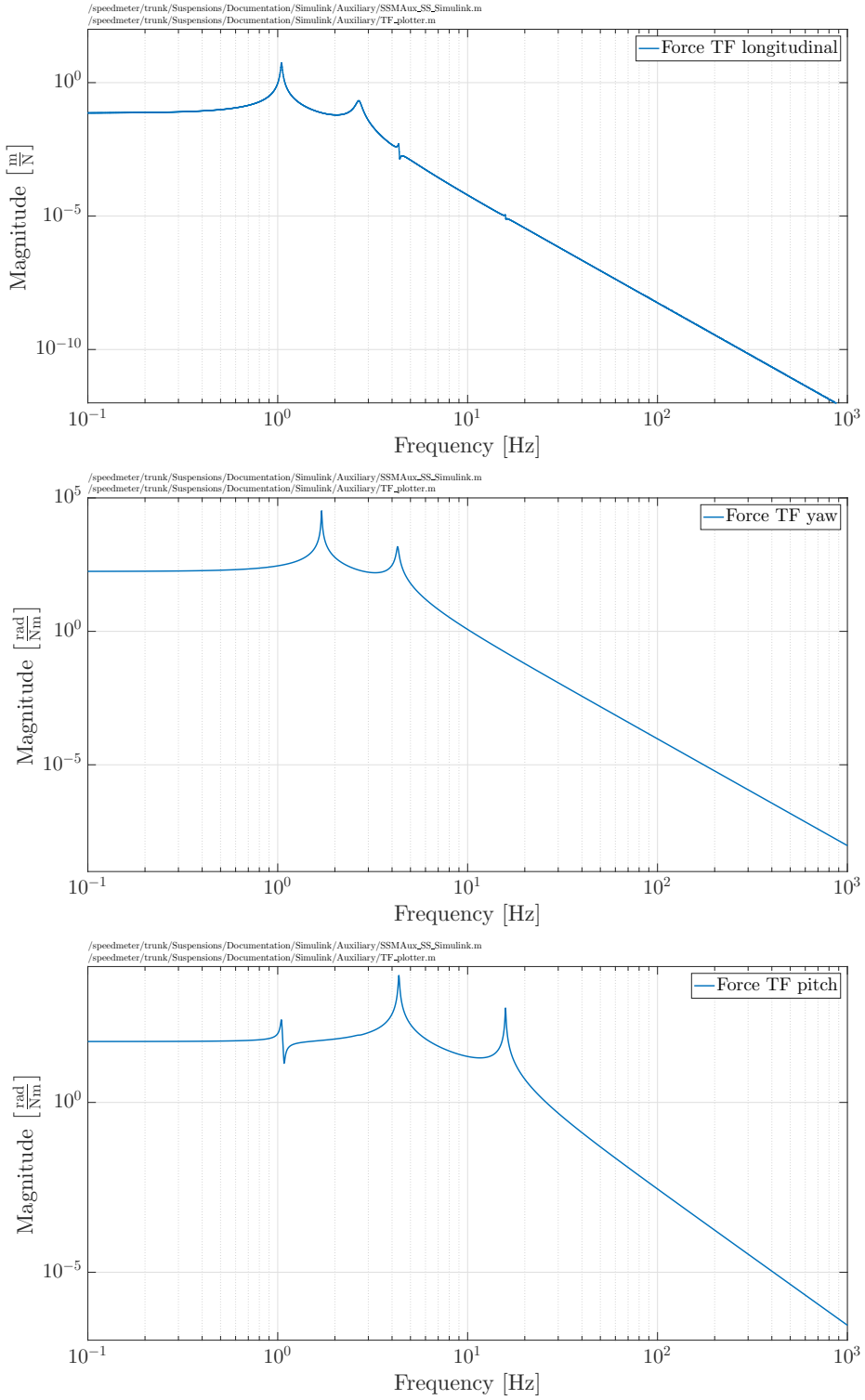

Figure 5.6: Top: Force-displacement transfer function for longitudinal excitation. Middle: Torque-angle transfer function for yaw excitation. Bottom: Torque-angle transfer function for pitch excitation.

5.4 Displacement noise due to seismic noise

The transfer function from vertical ground motion at the top suspension point to vertical motion of the test mass can be used to estimate the coupling of vertical seismic noise into longitudinal displacement noise. In a similar way the coupling from horizontal ground motion to longitudinal displacement noise can be estimated. Figure 5.7 shows both cases of the displacement spectrum for the measured seismic noise in the lab in Glasgow (shown in purple), with vertical in the top panel of Figure 5.7 and horizontal in the bottom panel of Figure 5.7. The measurements of the seismic noise in the lab were taken with an S-13 Seismometer which can be used to measure either vertical or horizontal seismic motion

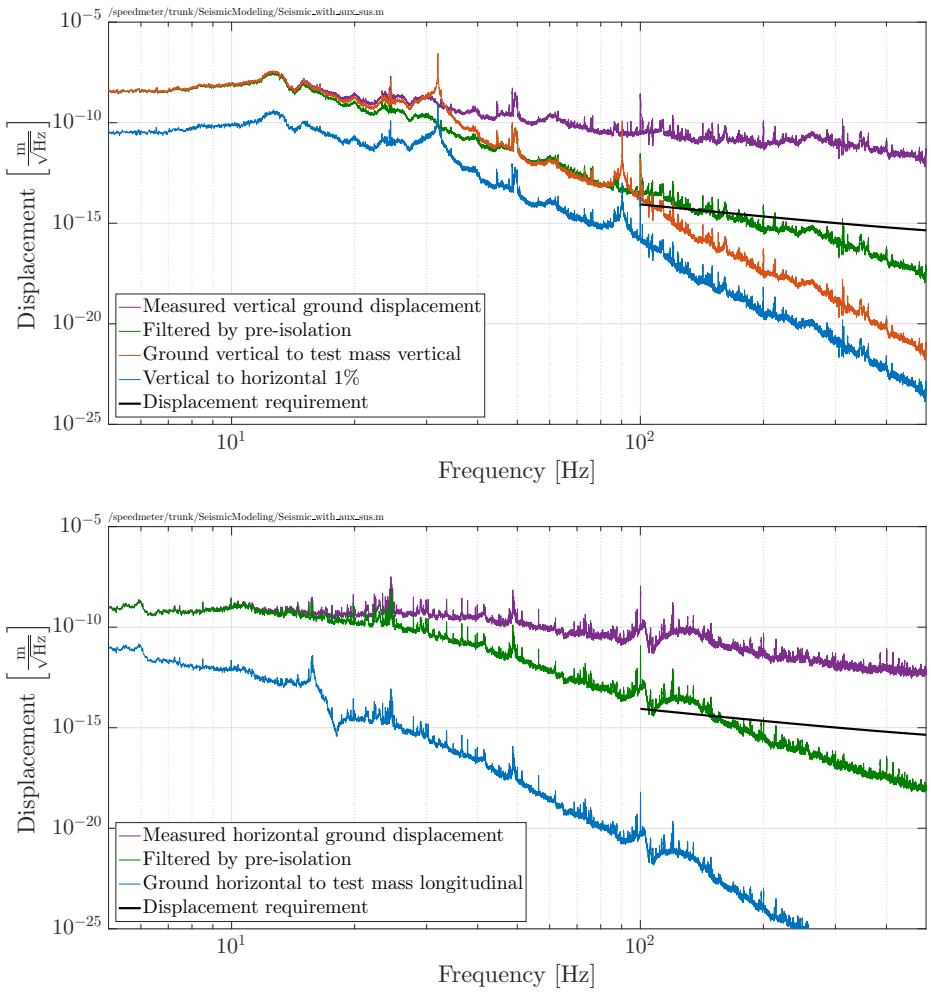

Figure 5.7: Top: Measured vertical ground displacement (purple) using a S-13 seismometer, filtered by simulated passive pre-isolation stacks with corner frequency 18 Hz (green), simulated auxiliary suspension vertical transfer function (red), added estimated vertical to horizontal coupling due to misalignments and manufacturing tolerances (blue) and compared to the displacement requirement for the auxiliary suspension (black). Bottom: Measured horizontal ground displacement (purple), filtered by simulated passive pre-isolation stacks with corner frequency 18 Hz (green), simulated auxiliary suspension longitudinal transfer function (blue) and compared to the displacement requirement for the auxiliary suspension (black).

[106].

In the top figure the green trace shows the estimated effect of the passive pre-isolation stack inside the vacuum system. This stack is composed of four 90 cm diameter steel plates with a weight of 60 kg each with three stages of fluorel rubber springs in between. In the vertical direction a resonance frequency for the passive stack of ∼18 Hz was estimated. It is assumed that the horizontal performance of these stacks is at least as great as the vertical isolation. The red trace in the left figure shows the filtering effect of the double pendulum above its highest resonance frequency. In both, common and differential vertical resonance frequencies at 32 Hz and 90.3 Hz can be identified. The blue trace on the left shows the estimated longitudinal displacement noise due to vertical seismic noise assuming a coupling of 1 % from vertical to horizontal motion due to misalignments and manufacturing tolerances.

In the bottom figure the green trace shows the effect of the passive pre-isolation and the blue trace shows the estimated longitudinal displacement noise due to coupling from horizontal seismic noise. Again, it is possible to identify one resonant feature at 15.8 Hz, the differential pitch mode. The black trace in both figures denotes the design sensitivity of the Glasgow Sagnac speed meter. For both vertical and horizontal seismic noise, the estimated displacement noise lies below design sensitivity.

5.5 Force-displacement and torque-angle transfer function measurements

The force-displacement and torque-angle transfer functions shown in Figure 5.6 can be directly measured. In order to do so, the local control assembly on the top stage of the auxiliary suspension is used to excite the mode frequencies of interest. For the yaw mode the two horizontal coils are used, for pitch the two vertical coils and for longitudinal all four coils in unison. As a sensor for measuring the resulting motion of the test mass a Polytec OFV-505 Vibrometer [107] is used for the longitudinal degree of freedom and a quadrant photo-detector (QPD) for the rotational degrees of freedom, yaw and pitch.

Longitudinal measurement

For the measurement of the longitudinal force-displacement transfer function, the vibrometer was aligned to point at the centre of the test mass. The vibrometer senses the velocity of the mirror surface with an interferometer in a commercial unit that produces output data in $\mathrm{m\,s^{-1}}$. To excite the longitudinal mode, band-limited Gaussian noise is injected in phase to all four coils of the local control assembly. The result of this measurement is plotted together with the simulated force-displacement transfer function in Figure 5.8. For this

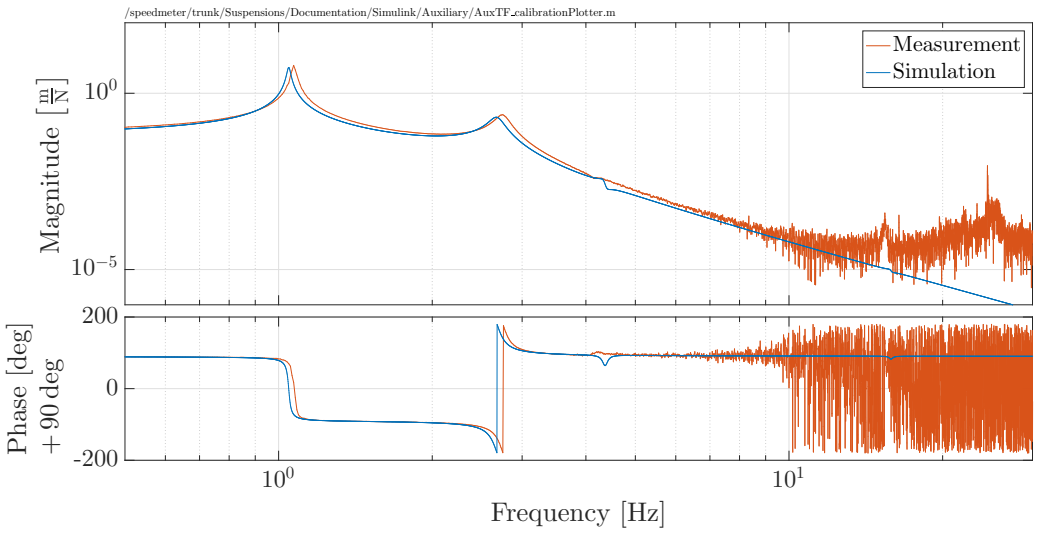

Figure 5.8: Measured longitudinal force-displacement transfer function. The measurement is plotted in red and the modelled force-displacement transfer function is shown in blue. The top part shows the measured magnitude response and the bottom part shows the measured phase response. In both, the measured resonances are predicted slightly lower in the model.

measurement 5 V band limited (300 Hz) Gaussian noise is injected to the four coils with the CDS tool diaggui [108], that is also used for initial analysis of the averaged measurement data. As the vibrometer senses the velocity of the test mass and the force-displacement transfer function is given in $\mathrm{N\,m^{-1}}$ the measurement data needs to be calibrated. Firstly, the velocity data is converted to metres per volt. Secondly, the plot is scaled for the measured response of the vibrometer head. Thirdly, the coil-magnet actuator data is converted to newtons per volt before the data is finally calibrated to metres per newton. It can be seen that the model represents the measurement well, even though resonances are represented slightly lower in the model than they are measured. It is easy to identify the two longitudinal mode-frequencies nominally at 1.05 Hz and 2.68 Hz. The mode at 1.05 Hz is measured at 1.07 Hz and the mode at 2.68 Hz is measured at 2.74 Hz. Due to the pendulum characteristics and the $1/f^4$ response above the highest pendulum frequency the measurement is dominated by noise above 10 Hz. The phase response is represented well by the model along with the same differences in locations of 180° phase shifts due to the resonances. It can be seen that the phase has been shifted by 90° in order to avoid phase jumps due to wrapping of noisy data. Appendix A presents an example of the effect of phase shifting prior to wrapping.

Yaw and pitch measurement

For the two rotational degrees of freedom, yaw and pitch, the sensor is a QPD in an optical lever set-up. A He-Ne laser and two silver-coated mirrors direct the beam onto the suspen-

sion test mass and then onto the QPD. The schematic of the optical lever set-up is depicted in Figure 5.9. Whenever the suspended test mass in the auxiliary suspension rotates (yaw

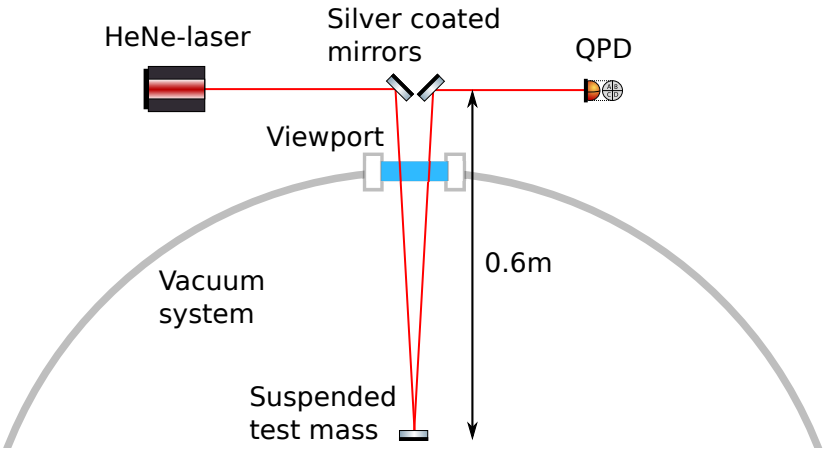

Figure 5.9: Optical lever set-up for the measurement of the torque-angle transfer functions for yaw and pitch. A HeNe-laser is reflected off the suspended test mass. The rotation is sensed by a QPD.

or pitch) the laser spot moves on the QPD. For a calibration of the measured data it is thus necessary to know the range of the auxiliary suspension in yaw and pitch. This measurement was taken with a direct reflection of the beam off the test mass. For an input current of 5 mA through each coil a total range of 12.6 mrad in yaw and 4.6 mrad in pitch can be measured.

With this pre-measurement, the measured data is calibrated with the following steps. Firstly, the QPD data is calibrated to get radians per output voltage. Secondly, the the raw data of the QPD is multiplied with the total amount of counts measured in CDS with the QPD. Thirdly, the force for two coils is calculated, before the data is finally calibrated to radians per newton-metre. Both measurements for yaw and pitch are shown in Figure 5.10. The top figure shows the yaw measurement where it can be seen that the model again represents the measurement very well except for a very slight mismatch of the second peak. Both yaw mode-frequencies can be easily identified. The lower figure shows the pitch measurement where the pitch to longitudinal coupling and the two pitch mode frequencies can be seen. However, it is here that a larger difference between the model and the measurement can be seen. The first pitch mode is measured to be 4.17 Hz where the model predicts 4.35 Hz and the second pitch mode is measured to be 15.49 Hz instead of 15.8 Hz. This could be caused by small differences in the location of the wire break-off points at top and test masses. In the following section this thesis will present a short parameter-study to identify the parameters that need to be changed in the model to represent the measurement more effectively. The phase response in both cases is represented well by the model with the same shifts in location of 180° phase changes due to the resonances.

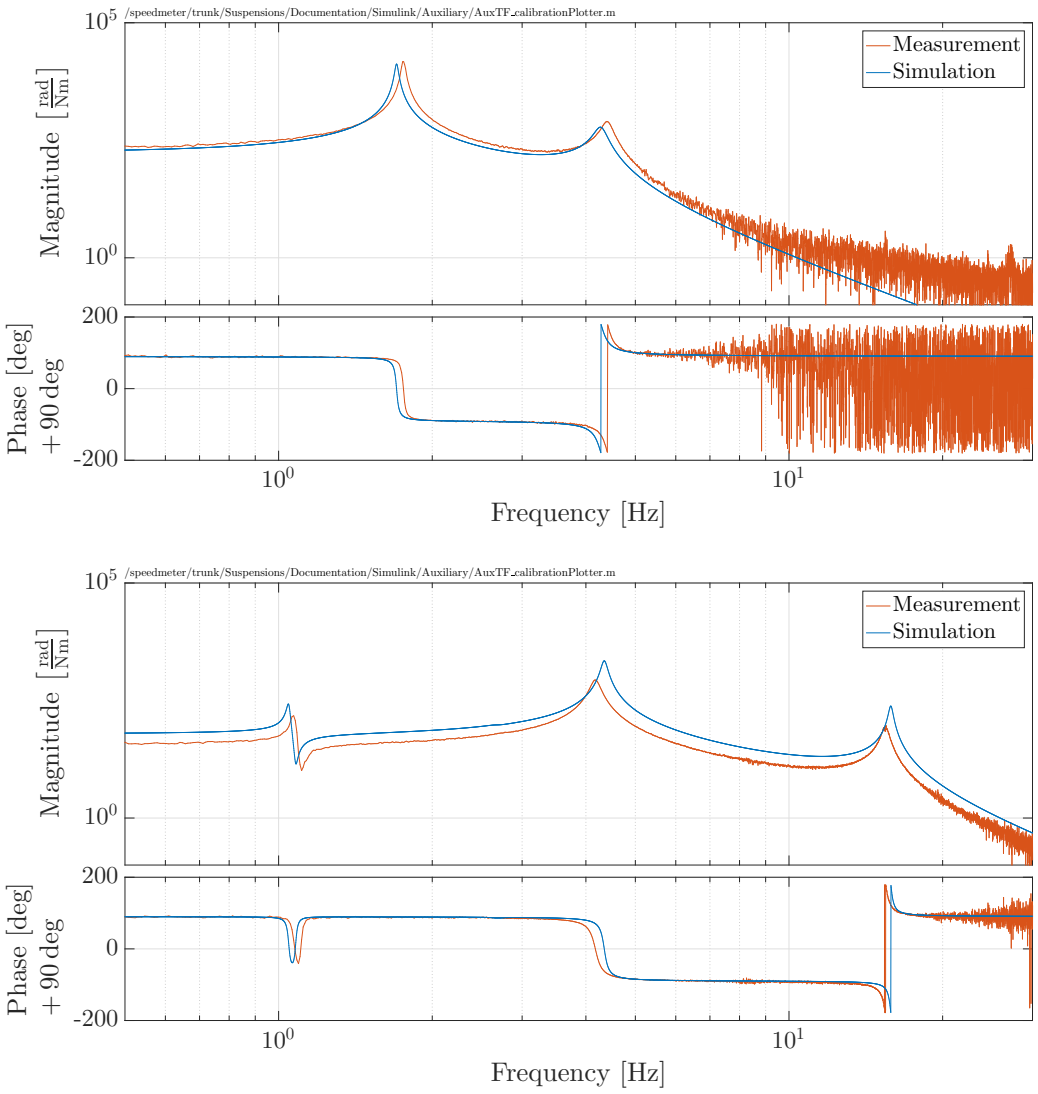

Figure 5.10: Measured torque-angle transfer functions compared to the model. Top: yaw mode. Bottom: Pitch mode. For the pitch mode measured mode frequencies are lower than the ones predicted by the model whereas for the yaw mode they appear higher than in the model. The phase response is represented well by the model.

5.6 Adjustment of model parameters

A second auxiliary suspension was measured to verify the previously measured force-displacement and torque-angle transfer functions of the first auxiliary suspension and to investigate potential differences between builds. In order to adapt the model to fit the measurements, a parameter study was conducted. For the second measurements the same set-up as described in the previous section was used. The result of the measurements can be found in Figure 5.11. The results of both suspensions are plotted together with the modelled force-displacement and torque-angle transfer functions. To more clearly convey where differences between the builds lie, the ratio of the two force-displacement and torque-angle

transfer functions has been plotted.

In the longitudinal measurement it can be seen that the first resonance peak overlaps closely. The second resonance peak however differs by ∼0.06 Hz. This is a small difference and can be explained by differences in wire length of the upper wires and/or differences in the position of the upper wire clamps on the top mass within manufacturing tolerances of the mechanical parts. The same explanation is valid for the differences that can be seen in the second resonance peak of the yaw measurement. It can be seen that the first peak overlaps well but the second peak is different by ∼0.1 Hz. The pitch measurement seems to overlap well between the two suspensions even though the model is further off for this measurement. In general it can be said that the differences between the two auxiliary suspensions are below 5 %.

To facilitate a better understanding, and for ease of use, the analytical MATLAB® model was used for a more detailed parameter study. In order to quantify the change in mode frequency of a certain mode, parameters were changed independently from each other by a fixed percentage. The impact of that change for each resonance peak was noted. The results of that parameter study can be found in Table 5.3. The biggest changes for the two pitch modes are marked red. It can be seen that the wire separation (down by 5 %) of the two wires on each side of the top and test masses has a significant influence on the higher pitch mode (down by 4.45 %). In general this change does not seem unreasonable as the changes in wire separation are of the order 100 µm which is well within the manufacturing tolerances of the mechanical parts that define this parameter. The same can be said about the changes of the wire break-off points. These are defined by metal clamps whose positions are defined by slide-fit dowel pins. By adding up tolerances, a maximum uncertainty in the clamps' position of 250 µm is easily reached.

With changes made to these parameters it is possible to adjust the model to match the measurement. In Figure 5.12 the adjusted model is plotted against the two measured suspensions for the pitch mode. The model now closely fits the two resonance peaks. The difference in magnitude between the two suspension measurements is a direct result of equal calibration of force being applied to both suspensions. Although differences between the responses of the coil-magnet actuators are likely, e.g. from different distances of the local control assembly to the top mass and thus the magnets.

5.7 Conclusion

In this chapter, the first type of suspension developed in the course of this thesis was presented, the auxiliary suspension. The design considerations and constraints were explained that lead to the mechanical design of the suspension. The modelling of the auxiliary suspen-

Changed parameter	1st long change in %	2nd long change in %	1st pitch change in %	2nd pitch change in %	1st yaw change in %	2nd yaw change in %
Top wire length (up 1 %)	-0.19	-0.37	N/A	N/A	-0.17	-0.3
Bottom wire length (up 1 %)	-0.19	-0.11	N/A	-0.2	-0.17	-0.14
Wire separation in x bottom (down 5 %)	N/A	N/A	-0.11	-4.45	N/A	N/A
Wire separation in y top (up 1 %)	N/A	N/A	N/A	N/A	+0.23	+0.32
Wire separation in y bottom (up 1 %)	N/A	N/A	N/A	N/A	+0.29	+0.21
Upper break off point TOP (up 10 %)	N/A	+0.07	+1.36	+0.31	N/A	N/A
Lower break off point TOP (up 10 %)	-0.09	-0.04	+1.56	+0.3	N/A	N/A
Break off point TM (down 10 %)	+0.09	+0.04	-1.86	-0.04	N/A	N/A
MOI y TOP (down 0.5 %)	N/A	N/A	+0.09	+0.31	N/A	N/A
MOI z TOP (down 0.5 %)	N/A	N/A	N/A	N/A	+0.06	+0.39
MOI y TM (up 0.5 %)	N/A	N/A	-0.25	-0.01	N/A	N/A
MOI z TM (up 0.5 %)	N/A	N/A	N/A	N/A	-0.29	-0.02

Table 5.3: Influence of auxiliary suspension parameter changes on the simulated mode frequencies. The most significant changes for the pitch modes are marked in red. In this table, TM stands for test mass, TOP denotes the top mass, x is the direction orthogonal to the mirrors plane, y is sideways and z is vertical.

sion dynamics was performed in Mathematica®. Modelling of the transfer functions of the double pendulum was done in Simulink®, in which damping was implemented in the form of passive eddy-current damping. With estimations of the horizontal and vertical seismic ground motion in the lab it was possible to estimate the displacement noise of the suspension. The performance of the auxiliary suspension was quantified by the measurement of force-displacement and torque-angle transfer functions for the longitudinal, the yaw and pitch mode from top mass excitation to test mass motion. As the model did not perfectly represent the measurement, a parameter study was conducted to find parameters that cause the biggest changes in mode-frequencies and with this study the model was adjusted to fit the measured force-displacement and torque-angle transfer functions.

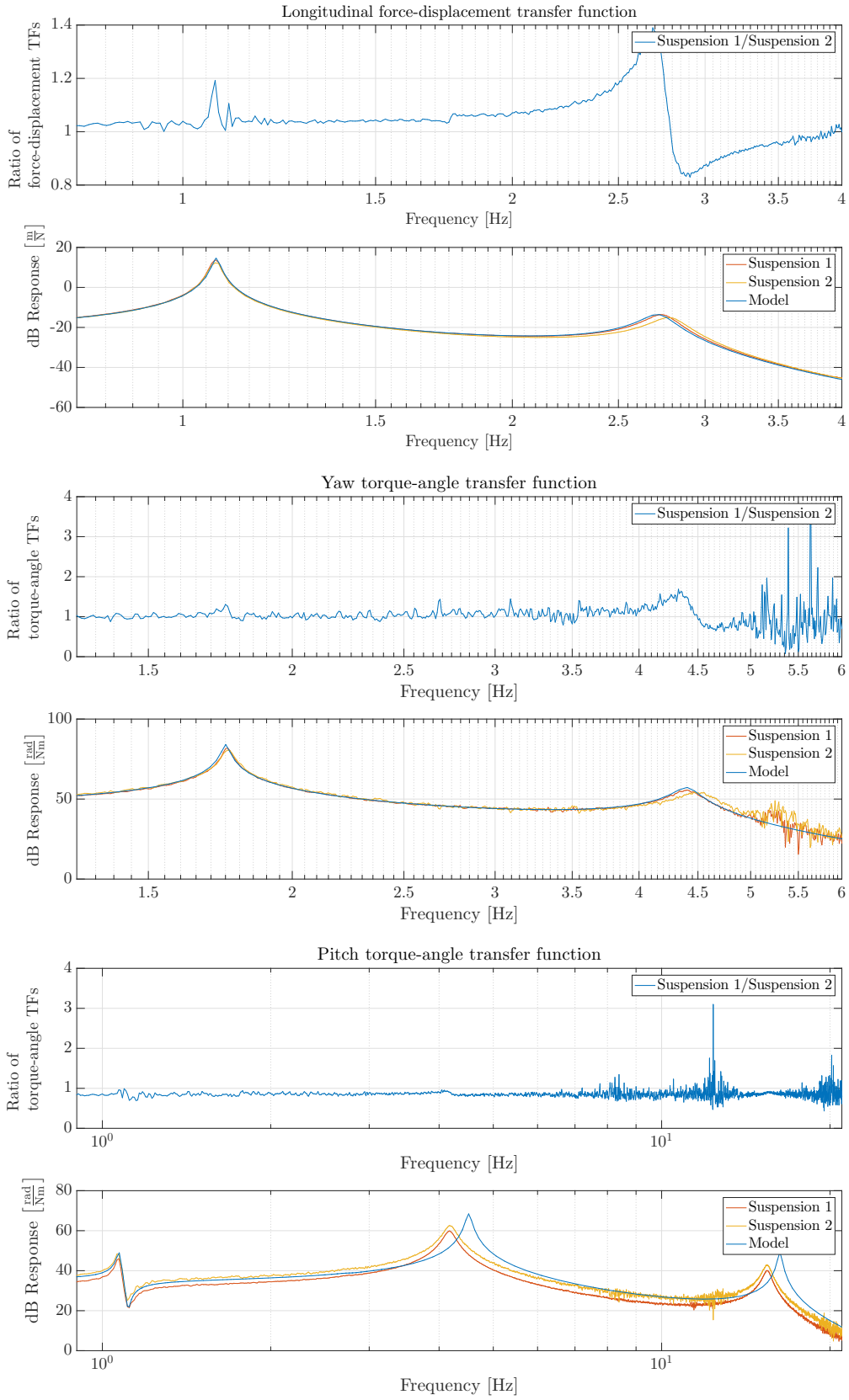

Figure 5.11: Differences in mode-frequencies of two assembled auxiliary suspensions. Plotted are ratio of the measured force-displacement and torque-angle transfer functions for two suspensions and the measured force-displacement and torque-angle transfer functions in comparison to the model for longitudinal (top), yaw (middle) and pitch mode (bottom).

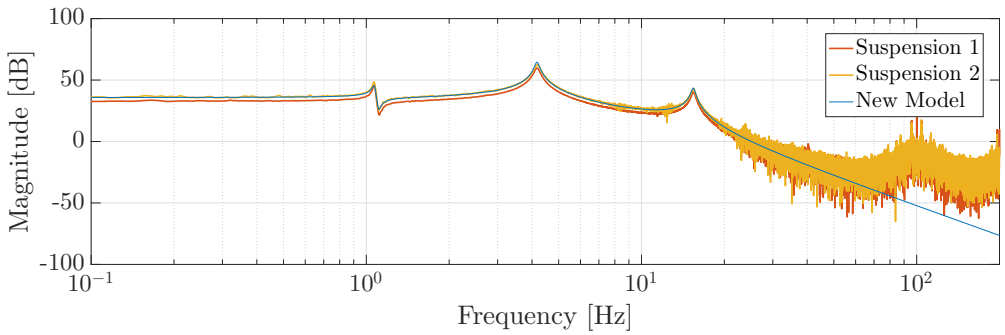

Figure 5.12: The torque-angle transfer function for pitch in blue is plotted against the two suspension measurements. It is easy to see that the model fits the measurements nicely. The slight difference in magnitude between the suspension measurements is due to the different response of the coil-magnet actuators on the suspensions.

Chapter 6

100 g end test mass suspension

In this chapter the 100 g end test mass suspension of the Sagnac speed meter experiment is discussed. Designed as a triple pendulum with two additional stages of vertical isolation blade springs, these suspensions are part of the triangular cavities and thus their displacement noise is required to be below 1.5×10^{-18} m/$\sqrt{\text{Hz}}$. Their design has been studied in detail as the suspended chain is the same as the design used in the AEI 10 m prototype [109]. To minimise thermal noise in the suspension elements (suspension thermal noise), the lowest stage in these suspensions is made entirely of fused silica, a low loss material. The creation of this lowest stage had not been fully investigated previously and will be highlighted in this chapter in which all necessary manufacturing steps and procedures are described. In addition the suspension dynamics were verified by measuring force-displacement and torque-angle transfer functions from top and penultimate masses to test mass motion.

6.1 Mechanical Design

The 100 g end test mass suspension for the Sagnac speed meter experiment is designed as a triple pendulum with two stages of vertical blade springs at the top. The schematic layout can be seen on the left hand side of Figure 6.1. The 100 g test mass is suspended by four fused silica fibres from a penultimate mass of the same weight in order to gain control over the pitch of the test mass from the penultimate stage. The four fibres are welded to small interface pieces (ears) on the sides of the masses that are attached to the masses by hydroxide catalysis bonding (HCB) [110] to create a fully monolithic assembly prior to welding. Due to the use of a low-loss material such as fused silica for all components, thermal noise in the monolithic suspended elements can be minimised. The penultimate mass is suspended by four 50 µm stainless steel wires from Fort Wayne Metals (type: 304V, condition: Hyten, finish: SLT®wire) [111] arranged in two loops. Again four wires allow control of pitch from the top mass of the pendulum and the wires are fixed on vertical

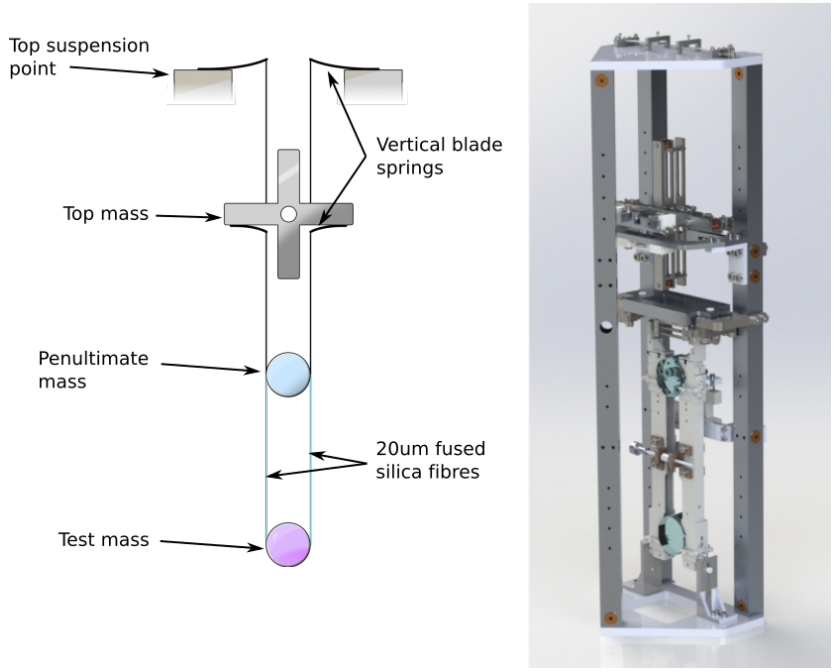

Figure 6.1: On the left side a schematic of the triple pendulum for the 100 g ETM suspension is shown. The test mass is suspended monolithically with four fused silica fibres from the penultimate mass. Two stages of vertical isolation blade springs can be found at the top suspension point and inside the top mass. Depicted on the right hand side is a rendered image of the computer-aided-design model. The suspension is housed in a cage with a triangular footprint so that four suspensions can be placed in one 1 m diameter vacuum tank.

blade springs that are mounted in small cartridges inside the top mass. These vertical blade springs are designed to reduce the vertical bounce modes of the pendulum. The natural frequency of the blades can be estimated from [112]

$$f_{\text{blade}} = \frac{1}{2\pi}\sqrt{\frac{Ebd^3}{4m_{\text{sus}}\alpha l^3}}, \tag{6.1}$$

where E is the Young's Modulus of the blade material, b is the width of the blade base that is clamped, d is the thickness of the blade, l is its length and α is a dimensionless shape factor[1]. Assuming a triangular shape for ease of calculation, the loaded blades inside the top mass have a natural frequency of 2.93 Hz.

The top mass is designed as a composite cross to be able to host the aforementioned blade cartridges and to create long lever arms for coil-magnet actuators that are used for alignment and slow actuation on the pendulum. The top mass is suspended by two 100 µm stainless steel wires from the top suspension point where these wires are attached to a second set of vertical blade springs. These top blades are slightly bigger and have a loaded natural frequency of 2.66 Hz assuming a triangular shape as above. At the top stage only

[1]The shape factor is 1 for a rectangular blade, 1.5 for a triangular shape and between 1.36 and 1.44 for a trapezoidal shape [112].

two wires are used as there is no desire for actuation at the top suspension point.

In their original design for the AEI 10 m prototype [109] the suspended chain was mounted in a large four-legged suspension cage. Due to space constraints in the Sagnac speed meter experiment this cage was altered to fit four suspensions independently into one of the vacuum tanks (compare Figure 3.11). As part of the triangular cavities, the test masses are used at a 42.8 degree angle of incidence compared to zero degree angle of incidence in the AEI 10 m prototype case. This allowed us to change the cage design into a more compact triangular structure with one leg in front of the optic. A CAD model of this design can be seen in Figure 6.1 on the right hand side. The suspended chain was slightly modified to further shrink the initial design. Instead of angled wires in the top stage of the suspension these were made vertical for the Sagnac speed meter experiment. This will have a slight (but negligible) impact on the sideways and yaw mode-frequencies of the triple pendulum.

6.2 Actuators

The top stage of the pendulum can be driven with coil-magnet actuators similar to the auxiliary suspension. The coils are made from the same Kapton-enamelled copper wire with 150 µm diameter and 60 turns. A computer-aided-design model of the local actuator assembly with the top mass can be seen in Figure 6.2. The coils are wound around copper

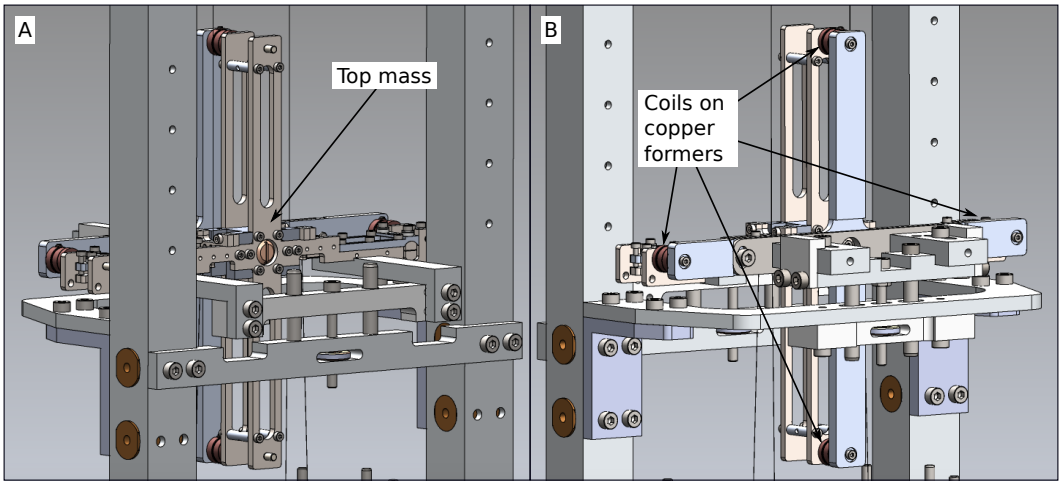

Figure 6.2: Computer-aided-design model of the local control assembly and the top mass. Picture A and B show isometric views from different angles. The coils are mounted on a cross that can be adjusted laterally in all three directions and rotated around the centre in order to align the coils to the magnets on the top mass.

formers and together with a 3 mm × 6 mm (diameter × length) magnet, allow the coils on the copper former to provide passive eddy-current damping and actuation. The modelled damping constant for four coils in the longitudinal direction is 0.12 kg s^{-1}. The response for

a single coil-magnet actuator can be calculated with the Mathematica® script previously introduced to be 32 mN A^{-1} analogous to Section 5.2. At the top stage level it is planned to only apply DC-offsets for beam steering, since fast actuation at this stage is not easily possible due to filtering of any induced force by the two stages of pendulum below.

The penultimate stage can be driven in a similar way using coil-magnet actuators. The coil dimensions and wire material are identical, however the coil-former are in this case made of polyether ether ketone (PEEK) and smaller 2 mm × 2 mm (diameter × length) magnets are used. A computer-aided-design model of the global control assembly and the penultimate mass is shown in Figure 6.3. The material choice of the former eliminates additional

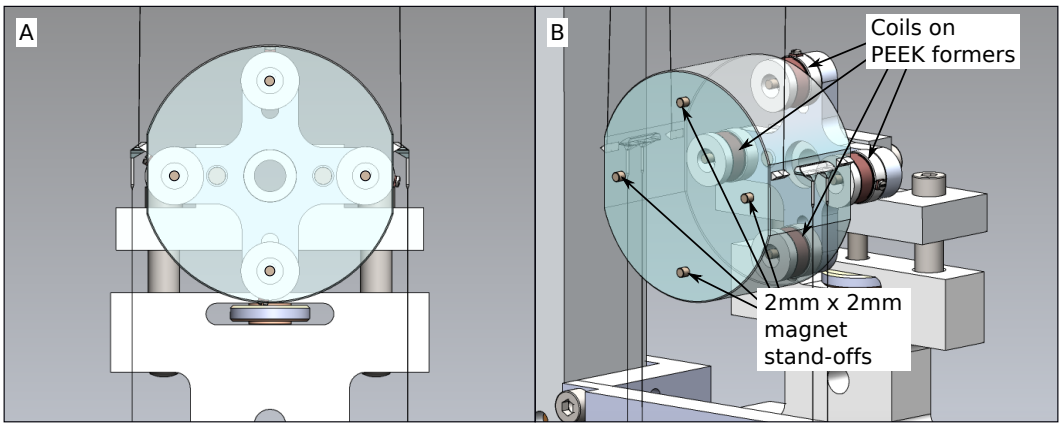

Figure 6.3: Computer-aided-design model of the global control assembly and the penultimate mass. Picture A and B show isometric views from different angles. The coils are mounted on a cross that can be adjusted laterally in all three directions and rotated around the centre in order to align the coils to the magnets on the top mass.

passive damping from induced eddy-currents in the former. As will be seen in Chapter 8, dissipation in a conductive former gives rise to force noise of the damping system [96] that can spoil the desired displacement sensitivity of the suspension. The magnets on the penultimate mass are smaller 2 mm × 2 mm neodymium magnets and in order to position them at the sweet-spot of the actuator—that is the separation of coil and magnet at which the actuator response is at maximum and hence coupling from external motion of the coils at a minimum—the magnets are mounted on 2 mm × 2 mm (diameter × length) stand-offs that are directly glued to the substrate with Masterbond EP30-2. The response of these coil-magnet actuators can be calculated in Mathematica® to be 5.8 mN A^{-1} per coil-magnet actuator.

The coil driver electronics for the 100 g ETM suspensions are designed as current drivers. It is planned to use a maximum of about 33 mA for driving the coils at the top mass and penultimate mass level. With the calculated coil responses the maximum force per coil is 1.07 mN on the top mass and 191 µN on the penultimate mass.

Direct actuation with coil-magnet actuators on the test mass would introduce additional

noise due several potential noise sources, including Barkhausen noise [113] of the actuator and the fact that no further pendulum stage would filter this noise. Instead it is planned to use a plate capacitor electrostatic drive (ESD) that has been studied for the AEI 10 m prototype [114]. A computer-aided-design model of the plate-capacitor ESD with the test mass, as used in the 100 g ETM suspension, can be found in Figure 6.4. ESDs have been

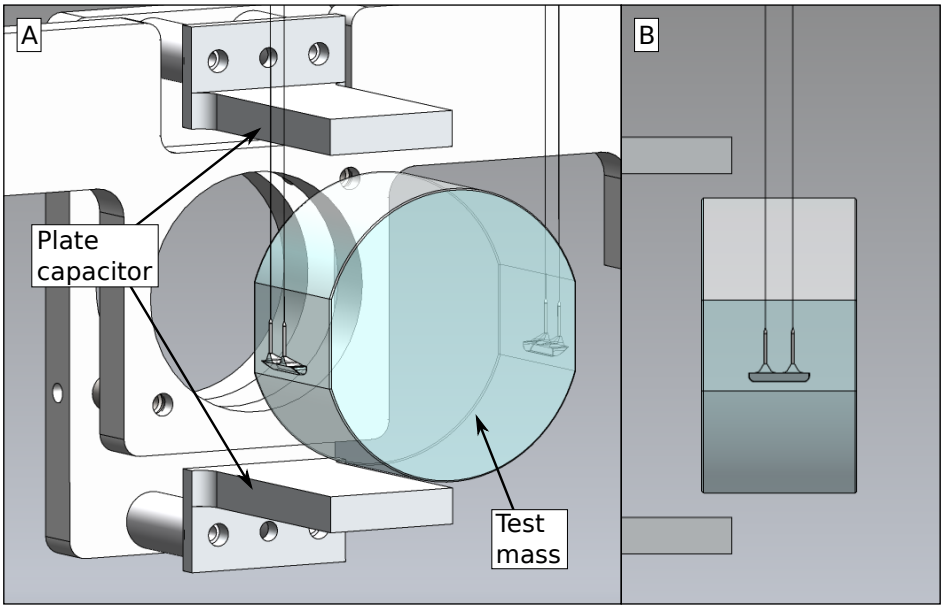

Figure 6.4: Computer-aided-design model of the ESD plate-capacitor and the test mass. Picture A show isometric view and Picture B shows the side view of the test mass inside the ESD. The capacitor plates are oriented along the vertical axis of the test mass.

introduced in large scale interferometers such as GEO 600 and Advanced LIGO. In these two cases the ESD is a comb design of electrodes and anodes that are mounted on the surface of a reaction pendulum mass directly behind the test mass [115]. For the Sagnac speed meter experiment a plate capacitor design was chosen, which eliminates the need of a reaction mass with similar performance to the test mass due and allows to make use of the maximum clear aperture of the test mass. The plate capacitor in this configuration can be mounted directly on the breadboard due to negligible coupling from ground motion to force on the test mass. Considering the inhomogeneous field of the capacitor at its ends and a dielectric medium in this field, there is a small component of force pulling the dielectric medium further into the plate capacitor towards its homogeneous field. It is important to note here that the following calculation is for a simplified case in which the dielectric medium is a slab that fully fills the space in between the two plates. This electrostatic force F can be calculated from the electrostatic field energy U following Reference [116]

$$U = \frac{1}{2} w d (\Delta\phi/d)^2 [\epsilon x + \epsilon_0 (l - x)], \tag{6.2}$$

where w is the width of the plates, d is the thickness of the dielectric medium in between

the plates, $\Delta\phi$ is the potential difference between the plates, ϵ and ϵ_0 are the permittivity of the dielectric medium and vacuum respectively, l is the length of the plates and x is the distance to which the medium is inserted into the plates. The x-component of the force on the dielectric medium is then given by

$$F_x(x) = (\epsilon - \epsilon_0)\frac{w\Delta\phi^2}{2d}. \tag{6.3}$$

It can be seen that the force on the medium can be increased by wider plates (which comes with the need of a wider medium) and by increasing the potential difference between the plates. A more detailed analysis in ANSYS® for a realistic plate capacitor test mass combination has been carried out for the AEI 10 m prototype [114] showing that for a voltage of 1 kV a 100 g mirror could be displaced 0.28 µm. This motion is equivalent to a force of 1.4 µN on the mirror. For the Sagnac speed meter experiment it is planned to use a maximum of 750 V limited by the safe operating voltage of the vacuum feedthrough connections. The altered design of the electrostatic drives for the Sagnac speed meter experiment can be found in Reference [117]. Further ANSYS® simulations have shown that with the plate geometry suggested in [117] a maximum force of 1.48 µN could be achieved for 750 V between the plates.

6.3 Modelling

Analogous to the auxiliary suspension, the modelling of the 100 g end test mass suspension follows the Lagrangian approach in Mathematica®, and was adapted from the initial model for the AEI 10 m prototype, assembled by Giles Hammond. For the Sagnac speed meter experiment this model was re-written and all undefined and example parameters set to their design values. The most significant change in the model was the re-definition of the monolithic assembly with realistic fibre geometry and break-off locations, and the wire orientation at the uppermost stage. The model includes two stages of vertical blade springs and can be used in the same fashion as before to extract transfer functions for the displacement of the top suspension point to motion of the test mass or for force-displacement and torque-angle transfer functions from the actuators to motion of the test mass. From this it is possible to export state space matrices of the full suspension dynamics into MATLAB® where these can be loaded into a Simulink® model. A linearisation of the Simulink® model allows the production of transfer and linear response functions of interest for analysis.

6.3.1 Coupling of seismic ground motion

In the same way as described in Section 5.4 it is possible to estimate longitudinal displacement noise due to coupling from seismic ground motion. Again the cage is assumed to be fully rigid meaning the top suspension point moves in the same way as the ground on which the suspension is placed. The filtering due to the seismic pre-isolation stacks is modelled as before and the stacks are assumed to act in the same way in the vertical direction with a resonance frequency of 18 Hz and in the horizontal direction with performance at least as good as in the vertical direction. For this estimation the displacement transfer functions from top suspension point displacement to displacement of the test mass for vertical and longitudinal (orthogonal to the front surface of the mirror) were plotted and can be seen in Figure 6.5. The highest resonance in the longitudinal transfer function at 16 Hz couples

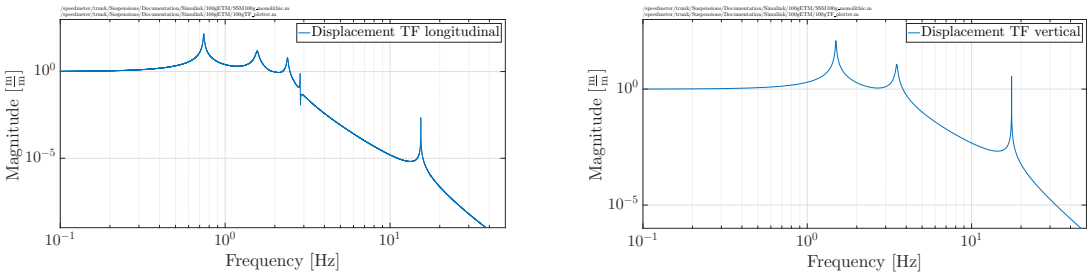

Figure 6.5: Horizontal and vertical displacement transfer function for the 100 g ETM suspension. The left plot shows the horizontal displacement transfer function from top suspension point to horizontal motion of the test mass. The right plot shows the vertical displacement transfer function.

from pitch motion into longitudinal motion of the lowest pendulum stage. In the vertical transfer function the highest resonance frequency at 17.52 Hz is the vertical mode of the lowest pendulum stage in which the fibres act as vertical spring elements.

In contrast to the auxiliary suspension, the 100 g ETM suspension has a stricter displacement requirement for residual motion due to seismic ground motion. The goal is to keep a safety factor of 10 below design sensitivity, meaning below $1.5 \times 10^{-18}\,\mathrm{m}/\sqrt{\mathrm{Hz}}$, to ensure that this technical noise source does not contribute more than 1 % to the total noise of the experiment (e.g. assuming that it is not correlated with any other noise source). In Figure 6.6 and Figure 6.7 the estimated longitudinal displacement noise of the test mass is plotted for horizontal and vertical seismic ground motion respectively. For the vertical ground motion a coupling of 1 % from vertical into longitudinal motion of the test mass is assumed as in Section 5.4. In purple, the measured seismic ground displacement is plotted. The green shows the simulated filtering effect from the seismic pre-isolation stacks and in blue the estimated longitudinal displacement of the 100 g test mass can be seen. For both cases, horizontal and vertical seismic, the displacement of the test mass is well below the design sensitivity of the Sagnac speed meter experiment due to the added $1/f^6$ response

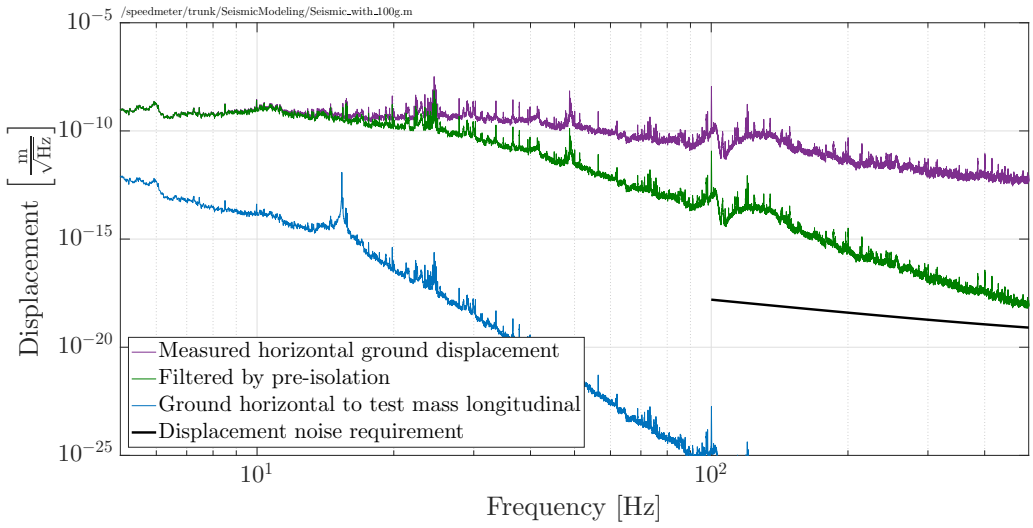

Figure 6.6: Measured horizontal ground displacement (purple) using a S-13 seismometer, estimated horizontal filtering by passive stacks (green), filtering by 100 g ETM horizontal to horizontal transfer function (blue) and displacement noise requirement for the Sagnac speed meter experiment (black). The estimated displacement noise is well below design sensitivity.

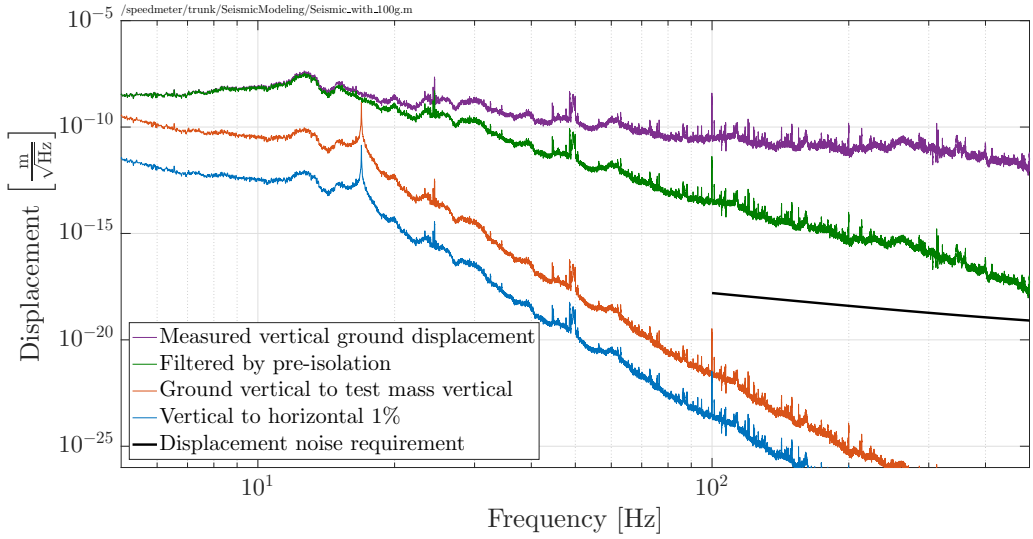

Figure 6.7: Measured vertical ground displacement (purple), estimated vertical filtering by passive stacks (green), filtering by 100 g ETM vertical to vertical transfer function (red) and added estimated vertical to horizontal coupling (blue) and displacement noise requirement for the Sagnac speed meter experiment (black). The estimated displacement noise is well below design sensitivity.

of the suspension above the highest pendulum mode-frequency. It should be noted that the internal mode frequencies of the blade springs are not included in this modelling[2].

[2]The first four mode frequencies of the upper blades were simulated in ANSYS® at 2.67 Hz, 60.49 Hz, 286.26 Hz, and 422.08 Hz. For the lower blades the first four mode frequencies were simulated at 2.87 Hz, 22.56 Hz, 339.38 Hz, and 554.05 Hz.

6.3.2 Measurable force-displacement and torque-angle transfer functions

With the coil-magnet actuators at the top and penultimate mass of the 100 g ETM suspension it is possible to confirm corresponding force-displacement and torque-angle transfer functions of the test mass. With the four coils it is possible to excite longitudinal motion, yaw and pitch of the suspension. The six force-displacement and torque-angle transfer functions are depicted in Figure 6.8. The left column of figures, top to bottom, are

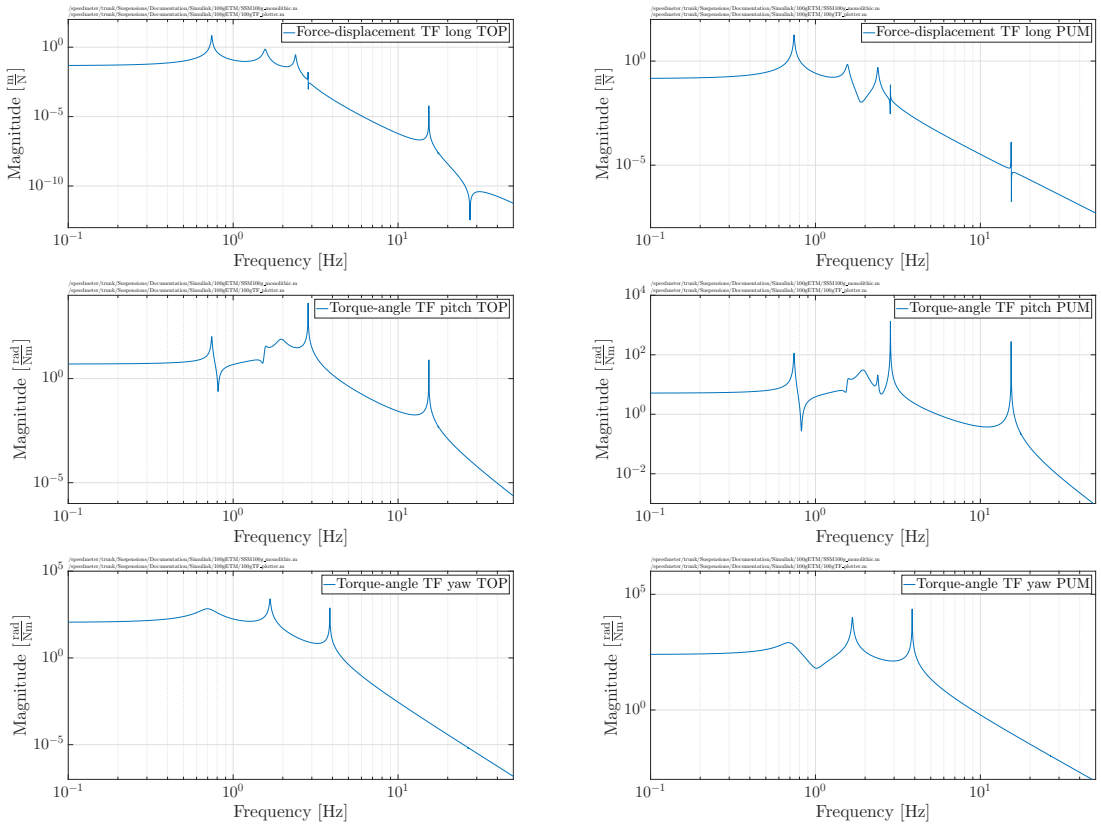

Figure 6.8: Force-displacement and torque-angle transfer functions for the 100 g ETM suspension which can be measured to verify their dynamics. The left column of plots shows (from top to bottom) the force-displacement and torque-angle transfer function from longitudinal, pitch and yaw excitation of the top mass to test mass motion. The right column shows the force-displacement and torque-angle transfer functions from penultimate mass excitation to test mass motion in the same order.

the longitudinal, pitch and yaw force-displacement and torque-angle transfer functions from top mass to the test mass motion. The right column shows the corresponding force-displacement and torque-angle transfer functions from penultimate mass to test mass motion. The longitudinal force-displacement transfer functions are given in $\mathrm{m\,N^{-1}}$ and the torque-angle transfer functions for yaw and pitch are given in $\mathrm{rad\,N^{-1}\,m^{-1}}$.

6.4 The monolithic assembly

The monolithic assembly of the 100 g ETM suspension consists of the fibres, the ears and the test and penultimate masses. As the name of the suspension indicates, the test and penultimate mass of this suspension are designed to have a mass of 100 g. The substrates are made from fused silica and are designed as a cylindrical barrel (see Section 6.4.1) with parallel flats polished to the sides of the barrel which are used for attaching an interface piece (the so-called ear). The test mass substrate is suspended by four fused silica fibres from the penultimate mass which are welded directly onto the ears. The penultimate mass additionally hosts four magnet stand-offs on both the front and back surface as well as two break-off prisms on either side. A schematic of the monolithic assembly is depicted in Figure 6.9. In this schematic it can also be seen that the fibre stock at the ends is of a thicker diameter of 400 µm compared to the central section of just 20 µm diameter. In

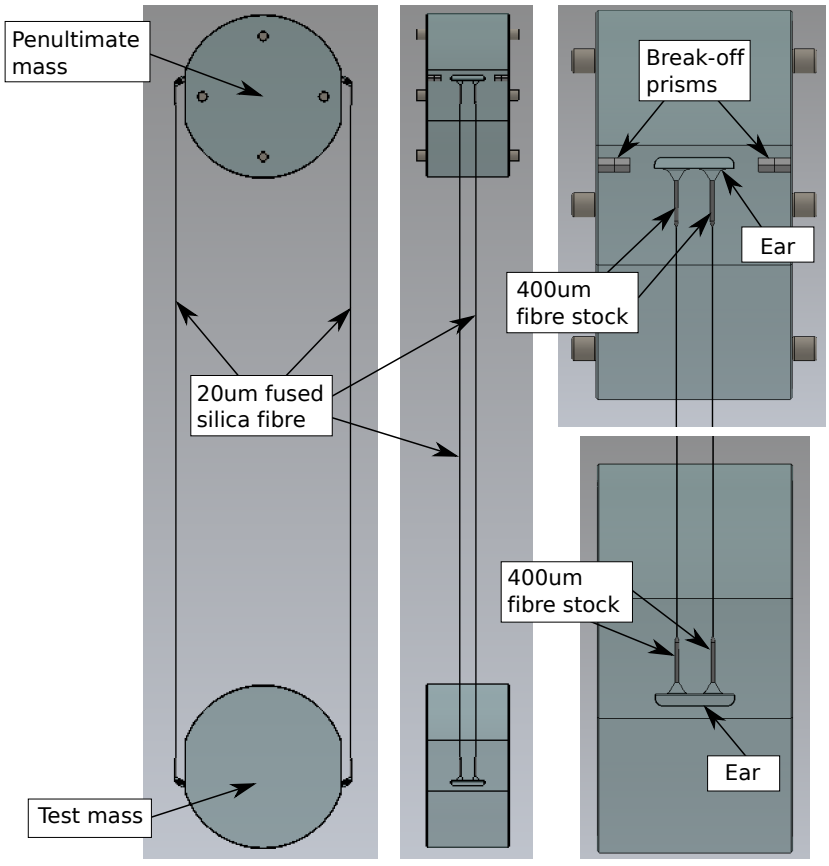

Figure 6.9: The figure shows the monolithic assembly as a computer-aided-design model. The left picture shows the front view, the central picture a side view, the top right picture shows a side view close-up of the penultimate mass and the bottom right shows the same for the test mass. On the flat sides of the test and penultimate mass are the ears, the interface pieces between substrate and fibres, located. The penultimate mass additionally hosts break-off prisms for the wire loops from the top mass. On front and back surface of the penultimate mass magnet stand-offs are located. The test mass is suspended by four 20 µm fibres from the penultimate mass.

order to protect the very thin fibres the masses are held in so-called fibre guards which can already be seen in the CAD model in Figure 6.1. The guards are meant to remain on the suspension at all times to prevent accidental damage of the fibres and to serve as a mass catcher in case any fibre of this stage or any wire of an upper stage breaks. Their design and features will be discussed later in Section 6.9. The distance between the centre of mass of the penultimate mass and the centre of mass of the test mass was chosen to be 200 mm, driven by the initial design of the fibre guards for the monolithic stage.

6.4.1 Test and penultimate mass

The two masses of the monolithic assembly, the penultimate and test mass, are of 100 g weight. The substrates are identical and the masses can only be distinguished by the optical coatings on the main and back surface of the test mass, where the penultimate mass is kept uncoated. Magnet stand-offs on the penultimate mass are made from type 430 stainless steel and are used for magnetic mounting of the four 2 mm × 2 mm (diameter × length) magnets which are part of the coil-magnet actuators at the penultimate stage. The mechanical design of the substrate can be seen in the CAD model in Figure 6.10. Picture A on the left shows

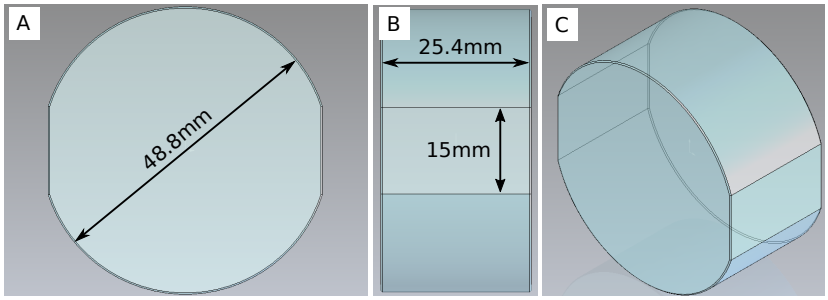

Figure 6.10: CAD model of 100 g test and penultimate mass substrates in front (A), side (B) and isometric view (C). The dimensions and shape for both test and penultimate mass are the same. With 48.8 mm diameter, a thickness of 25.4 mm and 15 mm flats on the sides these substrates weigh 104 g.

a front view of the substrate with its nominal diameter of 48.8 mm and Picture B shows the side view of the substrate. The masses are 25.4 mm thick and have a 15 mm wide flat polished to both sides. Picture C shows the isometric view of the substrate. The main and back surface of these substrates are polished to minimise scatter and thus optical losses. Further information about the main surface figures can be found in [118]. The two flats on the substrate sides are polished to allow hydroxide catalysis bonding (HCB) [110] of the ears. The two main surface figures for bonding quality are a peak-valley flatness of <60 nm (or better than $\lambda/10$) and roughness <1 nm. The substrates were manufactured and polished by Coastline, a US based company that also polished all cavity mirror substrates for Advanced LIGO.

The optical coatings for the Sagnac speed meter test masses were produced by Laboratoire des Matériaux Avancés (LMA) in France. The coatings are produced using the ion beam sputtering technique and their specifications can be found in Table 6.1. The coatings of

Property	**Main Surface**	**Back Surface**
Type of coating	High-Reflection (HR)	Anti-Reflection (AR)
Angle of incidence	42.8°	42.8°
Transmission @ 1064 nm	2 ppm for s-pol light	>99.7 % for s-pol light
Material	SiO_2 and Ta_2O_5	SiO_2 and Ta_2O_5
Absorption @ 1064 nm	<1 ppm	<10 ppm
Scattering @ 1064 nm	<1 ppm	<10 ppm

Table 6.1: Summary of properties for the optical coatings on the mirrors of the 100 g ETM suspensions.

both surfaces consist of alternating layers of silicon-dioxide (SiO_2) and tantalum-pentoxide (Ta_2O_5). To minimise optical losses in the triangular cavities of the Sagnac speed meter experiment, scattering and absorption in the HR coatings of the test masses is specified to be <1 ppm. A picture of one of the real coated 100 g ETM mirrors can be seen in Figure 6.11, where the border of the coating can be seen as a line surrounding the central area of the

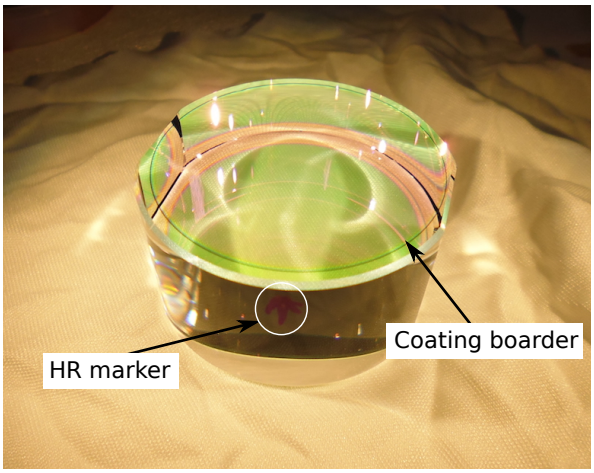

Figure 6.11: Picture of one ETM substrate after unpacking. The picture shows the optical coating and its border around the top surface. On the barrel it is possible to see an arrow marking the HR surface.

substrate. It is possible to see a small arrow marking the HR surface of the mirror which is pointing up in this example. The green and red shimmer that can be seen are due to the coatings partially reflecting green and red light.

6.4.2 Ears

The ears in the monolithic assembly serve as the interface piece between the substrates for the mirror and penultimate mass and the four fused silica fibres that suspend the mirror from the penultimate mass. The design of the ears for the Sagnac speed meter experiment follows experience with similar ears from Advanced LIGO [115]. To create a monolithic connection between the two pieces hydroxide catalysis bonding (HCB) [110] (see Section 6.7) is used. The design of the ear is required to keep stress in the bond layer below breaking stress and to restrict the bond area in order to minimise noise from thermal fluctuations in the bond. The mechanical design of an ear is depicted in a CAD model in Figure 6.12. The ear for the 100 g ETM suspension is 10 mm wide and its bonding surface

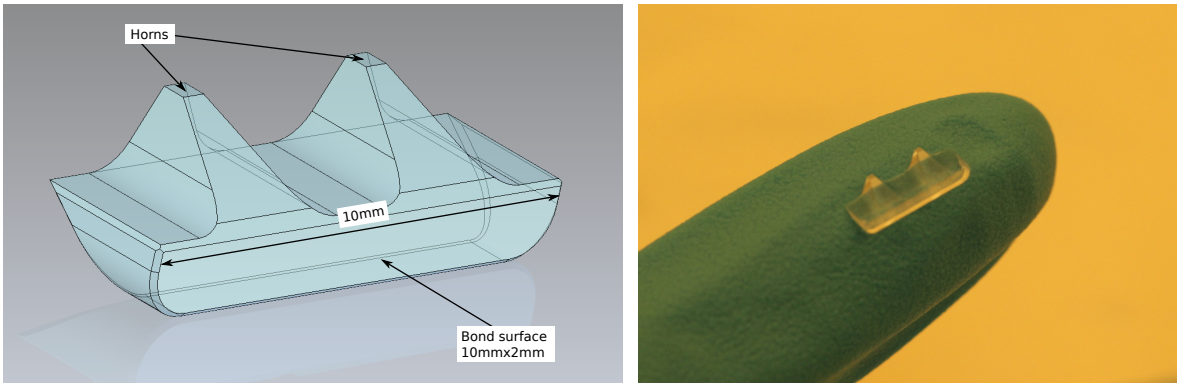

Figure 6.12: Computer-aided-design model of an ear on the left and a picture of one ear on a fingertip on the right. The ears are only 10 mm wide and are used as interface pieces between the substrates and the fibres which are welded to the horns on the ear.

is about 2 mm × 10 mm. The two 'horns' that can be seen in the figure are the attachment points for the fibres that are welded to the ear. As can be seen in Section 6.9 a CO_2 laser is used to melt the horn while stock material of the fibre is fed into the weld. The surface figures for the bonding surface are the same as for the flat sides of the 100 g substrates, peak-valley (PV) flatness of 60 nm and roughness <1 nm. However, meeting these requirements is challenging due to the small size of the ear and its geometry, as mounting becomes difficult. The ears for the Sagnac speed meter experiment were manufactured by Femtoprint in Switzerland. They were characterised by measuring flatness and roughness of the bonding surface after receiving them. The flatness was measured at the University of Glasgow with a Zygo interferometer and the roughness with a Veeco interferometer. An example of a flatness measurement can be seen in Figure 6.13. In this example the PV flatness along the ear is <60 nm. The full set of both flatness and roughness measurements are presented in Reference [118].

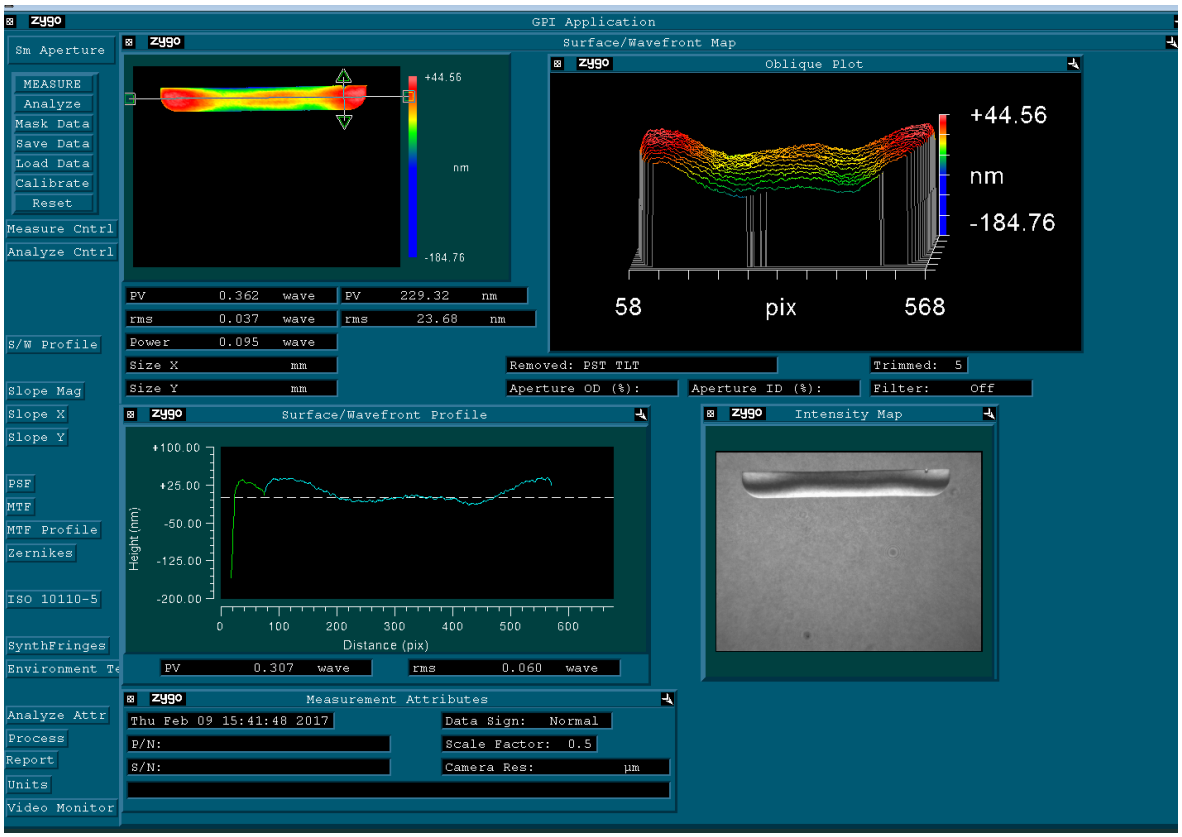

Figure 6.13: Screenshot of the Zygo software during an ear measurement. The top left and top right show contour plots in 2D and 3D of the ears flatness. The bottom left shows a line-profile through the contour plot and the bottom right shows an intensity map that is used for initial alignment of the Zygo interferometer.

6.5 Mass caps

Once the test and penultimate masses are initially unpacked and cleaned with high-grade methanol, they must be kept clean and protected from potential damage and contamination. An ideal protection would seal the mirror surfaces and not allow any contamination to pass through the seal. The mass caps are made of two aluminium parts that can be connected and which are covering both main and back surface. A CAD image of one of the mass caps can be seen in Figure 6.14, where the two end faces of the cap are connected by two spacer rods. The substrate is held between the two end faces with two o-rings that are located in grooves inside each cap side. The o-rings have a 2 mm cross section and an inner diameter of 41 mm. They seal the main and back surface of the substrates to protect the optical coatings and are used in compression to hold the mass tightly in the caps. For this reason the spacer rods are designed to allow for a total of 100 µm compression of both o-rings (50 µm each). The two end faces of the cap can be distinguished by an additional feature on the cap that protects the AR surface, where the cap on that side has an opening that can be closed by a PEEK screw-cap. This feature was thought to be useful for setting up an optical lever

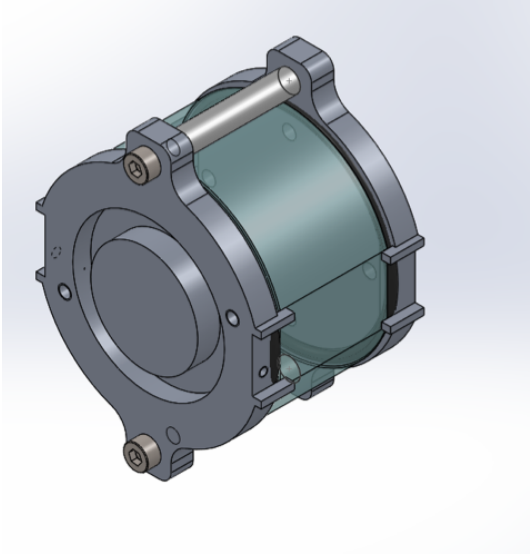

Figure 6.14: Computer-aided-design model of a 100 g ETM substrate in a mass-cap to protect the optical coatings from possible contamination. On each side are located four alignment pins that line up with the flats on the substrates.

to determine any pitch of the substrates during welding of the fibres but was not used for the production of the monolithic assemblies for the Sagnac speed meter experiment (see Section 6.9). On the sides of the cap end-faces small alignment pins can be found that align with the flats on the substrates. This reference is important to avoid lateral shifts of the substrate inside the caps. Between those alignment references a tapped hole is present to attach either a small adapter plate to increase the alignment accuracy (see Figure 6.15), a bonding template (see Section 6.7) or a weld mirror (see Section 6.9).

The procedure for placing the substrates inside the mass caps starts with cleaning the substrate after unpacking it. A 'drag-wipe' method was adopted for the cleaning which used high grade methanol and Anticon® Gold wipes. These are soft fabric wipes and were specifically chosen to avoid possible scratching of the surfaces. A 'drag-wipe' is performed by placing a wipe over the substrate surface and dripping a few drops of high-grade methanol on the wipe so that the wipe adheres to the surface. The wipe is dragged across the surface only once then is immediately disposed of and not used again. With this procedure any dust is pulled away from the surface without any pressure on the wipe that could damage the surface. The full procedure to place a substrate into mass caps can be found in Appendix C.2.1. Four steps of this procedure can be seen in the picture in Figure 6.15. Picture A shows the two cap pieces as well as the 100 g substrate. In Picture B the inspection for dust of the substrate barrel can be seen. Picture C depicts the substrate sitting on the solid end-face mass cap with the adapter plate for alignment. Picture D shows the placing and alignment of the second end-face cap on the AR surface of the substrate. All substrates, test and penultimate masses, were placed inside mass caps immediately after unpacking. All the work described above and in the following is performed in a cleanroom environment.

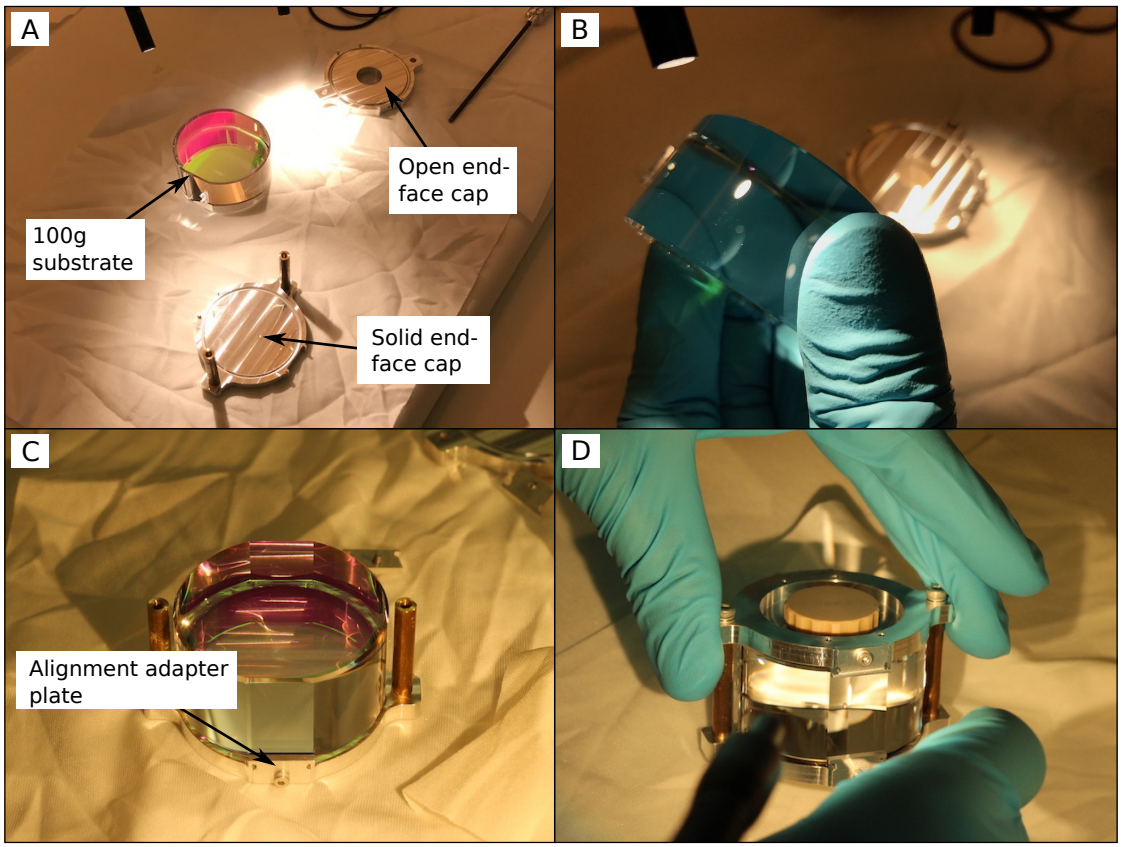

Figure 6.15: The series of picture shows the placement of a 100 g substrate into the mass caps. Picture A shows all parts necessary, Picture B shows the inspection for dust on the substrate, Picture C shows the aligned substrate placed on one end-face and Picture D shows the alignment of the second end-face of the mass cap on the substrate.

6.6 Ozone cleaning

The bond surfaces of the ears and substrates should be free of any chemical contamination and made atomically clean and hydrophilic in order to create good quality bonds [110]. Different cleaning approaches can be used to remove surface contamination, one method being wet-cleaning of the surface with cerium oxide and sodium bicarbonate. In this procedure cerium oxide lightly polishes the surface and removes any contamination. Sodium bicarbonate is used to remove any residual cerium oxide particles from the surface. The surface is afterwards rinsed under de-ionised water and methanol to remove any residual water. However, this cleaning procedure proves not to be applicable for parts such as the ears and small optical components (100 g and 1 g mirrors) of the Sagnac speed meter experiment due to their size. Instead of wet-cleaning it has been demonstrated that cleaning in an UV/ozone atmosphere can be also be used to remove any organic contamination and create a hydrophilic surface [119]. One cleaning procedure in this reference suggests ethanol drag wipe of the surface followed by exposure of the surfaces to O_3 for 15-20 minutes. For the substrates and ears of the Sagnac speed meter experiment it was decided to perform an

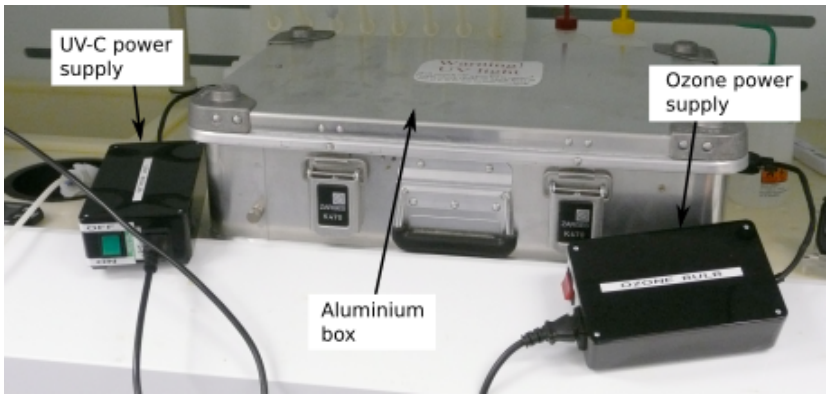

Figure 6.16: The picture shows the ozone chamber in which all substrates and ears for the 100 g ETM suspensions were cleaned. The chamber consists of an aluminium box and two light bulbs with separate power supplies. One lamp is used to generate ozone to an equilibrium and the other to decay ozone.

initial cleaning with methanol and Anticon Gold wipes of the bonding surfaces followed by exposure to O_3 for 11 minutes. Internal tests have shown that an exposure for 11 minutes in a minimum of 15 ppm O_3 is sufficient for cleaning.

The ozone chamber used in the lab in Glasgow consists of a Zarges aluminium box that is equipped with two UV-C light bulbs along the opposing long walls of the box. The first buls is a 36 W Hg-bulb with fused quartz or UV grade fused silica envelope (Dinies U36W-411ozon) that emits UV-C primarily at 184.9 nm and 253.7 nm. The second bulb is a 36 W Hg-bulb with high silica glass envelope (GE BIAX GBX36/UVC) which emits primarily at 253.7 nm but not at any shorter wavelength. A picture of the box with two separate power supplies for the two bulbs can be seen in Figure 6.16. Ozone is created due to absorption of UV-C light below 245.4 nm in diatomic oxygen (O_2) [120] and can be dissociated by absorption of UV light at longer wavelengths, such as 253.7 nm. In this sense the first bulb creates ozone, but also limits its creation by emitting some UV at 253.7 nm. The second bulb is used as an ozone killer [120] to dissociate any ozone inside the chamber. The ozone chamber is operated for 11 minutes with the ozone creating bulb and for further 15 minutes with the second bulb. During the whole procedure the ozone level outside the box is monitored with a UV-100 ozone analyser from EcoSensors. A threshold for safe operation is set at 0.1 ppm[3] outside the chamber.

One downside of the ozone cleaning is the use of UV-C light. Even though it is used for creation and control of ozone content inside the chamber, UV light can be harmful for the optical coatings on the 100 g mirrors of the Sagnac speed meter experiment. It has been reported [**Zhang2014**] that exposure to UV-A light can temporarily increase the absorption in the coating layer due to the built of UV induced colour centres. The UV lamp used in this

[3] At levels of 0.3 ppm ozone exposure can cause irritation in nose and throat, at 1-2 ppm pain in the chest and headache, and exposure at 50 ppm for an hour can be fatal.

test was emitting between 315 nm and 400 nm. In principle harder UV irradiation at even lower wavelength might create practically irreversible colour centres in the optical coating. The mass caps presented in Section 6.5 were used as a first layer of protection, however, the open sides of the caps could still allow UV light to reach the coatings. In order to build a second layer of protection a double-shield was designed to be used inside the ozone chamber. In order to verify its usability residual UV light and ozone content inside the shield were measured. A picture of the double-shield can be seen in Figure 6.17. The inside

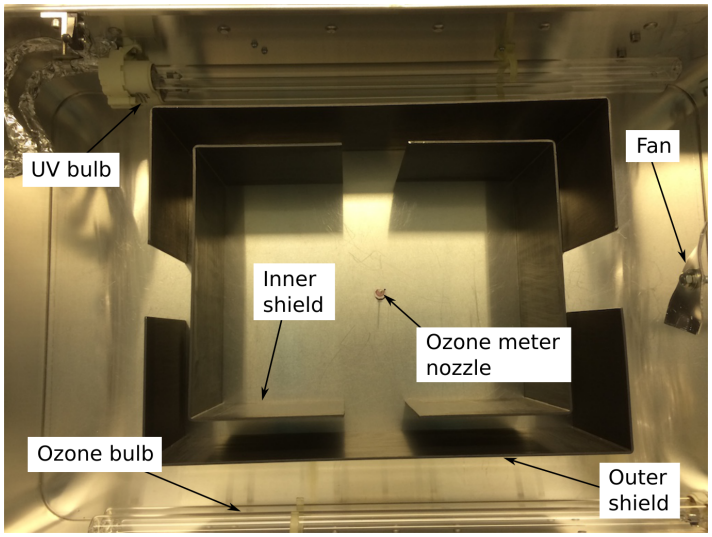

Figure 6.17: The picture shows the inside of the ozone chamber with a double shield inside. The shield is used to protect the optical coatings from UV exposure. In order to minimise the reflection coefficient of the shield all surfaces have been painted with colloidal graphite.

of the ozone chamber can be seen with the two bulbs along the top and bottom. The double-shield was made from aluminium sheets and coated with colloidal graphite (Aquadag) to minimise the reflection coefficient for UV-C of the bare aluminium surface of the shield. In the centre of this figure the nozzle of the ozone meter which was used to measure the ozone content inside the shield can be seen. On the right hand side the blades of a fan used to increase flow of ozone through the double shield can be identified. The UV content in the chamber was measured with a GaP photodiode (FGAP71) from Thorlabs that is responsive to wavelength between 150 nm and 550 nm and compared to UV from a standard light bulb inside the flowbench in which the mirrors were planned to be stored during curing of the bonds. The light levels during storage are considered safe and thus set a requirement for maximum UV exposure. It was found that the shield significantly reduces the UV content and that the residual content is a factor 100 lower than exposure under a normal light bulb. Figure 6.18 shows the result of the measurement that was taken to verify the ozone level inside the shield in comparison to previous measurements. The traces in green, red and blue show that without a shield ozone levels of 255 ppm can be reached inside the chamber. With a single shield levels of 90 ppm could be reached as depicted in the purple trace. In the

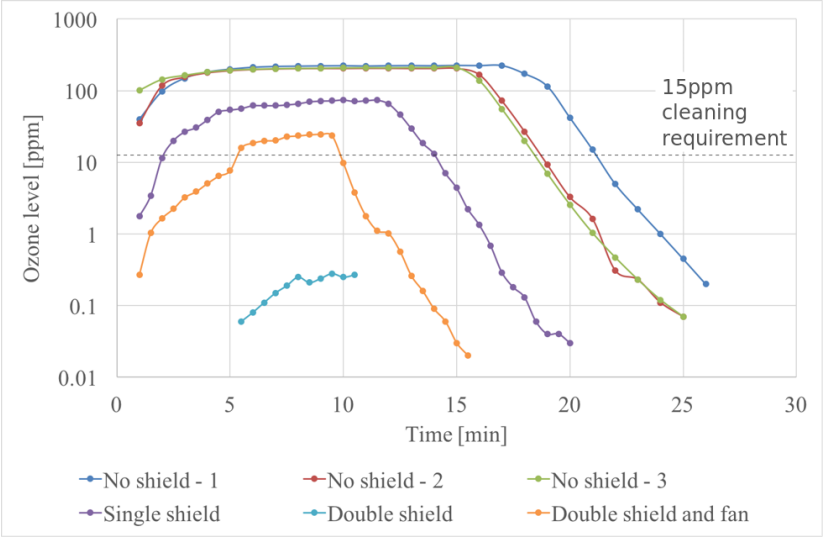

Figure 6.18: Evolution of ozone content in the ozone chamber with time for different situations. Red, green and blue show measurements without any shield in the chamber. The purple trace shows the measurement with a single wall shield inside the chamber. The light blue curve shows the measurement with the double shield and the orange curve the measurement with an additional fan system. An ozone content of about 15 ppm is necessary to sufficiently clean surfaces for bonding.

cyan trace the ozone content inside the double shield without the additional fan can be seen and it becomes clear that only levels of 0.5 ppm would be reached which is not sufficient for cleaning. The orange trace shows the measurement of ozone content in the chamber using the fan. In this combination the ozone content reaches a level of 20-25 ppm inside the double shield which is sufficient for cleaning.

All ears and substrates were initially cleaned with methanol and wiped down thoroughly. The substrates were then transferred to their mass caps (see Section 6.5). The masses and ears were then cleaned in the ozone chamber following the procedure described above. A picture of the filled ozone chamber can be seen in Figure 6.19. The ears were separately placed in aluminium foil pouches to be able to distinguish them. The substrates, test and penultimate masses, were placed in the centre of the box with the PEEK screw cap down. A full cleaning procedure can be found in Appendix C.2.2.

6.7 Bonding of 100 g substrates

6.7.1 Theory of hydroxide catalysis bonding

The method of hydroxide catalysis bonding (HCB) creates chemical bonds between oxide or oxidisable materials with an aqueous hydroxide solution, and has been the preferred technique in current and future ground-based GW detectors to create quasi-monolithic test mass suspensions [115, 121, 122]. The chemistry of HCBs consists of three main stages:

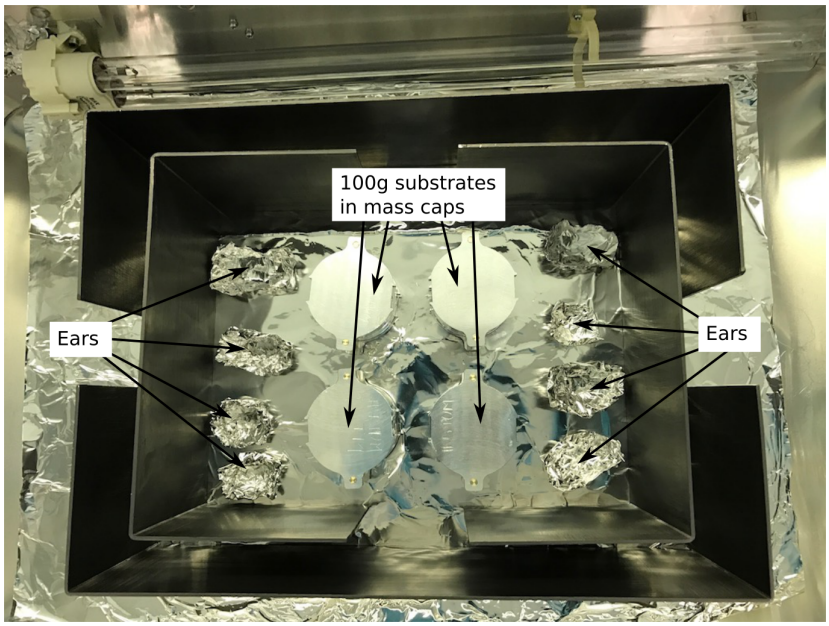

Figure 6.19: This picture shows the inside of the ozone chamber with the 100 g substrates in their mass caps and the ears before cleaning inside the double shield.

hydration and etching, polymerisation, and dehydration. Following Reference [110], the first stage describes the effect of the alkaline bonding solution; a sodium silicate hydroxide solution was used for the bonds in this thesis. In the hydration and etching stage the OH^- ions in the solution flood the fused silica substrates, acting as a catalyst and etching the bonding surface, which releases silicate ions:

$$SiO_2 + OH^- + 2\,H_2O \longrightarrow Si(OH)_5^-. \tag{6.4}$$

During the hydration and etching stage in Equation 6.4 the pH of the bonding solution is decreased due to the consumption of OH^- ions. $Si(OH)_4$ is formed once the pH of the solution drops below 11 [123]:

$$Si(OH)_5^- \longrightarrow Si(OH)_4 + OH^- \tag{6.5}$$

Once formed the $Si(OH)_4$ molecules combine and form siloxane chains and water during the polymerisation stage:

$$2\,Si(OH)_4 \longrightarrow (HO)_3SiOSi(OH)_3 + H_2O. \tag{6.6}$$

The last stage of bonding is dehydration. During this stage water evaporates or migrates into the bulk of the bonded fused silica, leaving behind a 3D network of tangled siloxane chains which connects the two substrate surfaces. It is assumed that after four weeks at room temperature [110] the bond is cured enough for the bonded substrate to be installed.

6.7.2 Ear bonding

Bonding of the ears on the sides of all 100 g substrates is done with a laser-cut stainless steel template. The machining tolerances of the template that is depicted in Figure 6.20 are 50 µm and the reference surfaces of the template are marked in red. The template can

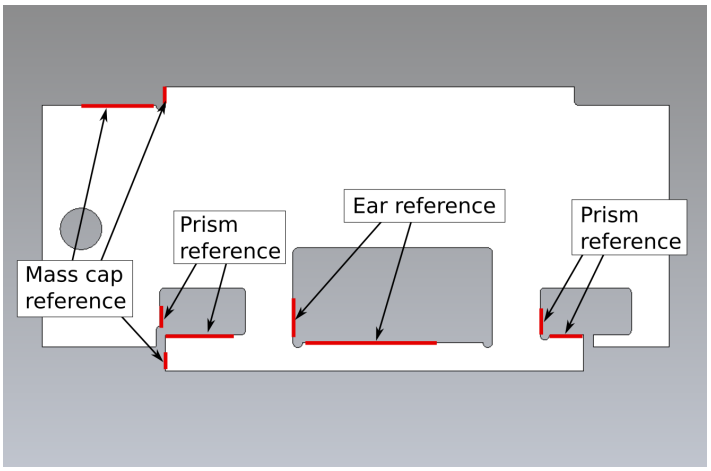

Figure 6.20: Computer-aided-design model of one bonding template for bonding of the 100 g ear to the substrates of test and penultimate mass. The surfaces marked in red are used to reference the template to the mass caps. The bonding templates were used for ear bonding and prism gluing as can be seen from the several cut-outs.

be referenced to the alignment pins of the mass caps and fixed in place making use of the tapped hole on the cap. The template has three main cut-outs, two of which are used to reference the break-off prisms on the penultimate mass and one for the ear. All parts are referenced to the same corner inside the template allowing the template to be shifted away from one side of the bonded or glued parts, thus releasing potential pressure on the part, before removal of the template. A picture of the bonding template attached to one of the mass caps can be seen in Figure 6.21. During the bonding process it is essential to keep all equipment free from contamination and dust as any particle on the bond surface could create a weak bond and of course spoils the flatness required for the bond. Here only the important steps are highlighted but the full procedure including all cleaning steps can be found in Appendix C.2.3. Figure 6.22 shows four parts of the bonding procedure. Picture A shows the application of 0.2 µL bonding solution to the 100 g mass with a calibrated pipette. Picture B shows the last methanol wipe of the ears flat bonding surface. In Picture C the ear is placed in the bonding template and aligned to the corner highlighted in Figure 6.20. Picture D shows a close-up of the ear in the bonding template. The ear is left in the template for an hour before the bond is settled and the template can be removed. The mass can be rotated and the other side bonded on the same day.

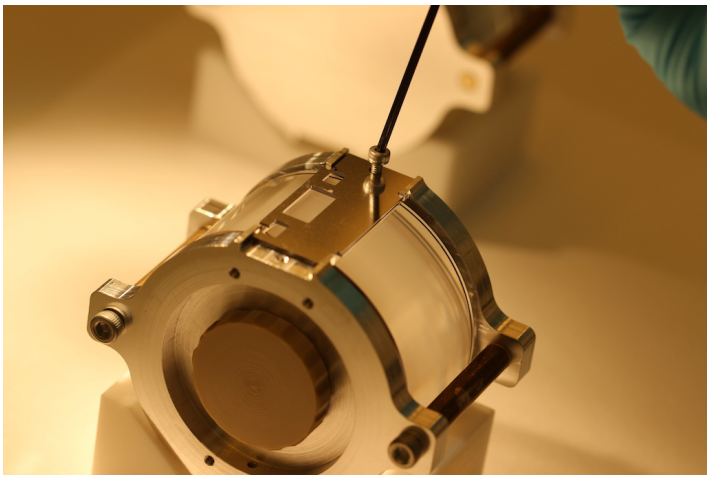

Figure 6.21: The picture shows a bonding template and how it is fixed to the mass cap. After referencing the template to the mass the template is fixed with an M2 screw.

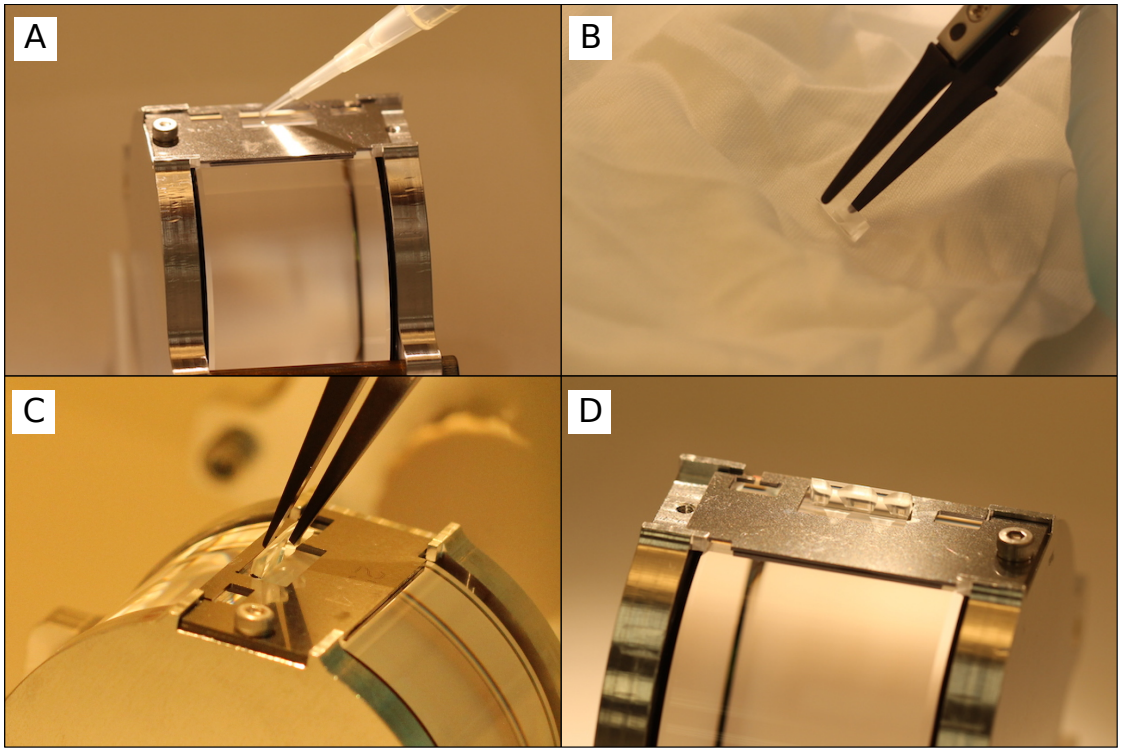

Figure 6.22: The four pictures show different steps during the bonding procedure of an ear to a substrate. Picture A shows the application of bonding solution to the flat on the substrate. Picture B shows the final wiping of the ear bonding surface with methanol to remove potential (dust) particles from this surface. Picture C depicts how the ear is placed into the template with a set of tweezers. In Picture D the ear has been aligned to the template and is left to cure for an hour before removing the template. The full curing time of these bonds was four weeks.

6.7.3 Prism and magnet stand-off gluing

The penultimate masses in the monolithic assembly host small break-off prisms additional to the ears on their sides. The break-off prism defines a clear break-off for the wire loops

from which the monolithic assembly is suspended. The prisms are made from stainless steel and glued directly to the flat of the penultimate masses with Masterbond EP30-2. The gluing procedure can be also found in Appendix C.2.3 as part of the bonding procedure. A few steps are highlighted in Figure 6.23. Picture A shows the prism as a small dot of glue is

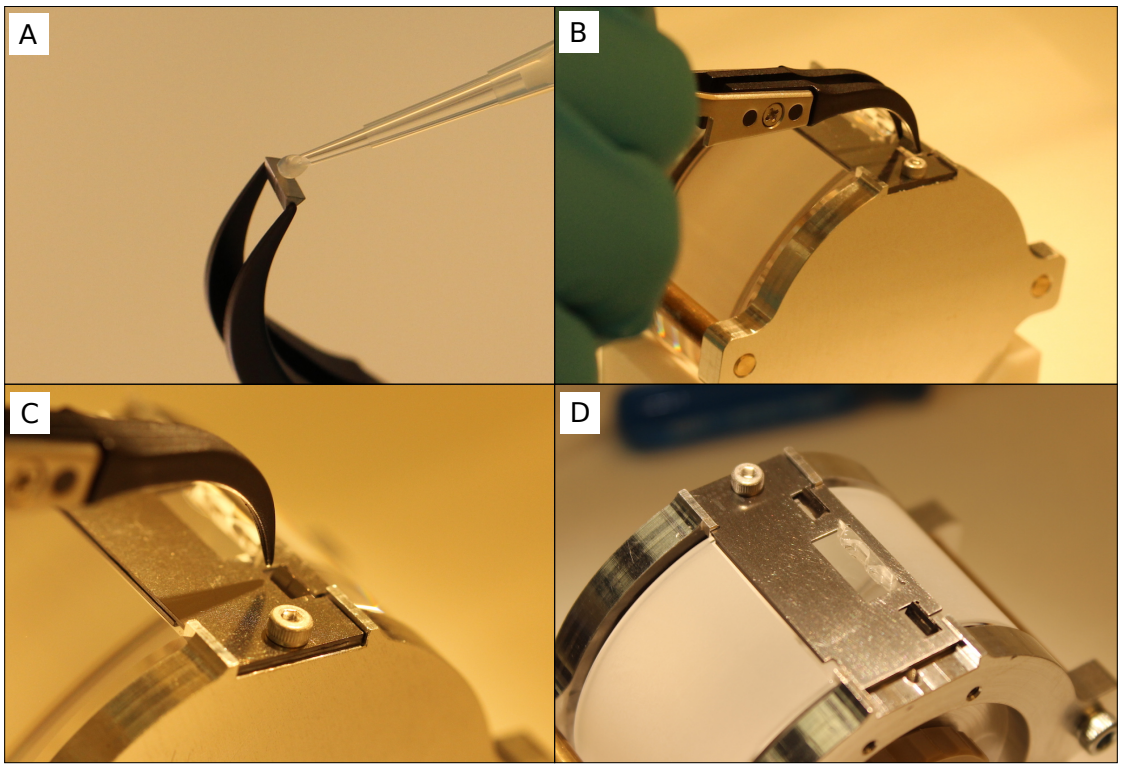

Figure 6.23: Picture A shows the application of a small drop of Masterbond EP30-2 to the gluing surface of the prism. In Picture B the prisms is placed in one of the cut-outs of the bonding template. Picture C shows the alignment of the prism inside the template. Picture D shows the final image of the prism in place. The prisms were left curing inside the template over night.

applied. Picture B depicts the dropping of the prism into the template cut-out. In Picture C the alignment of the prism in the template can be seen and Picture D shows a close up of the fully populated bonding template. The glue is left to settle over night and takes 48 h at room temperature to fully cure.

On the front and back surface the penultimate masses host magnet stand-offs. As described in Section 6.2 coil-magnet actuators are used at the penultimate stage of the 100 g ETM suspension. The mechanical design of these actuators requires the magnets to be lifted from the penultimate mass surface by 500 µm to allow placement in the sweet-spot of the actuator. This is realised with 2 mm long and 2 mm diameter 430 stainless steel stand-offs on which the magnets are mounted magnetically. In order to minimise shifts in the centre-of-mass of the penultimate mass it was decided to attach the stand-offs on either side. A dedicated template and Masterbond EP30-2 was used for this gluing step. Figure 6.24 shows the gluing procedure. In the left picture the template with the stand-offs placed in fitting

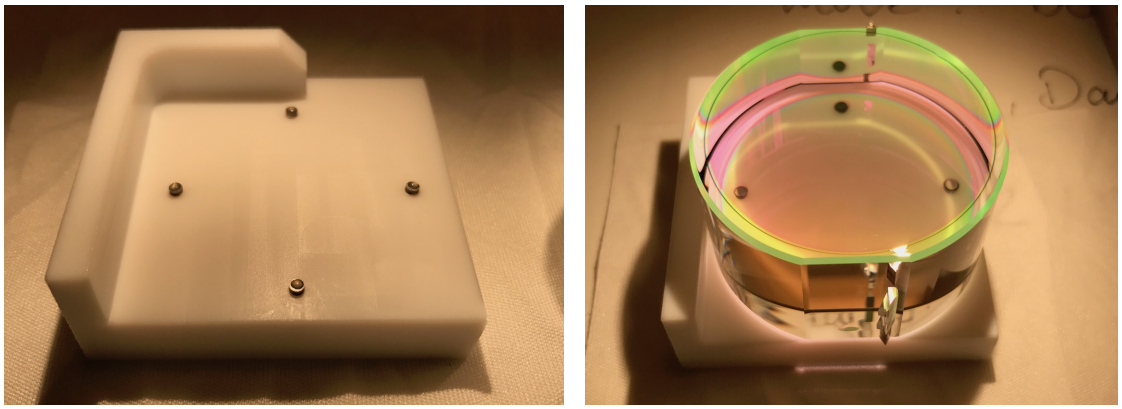

Figure 6.24: The left picture shows the gluing template that was used for attaching magnet stand-offs to the penultimate masses. In this picture the stand-offs are placed in little recesses in the template and dots of Masterbond EP30-2 have been applied. The right picture shows one of the penultimate masses in the template. The mass is aligned with one flat and its barrel to the template. The masses were left in this position over night to initially cure the glue.

recesses can be seen. Further it is possible to see the small dots of glue on the stand-offs. The flat side of the substrate and its barrel can be referenced to the slightly raised wall of the template. In the picture on the right the penultimate mass is placed on the template and thus on the stand-offs.

6.8 Fused silica fibres

The last parts required to create the monolithic assembly are the fused silica fibres that suspend the test mass from the penultimate mass. Their geometry had to be defined in order to model the suspensions dynamics in Section 6.3. A fibre can be divided into three main sections. The first section is the stock from which the fibre is pulled. As will be seen later in Section 6.8.2 the fibres for the Sagnac speed meter experiment are initially pulled from 2 mm diameter stock material to a new stock diameter of 400 µm. The second section is the neck of the fibre that defines the transition between stock and thin section. The third section is the thin section of the fibre that was originally chosen to be 20 µm. However, over the course of the last year the diameter was re-defined to be 25 µm and below as there is no limitation by suspension thermal noise for this diameter and usefully relaxes the manufacturing tolerance. Break-off points were chosen to be 3 mm above centre-of-mass of the test mass and 3 mm below centre-of-mass of the penultimate mass. A trade-off had to be made between a low pitch mode of the lowest pendulum stage and a safe length of stock for manufacturing as the stock is held by tweezers during welding. A sketch of the chosen geometry of the fibres can be seen in Figure 6.25. The total stock length is 6 mm at either end of the fibre.

With a total separation of test and penultimate mass of 200 mm the thin section of the fibre

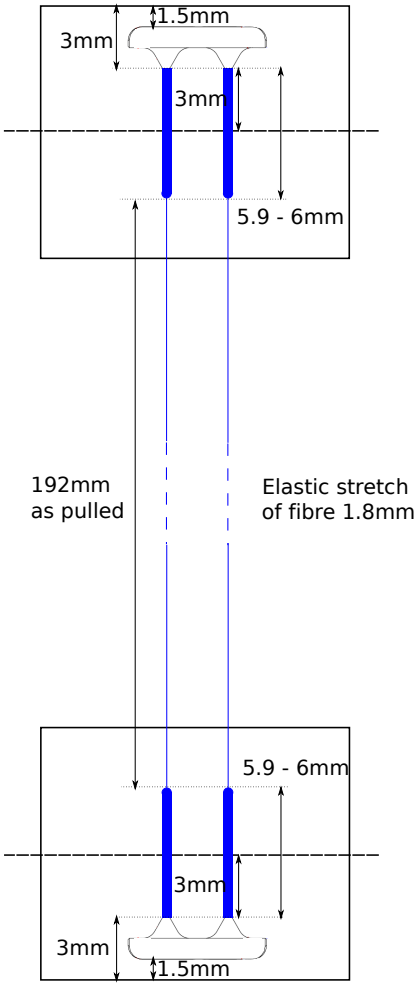

Figure 6.25: Schematic of the planned geometry for the 20 µm fibres that are used for the monolithic assembly of the 100 g ETM suspension. The stock lengths are chosen to place the fibre neck 3 mm above/below centre-of-mass of the test and penultimate mass. The thin section of all four fibres will stretch about 1.8 mm under the test mass load and is thus pulled to a length of about 192 mm resulting in a COM-COM distance of about 200 mm.

needs to be 194 mm under the load of the suspended test mass. This needs to be taken into account for the initial geometry of the fibre as it will be produced (pulled). The elastic stretch of a fibre with a circular cross section can be calculated from

$$l_{\text{stretch}} = \frac{mgl}{E\pi r^2}, \tag{6.7}$$

where m is the mass suspended from one fibre, l is the length of the thin section, E is the Young's Modulus of the fibre material and r is the radius of the thin section. In this calculation, stretch of the 400 µm stock is neglected. With a total weight of 104 g each fibre carries 26 g of load. Considering a thin section of the fibre of 192 mm length and 25 µm diameter the elastic stretch of the fibre can be calculated to be 1.4 mm. As will become apparent later, the diameter of the pulled fibres is about 22-23 µm. The elastic stretch for this diameter can be calculated to a maximum of about 1.8 mm resulting in a suspended

length thin section of about 194 mm. The stress in a 22 µm fibre can be calculated from

$$\sigma = \frac{mg}{\pi r^2} \tag{6.8}$$

to be 671 MPa which is similar to the stress in the thin section of Advanced LIGO fibres of about 800 MPa for a 40 kg test mass suspended by four fibres of 400 µm diameter. This value is more than a factor of five below the ultimate tensile strength of the fused silica fibres produced with the pulling technique described below.

6.8.1 Suspension thermal noise

As a technical noise source, suspension thermal noise of the monolithic stage was required to be at least a factor of 10 below design sensitivity of the Sagnac speed meter experiment. The suspension thermal noise calculation is analogous to the theory presented in Section 2.2.3. Figure 6.26 shows the calculated suspension thermal noise of the 100 g ETM suspension compared to the design sensitivity of the Sagnac speed meter experiment. It is

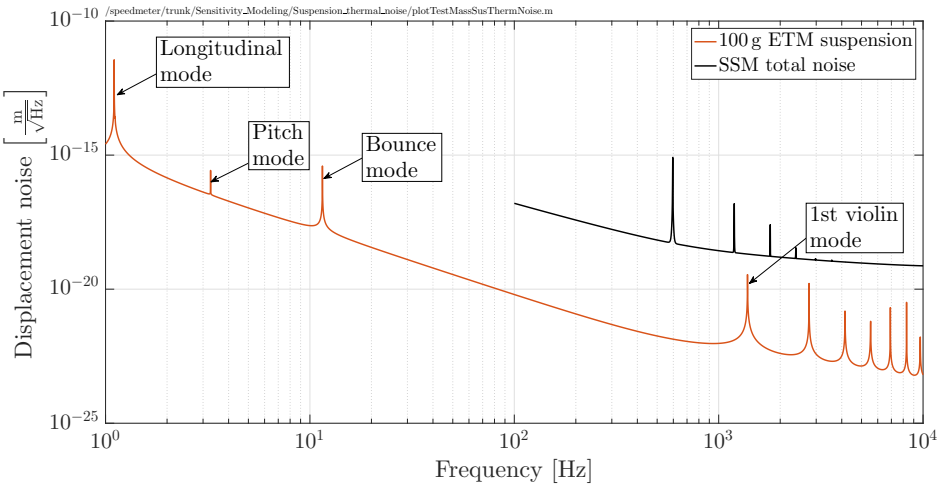

Figure 6.26: The plot shows the estimated suspension thermal noise for one 100 g end test mass suspension due to thermal fluctuations in the suspension elements of the monolithic assembly. The modelling shows that suspension thermal noise will be about 3.5 orders of magnitude below design sensitivity. It is possible to identify the longitudinal, vertical and violin modes of the monolithic assembly.

possible to identify the different pendulum modes that contribute to the suspension thermal noise. Around 1 Hz the longitudinal pendulum mode can be located, at about 10 Hz the vertical or bounce mode of the pendulum stage shows up and above about 1 kHz the first seven violin modes of the fused silica fibres can be found. The total suspension thermal noise of the 100 g ETM suspension is more than a factor 1000 below design sensitivity of the Sagnac speed meter experiment. With this level of suspension thermal noise, the 100 g

ETM suspension fulfils the requirement for the Sagnac speed meter experiment and is further available for future upgrades of this or other experiments in which higher sensitivities are desired.

6.8.2 Production of fibres

All fibres for the Sagnac speed meter experiment were pulled with a fibre puller designed and constructed by Karl Toland [124]. In contrast to the pulling machines for Advanced LIGO this fibre puller operates horizontally. A schematic of the pulling machine can be seen in Figure 6.27. The light of a 35 W CO_2 laser is guided towards an axicon mirror. At

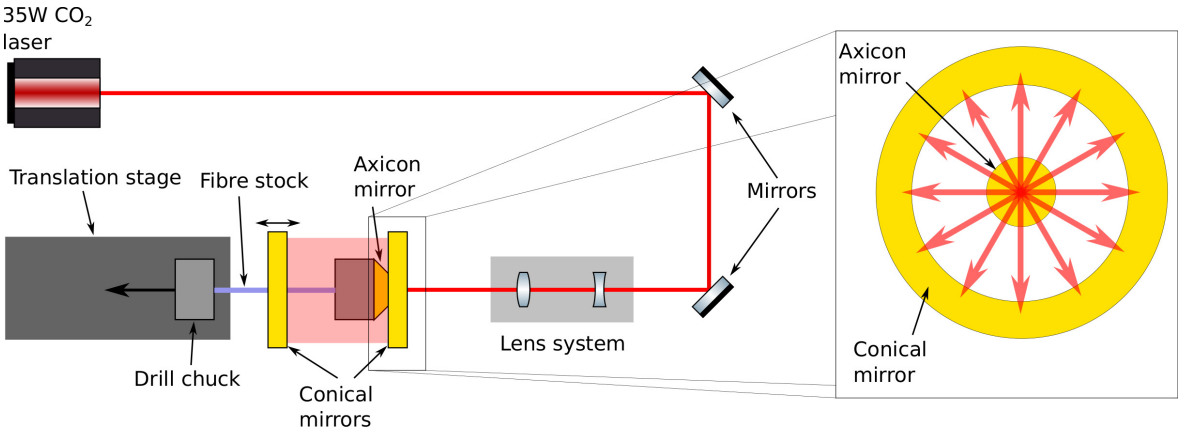

Figure 6.27: Schematic layout of the thin fibre puller to produce the 20 µm fibres for the 100 g ETM suspension. A CO_2-laser is directed on an axicon mirror. There the light is split orthogonally to a conical mirror. A second conical mirror combines the beam back onto a piece of stock that is fixed at the axicon mirror at one end. The other end is fixed to a fast horizontal translation stage. The stock is heated to its melting point and the translation stage pulls the fibre. Depending on the velocity profile of the stage, different diameters can be realised.

this mirror the beam is split orthogonal to the impinging beam. With two conical mirrors the beam is re-combined onto the stock material of which the fibre is pulled. A set of lenses is used to focus the beam at the location of the stock material. The second conical mirror is movable to allow feeding of material into the pull. One end of the fibre is fixed at the axicon mirror and the second is attached onto a fast horizontal translation stage from Newport (IMS-400LM) allowing a maximum travel distance of 400 mm. The stock material is held on both ends in an ER11 collet with conventional drill chucks. After the fibre has been pulled, distance rods can be attached to create a fixed fibre cartridge as can be seen in Figure 6.28. These cartridges are stored on an aluminium board inside a conventional fridge, protecting the fibres from dust and other contamination. Over the course of this thesis a set of 45 fibres were pulled for storage and six fibres were allocated to each monolithic assembly. The full procedure of fibre production can be found in Appendix C.1.

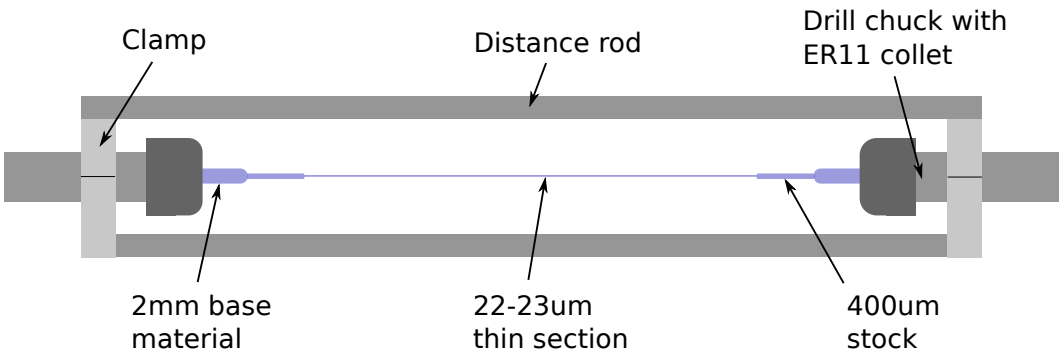

Figure 6.28: Schematic of a fibre cartridge. The base stock material with a diameter of 2 mm is held by conventional drill chucks with ER11 collets. The chucks are mounted in clamps that can be connected with distance rods. These rods are cut to length in order to build a rigid cartridge for the 20 µm fibres.

2 mm Suprasil-2 fused silica stock from Hereaus was used as the base material. The stock material is cleaned with isopropanol to remove any oil from its surface. In a first stage pull this base material is reduced to a diameter of 400 µm over roughly 58 mm. Heating the stock material to temperatures above 1600 °C removes any residual contamination and creates an immaculate surface[4]. With 20 mm offset from the fixed fibre end this section is pulled down to roughly 22-23 µm in a second stage pull and creates the final fibre. The length of the thin section was set to be 192 mm to reach a suspended length of about 194 mm as outlined above.

All fibres were profiled in a dedicated fibre profiler [126]. In this machine the diameter of the fibre is measured in a shadow projection with a CCD camera. Figure 6.29 shows a schematic and a real time picture of a measured fibre. The fibre profiler is calibrated using

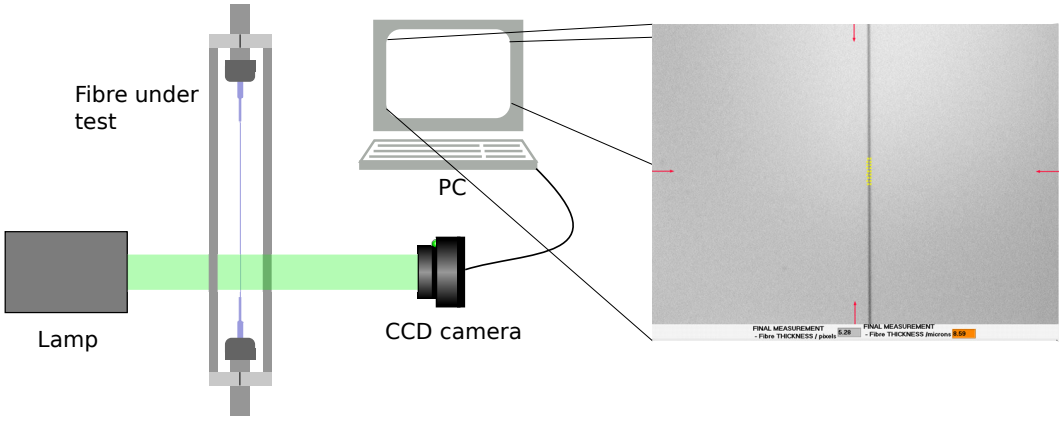

Figure 6.29: Schematic of the fibre profiler for characterising fused silica fibres. The fibre profile is taken by a CCD-camera as a shadow projection. In order to calibrate the fibre profiler a tungsten wire with diameter 25 µm is measured at ten random locations along its length. The resolution/travel distance between single measurements can be chosen freely.

[4]In Advanced LIGOthe base material is laser-polished to remove impurities and micro-cracks from its surface. [125].

25 µm Tungsten wire from Goodfellow. The diameter of this wire is accurate to 2.5 µm and is thus a reliable reference for calibration. In order to increase accuracy the diameter is averaged over 10 positions along the wire. All 45 produced fibres were profiled on the day of their production. They were matched into sets of six for each monolithic assembly of which four were used. The fibre profiles can be seen in Figure 6.30. It can be seen that all

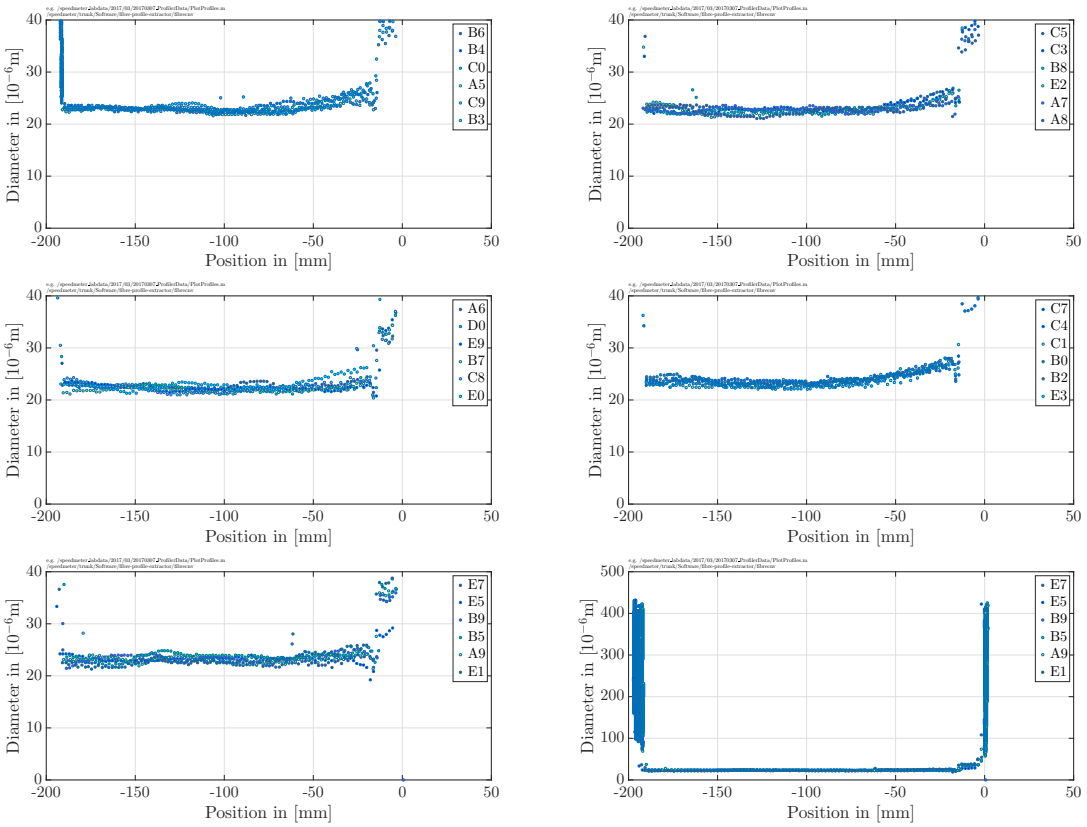

Figure 6.30: Measured fibre profiles of the fused silica fibres for the five 100 g monolithic assemblies. After profiling all fibres they were matched up by diameter and general shape into five sets of six fibres. The fibres have a uniform 22-23 µm diameter profile that slightly tapers up to about 26-27 µm on one end. The bottom right panel shows set five in an expanded view to show the 400 µm stock diameter.

fibres have a similar diameter along their length. However, small variations are present and most likely occur due to varying power level or beam alignment between pulls.

6.9 Welding

The final step in creating the monolithic assembly is the welding of the four fused silica fibres to the ears on penultimate and test mass. During the entire welding process both masses are mounted in a sophisticated weld tool. A CAD image of the weld tool with the two masses can be seen in Figure 6.31. The coatings of the test mass are still protected by the mass caps as silica vapours due to evaporation of material could settle on the main

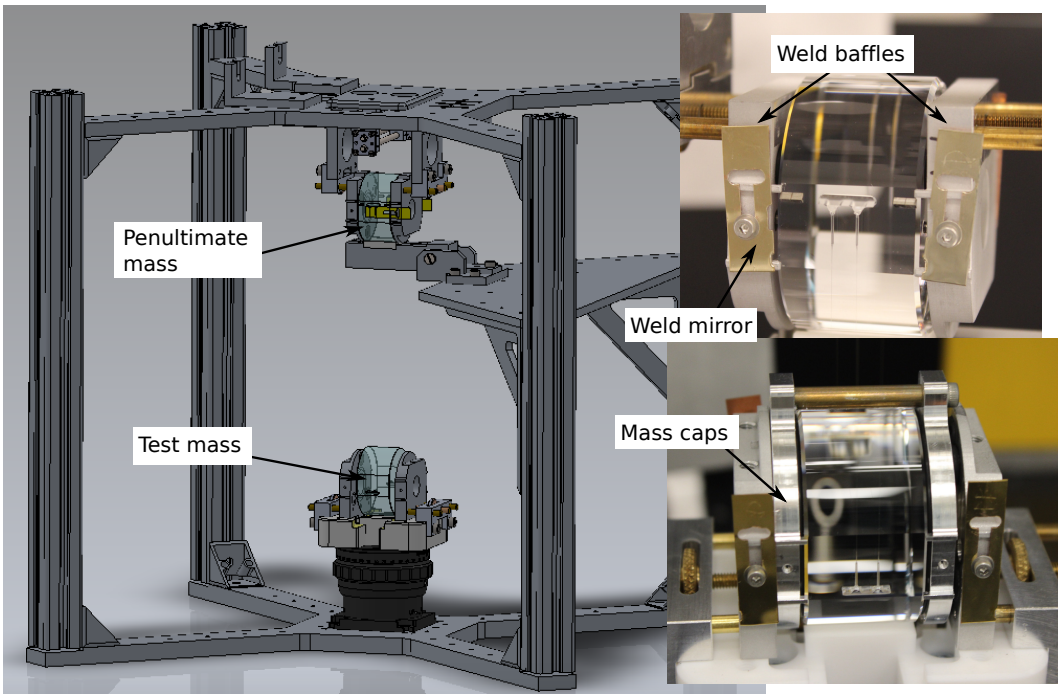

Figure 6.31: The computer-aided-design model if the 100 g weld tool is depicted on the left. Both masses are held in weld baffles on which weld mirrors are attached. The test mass is mounted on a vertical micrometer stage to adjust the mass to mass distance and to pre-stress the fibres after welding. The picture in the top right shows a real image of a penultimate mass in weld baffles and the lower right picture shows the test mass. Both pictures were taken after the fibres were welded to the masses and the weld mirrors have been retracted.

surfaces. Both masses are held in position with so called weld baffles. These are also used for mounting of gold-coated weld mirrors that are slid behind the horns of the ears to prevent damage of the substrate due to the high power laser beam. These baffles also provide heating of the weld from the back side. For the welding a water-cooled 100 W CO_2-laser was used. The fully detailed weld-procedure can be found in Appendix C.2.4. A weld is achieved by melting the tip of the horn on the ear and carefully feeding the 400 µm stock into the weld. A schematic of this procedure can be seen in Figure 6.32. In part 1 of this schematic the stock is brought close to the horn on the ear. In part 2 the stock is moved closer until the stock slightly touches the horn. In part 3 the horn is heated until the melt-point is reached and the horn starts melting. At constant power the stock is carefully fed into the weld. Shortly after, a join between stock and horn is created which can be adjusted by feeding more stock material into the weld. Care needs to be taken here, as shifts can occur whenever the horn is not molten enough or the power of the laser is not sufficient to melt both parts, stock and horn, while feeding in the stock. Part 4 shows the final weld with the tweezers removed. Note that the fibre is now under tension.

For the monolithic assemblies, the fibre is cut out of the cartridge with the CO_2-laser to the desired length. The total length includes additional stock material that is fed into the

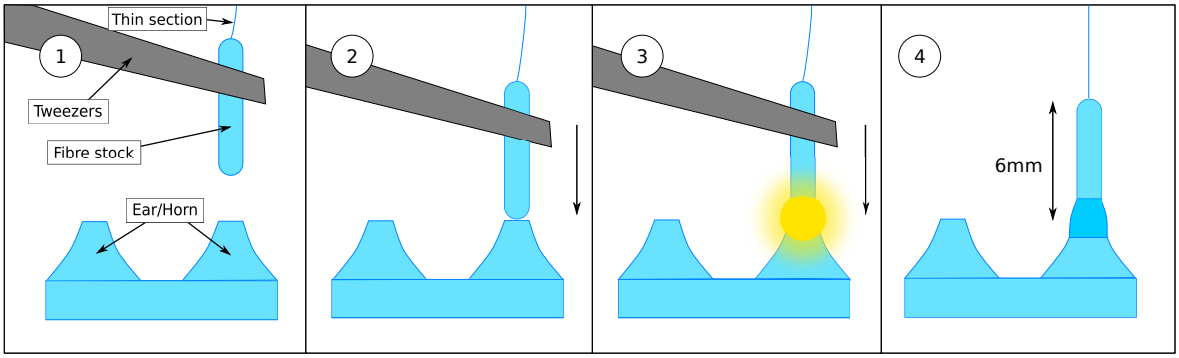

Figure 6.32: Schematic of a laser weld on a 100 g ear. Image 1 shows the initial set-up. The stock material is held by a set of tweezers. The thin section of the fibre is relaxed. Image 2 shows moving of the fibre stock to the ear horn until contact. In Image 3 the horn is heated until melting point and the stock is carefully fed into the weld. Image 4 shows the final weld. The stock is fed into the weld until the desired position of the start of the thin section is reached and it is just under tension.

weld during the procedure. While cutting and for further handling the fibre is held in a tweezer-assembly by two sets of tweezers that are mounted on micrometer stages for fine alignment and positioning of the fibre stock. The tweezer-assembly is rigidly mounted to the weld tool and positions the fibre roughly 1 mm above the horn. The stock is brought closer to the horn until it slightly touches it. Now the horn is heated with the laser until it starts to melt. At his point the fibre stock is fed into the weld. This is an iterative process to do in-situ analysis with high resolution images to check the weld quality. During the weld procedure the fibre is relaxed for most part. It is only judged by eye at the end of a weld when the fibre gets under a small amount of tension in order to weld it at its the correct unsuspended length. The relaxed fibre becomes a challenge when performing the second weld on one side (second horn of the ear). The separation of the fibres is designed to be 4 mm and it is not desirable to have one thin section touch the other during welding as this can break the fibre or significantly compromise it strength. A small fan is used in order to separate the fibres during welding of the second fibre. Figure 6.33 shows a few pictures during the welding of a monolithic assembly. Picture A shows the cutting of a fibre from its cartridge. Picture B shows fibre stock on one horn of an ear on a test mass. Picture C shows heating the stock further on the horn. Picture D depicts two welded fibres on a penultimate mass. Pictures E and F show the welded ear of a test mass after removal of the tweezers and after the weld mirrors have been shifted away from the mass.

In a last step the fibre guards that protect the fibres from accidental touching and serve as mass-catcher for both test and penultimate mass are introduced. Prior to this the fibres are stretched to their suspended length as they are held rigidly in the guards and released only after being mounted in one of the suspensions. Without pre-stretching, the test mass would drop by the above calculated 1.8 mm which could be harmful for the fibres. The guards are adjusted for the suspended length and are introduced on a rail-system from left and right

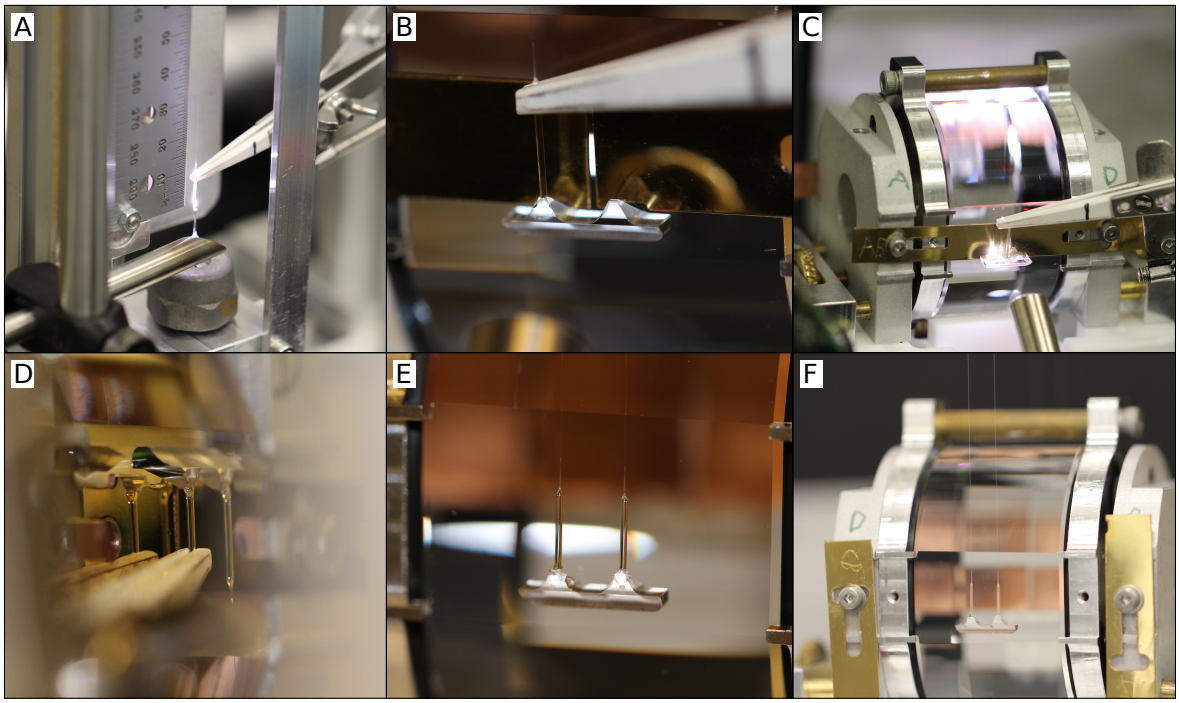

Figure 6.33: The series of pictures was taken during the weld procedure for the 100 g monolithic assemblies. Picture A shows the cutting of the fibre out of its cartridge. Picture B shows positioning of the fibre stock on one of the ear horns. Picture C shows the welding of a fibre to a test mass ear. Picture D shows a second fibre on a penultimate mass ear just after welding. Pictures E and F show close-ups of welded ears on a test mass. In Picture F the 20 µm fibres can be seen.

to the monolithic assembly. In the centre of the guard assembly, a locking mechanism is used to tightly clamp the test and penultimate mass. The test mass further remains in the mass caps which are only removed before releasing the masses in the suspension inside the vacuum system. The guards are transported in a dedicated container which allows the assembly to be fixed as in a suspension cage. The procedure for introducing fibre guards can be found in Appendix C.2.4 as part of the weld procedure. Figure 6.34 shows a set of pictures taken during the introduction of the fibre guards. Picture A shows the introduction of the first side of the fibre guard. In Picture B the installation of the guard locking mechanism is depicted. Picture C shows the monolithic assembly in the fibre guard mounted in a Bosch-frame for storage and transportation. Picture D shows a set of three monolithic assemblies. A total of five assemblies have been produced for the Sagnac speed meter experiment. Table 6.2 summarizes the monolithic assemblies with information about which ears and which fibres have been used on which substrate in which location.

6.10 Installation of monolithic assemblies

Before testing the suspensions dynamics with the monolithic stage in order to use them in the triangular cavities of the Sagnac speed meter experiment, the monolithic assemblies

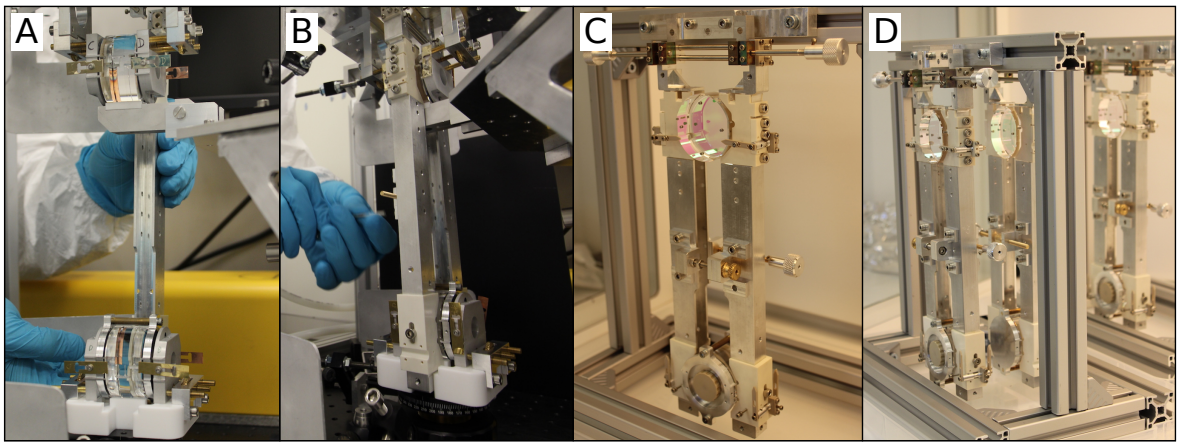

Figure 6.34: Pictures during extraction of the monolithic assemblies from the weld tool. Picture A shows the introduction of one side of the fibre guards. In Picture B the attachment of the central guard opener to the fibre guards is shown. Pictures C and D show finished monolithic assemblies in their fibre guards mounted in a storage and transport container.

need to be installed. The installation is done inside the vacuum system in pre-assembled suspension cages. These triangular cages were prepared with the blade springs, top mass and wires installed to the point at which only the monolithic assembly needs to be introduced. The wire loops to suspend the monolithic assembly were prepared beforehand and small counterweights have been used to separate the loops.

For the installation, the fibre guard assembly is attached to the triangular suspension cage, then the guard assembly is then lifted in a dedicated mechanism to a point where both wire loops can be placed around the penultimate mass. The counterweight stays in the wire loop underneath the penultimate mass to straighten the wires. With two tweezers the wire is now guided over the break-off prisms around the penultimate mass. Once this is achieved the guard assembly is carefully lowered and the counterweights removed. The final position is determined by the small blades inside the top mass. These were originally pre-stressed to mimic a load of approximately 200 g and held in that position with a small screw from the top. Once the guard is lowered enough the blades get pulled further down. This is the point at which the mass-caps are carefully removed from the test mass and the guards are opened to release the masses. This is done iteratively to check for potential slipping or displacement of the masses during release. A set of pictures from this procedure can be found in Figure 6.35. Picture A shows the attachment of the guard assembly to the suspension cage. Picture B depicts the use of the two tweezers to loop the wire around the penultimate mass. Picture C shows the guard assembly before lowering with the counterweight still in place and the mass caps on the test mass. Picture D shows the guard assembly just before opening the guards with the mass caps off the test mass and the counterweight removed.

Assembly	TM	PUM	Fibres		Ears	
			left	right	left	right
1	8	6	E7 front	C6 front	S21 TM	S14 TM
			A9 back	E6 back	S26 PUM	S29 PUM
2	10	9	B2 front	B0 front	S27 TM	S24 TM
			C4 back	C7 back	S08 PUM	S15 PUM
3	3	5	D0 front	E0 front	S11 TM	S18 TM
			E9 back	C8 back	S20 PUM	S17 PUM
4	7	4	E2 front	B8 front	S07 TM	S09 TM
			C3 back	C5 back	S12 PUM	S19 PUM
5	2	1	B6 front	C9 front	S02 TM	S05 TM
			B4 back	A5 back	S03 PUM	S01 PUM

Table 6.2: Monolithic assemblies for the Sagnac speed meter experiment. In this table left and right are defined by looking face-on the HR surface of the mirror or solid cap on the penultimate mass during and after cleaning. The cap is taken off the penultimate mass prior to gluing of the magnet stand-offs. Front denotes the fibre closest to the HR surface back closest to the AR surface.

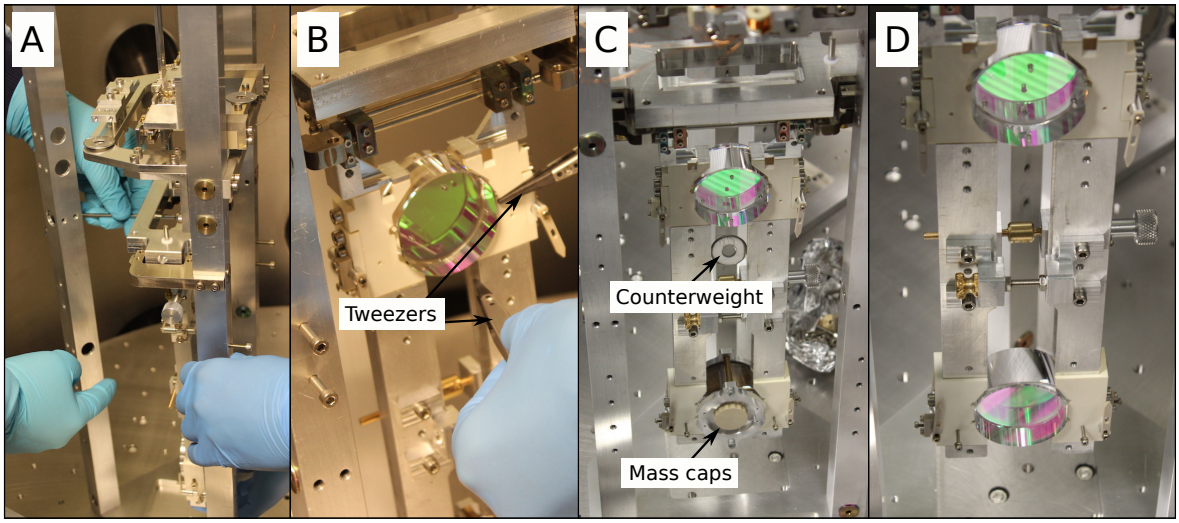

Figure 6.35: The pictures in this figure were taken during installation of the first 100 g monolithic assembly in one of the suspension cages. Picture A shows how the fibre guards with the monolithic assembly are attached to the suspension cage. Picture B depicts the handling of the wires from the top mass that loop around the penultimate mass with tweezers. Picture C shows the installed monolithic assembly in fibre guards with the wires looped around the penultimate mass with mass caps still on the test mass and Picture D shows the assembly with the mass caps removed.

6.11 Measurements

In order to characterise the suspension dynamics and performance, the torque-angle transfer functions from top and penultimate mass to test mass motion were measured. The force-displacement transfer function was not separately measured as longitudinal modes couple into the pitch degree of freedom and can be observed in the torque-angle transfer

function for pitch. With these measurements, the validity of the model was checked and parameters could be adjusted accordingly. As the 100 g ETM suspension cages are designed to operate under an angle of 42.8° a slightly modified optical lever set-up was used as shown in Figure 6.36. The beam of a helium-neon laser is reflected off the test mass main surface

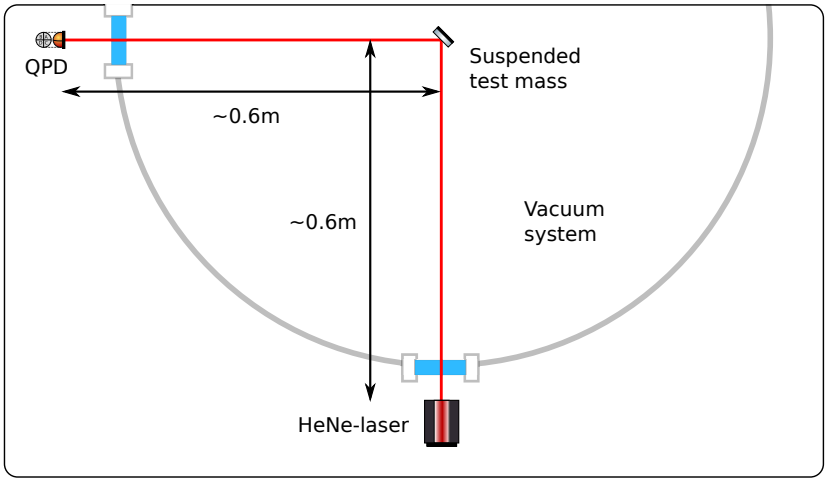

Figure 6.36: Schematic layout of the optical lever for 100 g torque-angle transfer function measurements. A HeNe-laser is reflected off the main mirror surface under ~45° and sensed with a quadrant photo-detector. For a measurement pendulum modes are excited with the coil-magnet actuators on the top or penultimate stage.

(angle of incidence ~45°) and sensed with a quadrant photo-detector at ~90°. Analogous to Section 5.5 the coil-magnet actuators at the top and penultimate mass excite the pendulums rotational degrees of freedom and sense the transferred test mass motion with the quadrant photo-detector. The two horizontal coils are used for excitation of the yaw mode and the two vertical coils are used for excitation of the pitch mode.

6.11.1 Torque-angle transfer functions from penultimate mass

The measurement from yaw excitation at the penultimate mass to yaw motion of the test mass can be seen in Figure 6.37. The red trace in this figure shows the measurement data. In blue, the corresponding torque-angle transfer function from the Simulink® model is plotted. It can be seen that the overall shape of the model agrees well with the measurement. However, both yaw resonance peaks at 1.69 Hz and 3.89 Hz are predicted slightly lower at 1.67 Hz and 3.86 Hz in the model than they occur in the measurement. A possible explanation for this could be slightly shorter wire length between the stages. Above about 10 Hz the measurement is dominated by noise as a consequence of vanishing response. In order to allow a clear representation the measured phases are shifted by 90 deg to avoid phase jumps. The phase shifting and re-wrapping of the measured phases is described in an example in Appendix A.

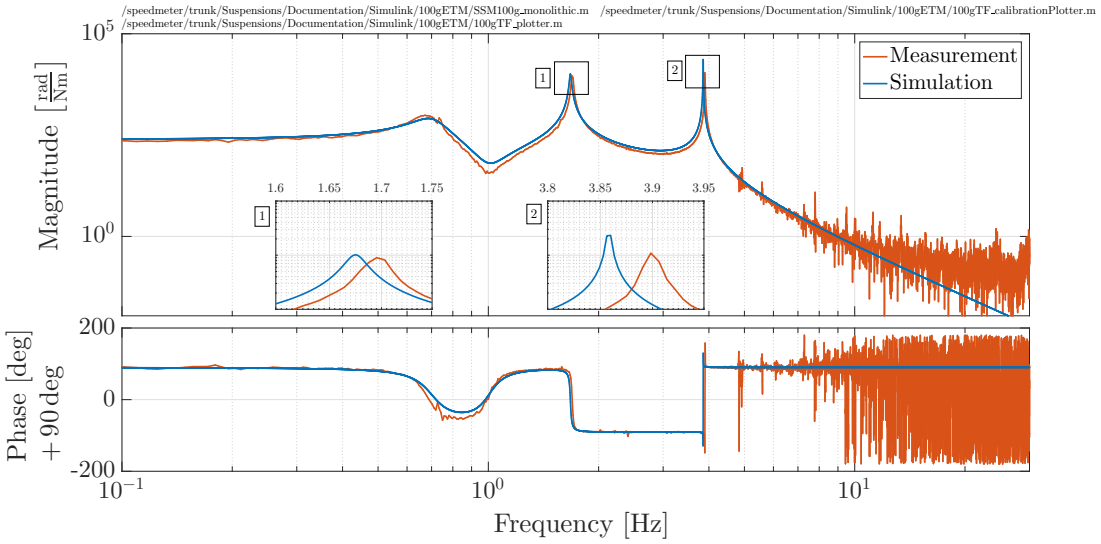

Figure 6.37: The red traces show the measurement data. The blue traces are the simulated torque-angle transfer function from penultimate mass yaw excitation to test mass yaw motion. Model and measurement agree on the general shape for magnitude and phase. Differences occur in the main resonance peaks at 1.69 Hz and 3.89 Hz which are represented as lower frequencies in the model. The measured phase is shifted by + 90 deg and represented well by the shifted modelled phase.

The second measurement from pitch excitation at the penultimate mass to pitch motion of the test mass can be seen in Figure 6.38. The measurement data can be seen in red. The torque-angle transfer function from the Simulink® model is plotted in blue. Cross-coupling from longitudinal motion into pitch motion can be seen as resonance/anti-resonance pairs

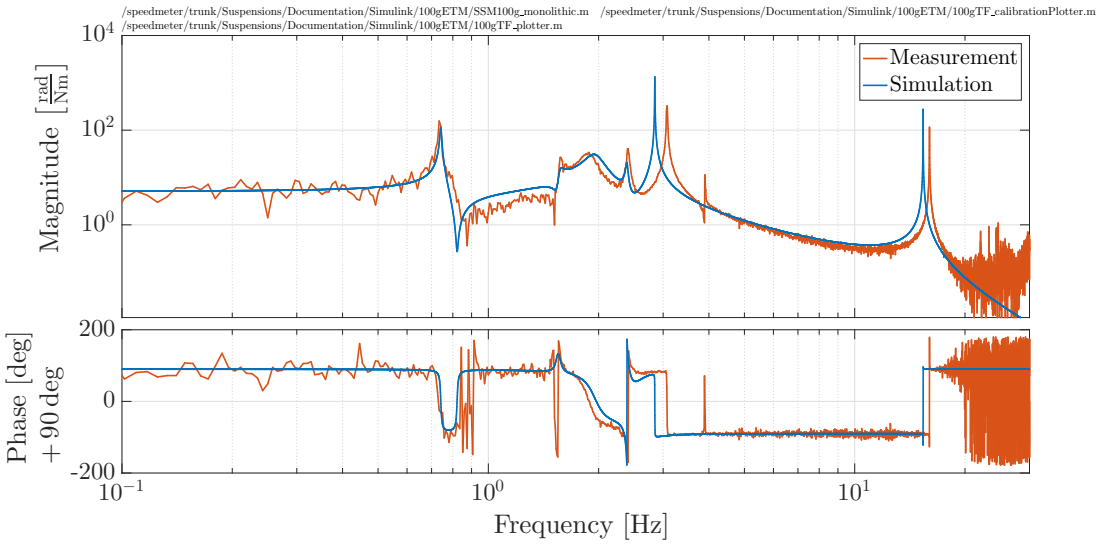

Figure 6.38: The red traces show the measurement. The blue traces are the simulated torque-angle transfer function from penultimate mass pitch excitation to test mass pitch motion. The general shape of the model fits the measurement nicely in magnitude and phase. The two main pitch resonances at 3.08 Hz and 16 Hz are modelled at slightly lower frequencies. The anti-resonance resonance pair at about 3.9 Hz is due to coupling from yaw motion.

at 0.74 Hz and 1.58 Hz. Both measured pitch resonances at 3.08 Hz and 16 Hz are represented slightly lower at 2.85 Hz and 15.37 Hz in the model. An explanation for this could be different break-off points at the test and penultimate mass. The measurement is dominated above about 20 Hz by noise as a consequence of vanishing response. Section 6.11.3 will give a closer look on which realistic parameter changes in the model can be made to fit the measurement.

6.11.2 Torque-angle transfer functions from top mass

The torque-angle transfer functions were also taken using the coil-magnet actuators at the top mass. Again, the two horizontal coils were used for excitation of the yaw mode and the two vertical coils for excitation of the pitch mode. Figure 6.39 shows the torque-angle transfer function from top mass yaw excitation to test mass yaw motion. All three

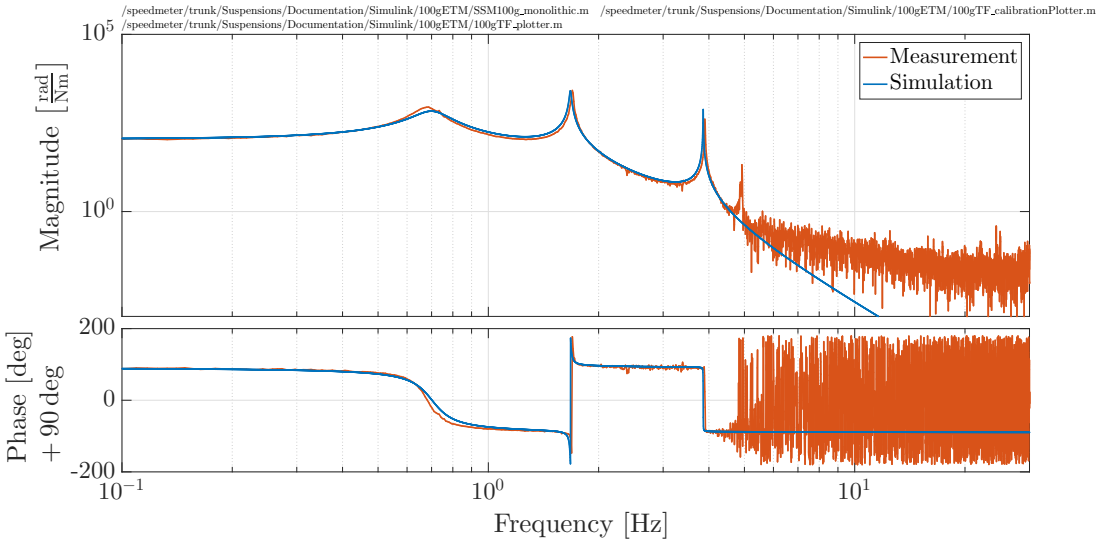

Figure 6.39: The red traces show the measurement data. The blue traces are the simulated torque-angle transfer function from top mass yaw excitation to test mass yaw motion. The overall shape of measured and modelled torque-angle transfer function are in good agreement in magnitude and phase except the model predicts the upper two yaw modes at lower frequencies than they occur. The first yaw mode at 0.69 Hz is modelled at 0.7 Hz. At about 4.9 Hz coupling from roll motion can be observed.

resonance peaks can be seen very clearly. In the same fashion as in the measurement above, the resonance peaks of the model are slightly lower than they occur in the measurement. Above about 5 Hz the measurement is dominated by noise as a consequence of vanishing response.

In Figure 6.40 the torque-angle transfer function from top mass pitch excitation to test mass pitch motion can be seen. It can be seen that most peaks line up very nicely. As above the main resonance peaks at 3.08 Hz and 16 Hz are not represented well in the model as they are

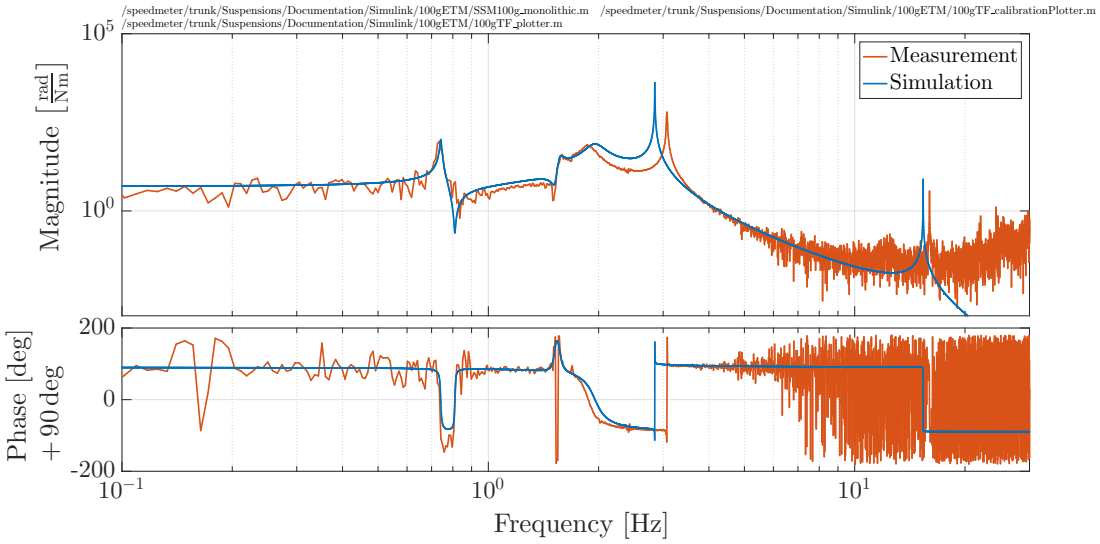

Figure 6.40: The red traces show the measurement data. The blue traces are the simulated torque-angle transfer function from top mass pitch excitation to test mass pitch motion. The shape of the modelled torque-angle transfer function is in good agreement with the measurement for magnitude and phase. As in Figure 6.38 the measured resonances at 3.08 Hz and 16 Hz are seen at slightly different frequencies in the model.

modelled lower than observed in the measurement. The measurement is dominated above about 6 Hz by noise as a consequence of vanishing response.

6.11.3 Adjustment of model parameters

In order to have a model that represents the actual dynamical behaviour of the 100 g ETM suspension a short parameter study similar to Section 5.6 was done. The goal of this study is to match up the main resonance frequencies for pitch and yaw. The main frequencies for the pitch modes at 3.08 Hz and 16 Hz are the common-mode and differential pitch modes of test mass and penultimate mass respectively. In order to shift these, the modelled attachment points of wires and fibres were changed on the two masses. For the penultimate mass the wire separation in the x-direction, that is that is the direction orthogonal to the mirror main surface, on the break-off prisms for the wire loops from above was changed by 350 µm, which can be considered inside manufacturing tolerances of the small break-off prisms. The wider separation of the wires will make the mode shift up in frequency. For the test mass the nominal break-off points of the fibres in vertical direction were changed by 1.2 mm. On first glance this seems to be an unrealistic change, however, considering a non-zero length neck section of the fibres (see Figure 6.30) this change is valid. Additionally the break-off location of the fibre at the penultimate mass was changed by 2 mm.

The main yaw frequencies for the penultimate and test mass are measured at 1.69 Hz and 3.89 Hz and the model already predicts them at 1.67 Hz and 3.86 Hz. The model was slightly

altered by increasing the fibre separation in y-direction by 200 µm on either side of the test and penultimate mass. The increase shifts both frequencies to slightly higher values.

The resulting modelled torque-angle transfer functions for yaw and pitch from top and penultimate stage are now in very good agreement with the measured data. Figure 6.41 and Figure 6.42 show all four measured and calibrated torque-angle transfer functions with the corresponding modelled torque-angle transfer function. It can be seen that all measurements are well represented by the model.

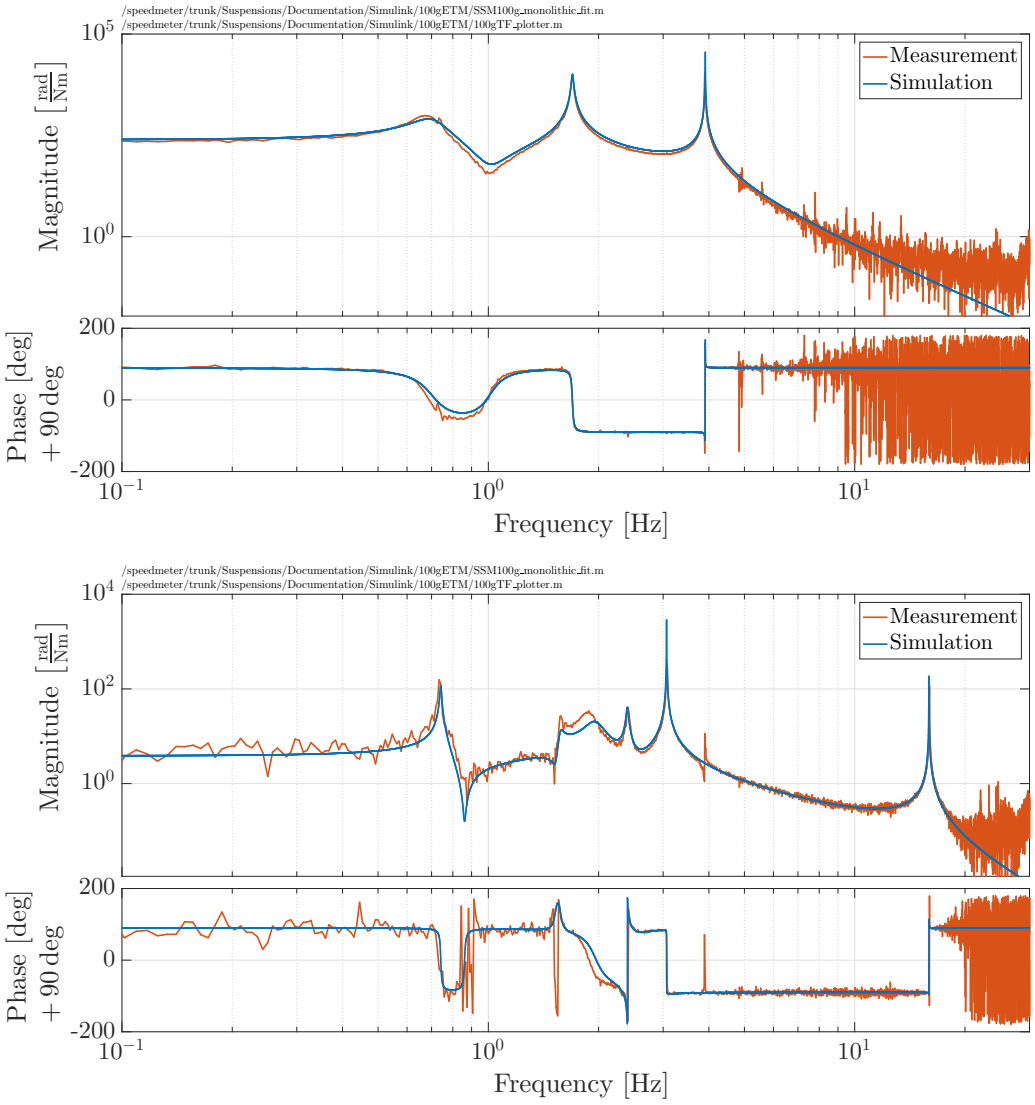

Figure 6.41: The red traces in both panels shows the measurement data. The blue traces are the simulated torque-angle transfer function from penultimate mass excitation in yaw (top) and pitch (bottom) to corresponding test mass motion for the fitted model. It can be seen that the simulation represents the measurement almost perfectly. The anti-resonance resonance pair at about 3.9 Hz is due to coupling from yaw motion.

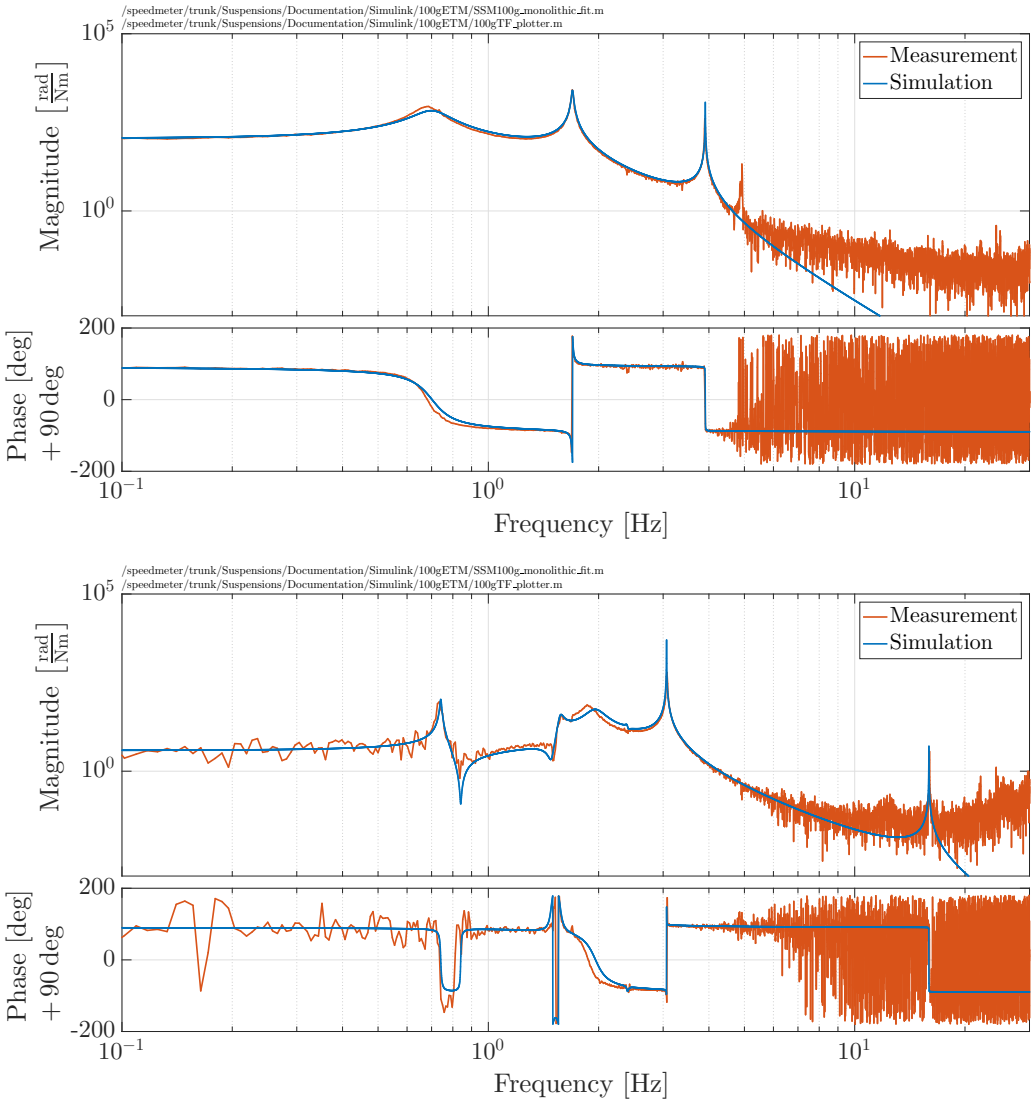

Figure 6.42: The red traces in both panels shows the measurement data. The blue traces are the simulated torque-angle transfer function from top mass excitation in yaw (top) and pitch (bottom) to corresponding test mass motion for the fitted model. It can be seen that the simulation represents the measurement almost perfectly. At about 4.9 Hz coupling from roll motion can be observed

6.12 Conclusion

In this chapter the 100 g ETM suspension was discussed. The mechanical design was described and the initial modelling showed their performance in attenuating ground motion, both vertical and horizontal to the desired level. The chapter was then focussed on the monolithic assembly, together with the vertical blade springs, the key feature of the ETM suspension. All steps from unpacking the 100 g substrates to installing the monolithic assemblies in the suspension have been described in detail and all corresponding procedures can be found in Appendix C.2.3. In the last sections the first characterisation measurements for the 100 g ETM suspension in form of torque-angle transfer functions from top

and penultimate mass to test mass motion were presented. Comparing the model to these measurements showed that a short parameter study was necessary in order to make the model fit the measured resonance peaks. This is necessary as the dynamics of the pendulum will be fed into a sensing and control scheme for the Sagnac speed meter experiment as described in [117]. It was shown that the ETM suspension with the monolithic assembly does fulfil the displacement requirements as well as thermal noise requirements for the suspended elements.

Chapter 7

1 g input test mass suspension

In this chapter the 1 g ITM suspension is discussed. This suspension is of particular importance as the 1 g mirror combined with two 100 g mirrors in the triangular cavities ensures limitation by radiation pressure noise. In order to utilise the same vertical blade springs as in the 100 g ETM suspensions, while meeting the demand for damping of test mass motion, this suspension is designed as a quadruple pendulum. Thermal noise in the suspension elements of the lowest stage is minimised by making it fully monolithic (similar to the 100 g ETM suspension). The main differences to the 100 g design are a changed ear geometry due to the size of the test mass and only two fibres suspend the test mass from the penultimate mass instead of four. It is initially planned to use the two 100 g ETM suspensions in each cavity to compensate for any pitch misalignments of the 1 g ITM. The displacement noise requirements for the 1 g ITM suspensions are the same as for the 100 g ETM suspension. As a technical noise source, the total noise of the 1 g ITM suspension is required to be a factor 10 below the $1.5 \times 10^{-18}\,\mathrm{m}/\sqrt{\mathrm{Hz}}$ design sensitivity of the Sagnac speed meter experiment at 100 Hz.

7.1 Current technologies

Light mirrors, such as the 1 g test mass utilised for the Sagnac speed meter, are used in challenging opto-mechanical experiments, aiming to investigate the photo-thermal feedback [127] in the context of optical springs [128], trying to directly measure radiation pressure noise [129, 130], or to measure thermal noise in thin flexures [131].

The Sagnac speed meter experiment places a strict displacement requirement for the 1 g mirror of $<1.5 \times 10^{-18}\,\mathrm{m}/\sqrt{\mathrm{Hz}}$ at 100 Hz. None of the available technologies can provide this level of displacement and suspension thermal noise. It can only be achieved by suspending the mirror from multiple stages and making the lowest stage of the suspension

fully monolithic. Additionally, the suspension designs in the MIT and Syracuse experiments [128, 129] do not allow damping of the low-mass mirror, which is essential in the Sagnac speed meter. In the remainder of this chapter the mechanical design, technology developments, and the first assembly with a glued test mass of the 1 g ITM suspension will be explained.

7.2 Mechanical design

The 1 g ITM suspension is designed as a quadruple pendulum. The main reason that an increase in the complexity of the design is considered to be acceptable is in order to re-use the vertical blade springs and top mass from the 100 g ETM suspension for the 1 g ITM suspension. Figure 7.1 shows a schematic of the 1 g ITM suspension as a triple (left) and a quadruple (right) suspension. The 1 g test mass is in both cases suspended from two

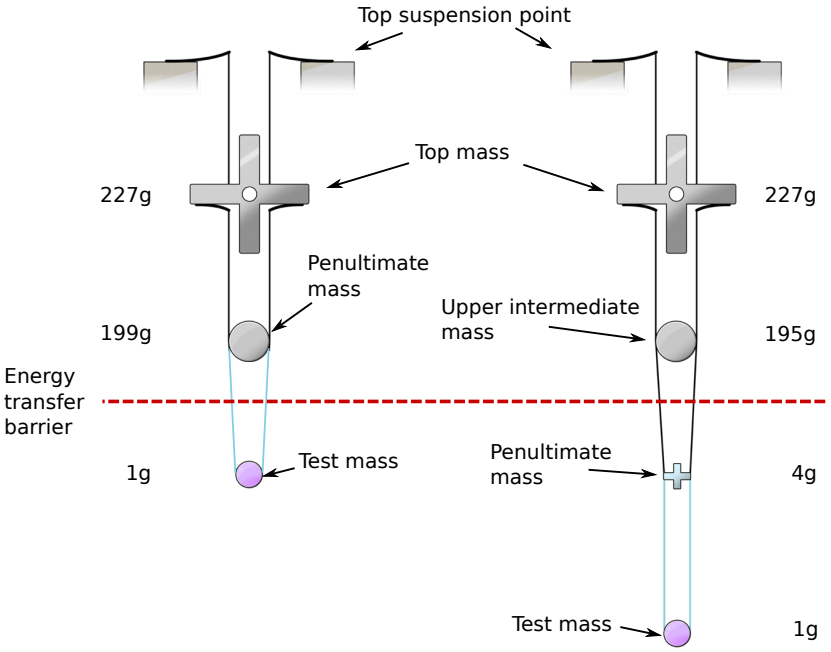

Figure 7.1: Schematic of the 1 g ITM suspension. On the left is a 1 g schematic as a triple pendulum. In this case it is impossible to damp test mass motion at any pendulum stage above due to the high mass imbalance between test and penultimate mass. The picture on the right shows the schematic of the 1 g suspension as a quadruple pendulum. With the additional fourth pendulum stage it is possible to damp motion of the test mass and create a coupled pendulum system of a two stage heavy pre-isolator with vertical blade springs from which a low-mass double stage pendulum is suspended.

10 µm fused silica fibres. On the left side of the figure the triple pendulum case can be seen. The top mass is the same as used in the 100 g ETM suspensions. In the triple suspension design the smallest blades are designed to operate under a nominal load of 100 g. In terms of manufacturing, these blades are on the threshold of feasible machining and cannot be made

smaller or thinner to take less load. For the 1 g ITM suspension, the same blade springs are being used and require the introduction of an additional pendulum stage above the test mass to the design.

The case for the quadruple pendulum can be seen on the right of Figure 7.1. The reason for this four stage design is the otherwise high mass imbalance of the test mass to the above pendulum stage of a factor of 199, which would create a barrier for energy transfer between the stages. The penultimate mass in the quadruple design weighs 4 g and allows the introduction of damping to the test mass. In the Sagnac speed meter experiment the power in the arm cavities is planned to be of the order 1 kW. The power build-up in the two triangular cavities will thus displace the 1 g mirror by roughly 30 µm. Whenever the triangular cavities fall out of lock, the 1 g mirror gets a kick due to the restoring force of the pendulum. This behaviour can be simulated as an impulse response to the test mass in a Simulink® model.

In order to avoid limitation by suspension thermal noise (see Section 2.2.3) the lowest stage is fully monolithic using 10 µm fibres and creates a high-Q system. The suspension can be seen as a two-stage heavy pre-isolator and a low-mass high-Q double pendulum due to the high mass imbalance between upper intermediate mass (195 g) and penultimate mass (4 g). Damping at the test mass level is not desired because it is planned to leave the maximum clear aperture for the beam to pass the ITM and in the case of passive damping force noise due to thermal noise in the damper (see Chapter 8 for details) would spoil the displacement requirement.

The top mass is suspended by two 100 µm stainless steel wires from the blades at the top suspension point, and the upper intermediate mass is suspended by four 50 µm stainless steel wires in order to allow adjustment of the upper intermediate mass in the rotational degrees of freedom from the top mass. The monolithic 1 g assembly is then suspended by four 25 µm stainless steel wires from the upper intermediate mass allowing static alignment of the penultimate mass from the top mass stage. In the monolithic assembly the test mass is suspended by two 10 µm fused silica fibres from the penultimate mass. It should be noted that the 'two-fibre design' does not allow static pitch adjustment of the test mass from pendulum stages above.

7.2.1 Top mass

The top mass in the 1 g ITM suspension is identical to the top mass in the 100 g ETM suspension (compare Section 6.1) and is designed as a composite cross allowing the mounting of small cartridges hosting the vertical blade springs from which the upper intermediate mass is suspended. A computer-aided-design image of this top mass design can be seen in Figure 7.2.

In the centre of the mass is a movable phosphor-bronze core. By shifting the core inside the mass it is possible to adjust the centre of mass and thus allow compensation of pitch misalignment of the top mass. The two blade cartridges which host the lower vertical blade springs are located in the two horizontal arms of the cross and can be installed and removed independently. At the ends of the cross four 3 mm × 6 mm (diameter × length) magnets are mounted and are used in the local control assembly as part of the coil-magnet actuators as well as the eddy-current dampers.

7.2.2 Upper intermediate mass

The upper intermediate mass for the four stage pendulum was required to be 195 g as discussed in Section 7.2 and it was decided to design this mass in a similar shape to that of the penultimate mass of the 100 g ETM suspension in terms of break-off locations for the wire loops from the top mass. This way the length of the wire loops would not have to be changed and existing wire jigs for the 100 g ETM suspension could be reused without

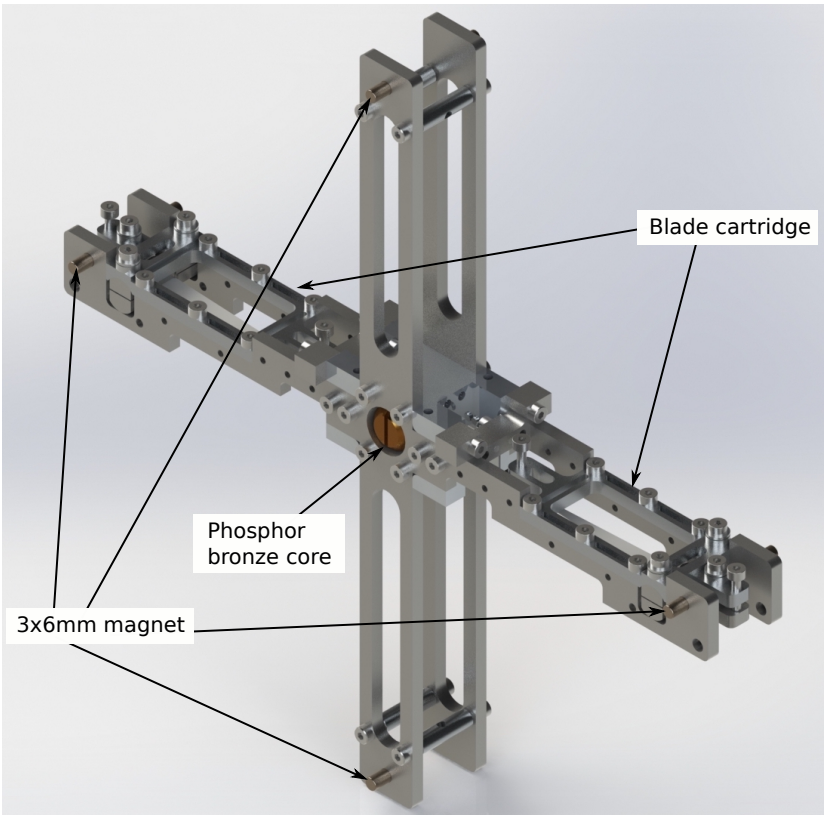

Figure 7.2: Computer-aided-design model of the ITM suspension top mass. Designed as a composite cross the mass hosts two cartridges that hold the two lower blade springs from which the upper intermediate mass is suspended. The phosphor-bronze core in the centre of the mass can be used for pitch adjustment. Four magnets which are mounted at the ends of the cross on either side of the mass are part of four coil-magnet actuators for local control and damping. Magnets are attached on either side of the mass to avoid shifts of the centre-of-mass.

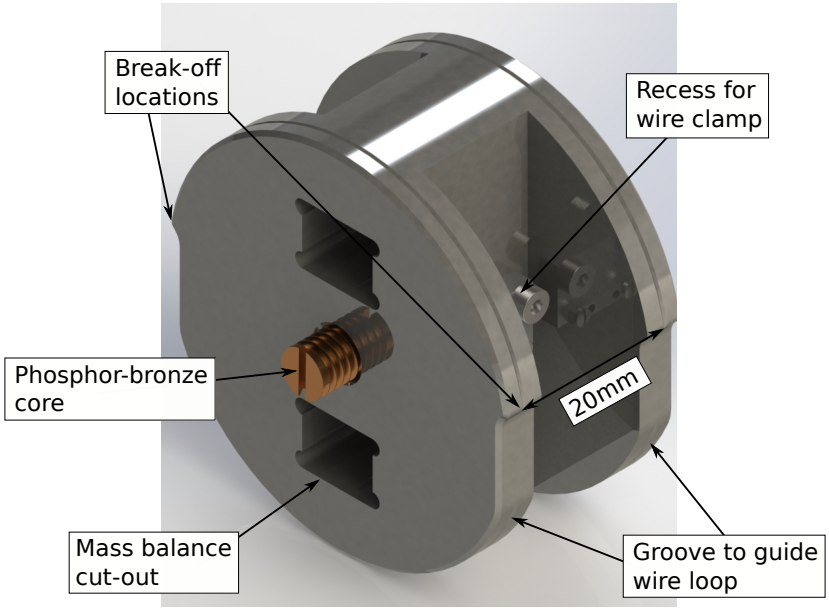

Figure 7.3: Computer-aided-design model of the ITM suspension upper intermediate mass. The special design of this mass eliminates the need for additional break-off elements. The grooves around the mass are for guiding the wire loops from which this mass is suspended. The phosphor-bronze core provides an adjustment of the centre of mass and thus can be used as a tool for pitch alignment. Wire clamps for wire loops to suspend the penultimate mass are located in recesses on the side of the mass. The two cut-outs through the mass were used for weight matching and will also be used for a dedicated mass catcher.

modification. A computer-aided design model of the upper intermediate mass can be found in Figure 7.3.

Two grooves can be seen running around the upper mass, intended as guides for positioning the suspension wires. The separation of the two grooves is set to 20 mm, which is the same as the break-off point separation on the prisms of the penultimate mass of the 100 g ETM suspension. The outer shape of the mass was designed to eliminate additional break-off elements, which is achieved by extending the radial shape slightly over the flats on the sides. The overlapping ends thus create break-off points about 4 mm above centre of mass in the same way as would conventionally be achieved using an additional prism. In the centre of the upper intermediate mass is another adjustable phosphor-bronze core, located to allow shifting of the centre of mass and to compensate for pitch misalignment of the penultimate mass.

The wire clamps that hold the wire loops for the penultimate mass are located in recesses on the sides of the upper intermediate mass in order to suspend the penultimate mass with close to vertical wires. The break-off points on the prisms on the penultimate mass are separated by 19 mm (see Section 7.2.3) which is the same as the separation of the wires inside the clamps on the upper intermediate mass. To allow for these recesses and still have enough weight the mass is made from stainless steel. The two cut-outs in the centre

of the mass are for further weight balancing and the upper cut-out is used for a dedicated mass catcher/holder (see Section 7.2.5).

7.2.3 Penultimate mass

The penultimate mass for the 1 g ITM suspension was required to be of low mass to allow energy transfer between the test and penultimate masses and thus allow damping of test mass motion at the stage above. At the same time, the penultimate mass was required to be large enough to host four coil-magnet actuators that could be used for actuation, but also for passive damping (see Chapter 8). In order to achieve these requirements, the penultimate mass was designed as a cross mass similar in shape to the top mass, but rather than being made of metal, the entire mass is made of fused silica leaving the option to make it fully monolithic. A computer-aided-design model of the 4 g penultimate mass can be seen in Figure 7.4.

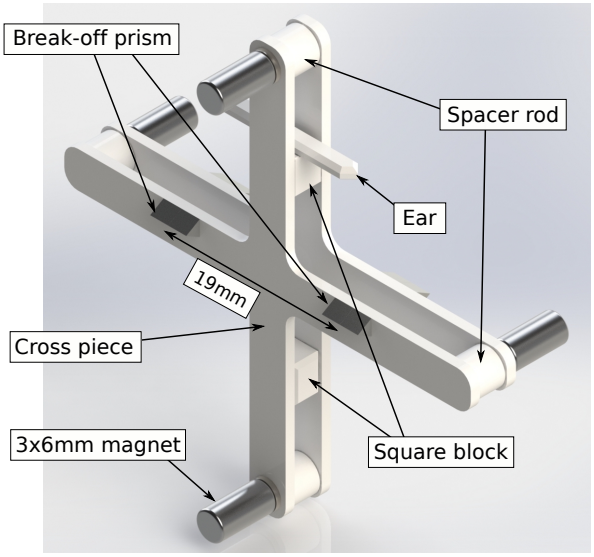

Figure 7.4: Computer-aided-design model of the ITM suspension penultimate mass. The mass is made from two cross pieces that are connected by four spacer rods at the ends of the cross. Additionally two square blocks are mounted in between the cross parts, one to connect the ear to the penultimate mass, the other to balance the centre of mass. Four break-off prisms are located along the horizontal cross arms defining break-off locations 19 mm apart for wire loops from the upper intermediate mass. Four 3 mm×6 mm magnets are mounted on the ends of the cross to allow actuation and damping at the penultimate stage of the 1 g ITM suspension.

The mass consists of multiple pieces and a full description of the assembly process is discussed in Section 7.9. The front surface is a cross piece connected by four spacer rods at the end of the arms to an identical cross piece serving as a back surface. Along the vertical axis of the cross two square blocks are located to balance the centre of mass of the penultimate mass and to host the cradle ear to which the 10 µm fibres are to be welded. In

order to save weight four 3 mm × 6 mm (diameter × length) magnets in total are used for the coil-magnet actuators, two located on the front surface at the ends of the horizontal cross arms and two located on the back surface at the ends of the vertical cross arms. In this configuration it is possible to cancel the total magnetic moment of the four magnets to minimise influence from varying magnetic field in the environment. These magnets are mounted magnetically on 3 mm × 0.5 mm (diameter × length) type 430 stainless steel discs in opposite polarity on the front and back of the penultimate mass cross. As the upper part of the monolithic assembly for the 1 g ITM suspension, this mass is suspended by four 25 µm wires from the upper intermediate mass. This is realised by two wire loops that loop around the horizontal arms of the cross, and over the break-off prisms to create break-off points separated by 19 mm (the same separation as the recess on the upper intermediate mass - see Section 7.2.2). With all its components attached, the penultimate mass has a total weight of 4 g.

In order to verify the mechanical rigidity of the penultimate mass cross a modal analysis in ANSYS® was conducted. The cross parts are made from 1.2 mm thick fused silica which could result in internal modes within the measurement band of the Sagnac speed meter experiment between 100 Hz and 1 kHz. The spacer rods at the ends of the cross were implemented to make the cross more rigid. Figure 7.5 shows the results of the ANSYS® simulation. The four images show the first four body modes of the penultimate mass cross

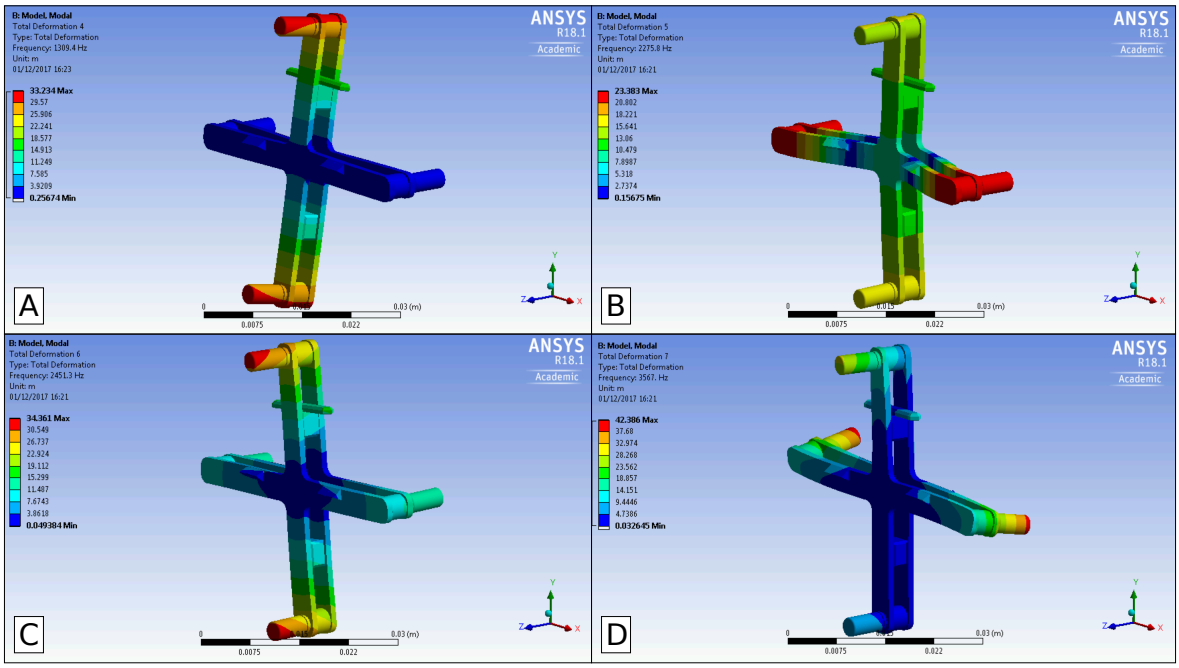

Figure 7.5: ANSYS® simulation of internal modes of the penultimate mass cross. The lowest internal mode is at about 1.4 kHz and thus above the measurement band of the Sagnac speed meter experiment. The lack of initial rigidity was counteracted with the implementation of the spacer rods at the ends of the cross.

and it can be seen that the lowest internal mode is at about 1.4 kHz (see Image A). All other internal modes are higher and well outside the measurement band.

7.2.4 Test mass

The core of the 1 g ITM suspension is the 1 g mirror. The substrate was designed in such a way as to allow different attachment points for ears from which to build the interface between substrate and fibres. In the beginning of the design process the possibility of directly welding fibres to a 45° rotated square mirror was discussed, however this procedure was rejected due to the high heat load on the coating during welding which can cause the coating materials to crystallise. The substrates have an outer diameter of 10 mm and a thickness of 5 mm, so in order to prevent any damage to the coating, ears are required to reduce the heat load. On the barrel of the substrate two sets of 4 mm × 5 mm parallel flats (orthogonal to each other) are polished to serve as attachment points for the ears[1]. One of these four flats is compromised to allow marking of the HR surface of the mirror that has a radius of curvature of about 7.91 m. A comparison of two different ear designs can be seen in Figure 7.6. Picture A shows an ear design where the ears are attached to the sides

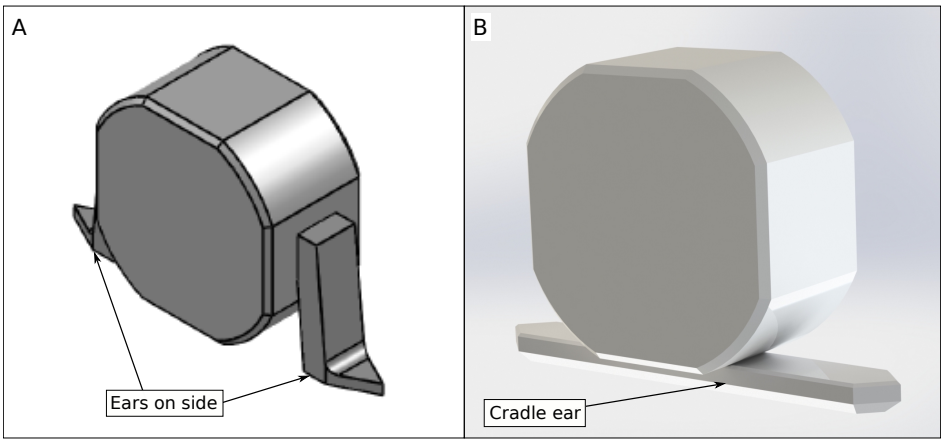

Figure 7.6: Computer-aided-design model of the ITM suspension test mass in two ear configurations. The substrate of the 1 g mass is designed to have two sets of parallel 4x5 mm flats around the barrel. This enabled different ear designs and attachment points for ears. The left picture shows two ears on the sides of the substrate. The attachment point for the fibre is deliberately below centre of mass to allow mounting of stock of the fibres during welding and to reduce heat load during welding on the optical coatings. The right picture shows the cradle design in which the test mass substrate is bonded onto a horizontal cradle, eliminating the need for a more complex ear design.

of the test mass. The shape of these ears was chosen to allow the weld point to be well below the centre of mass in order to allow a few mm of 400 µm stock required to hold the fibre during the weld process. This way the neck of the fibre (and thus its break-off point)

[1]Due to the long lead time of the polished mirror and the optical coating, the mirrors had to be ordered at a time when the design was still in progress.

could be kept close to the centre of mass in order to keep the pitch mode of the mirror low and to reduce longitudinal to pitch coupling in case it is ever desired to directly actuate on the mirror from the penultimate stage. However, it immediately became apparent that this could be effectively achieved using a cradle design. The cradle design, depicted in Picture B, attaches the test mass on a horizontal cradle ear, keeping the attachment points for the fibres roughly 5 mm below the centre of mass.

To determine the feasibility of this design, a modal analysis of the cradle ear was performed in ANSYS®. In this simulation the internal modes of the ear fixed to the test mass were investigated in order to verify that these modes do not contaminate the measurement band of the Sagnac speed meter experiment between 100 Hz and 1 kHz. The first four (lowest) internal modes of the cradle ear on the 1 g test mass substrate are shown in Figure 7.7, where

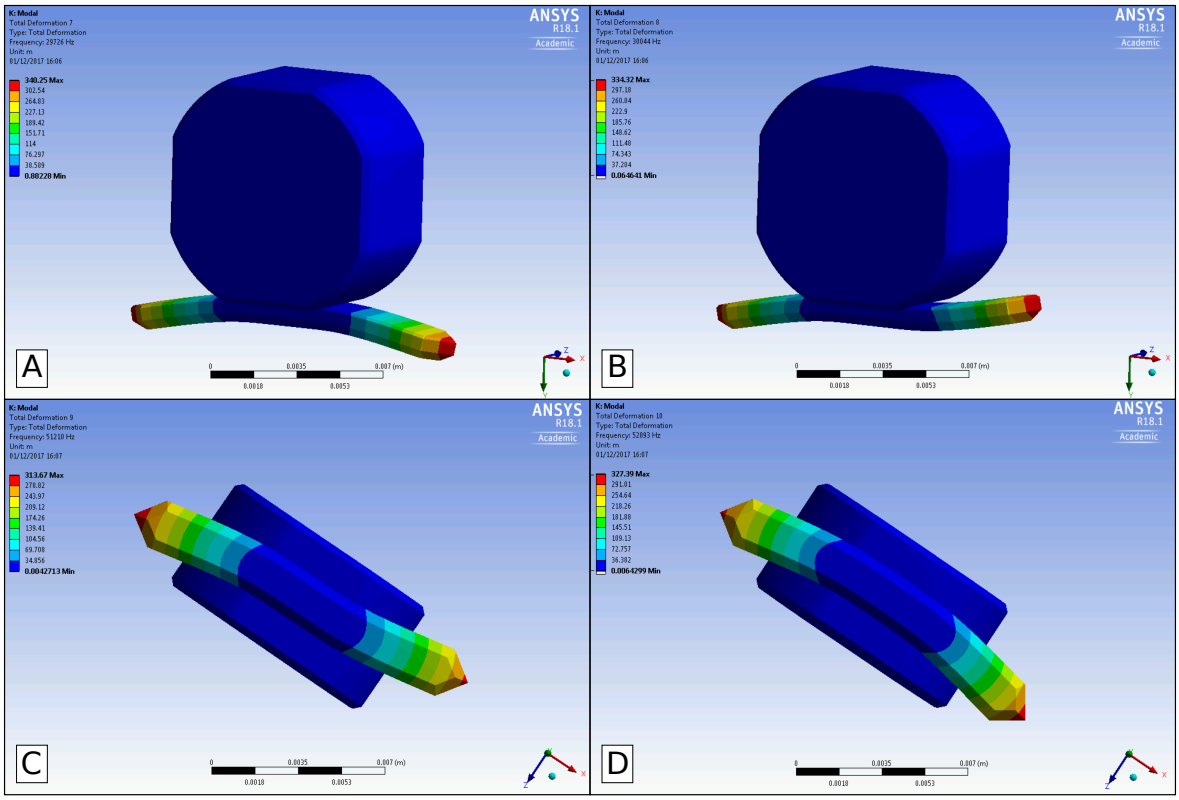

Figure 7.7: ANSYS® simulation of the internal modes of the cradle ear on a 1 g ITM substrate. The first internal mode shown in Image A has a resonance frequency of about 30 kHz. All following modes are at even higher frequencies and thus well outside the measurement band of the Sagnac speed meter experiment.

it can be seen the resonance frequency of the first mode (Image A) is at about 30 kHz. All other modes are found at even higher frequencies, and thus will not affect the Sagnac speed meter experiment in the 100 Hz to 1 kHz band.

The properties of the optical coatings on the 1 g ITM substrates are summarised in Table 7.1. As with the coatings for the ETM substrates (see Section 6.4.1), these coatings were

Property	Main Surface	Back Surface
Type of coating	High-Reflection	Anti-Reflection
Radius of curvature	(7.91 ± 0.02) m	∞
Angle of incidence	4.4°	4.4°
Transmission @ 1064 nm	700 ppm for s-pol light	>99.995 % for s-pol light
Material	SiO_2 and Ta_2O_5	SiO_2 and Ta_2O_5
Absorption @ 1064 nm	<1 ppm	<10 ppm
Scattering @ 1064 nm	<1 ppm	<10 ppm

Table 7.1: Summary of properties for the optical coatings on the mirrors of the 1 g ITM suspensions.

manufactured using the ion beam sputtering technique at LMA in France, and are made from alternating layers of silicon-dioxide (SiO_2) and tantalum-pentoxide (Ta_2O_5). As these mirrors are the input test masses for the triangular cavities the transmission of the HR surface is 700 ppm. The figures for scattering and absorption in the coatings are the same as for the end test masses with <1 ppm for the HR and <10 ppm for the AR surface. Further information on the specification of surface figures for the 1 g substrates can be found in [118].

Two pictures of a coated 1 g ITM mirror can be seen in Figure 7.8. In Picture A the coated

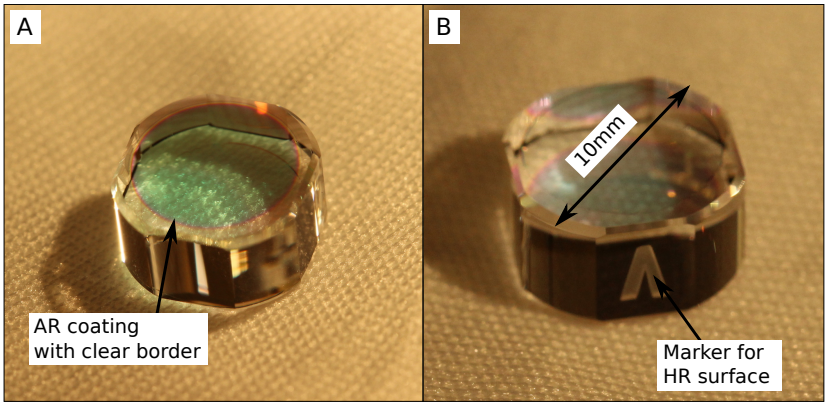

Figure 7.8: The two pictures show the two sides of the ITM mirror. In Picture A the AR surface pointing upwards can be seen. In this picture the coated area due to the use of a mask during the coating process is clearly visible. In Picture B the HR surface of the mass is pointing up, indicated by the engraved V-marker on one flat side. The 1 g ITM substrate has a diameter of 10 mm.

substrate can be seen with the AR surface pointing upwards. The circular shape of the coating comes from the use of a mask during the coating process.

7.2.5 Suspension cage

The suspension cage for the 1 g ITM was designed as a three-legged cage. Due to limited space in the vacuum system and additional constraints from the bridge structure that rigidly

connects the two breadboards of the Sagnac speed meter experiment, the design for this cage had to be compact. In the optical layout (compare Figure 3.11) the two 1 g ITM mirrors are separated by about 20 cm. Additionally, the requirement that the 1 g ITM suspensions should be capable of being installed or removed independently dictated two separate non-identical cages in order to fit the two suspensions in the confined space between the legs of the bridge structure. A computer-aided-design model of one of the cages can be seen in Figure 7.9.

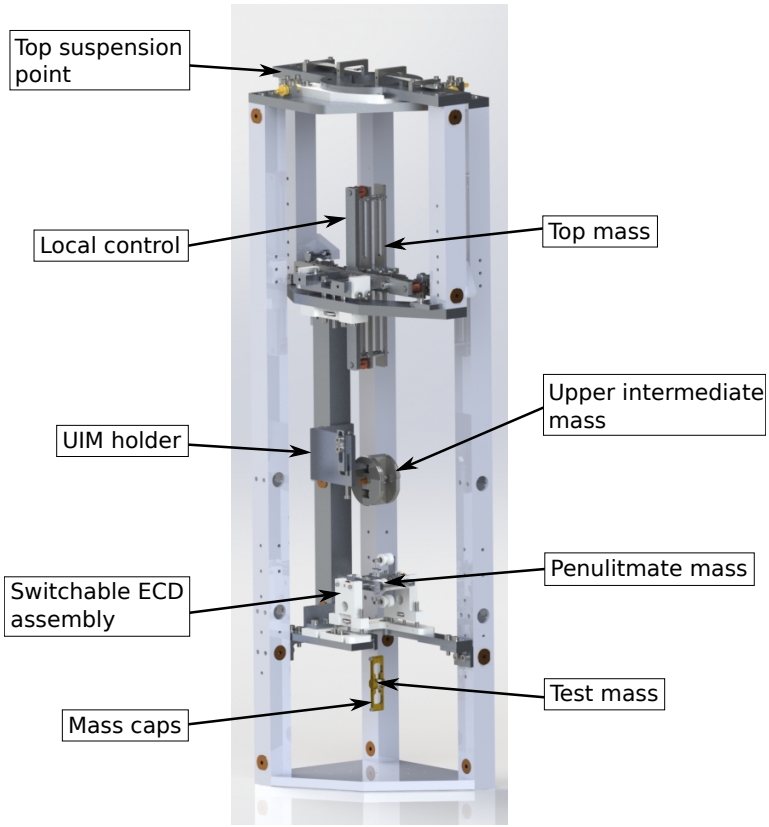

Figure 7.9: Computer-aided-design model of one 1 g ITM suspension. The four-stage pendulum suspension is mounted in a three-legged cage. The top suspension point is designed to allow lateral and rotational adjustment of the full suspended chain.

The quadruple pendulum chain is mounted at the top suspension point to an adjustable top plate, with a local control assembly located at the top mass level. The suspension cage also hosts an upper intermediate mass holder that can be used to adjust the upper intermediate mass height and serves as a mass-catcher when the masses are released. At the penultimate mass stage an additional platform for a control and damping assembly can be found, which is additionally used to introduce and remove the monolithic assembly during installation of the 1 g ITM suspension.

Top plate adjustment

The 1 g ITM suspensions will be placed and initially aligned with laser cut stainless steel templates which reference the suspension cage to the bridge structure connecting the two breadboards. In order to allow further alignment of the whole suspended chain, the top plate is adjustable in rotation and can be shifted laterally. To minimise friction between two metal surfaces this top plate assembly is designed in a sandwich configuration with a layer of PEEK in between two aluminium parts. A top view as well as a side view of the top plate assembly as a computer-aided-design model can be found in Figure 7.10. In

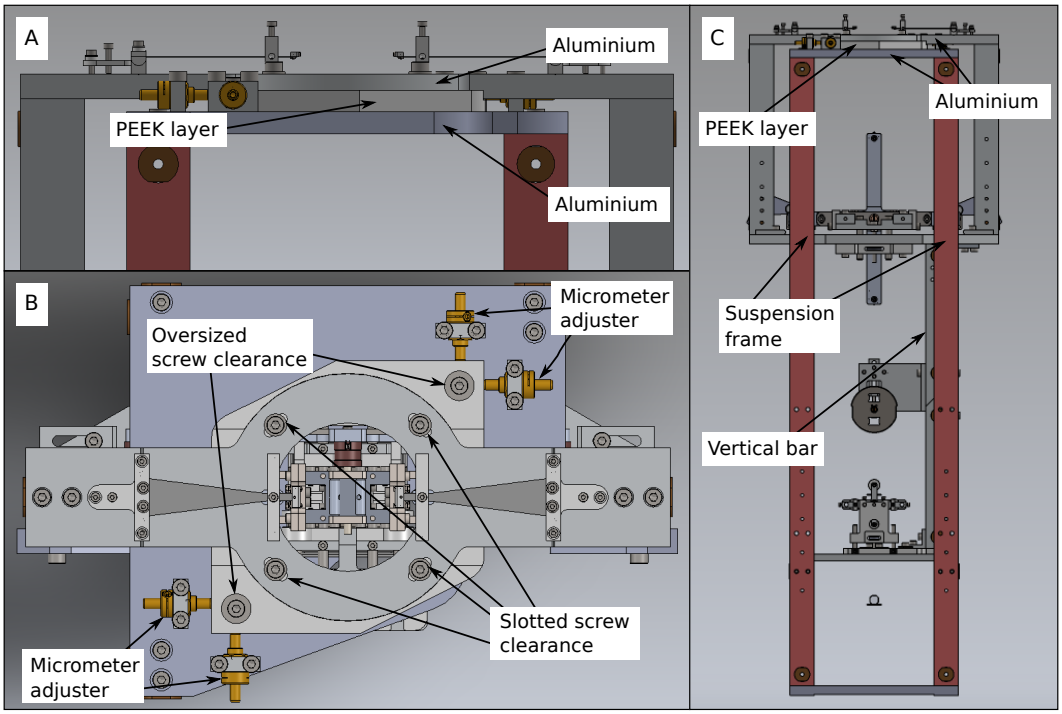

Figure 7.10: Computer-aided-design model of the top plate assembly. In Picture A a side view reveals the sandwich-configuration with a PEEK layer in between two aluminium plates. Picture B shows a top view of the top plate assembly. Lateral alignment can be realised with four micrometer adjusters pushing on the PEEK layer that can be fixed by two M4 screws. Rotational adjustment is possible with the recess in the PEEK layer that allows the top aluminium plate to rotate around the central axis of the suspended chain. In Picture C the whole suspension cage can be seen. The rotatable assembly is mounted to the top layer and the vertical bar allows transfer of rotational motion to the switchable ECD cage.

Picture A the side view can be seen. From this perspective it is easy to identify the sandwich configuration with the PEEK layer in between the two aluminium plates. Picture B shows a top view of the 1 g ITM suspension. Lateral alignment is achieved with four micrometer adjusters from Newport (AJS100-0.5H-V6) which push against the PEEK layer. The two M4 screws are used for rigidly fixing the PEEK layer after alignment. The PEEK layer itself has a recess to guide the upper aluminium part, which hosts the upper blade springs of the suspension. The recess is cut in such a way as to allow the aluminium part to rotate around

the vertical centre-line of the suspended chain. Lateral shifts of ± 1.5 mm and a maximum rotation of $\pm 5^\circ$ can be realised. Picture C shows the full suspension cage where the bottom aluminium layer is the top plate of the rigid suspension frame. The PEEK and top aluminium layer allow rotation of the suspended chain and with the vertical bar it is possible to transfer this rotation to the switchable ECD assembly. The initial nominal position of the top plate assembly will be aligned with reference templates to the lower aluminium plate.

Switchable ECD assembly

In the design for the 1 g ITM suspension a removable platform is located at the penultimate stage. A PEEK plate on this platform can be connected to the rotatable top plate of the suspension cage with a vertical bar assembly in order to transfer rotational motion to the switchable ECD assembly. After adjustments have been made the PEEK plate can be fixed to the platform. As mentioned above the penultimate mass is used for actuation on the test mass as well as damping of test mass motion, where the damping is realised using switchable passive eddy-current damping (see Chapter 8). Both actuation and damping are implemented with coil-magnet actuators. The switchable ECD assembly equips the suspension cage with the four coils needed for these actuators.

A computer-aided-design model of the switchable ECD assembly can be seen in Figure 7.11. Two vertical coils are mounted on one side of the penultimate mass and two horizontal coils are mounted on the opposite side. The coil assemblies, consisting of two coils and

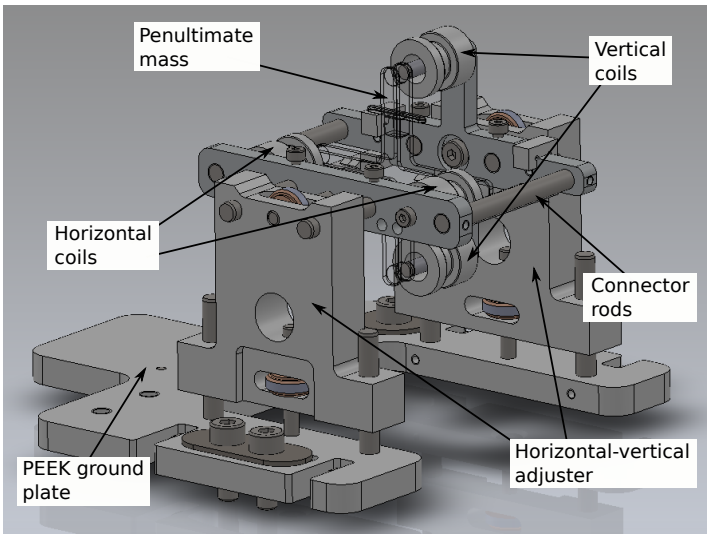

Figure 7.11: Computer-aided-design model of the switchable ECD assembly for actuation and damping at the penultimate stage. The assembly hosts a horizontal and a vertical mounted coil pair that make the coil-magnet actuators together with the 3 mm $\times$ 6 mm magnets on the penultimate mass. The coils are mounted on horizontal-vertical adjusters. The opposing coil assemblies can be made to a rigid cage with two additional connector rods. The adjusters are mounted on a PEEK ground plate that is mounted to an aluminium platform which can be connected to the suspension cage.

a mounting plate, are connected to horizontal-vertical adjusters, which use dowel pins as a rail system together with a thumbscrew to move the adjuster along the pins. With two connector rods on the right and left side of the coil holder assemblies, a rigid coil cage can be built around the penultimate mass. The horizontal-vertical adjusters are mounted on a PEEK ground plate which can be connected to the aluminium platform that can in turn be connected to the suspension cage. The screw clearances in the PEEK ground plate are dimensioned in such a way as to give a similar range of lateral and rotational shift as the adjustable top plate of the suspension cage.

The switchable ECD assembly also serves as a mass catcher for the penultimate mass. For this, two arms can be attached to the mounting plate of the vertical coil assembly. These catchers are made from PEEK and located 2 mm underneath the horizontal arms of the penultimate mass. In case of a wire failure in any of the pendulum stages above, the PEEK catchers will halt the fall of the penultimate mass and prevent any further damage. As will be presented in Section 7.11, the switchable ECD assembly is designed to interface with a weld jig and can be used to introduce the monolithic assembly of the 1 g ITM suspension to the suspension cage.

Vertical bar assembly and UIM mass catcher

The adjustability of the top plate assembly allows fine alignment of the suspended chain after placing the cage inside the vacuum system. This adjustability needs to be transferred to all other assemblies that host any ancillary parts or are intended as a mass catcher or hold one of the suspended parts at any given time. A good example of this is the switchable ECD assembly. As the assembly is mounted on a platform that is connected to the suspension cage, any rotational adjustment or lateral shifts of the suspended chain would result in misalignment of the coils relative to the magnets on the penultimate mass. To counteract this behaviour, a vertical bar assembly was implemented. A computer aided design model of the vertical bar assembly can be seen in Figure 7.12. The assembly connects the PEEK ground plate of the switchable ECD assembly to the adjustable top plate in order to directly transfer any rotational or lateral shifts and consists of two bars that can be connected in the centre. This allows the upper bar to be connected to the adjustable top plate and the lower bar to be connected to the PEEK ground plate, creating a handle that can be used upon removal and introduction of the ECD assembly. As can be seen in Figure 7.12 the upper bar also holds an upper intermediate mass holder and catcher. The mass catcher uses a horizontal bar that can be slotted into the upper cut-out in the upper intermediate mass (see Section 7.2.2) and is used as a mass holder to adjust its vertical position prior to suspending the mass. This horizontal bar can be lowered once the mass is suspended such that it will no longer restrict its motion, but in the case of a wire failure it can still serve as

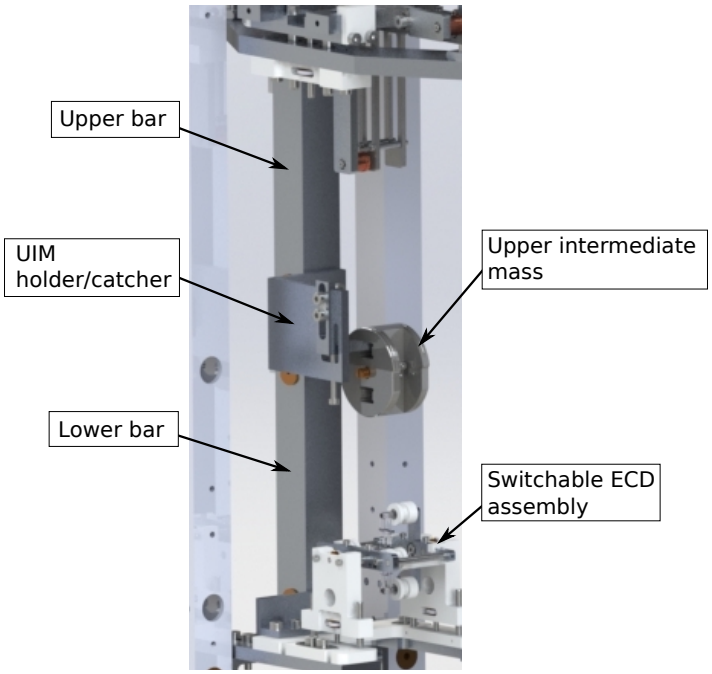

Figure 7.12: Computer-aided-design model of the vertical bar assembly. Consisting of an upper and lower bar this assembly connects the adjustable top plate to the switchable ECD assembly and transfers adjustment to the penultimate stage. The upper bar additionally hosts a mass holder/catcher for the upper intermediate mass. The lower bar can be used as a handle for introducing or removing of the switchable ECD assembly.

a mass catcher.

7.3 Actuators and damping

In an identical arrangement to the 100 g ETM suspension, the 1 g ITM suspension uses a local control assembly at the top mass stage for DC-offsets and thus alignment of the top mass and the whole suspended chain. The coil-magnet actuators are the same as in Section 6.2, consisting of 3 mm × 6 mm magnets, and coils made from 150 µm Kapton-enamelled copper wire with 60 turns wound on copper formers. The actuators have the same response of $32\,\mathrm{mN\,A^{-1}}$ and the same damping constant of $0.03\,\mathrm{kg\,s^{-1}}$ per coil due to passive eddy-current damping. A computer-aided design model of the local control assembly can be seen in Figure 6.2.

The coils on the switchable ECD assembly are made from the same 150 µm Kapton-enamelled copper wire with 250 turns. In contrast to the local control assembly, the coil formers are made from PEEK to minimise passive eddy-current damping due to the use of conductive former material. A more detailed discussion of the switchable eddy-current damping used in this stage will be provided in Chapter 8. The coil-magnet actuators are made with the same 3 mm × 6 mm magnets as at the top stage and have a response of $140\,\mathrm{mN\,A^{-1}}$ per

coil. The penultimate mass actuators are designed with a stronger response in order to provide sufficient damping in the switchable ECD configuration described in Chapter 8. A computer-aided-design model of the switchable ECD assembly with the four control coils can be seen in Figure 7.11.

7.4 Modelling

Modelling of the 1 g ITM suspension was performed in Mathematica® as for the 100 g ETM suspension, however the model had to be completely redefined for a quadruple pendulum suspension with two stages of vertical blade springs. All parameters for the top mass as well as the blade springs were taken over from the 100 g model, and in the same way as before, the displacement transfer functions can be modelled to estimate coupling from seismic noise into displacement noise of the suspension. Force transfer functions from actuator locations to motion of the 1 g test mass are modelled as well, and can be compared to measurements in the lab after the suspension is installed.

7.4.1 Coupling from seismic ground motion

Analogous to Section 6.3.1, the longitudinal and vertical displacement transfer functions from top suspension point to test mass motion can be used to estimate the coupling of seismic ground motion into displacement noise. As before, the seismic pre-isolation stack is modelled to have a resonance frequency of 18 Hz and is assumed to act the same way in horizontal and vertical direction. The longitudinal and vertical displacement transfer functions from top suspension point to test mass motion are depicted in Figure 7.13, where the

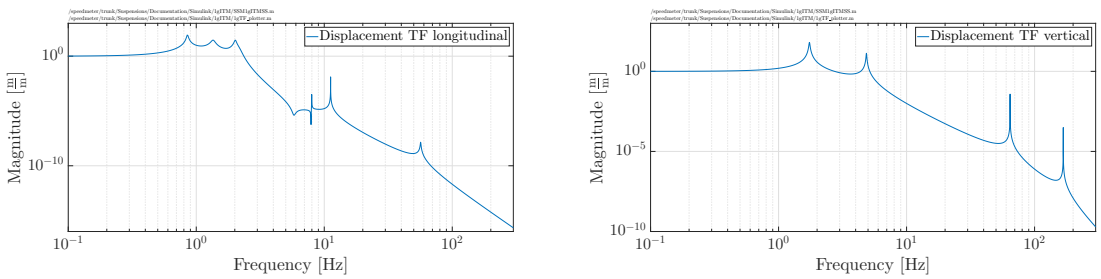

Figure 7.13: Horizontal and vertical displacement transfer function for the 1 g ITM suspension. The left plot shows the horizontal displacement transfer function from top suspension point to horizontal motion of the test mass. The right plot shows the vertical displacement transfer function.

highest frequency in the longitudinal transfer function is the coupling from pitch motion of the penultimate mass at 56.61 Hz. In the vertical displacement transfer function the highest frequency is the bounce mode of the penultimate mass at 167.6 Hz and is a result of the 25 µm steel wire that suspends the monolithic assembly from the upper intermediate mass.

Due to the modular nature of the wire clamps on the upper intermediate mass, the wire can be substituted with wire of smaller diameter to lower this high vertical bounce mode (15 µm result in a frequency of about 100 Hz). However, 25 µm wire was installed in the first instance for practical reasons, as wire of smaller diameter becomes exceedingly hard to handle.

The requirement for the displacement noise of the 1 g ITM suspension due to seismic coupling is the same as for the 100 g ETM suspension. As part of the triangular cavities the displacement noise of the 1 g ITM suspension is required to be a factor 10 below design sensitivity of the Sagnac speed meter experiment to contribute no more than 1 % to the total noise. Figure 7.14 and Figure 7.15 show the estimated displacement noise of the 1 g ITM suspension for horizontal and vertical ground displacement. Figure 7.14 depicts coupling

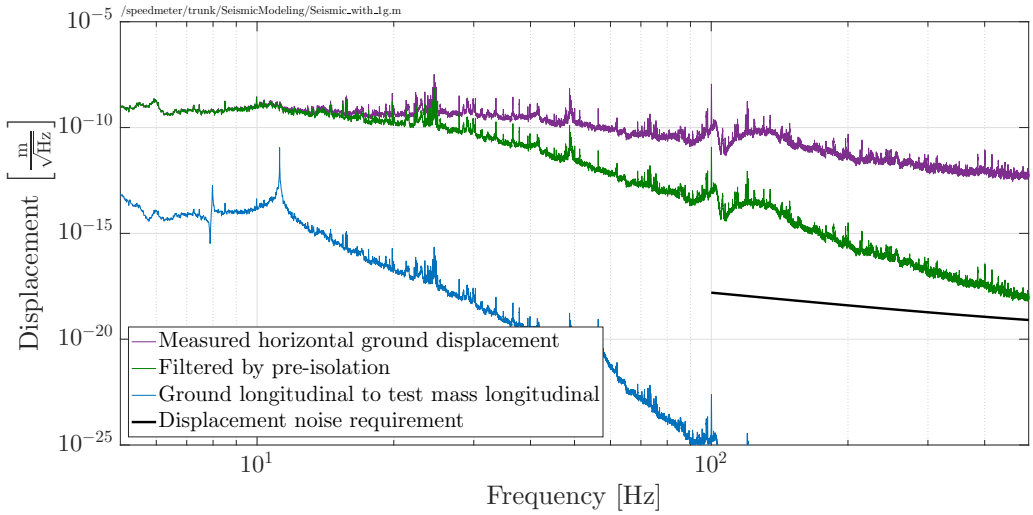

Figure 7.14: Measured horizontal ground displacement (purple) using a S-13 seismometer, estimated horizontal filtering by passive stacks (green), filtering by 1 g ITM horizontal to horizontal transfer function (blue) and displacement noise requirement for the Sagnac speed meter experiment (black). The estimated displacement noise is well below design sensitivity.

from horizontal ground displacement to longitudinal displacement of the 1 g test mass. The purple trace shows the measured horizontal ground displacement in the lab in Glasgow, the green trace adds the filtering from the pre-isolation stack and the longitudinal displacement noise of the 1 g ITM suspension is plotted in blue. For this last trace the longitudinal displacement transfer function from top suspension point to test mass motion is taken into account. Figure 7.15 shows the horizontal displacement noise due to coupling from vertical ground motion. Again the purple and green trace show the measured vertical ground displacement in the lab and added filtering from the pre-isolation stack. The red trace shows the filtering from the vertical displacement transfer function from top suspension point to test mass motion. It is assumed that 1 % of vertical motion couples into the longitudinal degree of freedom. The blue trace shows the estimated horizontal displacement noise due

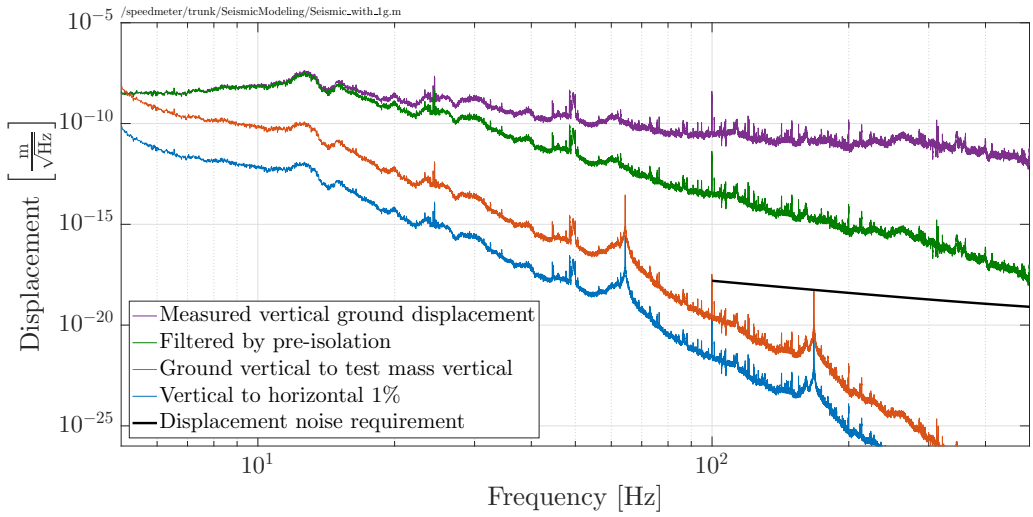

Figure 7.15: Measured vertical ground displacement (purple), estimated vertical filtering by passive stacks (green), filtering by 1 g ITM vertical to vertical transfer function (red) and added estimated vertical to horizontal coupling (blue) and displacement noise requirement for the Sagnac speed meter experiment (black). The estimated displacement noise is well below design sensitivity.

to coupling from vertical ground motion. It can be seen in both cases that the estimated displacement noise fulfils the initial requirement and is well below design sensitivity of the Sagnac speed meter experiment.

7.4.2 Measurable force-displacement and torque-angle transfer functions

In order to verify the dynamics of the 1 g suspension it is necessary to measure the force-displacement and torque-angle transfer functions from actuator locations at the top and penultimate stage to test mass motion. These force-displacement and torque-angle transfer functions can be simulated from the Simulink® model that was written for the 1 g ITM suspension. In Figure 7.16 six force-displacement and torque-angle transfer functions are plotted. The left column from top to bottom shows the simulated force-displacement and torque-angle transfer functions for longitudinal, pitch and yaw excitation at the top mass stage to test mass motion. The right column in the same order shows the force-displacement and torque-angle transfer functions from excitation at the penultimate stage to test mass motion. The drop in magnitude towards low frequencies for the pitch degree of freedom can be explained due to the way the test mass is suspended from the penultimate mass. With one fibre on either side of the test mass it is not possible to achieve static pitch adjustment as the restoring force toward the equilibrium position of the mirror will keep it straight. The highest pitch resonance is modelled at 56.61 Hz and can be associated with pitch of the penultimate mass. Similar to the highest vertical resonance there is a strong dependence

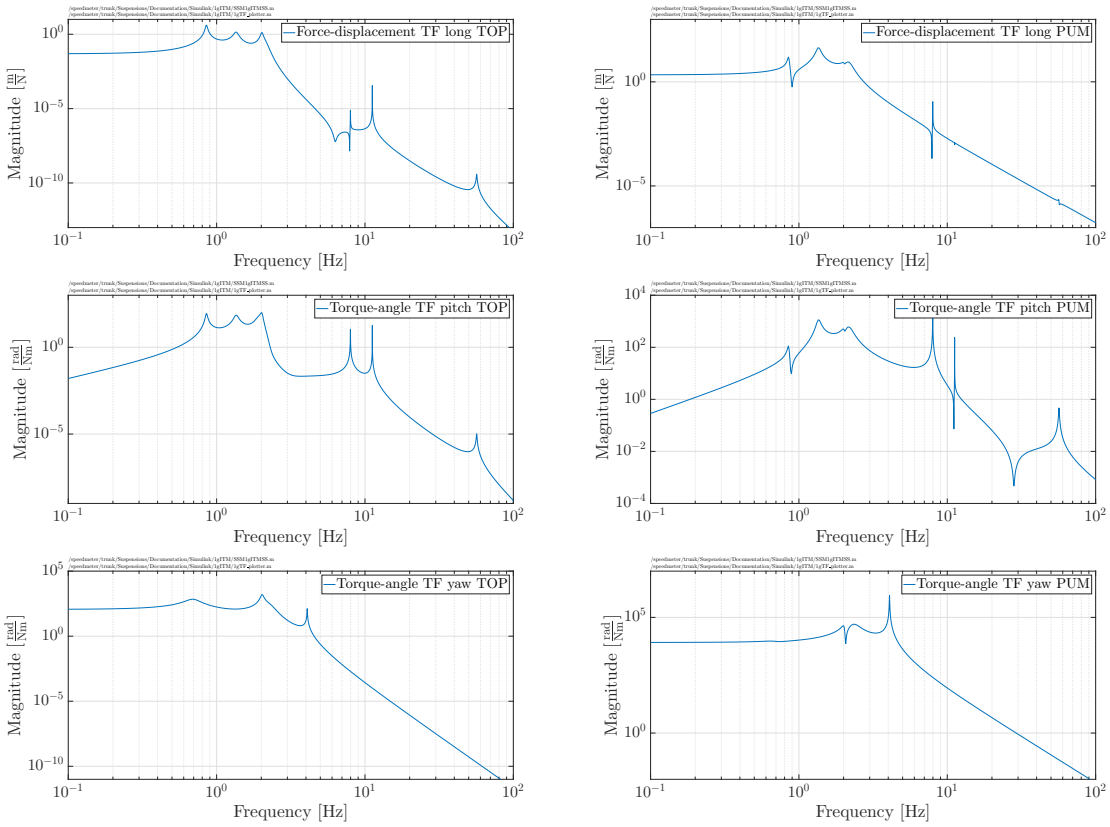

Figure 7.16: Force transfer functions for the 1 g ITM suspension which can be measured to verify their dynamics. The left column of plots shows (from top to bottom) the force-displacement and torque-angle transfer function from longitudinal, pitch and yaw excitation of the top mass to test mass motion. The right column shows the force-displacement and torque-angle transfer functions from penultimate mass excitation to test mass motion in the same order.

on the wire diameter that suspends the monolithic assembly. Reducing the wire diameter of these steel wires from 25 µm to 15 µm can reduce this highest pitch mode to about 40 Hz.

7.5 The monolithic assembly

To avoid limitations from thermal noise in the suspension elements, the lowest stage of the 1 g ITM suspension is made entirely from fused silica. The 1 g test mass is suspended by two 10 µm fibres from the penultimate mass and small cradle ears are attached to the two masses with hydroxide-catalysis bonding to create a quasi-monolithic connection between the parts and to minimise thermal noise from the bond layer. The ears will be attached to the masses as presented in Sections 7.2.3 and 7.2.4. A computer-aided-design model of the 1 g monolithic assembly can be seen in Figure 7.17.

The two 10 µm fused silica fibres are pulled in a similar two-stage pull as the 20 µm fibres for the 100 g ETM monolithic assembly (see Section 6.8.2) leaving 400 µm stock on either end of the fibre that is welded to the ear. Four break-off prisms are hosted on the penultimate mass

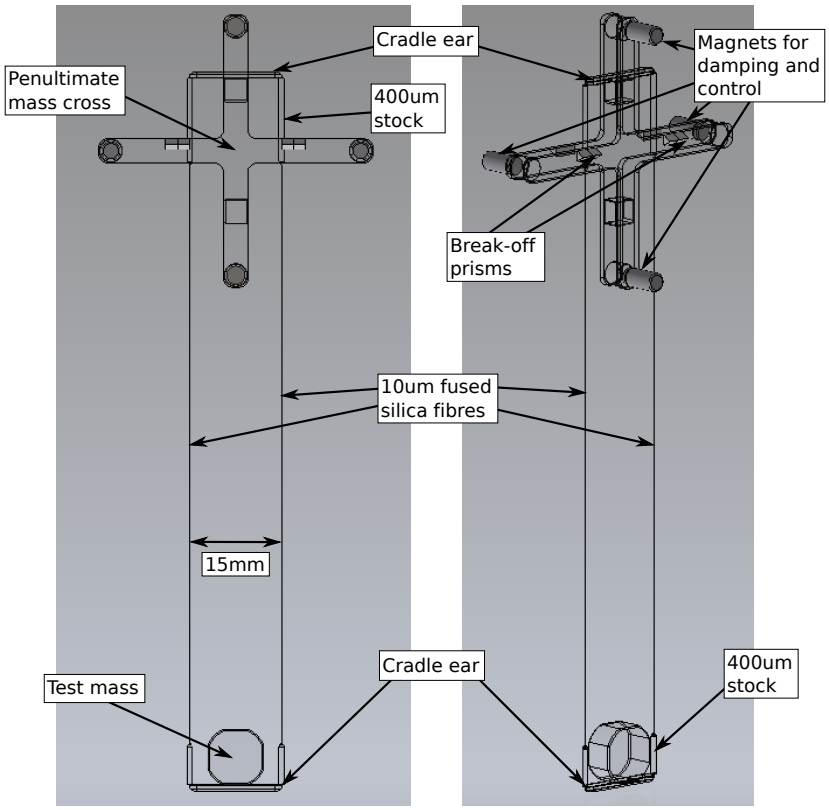

Figure 7.17: Computer-aided-design model of the 1 g monolithic assembly. The left image shows a front view in which the masses, ears and fibres are highlighted. In the right image is an isometric view that shows the magnets on either side of the penultimate mass as well as the break-off prisms for the wire loops from the upper intermediate mass.

to create well-defined break-off points for the wire loops from which the 1 g monolithic assembly is suspended. As presented in Section 7.3, the penultimate mass also hosts four 3 mm × 6 mm magnets for actuation and the switchable eddy-current damping system that will be explained in Chapter 8.

7.5.1 Test mass

The mechanical design of the 1 g test mass was presented in Section 7.2.4. After receiving the mirrors from LMA they were cleaned in a similar way to the 100 g ETM substrates. The barrel and flats on the sides of the substrate were wiped with high-grade methanol to remove any dust particles or other surface contamination, and the HR and AR surfaces of the 1 g substrates were cleaned with the same drag-wipe method that was used on the 100 g surfaces. Figure 7.18 shows a couple of pictures of the 1 g substrates during cleaning process. Picture A shows the unpacking process of the substrate. In Picture B the mirror is inspected for dust particles. These checks happened before and after wiping the substrate surfaces. In both pictures the coating is visible as a circular shape on one of the main surfaces. It can be seen that the coating for this substrate is not concentric on the surface as

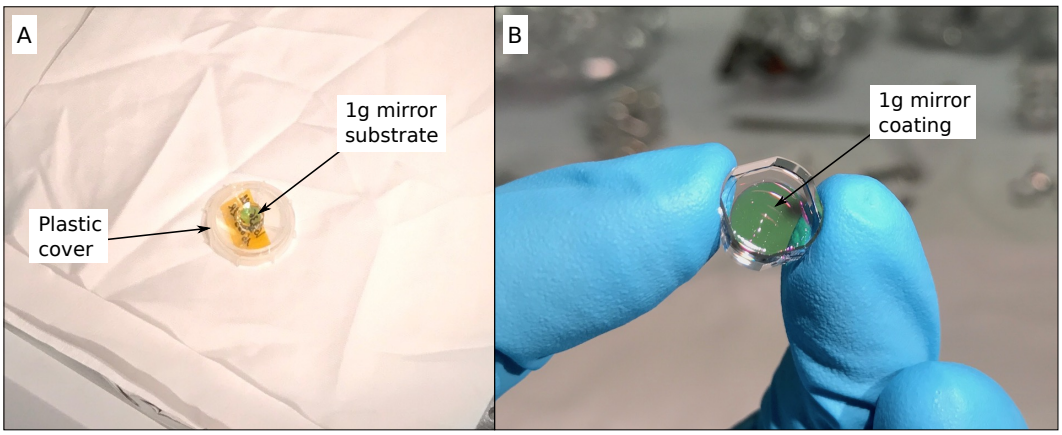

Figure 7.18: Two pictures taken during the initial cleaning of the 1 g substrates. Picture A shows the 1 g substrate after opening and removing the top plastic cover. In Picture B the 1 g substrate is inspected for dust or other contamination under high power light.

this substrate was used for calibration and testing of a coating mask at LMA. Four substrates were used for this calibration and will be used as spares for weld and gluing tests. For the Sagnac speed meter experiment four further substrates were coated as the real input test masses with centred coatings. Figure 7.19 shows a picture with a 1 g substrate and a one pound coin for size comparison. All 1 g substrates were then cleaned in an ozone

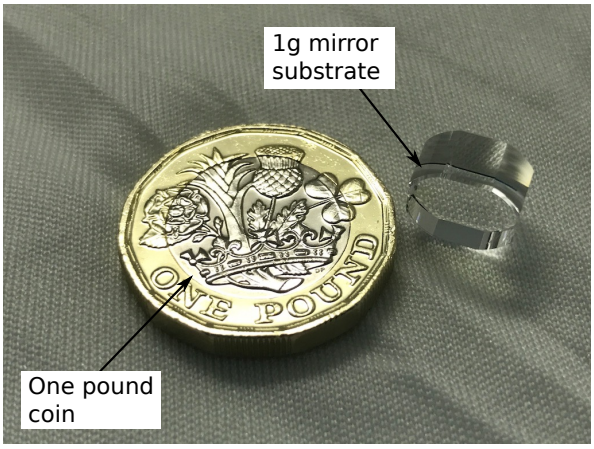

Figure 7.19: The picture shows a 1 g mirror substrate with a one pound coin as size comparison. The 1 g substrates have a diameter of 10 mm and a thickness of 5 mm.

atmosphere inside a double shield which is described in more detail in Section 7.6 below.

7.5.2 Penultimate mass

As shown in Section 7.2.3 the 1 g penultimate mass is designed as a cross made from multiple parts. The three main components of this mass are the cross part, the spacer rod and a square block. These parts together with the 1 g cradle ears which will be described below were produced by Crystran in the UK. Figure 7.20 shows two pictures of the parts that

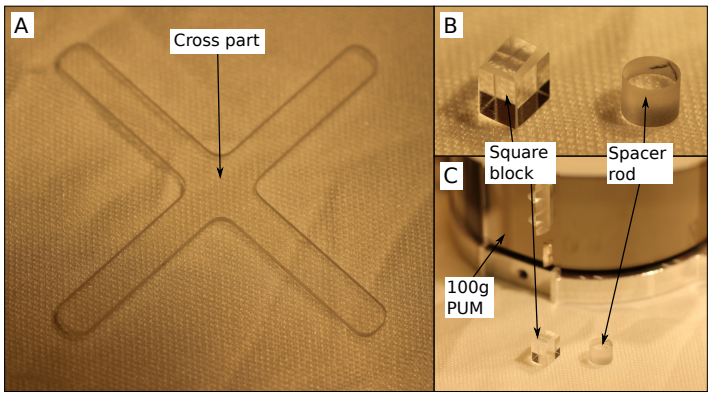

Figure 7.20: Pictures of 1 g penultimate mass parts. Picture A shows the cross piece and Pictures B and C show the square block and the spacer rod as well as a bonded 100 g substrate for size comparison.

make up the 1 g penultimate mass. Picture A shows the cross part, Picture B shows the spacer rod and square block as a close up and Picture C shows spacer rod and square block together with a 100 g penultimate mass for size comparison. One side of the square block was specified to bonding quality for a hydroxide-catalysis bond between the block and a cradle ear. All other surfaces that would be in contact with another part were specified for an inspection polish. This flatness still allows the creation of a hydroxide catalysis bond (HCB) between two fused silica parts. In the end it was decided to only use a HCB between the square block and the ear and to use Masterbond EP30-2 for all other connections. All penultimate mass parts were initially cleaned with methanol to remove dust particles, then later in an ozone atmosphere (see Section 7.6). In order to verify the surface specification of the square block bonding surface as well as the flatness of the end faces of the spacer rod, a sub-set of parts were measured with a Zygo interferometer. Figure 7.21 shows the flatness profile in a screen-shot from the Zygo software for the square block and spacer rod. For both parts the peak-to-valley flatness of the surfaces is <60 nm and thus of bonding quality.

7.5.3 Cradle ears

The cradle ears for the 1 g ITM monolithic assembly are the interface pieces between penultimate and test mass and the two 10 µm fibres. They were designed to be bonded underneath the 1 g mirror substrate and provide attachment points for the fibres 15 mm apart. A computer-aided-design model and a real picture of one cradle ear can be seen in Figure 7.22. The ear is 15 mm long, 2 mm wide and 1.2 mm thick as can be seen in Images A, B and C. One main surface has been polished to bonding quality and is shown in a real picture of the ear in Image D. To identify the bonding surface, 400 µm chamfers have been added to the opposite side. The ear is bonded centrally underneath the test mass in a dedicated bonding jig (see Section 7.7). The bond in this configuration are extended over the full width of the

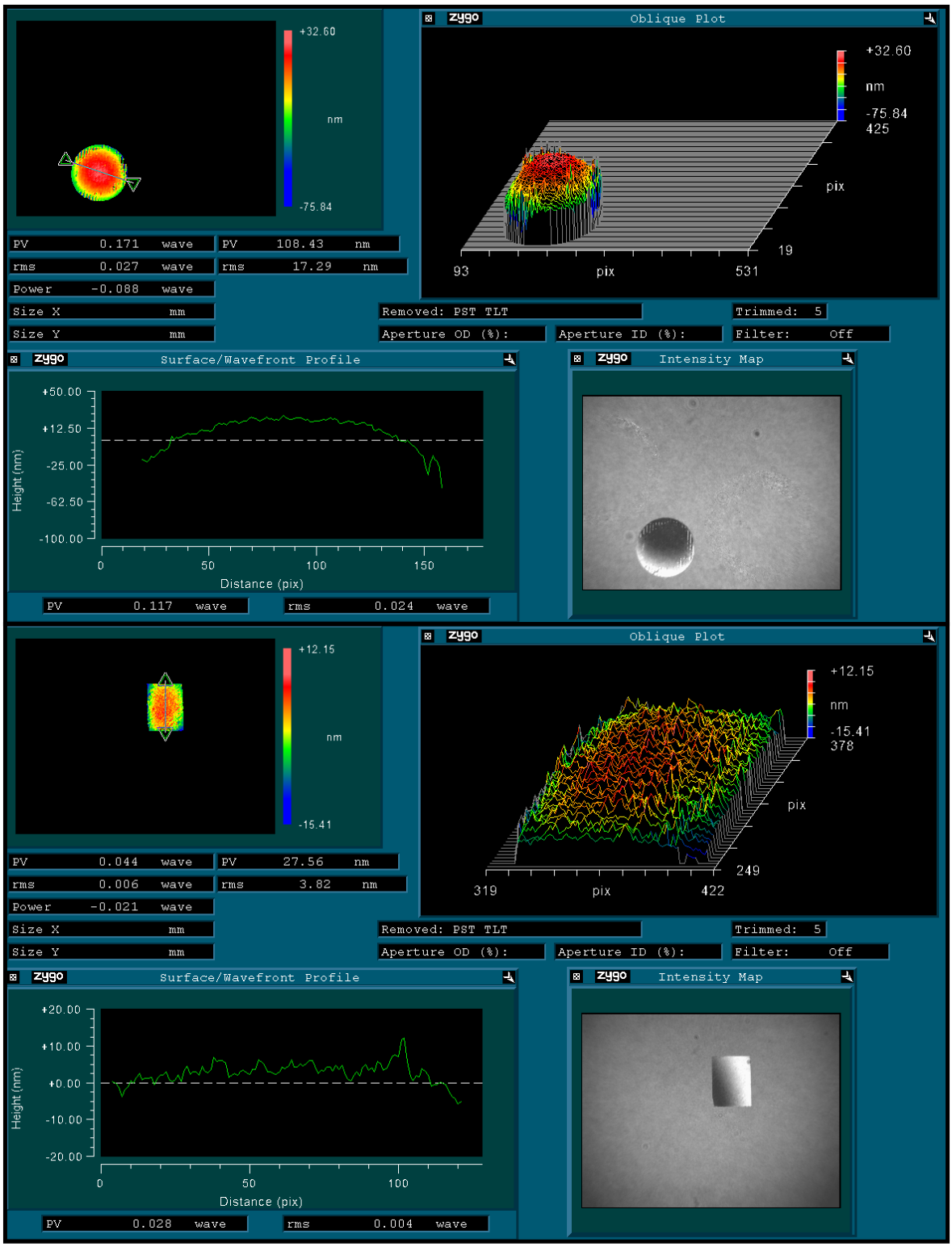

Figure 7.21: Both pictures show screen-shots of the Zygo software during an example flatness measurement for the square block and spacer rod of the 1 g penultimate mass. It can be seen in both pictures that the flat surfaces are of bonding quality with a flatness <60 nm peak-to-valley.

flat on the test mass, marking an area of 4 mm × 2 mm. All ears were thoroughly cleaned in the same fashion as the 1 g substrates and all penultimate mass cross parts were cleaned

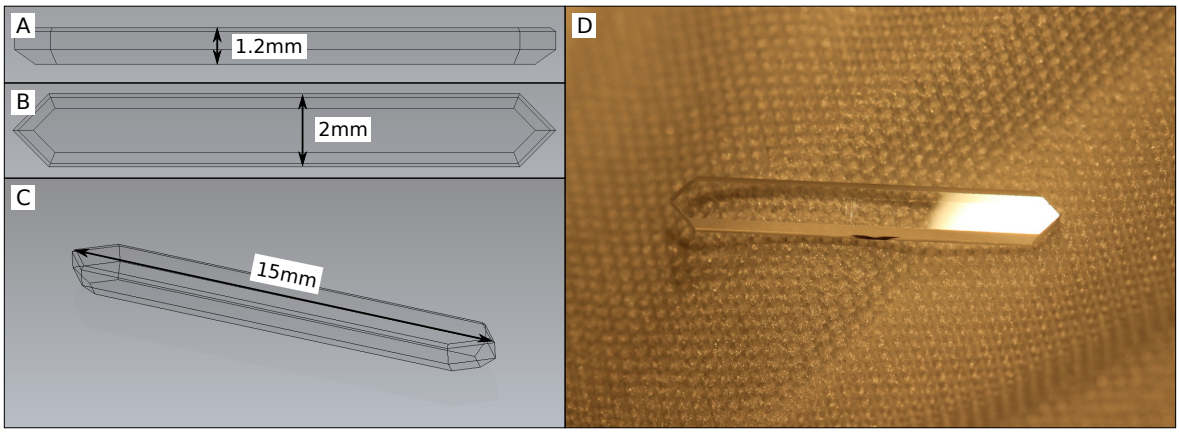

Figure 7.22: Images A, B and C show different views of a computer-aided-design model of a cradle ear with its main dimensions. Image D shows a real picture of the cradle ear in which the shape can be well identified. The triangular shaped ends will be used as weld points to which the 10 µm fibres will be welded.

with methanol followed by exposure to ozone.

7.6 Ozone cleaning

The cleaning of the 1 g test masses as well as all penultimate mass cross parts and all ears was performed analogously to the 100 g substrates in an ozone atmosphere. After initial cleaning with high-grade methanol, the parts are placed in an ozone chamber and exposed to an ozone atmosphere for eleven minutes. The cleaning procedure and underlying cleaning principle is explained in more detail in Section 6.6. The 1 g substrates were placed upside-down onto the flat that has the HR surface marker engraved. A picture of the populated ozone chamber can be seen in Figure 7.23. Five 1 g substrates are placed inside the double-shield to protect the optical coatings from the UV radiation of the ozone-creating and ozone-killing light bulbs. Placing the substrates upside-down onto the HR-marker ensures cleaning of all three remaining bonding quality flat surfaces. All penultimate parts and ears were cleaned in the ozone chamber together without the double-shield. The parts were placed so that the bonding surfaces were facing upwards to maximise exposure to the ozone atmosphere.

7.7 Bonding

After cleaning, the cradle ears were bonded to the 1 g ITM substrates and the penultimate mass square blocks. Both connections were bonded with hydroxide-catalysis bonding (Section 6.7). In contrast to the template bonding for the 100 g ears, the 1 g cradle ears were

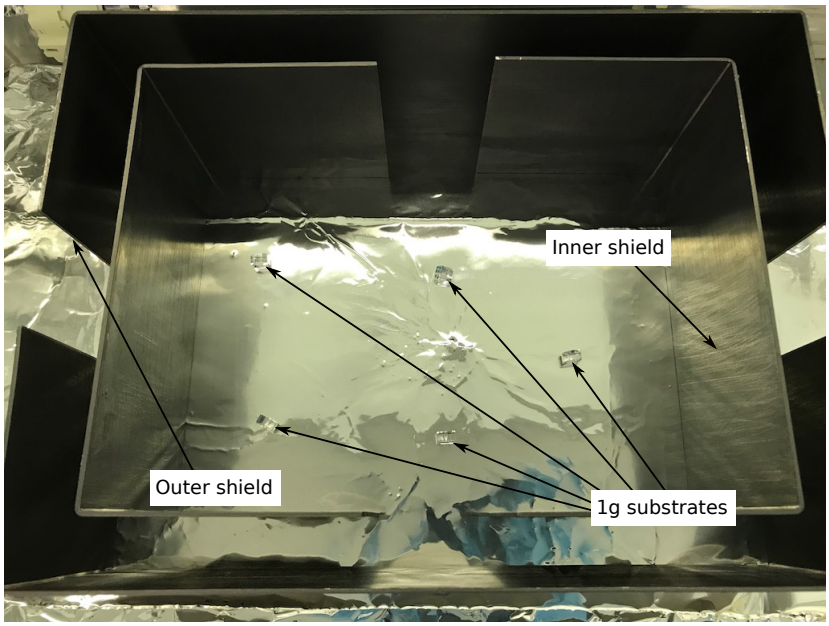

Figure 7.23: Picture of the inside of the ozone chamber with five the 1 g substrates. The substrates are placed on the flat with the HR-marker inside the double shield.

bonded in a dedicated jig which can be seen as Image D in Figure 7.24. The jig consists of a baseplate to which the cradle ear is aligned and an auxiliary plate which is used to clamp the ear into position. With two 6 mm dowel pins, two separate bonding templates can be attached to the baseplate. One template is used to create a reference for alignment of the square block to the ear and the second is used to align the 1 g ITM mirror relative to the ear (which is of different dimensions). For the ITM mirror, the template was designed to avoid compromising the optical coatings by only delivering two small reference points at the sides of the coating, below its centre-line (where the laser beam will impinge on the mirror).

7.7.1 1 g ITM bonding

For the bond between the cradle ear and the 1 g ITM substrate, the cradle ear is inspected for dust, and then cleaned and clamped with the auxiliary plate on the bonding jig baseplate. Figure 7.24 shows a series of computer-aided-design models of the bonding jig. Picture A shows the ear clamped on the baseplate, in Picture B the template has been attached to the baseplate, Picture C depicts the placed and aligned 1 g ITM substrate in the jig and Picture D shows the populated jig in isometric view. The full bonding procedure can be found in Appendix C.3.1. After the ear is fixed, 0.2 µL of bonding solution is applied to the ear as centrally as possible. The 1 g substrate is placed on the ear after the template is attached to the baseplate. The template aligns the substrate centrally on the cradle ear. For this step, the substrate touches the template on two edges on the AR surface and on one flat side. After

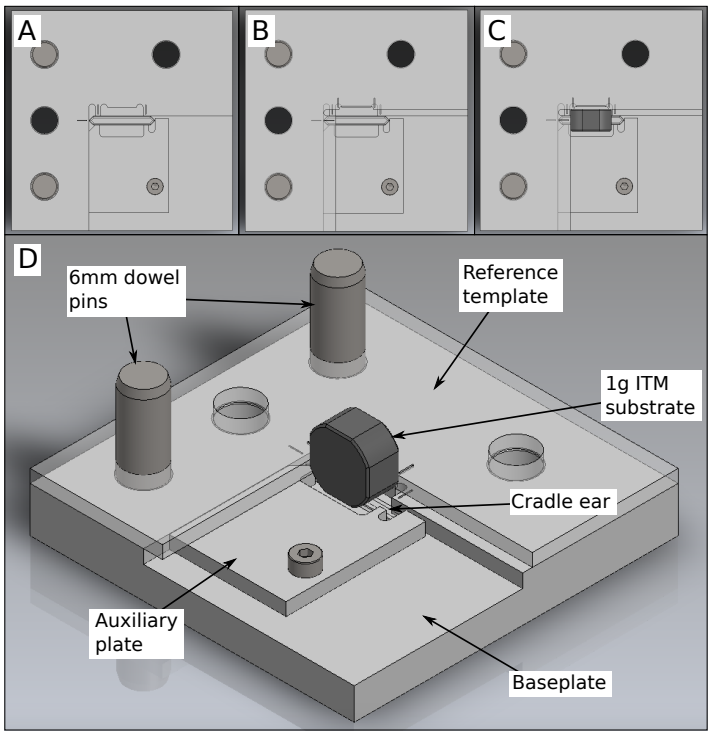

Figure 7.24: Computer-aided-design model of the bonding jig for the 1 g ITM substrate. Pictures A, B and C show the stages in which the ear is placed and fixed in the jig, the template is added to the jig and the ITM substrate is placed on the ear and aligned to the template. Picture D depicts the bonding jig in an isometric view. The jig consist of a baseplate to which the cradle ear can be aligned and clamped. A template can be attached to the baseplate with two dowel pins. Two different versions of this template deliver either a reference for the 1 g ITM substrate or for the square block of the penultimate mass cross. For better visibility the templates are cut from a transparent perspex plate.

placing and aligning the 1 g mass, it is left for one hour to settle before the bonded 1 g mass is transferred into dedicated mass caps as described below in Section 7.8. Figure 7.25 shows a set of pictures taken during the bonding procedure for the 1 g ITM substrates. In Picture A and B the 1 g ITM substrate as well as the ear can be seen prior to bonding. The cradle ear is then placed and fixed in the boding jig with the auxiliary plate as shown in Picture C and Picture D shows the final inspection for dust of the 1 g substrate. After applying bonding solution to the cradle ear the mass is placed in the jig and aligned with a set of tweezers as in Picture E. Finally, Picture F shows the bonded 1 g ITM substrate in the bonding jig during the initial settling time.

7.7.2 PUM square block bonding

Bonding of the cradle ear to the square block of the penultimate mass cross works in the same way as for the 1 g ITM substrate. The only change to be made is the use of a different template that centres the square block over the cradle ear during bonding. Figure 7.26 shows a series of computer-aided-design models as above for the square block. Image A shows

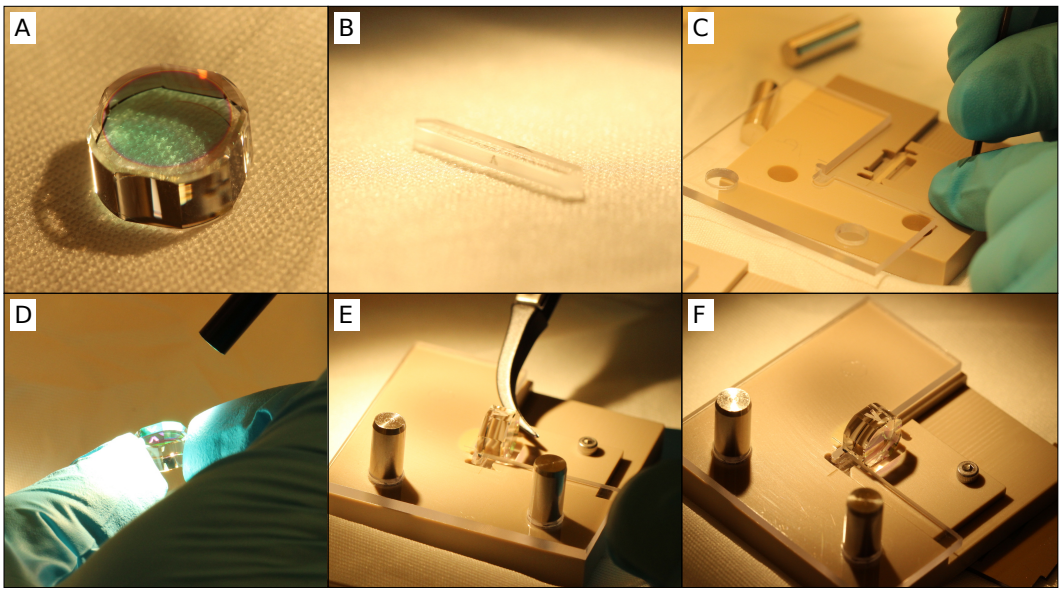

Figure 7.25: The series of picture was taken during the bonding procedure of a 1 g ITM substrate. Picture A shows a ITM substrate prior to bonding. In Picture B a cradle ear is depicted during inspection for dust. The ear is fixed in the jig with the auxiliary plate in Picture C. Before placing the 1 g ITM substrate it is inspected for dust as in Picture D. Picture E shows how the substrate is aligned in the jig with a set of tweezers. The bonded 1 g substrate in the bonding jig can be seen in Picture F.

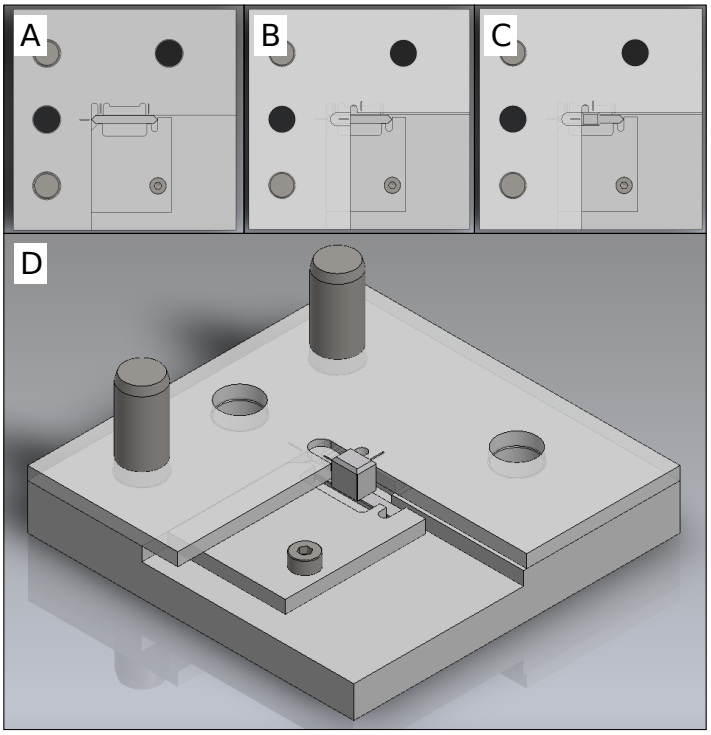

Figure 7.26: Computer-aided-design model of the bonding jig for the square block. Pictures A, B and C show the stages in which the ear is placed and fixed in the jig, the template is added to the jig and the square block is placed on the ear and aligned to the template. Picture D depicts the bonding jig in an isometric view.

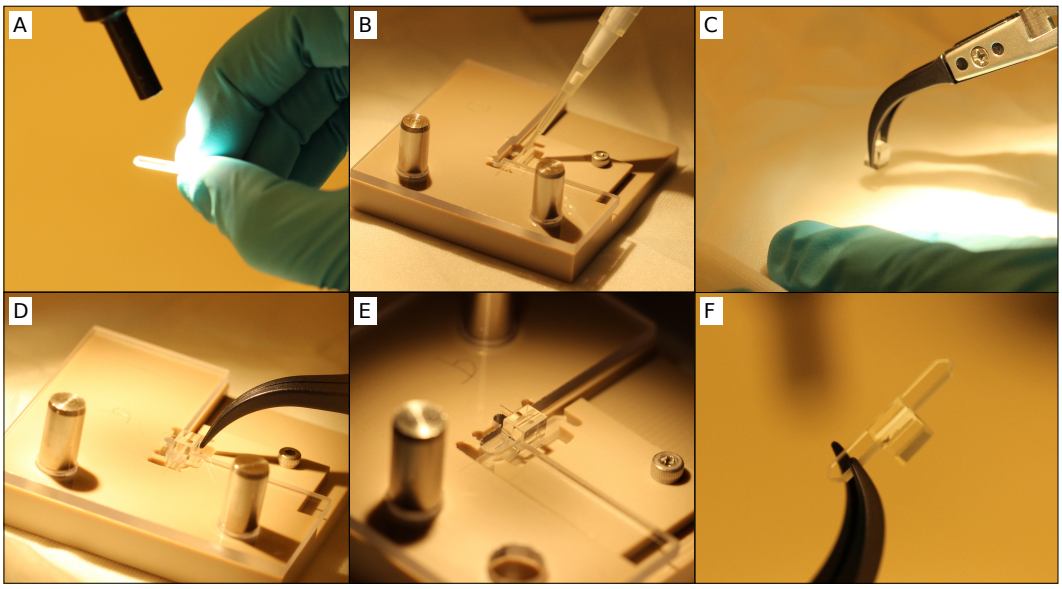

Figure 7.27: The series of pictures was taken during bonding of a square block. Picture A shows the inspection of a cradle ear under high power light. The bonding solution is applied to the cradle ear in Picture B. In Picture C the square block is held with tweezers and its bonding surface is cleaned with high-grade methanol. The tweezers are used to place the block in the template as in Picture D. The bonded square in the bonding jig during settling time can be seen in Picture E. A post-bond inspection of the square block was done to check for possible misalignments of the cradle ear on the square block as in Picture F.

the ear clamped with the auxiliary plate on the bonding jig baseplate, Image B depicts the jig with the template attached, in Image C the square block is aligned to the template, and Image D shows an isometric view of the populated bonding jig. The procedure for bonding of the square block can be found as part of the 1 g bonding procedure in Appendix C.3.1. A series of pictures taken during the bonding process are presented in Figure 7.27. Picture A shows the inspection of the cradle ear for dust under high-power light. In Picture B 0.2 µl bonding solution is applied to the ear that is clamped on the bonding jig baseplate. In Picture C the bonding surface of the square block is wiped a last time with high-grade methanol. Picture D depicts the alignment of the square block to the reference edges of the bonding template with a set of tweezers and Picture E shows the populated bonding jig for the initial cure of the bond. In Picture F a post-bond inspection of the bonded cradle ear is conducted, to check how well centred the ear was bonded on the square block. The bond is left to set in the template for at least one hour before the bonded assembly is removed from the jig.

7.8 Mass caps

Up to this point the 1 g ITM substrates were left unprotected and only handled with extreme care to avoid contamination or worse damage of the HR and AR surfaces. In order

to keep these surfaces clean and free from any particles during the final welding of the monolithic assembly a set of mass caps was required, similar to the ones used for the 100 g ETM substrates. During the welding procedure fused silica of the ear and fibre stock is partially evaporated and the silica vapour created could settle on the main surfaces of the ITM. To prevent this from happening, mass caps that seal the mirrors surfaces are required. In contrast to the mass caps used for the 100 g ETM substrates, the seal around the surface cannot be realised with a viton or any other plastic o-ring. Due to the short distance of the weld to the o-ring location, the risk of partially melting or compromising the o-ring material due to conducted heat would be too high. Instead it was decided to create an all-metal mass cap that would use a soft material to seal the front and back surface of the ITM. Figure 7.28 shows a computer-aided-design model of the 1 g mass caps. The material

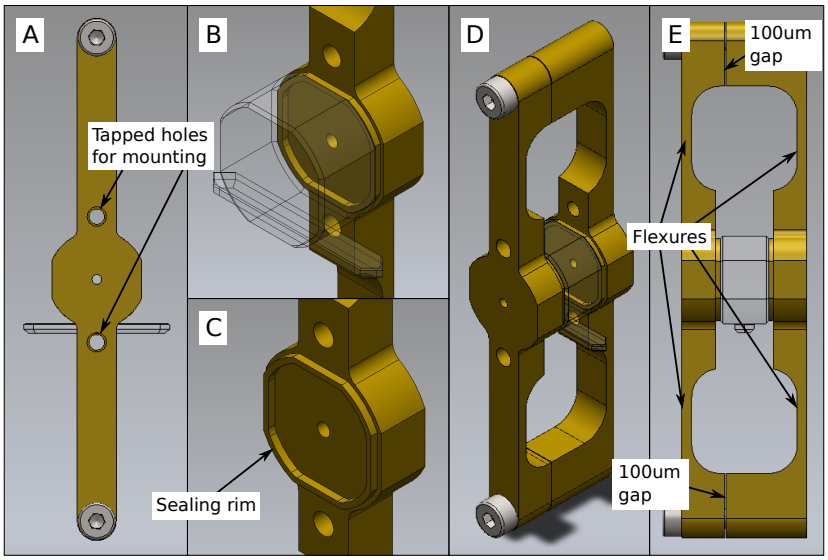

Figure 7.28: Computer-aided-design model of the 1 g mass caps. Picture A shows a front view. Pictures B and C are close-ups of the central section with and without 1 g ITM substrate. In these pictures the rim can be seen that seals the surface to prevent any contamination. Pictures D and E show isometric and side view of the caps. In the side view the flexible arms can be seen. The caps are designed to leave a gap of 100 µm at both ends to limit the force and pressure on the 1 g ITM substrate.

these caps are made from is free-cutting brass and the central section resembles the shape of the 1 g substrate, with a 400 µm wide and 500 µm high rim that seals the mirrors surface as can be seen in Pictures B and C. In the centre of the caps, a small 1 mm diameter hole counteracts any suction effects that might occur when removing the cap from the substrate. During welding, this hole is sealed with a piece of vacuum compatible kapton-tape. Two tapped holes (highlighted in Image A) closest to the central area are foreseen as mounting references during curing of the bonded 1 g ITM substrates and as attachment points for interfacing with a weld-jig (see Section 7.11). In order to firmly hold the 1 g substrate in the mass caps they are designed to leave a gap of 100 µm at either end between the two cap parts. Tightening the two screws at the ends compresses the caps by the amount of

the gap and clamps the 1 g substrate. To limit the force and pressure on the substrate the two arms have recesses to make them into elastic flexure elements designed to elastically deform under load. The thinner the remaining material the softer the flexures and the less force on the substrate.

The final thickness of the flexures was defined from an ANSYS® simulation. On the one hand, the pressure on the 1 g substrate was to be kept well below the compressive strength of fused silica (1150 MPa [132]) which can be achieved by making the flexures thinner. On the other hand no plastic deformation of the flexures was allowed to happen as this could result in slipping of the 1 g substrate. The yield strength of free cutting brass is 310 MPa [133] so the stress in the flexure has to be kept below this value. Figure 7.29 shows the result of the ANSYS® simulation for a flexure thickness of 1 mm. Picture A shows the stress in the

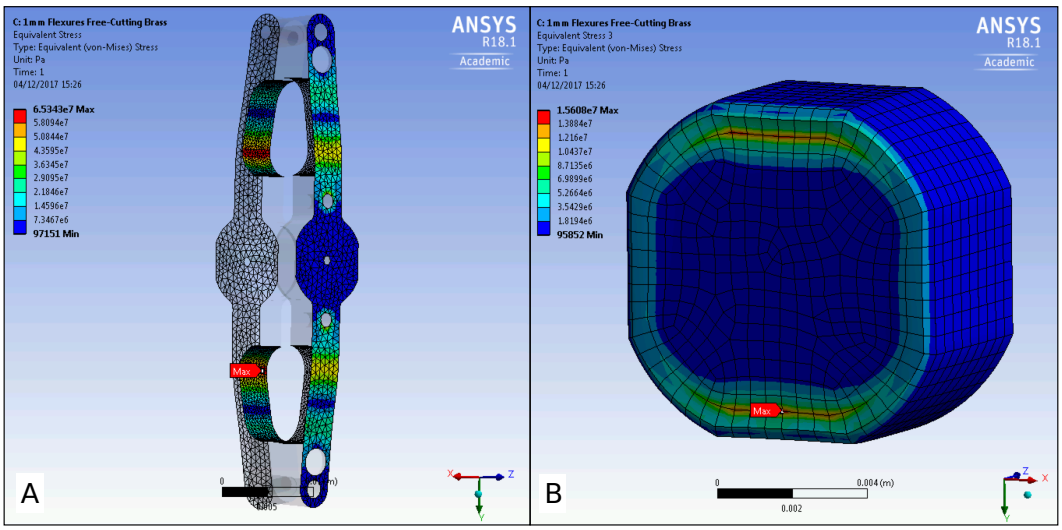

Figure 7.29: ANSYS® simulation of 1 g mass caps. For the simulation the ends of the caps are compressed by 100 µm. The stress in the flexures is about 65 MPa (see Picture A). The stress on the 1 g substrate from the mass cap rim (Picture B) is limited to about 16 MPa. These values are well below yield strength of free cutting brass (310 MPa) and compressive strength of fused silica (1150 MPa).

flexures of the mass caps and it can be seen that the maximum stress is at about 65 MPa and thus well below the tensile strength of free cutting brass. The stress on the 1 g substrate is presented in Picture B. After compressing the mass caps the maximum stress is limited to about 16 MPa for this flexure thickness and thus this is also well below the compressive strength of fused silica.

The bonded 1 g ITM substrates were placed into the mass caps after the initial settling time for the bond of one hour. In order to place the substrate with high accuracy and to prevent the mass cap rim from scratching over the mirror surface, a separate jig was used. The procedure on how to place the 1 g mirror into the mass caps can be found in Appendix C.3.1 as part of the bonding procedure.

A series of pictures taken during this procedure can be found in Figure 7.30. After releasing

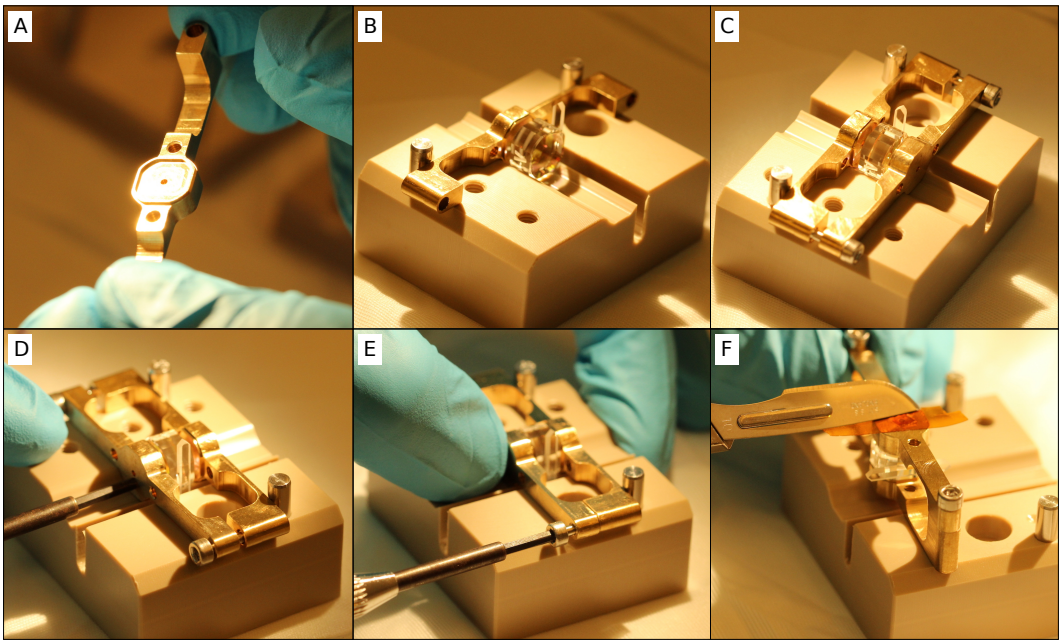

Figure 7.30: Series of pictures taken during placement of a bonded 1 g substrate into a set of mass caps. After inspecting the bonded 1 g ITM substrate as well as the mass caps for dust (Picture A) the bottom mass cap and the substrate are placed on the jig (Picture B). The top mass cap is added and all three parts are pushed towards two dowel pins (Pictures C and D). In this position the two screws are tightened and the substrate is clamped (Picture E). In a finishing step the central hole on the mass cap is closed with a piece of kapton tape to seal the main surfaces of the 1 g ITM substrate.

the bonded test mass from the bonding jig a final inspection for dust on the main surfaces was performed under high power light. The mass caps were checked for dust or other particles in the same fashion as can be seen in Image A. The bottom part of the mass caps is placed on the jig into the recess that resembles the 1 g ITM substrate and mass cap shape, then two dowel pins are used to give a reference for the mass cap. The recess is cut so as not to constrain the ear, as this could compromise the bond and its quality. Image B shows the 1 g substrate in the jig placed close to the bottom mass cap and in Image C the top mass cap has been added to the jig. In Image D the top cap and 1 g ITM substrate are pushed towards the bottom mass cap, and this pushing joins all three parts together. Image E shows the tightening of the two screws on the mass cap ends to finally clamp the 1 g ITM substrate in the caps. Image F shows the final step of attaching kapton tape to seal the central area of the cap and thus the main surfaces of the 1 g mirror.

All four real mirrors were handled in this way and placed in their mass caps as soon as possible after bonding of the cradle ear. Figure 7.31 shows two pictures of populated mass caps. Picture A depicts one of the mass caps after the 1 g ITM substrate was placed inside. In Picture B two mass caps are mounted on a curing plate upside down to allow the final four week curing time of the bonds.

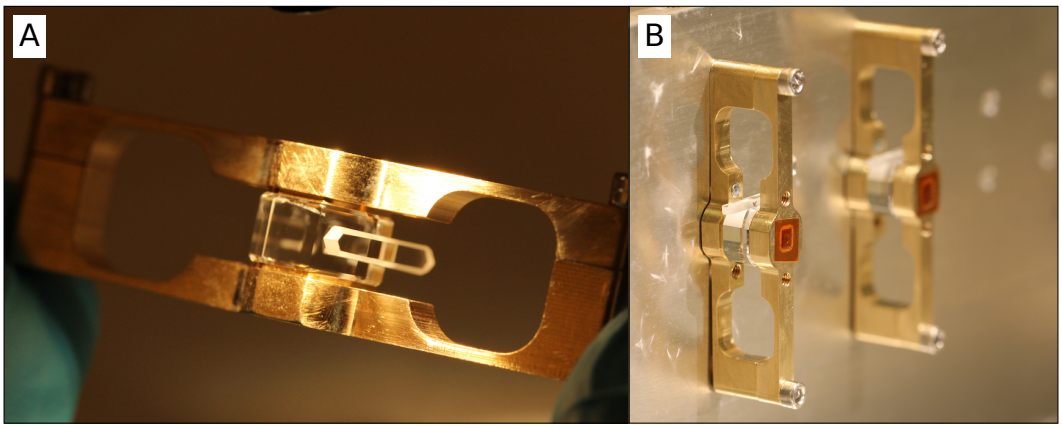

Figure 7.31: Two pictures of bonded 1 g substrates in mass caps. Picture A shows the inspection of the 1 g ITM substrate in the mass caps. In Picture B two populated mass caps are mounted on a vertical mount on which the bonds cure for 4 weeks.

7.9 Assembly of penultimate mass cross

The penultimate mass cross is only partially assembled prior to welding. As will be demonstrated in Section 7.11, the final gluing step will be done after the fibres are welded to the cradle ears. In order to position the fibre stock for the weld it is held by a set of tweezers mounted on micrometer adjusters. As the welded stock is between the two main cross pieces it was decided to keep the cross open during introduction and welding of the fibre and to attach the second cross piece afterwards. The pre-assembly of the two cross pieces (the piece with the square blocks and spacer rods attached, will be referred to as 'bottom cross' and the second cross piece will be referred to as 'top cross' in the following) is done in two separate jigs. All connections between parts were glued using Masterbond EP30-2. The jig for the bottom cross part is depicted in Figure 7.32. Image A shows the jig baseplate with

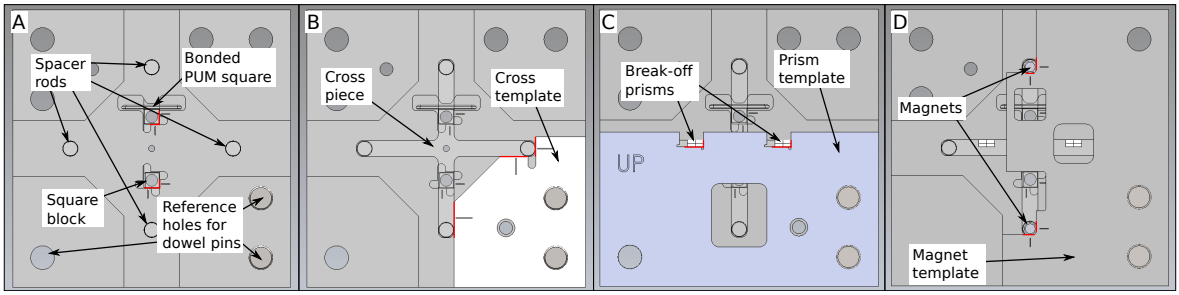

Figure 7.32: Computer-aided-design models of the bottom cross gluing jig for the different gluing stages for pre-assembly of the penultimate mass. Images A, B, C and D show the jig with different templates attached. The first gluing step is to glue the cross piece to the spacer rods and square blocks. After that the prisms and finally magnets are added to the opposite side of the cross piece.

recesses in which the bonded square block, the second square block and four spacer rods are inserted. In Image B the cross template is added to the jig and the cross piece aligned to the template, then Image C depicts the prism gluing jig for attaching the break-off prisms

and Image D shows the magnet jig that is used to glue the magnets on magnetic stand-offs to the bottom cross.

The jig for the top cross looks very similar as presented in Figure 7.33. The baseplate shown

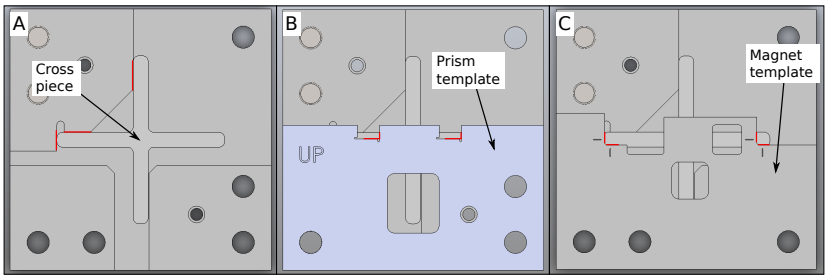

Figure 7.33: Computer-aided-design models of the top cross gluing jig for the different gluing stages for pre-assembly of the penultimate mass. In the jig the baseplate is used as a template for aligning the cross piece as in Image A. Images B and C show the corresponding templates for gluing of prisms and magnets to the top cross.

in Image A resembles the shape of a template to which the cross piece is aligned and this baseplate can be attached on top of the bottom cross baseplate for better stability. Images B and C show the same templates for prism and magnet gluing. The only difference is the orientation of the magnets which are attached to the horizontal arms compared to the vertical arms on the bottom cross.

The complete assembly procedure for the penultimate mass cross parts can be found in Appendix C.3.2. All jig and penultimate mass parts are thoroughly checked for dust and other contamination under high power light and are given a final wipe with high grade methanol prior to gluing. Figure 7.34 shows a series of pictures taken during gluing of the bottom and top cross. Picture A shows the baseplate used for the bottom cross populated with the bonded square, another square block and four spacer rods in recesses. In Picture B the cross template can be seen in the left bottom corner. After applying small dots of glue to the squares and rods, the cross piece is introduced and aligned to the template. After a gluing step the jig was left undisturbed for 24 hours to let the glue settle. In Picture C the two break-off prisms are glued using a laser cut template and Picture D shows the magnet template that is used to attach 500 µm thick, 3 mm diameter type 430 stainless steel stand-offs, on which 3 mm × 6 mm magnets are magnetically mounted, to the vertical arms of the bottom cross. Pictures E and F show the prism and magnet template on the second baseplate to prepare the top cross. The magnets on this part are attached to the horizontal arms.

The completed bottom and top cross parts can be seen in Figure 7.35. Picture A shows the two cross parts next to each other. In Picture B both parts are arranged as in their final configuration where they are glued together. For the welding of the fibres, the bottom cross will be mounted in a weld jig, and after the welds are done the top cross will be glued to

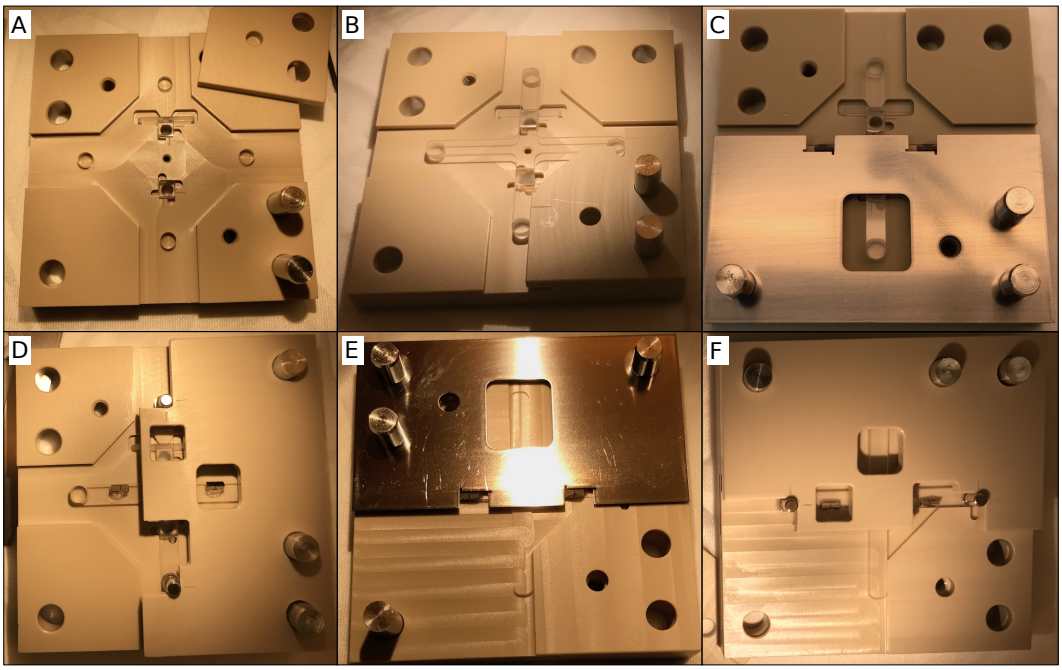

Figure 7.34: Series of pictures taken during assembly of the two cross parts for the penultimate mass cross. Picture A shows the bottom cross baseplate with square block, bonded square and spacer rods. Picture B depicts the cross piece attached on top of the aforementioned parts. Masterbond EP30-2 is used as a glue to connect all parts. In Picture C the prism template has been added to the baseplate and prisms are glued in place. For Picture D the prism template was exchanged for the magnet template to which 3 mm × 6 mm magnets on 500 µm thick stand-offs are glued. Pictures E and F show the second baseplate for the top cross with templates for prism and magnet gluing.

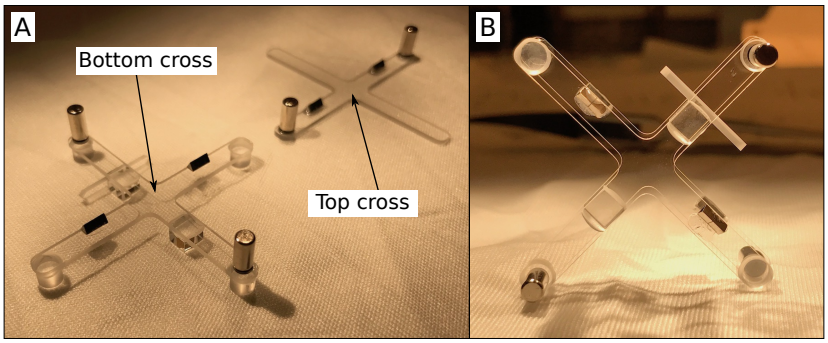

Figure 7.35: In Picture A both parts of the penultimate mass cross are laying next to each other. For Picture B they are arranged the same way they will be glued together post welding.

the bottom cross to complete the 1 g penultimate mass cross.

7.10 Fused silica fibres

The geometry of the fused silica fibres for the 1 g ITM suspension had to be defined in order to model the suspension dynamics in Section 7.4. The initial design idea was to use a 10 cm long 10 µm diameter fibre. The underlying reasoning for these values was from

suspension thermal noise modelling which is presented below in Section 7.10.1. In the mechanical design it was decided to separate test and penultimate mass by 100 mm, which meant reducing the length of the thin fibre section depending on the selection of break-off points above and below the centre of mass of the test and penultimate masses. The selected geometry is depicted in the schematic in Figure 7.36. The break-off points above the centre

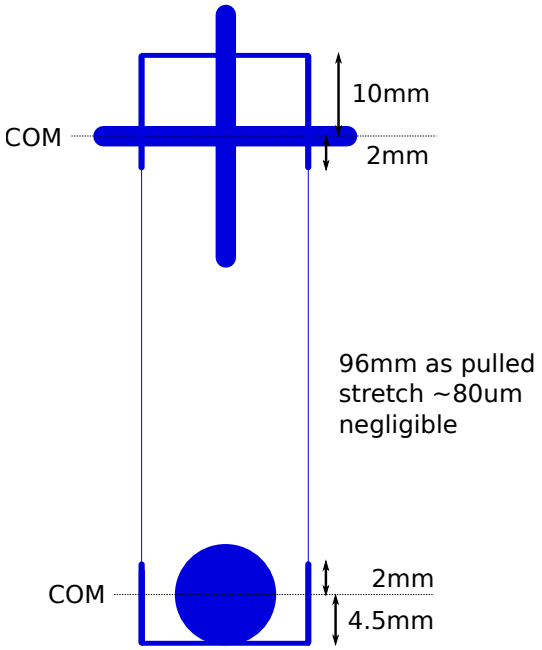

Figure 7.36: Schematic of the planned geometry for the 10 µm fibres that are used for the monolithic assembly of the 1 g ITM suspension. The stock lengths are chosen to place the fibre neck 2 mm above/below centre of mass of the test and penultimate mass. The thin section of all four fibres will stretch only about 80 µm under the test mass load and will be neglected in the pulled length of about 96 mm resulting in a COM-COM distance of about 100 mm.

of mass of the test mass and below the centre of mass of the penultimate mass were chosen to be 2 mm in each case. The thin section of the fibre was thus to be reduced to 96 mm. Due to negligible stretch of the fibre under load from the bonded 1 g ITM substrate (80 µm) this length is the production length of all 10 µm fibres. The total stock length on either side of the thin section is determined from the location of the cradle ear relative to the centre of mass of the penultimate and test masses. On the test mass side the total stock length is about 6.5 mm whereas on the penultimate mass the stock length is 12 mm. The stress in the fibres can be calculated the same way as for the 20 µm fibres from Equation 6.8 to be approximately 62.5 MPa, about a factor 10 below the stress in the 20 µm fibres.

7.10.1 Suspension thermal noise

Analogously to Section 6.8.1, suspension thermal noise of the 1 g ITM suspension is, as a classical noise source, required be a factor of 10 below design sensitivity of the Sagnac speed

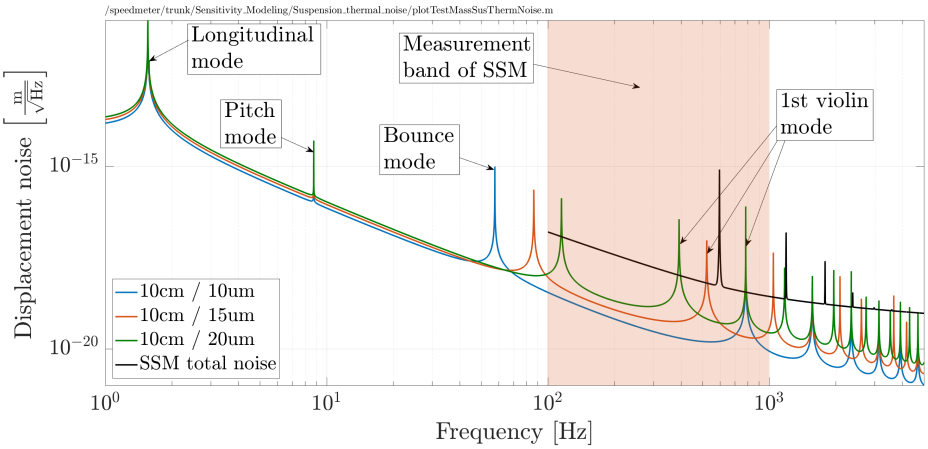

Figure 7.37: Comparison of suspension thermal noise for one 1 g ITM suspension with varying fibre diameter. The traces in blue, red and green show suspension thermal noise for fibre diameters of 10 µm, 15 µm and 20 µm. The fibre length is kept constant at 10 cm. The red-shaded area outlines the measurement band of the Sagnac speed meter experiment.

meter experiment. In order to determine the chosen geometry presented above, suspension thermal noise was calculated for varying fibre diameter and fibre length, keeping one of the two constant while changing the other. In Figure 7.37 the length of the fibre is kept constant at 10 cm, and the blue, red and green traces depict the suspension thermal noise for fibre diameters of 10 µm, 15 µm and 20 µm respectively. For all three diameters the frequency of the longitudinal mode stays constant as this mode is only dependent on the fibre length, while the vertical bounce mode increases with increasing fibre diameter. The first violin mode in contrast appears at lower frequencies with increasing diameter due to less stress in the fibre. The red-shaded area in the figure highlights the measurement band of the Sagnac speed meter experiment between 100 Hz and 1 kHz. It can be seen that the 10 µm fibre contaminates the measurement band least with resonance frequencies. 10 µm was set as a lower limit for production feasibility and ease of use in the lab. Fibres of even thinner diameter would be invisible even under illumination.

Keeping the diameter constant at 10 µm the suspension thermal noise can be calculated for varying fibre length as depicted in Figure 7.38. In this figure the red-shaded area again highlights the measurement band of the Sagnac speed meter experiment. The traces in green, red and blue show the calculated suspension thermal noise for fibre lengths of 20 cm, 15 cm and 10 cm respectively. It can be seen that the change in length influences the longitudinal mode frequency, the bounce mode frequency and the violin mode frequencies. The different mode frequencies decrease with increased fibre length. It can again be seen that the fibre length of 10 cm causes the least contamination of the measurement band. Shorter fibres than these were considered impractical as physical separation between test and penultimate mass would have been too small.

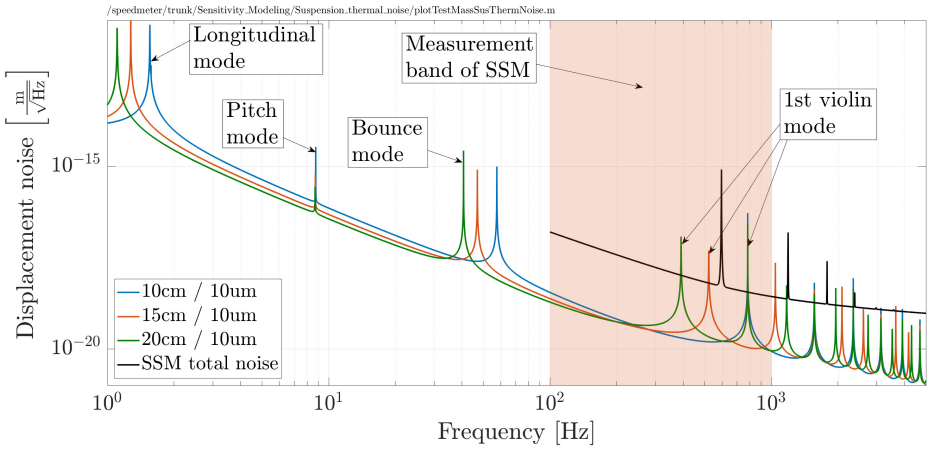

Figure 7.38: Comparison of suspension thermal noise for one 1 g ITM suspension with varying fibre length. The traces in blue, red and green show suspension thermal noise for fibre lengths of 10 cm, 15 cm and 20 cm. The fibre diameter is kept constant at 10 µm. The red-shaded area outlines the measurement band of the Sagnac speed meter experiment.

A comparison of suspension thermal noise from the 1 g ITM suspension and the 100 g ETM suspension is presented in Figure 7.39. The blue trace shows the suspension thermal noise from the 1 g ITM suspension with its thin section length of 96 mm. In this trace the longitudinal and vertical bounce mode of the lowest pendulum stage can be identified as well as the contribution from violin modes of the fibres. It is important to note that the fibre diameter for this trace is 12 µm, which explains the slight differences in mode frequencies compared to Figure 7.37 and Figure 7.38. The overall suspension thermal noise is about 1.8

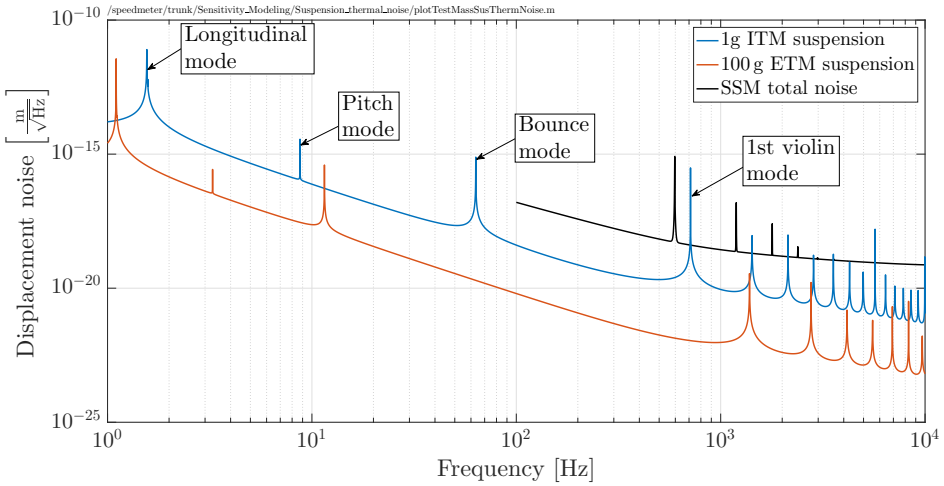

Figure 7.39: The plot shows the estimated suspension thermal noise for one 1 g end test mass suspension in the suspension elements of the monolithic assembly in the blue trace. As comparison the red trace shows the estimation for the 100 g ETM suspension. The modelling shows that suspension thermal noise of the 1 g suspension will be about 1.8 orders of magnitude below design sensitivity. It is possible to identify the longitudinal, vertical and violin modes of the monolithic assembly.

orders of magnitude below design sensitivity of the Sagnac speed meter experiment which fulfils the initial requirement and makes this suspension available for future upgrades of this experiment in which a higher sensitivity could be required. As comparison, the suspension thermal noise of the 100 g ETM suspension is shown in red and is another 1.8 orders of magnitude below the 1 g ITM suspension.

7.10.2 Production of fibres

The fibres for the 1 g monolithic assembly were produced in the same fibre puller that was used for the 100 g fibres. A detailed description of the puller can be found in Section 6.8.2. For production, the same fibre cartridges with shorter distance rods as presented in Figure 6.28 were used to accommodate the shorter and thinner fibres. The pulling process is a similar two-stage pull in which 2 mm diameter thick base material is pulled to 400 µm. In the second stage the 400 µm section is pulled down to a diameter of about 10 µm and a length of this thin section of about 96 mm. In order to have enough fibres for the 1 g monolithic assemblies as well as a set of spares for initial weld tests a total of 20 fibres were pulled. For the final set of monolithic assemblies six of these are required and it is planned to have a couple of dedicated spares per assembly. This leaves eight 10 µm fibres for initial weld tests.

After production the 20 fibres were characterised in the same fibre profiler as presented in Section 6.8.2 or Reference [126]. Figure 7.40 shows the profiles of three matched sets of four fibres and the remaining eight spare fibres. It can be seen that all fibres have a uniform

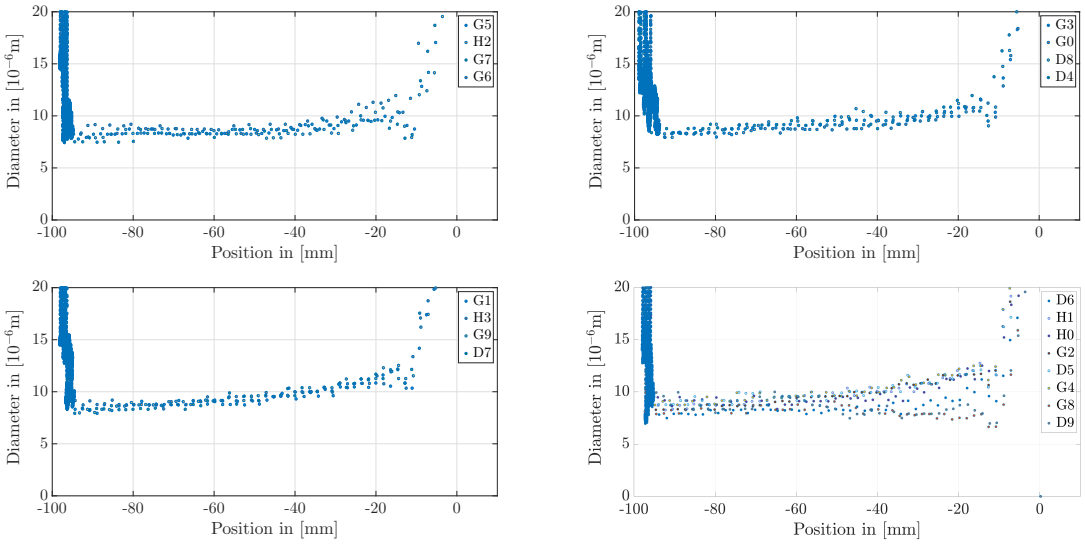

Figure 7.40: Measured fibre profiles of the 10 µm fibres for three 1 g monolithic assemblies and eight spare fibres. After profiling all fibres they were matched up by diameter and general shape into three sets of four fibres. The fibres have a uniform 8-10 µm diameter profile that slightly tapers up to about 12-13 µm on one end.

diameter of 8-10 µm diameter profile that tapers up to about 12-13 µm on one end.

7.11 Welding

In order to create monolithic assemblies for the 1 g ITM suspension the 10 µm fibres are welded to the penultimate and test masses in a similar way to the 100 g ETM suspension. Differences are in the shape of the ears and in the direction in which fibres will be attached to the masses. As presented in Figure 6.32 in Section 7.11 the 400 µm stock is welded onto the ear horns, feeding stock material into the weld from the vertical direction. For the 1 g monolithic assembly the plan is to introduce the stock material from to the ear from the side, keeping the fibre under tension at all times. The necessary tools will be described below in Sections 7.11.1 and 7.11.2. The described welding procedure is an area of active investigations and is likely to change over the course of the coming months as new information becomes available.

7.11.1 Weld jig

During the welding procedure for the 1 g monolithic assembly, the test and penultimate masses are held in a dedicated weld jig. This weld jig serves additionally as a transport and interface piece for the final installation of the monolithic assembly in the 1 g suspension cage. In contrast to the 100 g ETM monolithic assembly, no fibre guards that clamp the penultimate and test masses in position are foreseen for the 1 g ITM suspension due to the small size of the masses. For protection of the 1 g test mass a dedicated mass catcher will be installed in the suspension frame that offers a platform underneath the test mass. The 1 g weld jig allows for the inclusion of a U-shaped PEEK part to protect the fibre after welding and during transport and installation. After installation of the monolithic assembly into the suspension, additional shields can be mounted to the suspension frame baseplate that will protect the fibres and the 1 g test mass from accidental damage. A computer-aided-design model of the 1 g weld jig can be seen in Figure 7.41. In Pictures A, B and C the weld jig is depicted in front, side and isometric view. A set of mass caps with the bonded 1 g substrate is fixed to the jig with two screws and can be aligned for rotation with the help of two alignment pins. The penultimate mass is aligned with five pins, of which two shorter pins together with one longer pin provide a reference for the bottom cross and three longer pins can be used for referencing of the top cross after welding. At the location of the cradle ears the jig has recesses to allow better access of the laser-beam during welding of the two 10 µm fused silica fibres. The penultimate mass is raised on a slim phosphor-bronze platform to align the tips of the cradle ears vertically. With a clamping arm and a spring plunger the

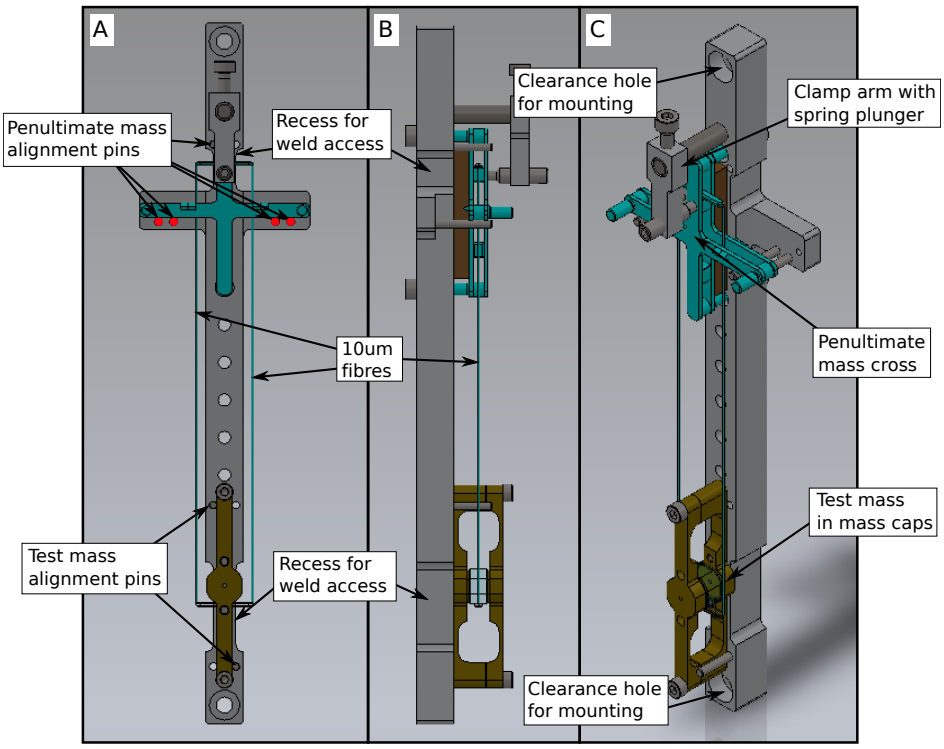

Figure 7.41: Computer-aided-design model of the 1 g weld jig. Pictures A, B and C show the front, side and isometric view of the weld jig. The 1 g mass caps with the bonded mirror is fixed to the weld jig by two screws and is aligned to two pins in order to avoid rotation of the mirror. The penultimate mass is aligned to five pins in order to align bottom and top cross independently. For better weld access the jig has recesses around the area of the ears. A clamp arm with a spring plunger is used to hold the penultimate mass. The spring plunger clamps on the bonded square block and limits the pressure on this part to 4.5 N. With two screw clearances at the ends of the weld jig it can be interfaced with any weld tooling structure.

penultimate mass can be clamped in position, where the spring plunger limits the force that is applied to the bonded square on which it acts to 4.5 N.

Initially only the bottom cross of the penultimate mass is held in the weld jig. Only after welding of the fibres is the top cross attached to complete the penultimate mass. In order to allow the spring plunger and clamping arm to be removed, a second holding mechanism was implemented and can be explained with reference to Figure 7.42. The bottom picture shows a rotated side view of the weld jig. Highlighted in this view are the reference pin for the mass caps as well as two magnetic screws. The two tapped holes for these screws can bee seen in the cross section of Figure 7.42. They are placed to allow magnetic mounting of the penultimate mass by interacting with its vertical magnets. The force that holds the penultimate mass can be modulated by varying the distance between screws and magnets. The cross-section also contains the phosphor-bronze support for alignment of the cradle ears.

The weld jig is also used to store, transfer and install welded 1 g monolithic assemblies in the 1 g suspension. For installation, the jig can be connected to one of the horizontal-vertical

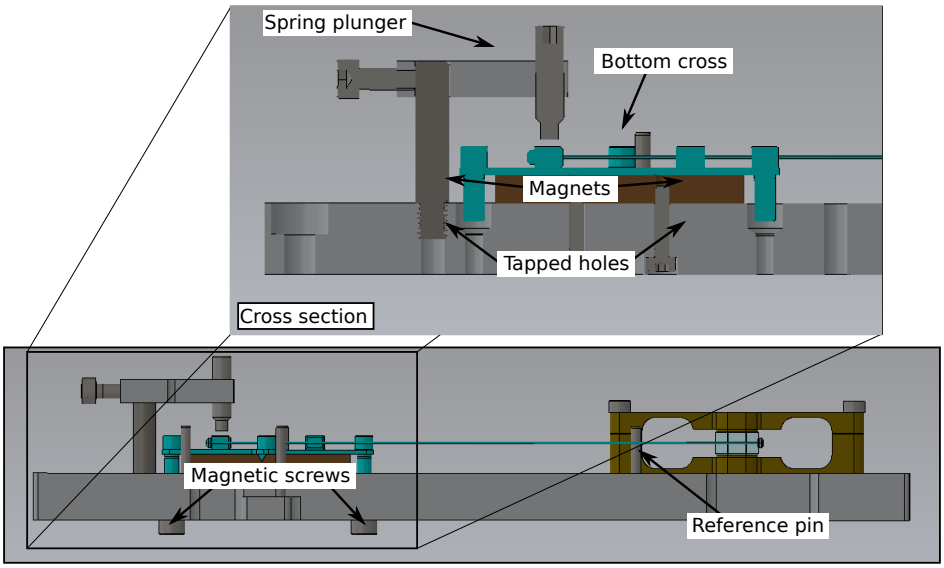

Figure 7.42: Computer-aided-design model of the weld jig and a cross section through the penultimate mass area. The bottom picture shows the weld jig with highlights reference pins for the 1 g mass caps and two magnetic screws. In the cross-section above the two tapped holes for these screws can be seen. They are placed to allow magnetic mounting of the penultimate mass by interacting with its vertical magnets.

adjusters of the ECD cage which was presented in Section 7.2.5. The mounting board for the horizontal coils can be rigidly fixed to the weld jig and still be used on the horizontal-vertical adjuster. The opposite horizontal-vertical adjuster hosts an additional part that can be connected to the top mass cap piece. Figure 7.43 shows a computer-aided-design model of the jig mounted in the switchable ECD assembly. Picture A shows a side view of the assembly in which the cap removal tool can be seen attached to the left horizontal-vertical

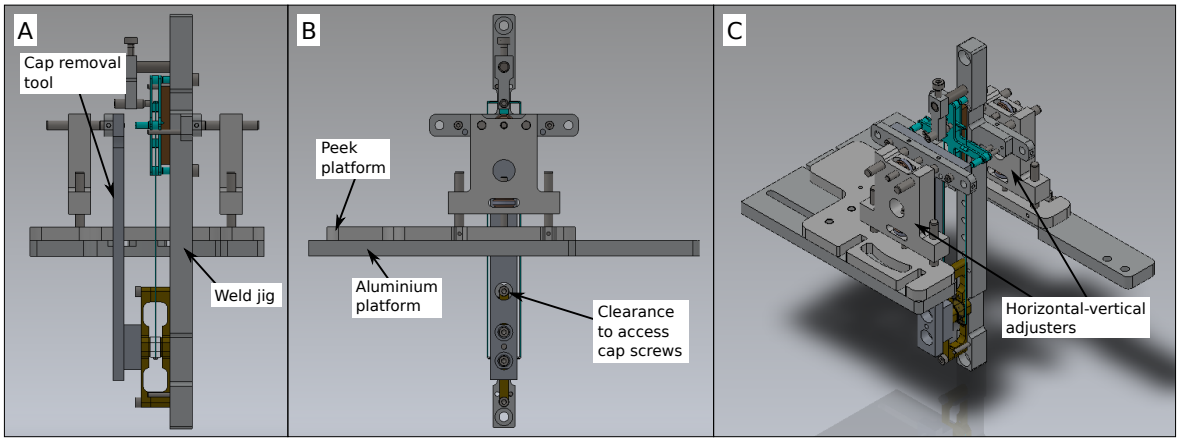

Figure 7.43: Computer-aided-design model of the weld jig in the switchable ECD assembly. Picture A shows a side view of the assembly in which the cap removal tool can be seen attached to the left horizontal-vertical adjuster and interfaced with the 1 g mass cap. Picture B depicts a font view of the assembly in which the back of the cap removal tool is shown. A clearance hole is implemented for access to the mass cap screws. In Picture C the isometric view of this assembly is presented.

adjuster. At its lower end, the tool interfaces with the 1 g mass cap and the top cap can be attached with two screws. Picture B depicts a front view of the assembly in which the back of the cap removal tool is shown. A clearance hole is implemented in the tool to access the mass cap screw, which would otherwise be inaccessible. In Picture C the isometric view of this assembly is presented.

It is planned to remove the whole platform together with the lower bar (as a handle) and install the weld jig (as well as the cap removal part as in Figure 7.43) before re-introducing the platform into the suspension. The horizontal-vertical adjusters are used to align the weld jig and thus the monolithic assembly in the suspension. To introduce wire loops the weld jig can be lifted. In this position the loops are placed over the horizontal arms of the penultimate mass. With the loops in position on the break-off prisms the jig is lowered until the wires are barely under tension. In this position, and with the cap removal tool attached to the top cap piece, the two mass cap screws are released. Once the top cap is free the removal tool can be fully retracted with the horizontal-vertical adjuster, while on the opposite side the clamping arm with the spring plunger is removed from the weld jig. The two magnetic screws are then carefully retracted and removed from the jig. Both the test and penultimate masses should then be entirely free and only suspended from the upper intermediate mass. The horizontal-vertical adjuster retracts the weld jig and the whole assembly with the removal tool, and the weld jig on the platform can be removed from the cage to exchange the tool and jig for the vertical and horizontal coils. Fully retracted, the coils can be re-introduced with the platform and aligned to the penultimate mass in a final step.

7.11.2 Weld tool

The structure in which the weld jig and the assembly that is hosting two sets of tweezers to hold the 10 µm fibres are mounted during welding is called the “weld tool”. In order to keep complexity at a low level the weld tool is made from 20 mm × 20 mm Bosch extrusion. Similar to the tweezer-assembly of the 100 g weld tool, two sets of tweezers, mounted on 3-axis translational micrometer stages (Newport M-MT-XYZ), will be used to introduce the fibre to the weld structure and for fine alignment of the fibre during welding. For this the micrometer adjusters are mounted on another piece of Bosch extrusion that can be interfaced with the weld structure. A computer-aided-design model of the initial weld tool can be seen in Figure 7.44. A front view of the weld tool with the weld jig is shown in Picture A, with the jig mounted centrally in the Bosch frame to allow access from either side with the tweezer-assembly. Mounted on 3-axis micrometer adjusters, the tweezers are used to align the fibres and hold them during welding. The tweezer-assembly is mounted on a separate piece of Bosch extrusion that can be interfaced with the weld structure. Analogous

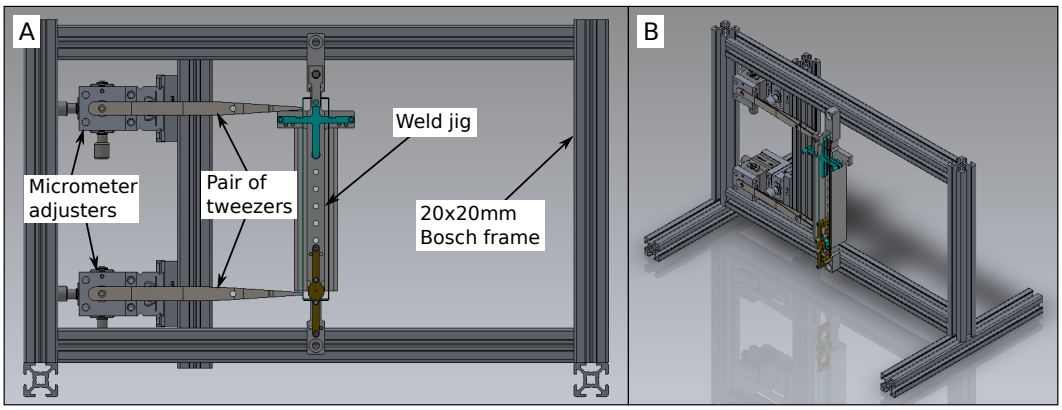

Figure 7.44: Computer-aided-design model of the weld tool. In Picture A the weld tool together with the weld jig is shown in a front view. The weld jig is mounted centrally in the weld structure. The two 3-axis micrometer adjusters are mounted on an additional piece of Bosch extrusion that is also mounted to the weld structure. A pair of tweezers is used to hold the fibre that can be aligned with the micrometer adjusters. Picture B shows an isometric view of the weld tool.

to the 100 g welding (see Section 6.9) this tweezer-assembly will be used for the initial cutting of the fibre from its cartridge. In pitcure B the weld tool is depicted in an isometric view.

7.11.3 Gluing test with weld jig and weld tool

In order to test the weld tool and weld jig, it was decided to do a first test by gluing two real fibres to a spare test and penultimate mass. In preparation for this test, a bonded 1 g spare substrate was mounted in mass caps following the procedure presented in Section 7.8. The weld jig was assembled and the mass caps and the bottom cross piece were fixed. A picture of the populated weld jig can be seen in Figure 7.45. Picture A depicts the weld jig with the bottom cross of the penultimate mass and the 1 g mass cap in place. In Picture B the upper half of the jig is shown with the bottom cross being aligned to the three alignment pins and clamped in position with the spring plunger. For Picture C the top cross has been added to the jig and is aligned for the final gluing step.

In order to glue the first ‘monolithic’ assembly, the jig initially hosts the configuration of Picture B with the bottom cross clamped and held with additional magnetic mounting as described in Section 7.11.1. The jig is mounted in the weld tool and placed in the centre to allow access for the tweezer assembly from either side. To emulate a realistic environment with real components, real 10 µm fibres were used in this test (fibres G8 and D6 from the spare set presented in Figure 7.40). After holding the fibre at the 400 µm stock section with the tweezer assembly the fibre was cut out of the cartridge with a hydrogen flame, with the cuts set at the transition of the 400 µm stock to the 2 mm base material. The fibre was cut to length using a diamond scribe and a conventional steel ruler, where the stock is broken

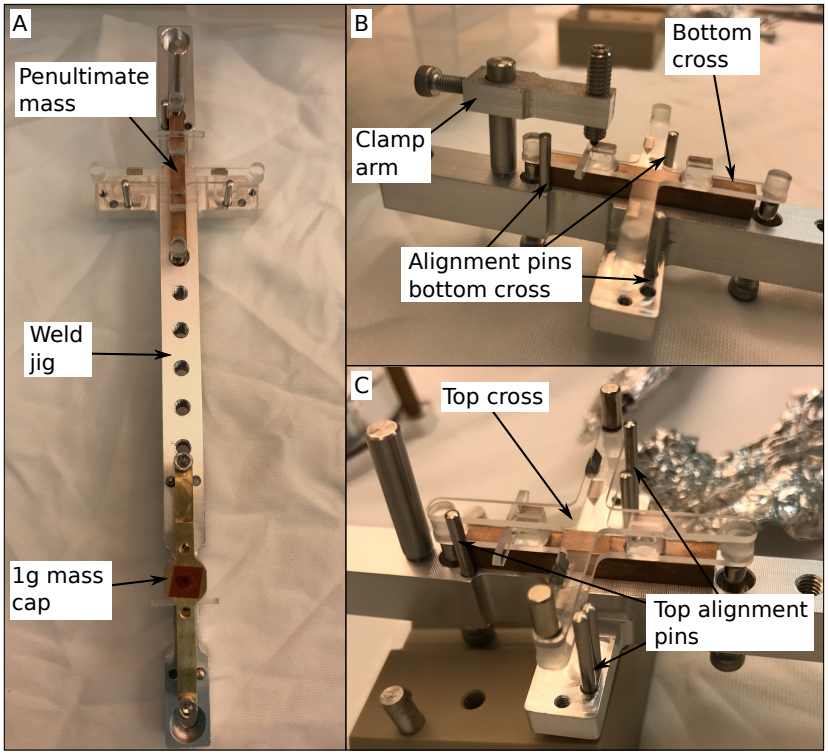

Figure 7.45: Pictures of the populated weld jig. Picture A has the bottom cross of the penultimate mass as well as the 1 g mass caps mounted to the jig. In Pictures B and C the upper half of the jig is shown with the bottom cross aligned to three alignment pins and the top cross aligned to the alternative horizontal alignment pins.

off at the weak spot due to the scribe. Pictures of fibre-cutting and the tweezer assembly mounted in the weld tool together with the weld jig can be found in Figure 7.46. Picture A

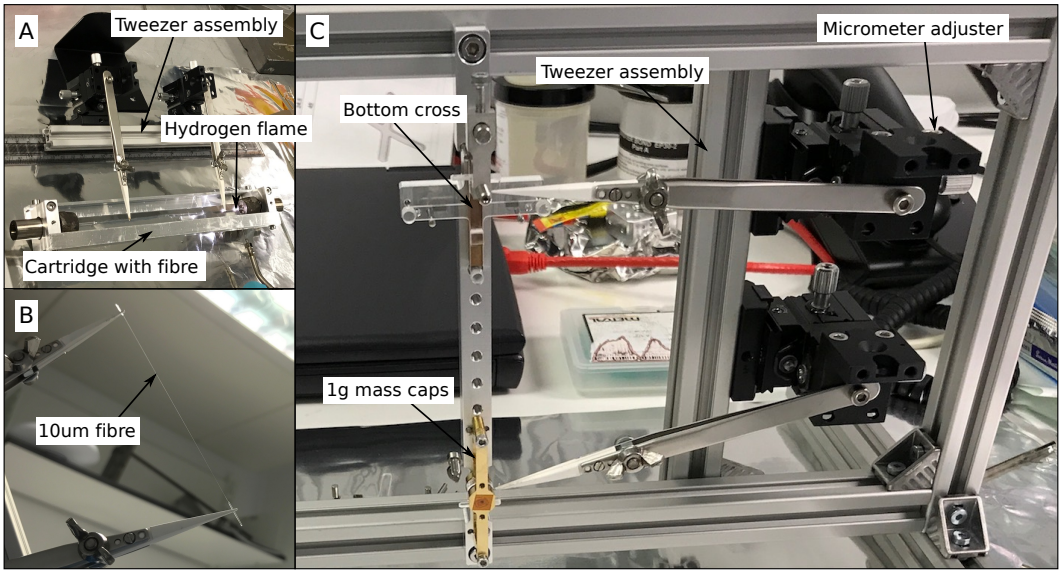

Figure 7.46: Picture A shows the tweezer assembly interfaced with the cartridge during cutting of the fibre with a hydrogen flame. The 10 µm fibre held with the tweezer assembly can be seen in Picture B. For Picture C the tweezer assembly is mounted in the weld tool to allow gluing of the first fibre to test and penultimate mass.

shows the tweezer assembly interfaced with the fibre cartridge. The fibre is cut out of the cartridge with a hydrogen flame. The 10 µm fibre can be seen in Picture B where it is held in the tweezer assembly, which is then mounted in the weld tool as depicted in Picture C. The fibre is roughly aligned with the whole assembly and can be adjusted precisely with the micrometer adjusters on which the tweezers are mounted.

The fibres were glued to the cradle ears with Masterbond EP30-2. To accomplish this, the fibre is positioned close to the cradle ear until the two parts touch before a small amount of glue is attached to the connections at the test and penultimate masses. The glue is left over-night to settle before the tweezers are removed. In a last step the top cross is added to complete the penultimate mass. Pictures during gluing of the second fibre and of the ultimate gluing step are shown in Figure 7.47. In Pictures A and B the second fibre is glued

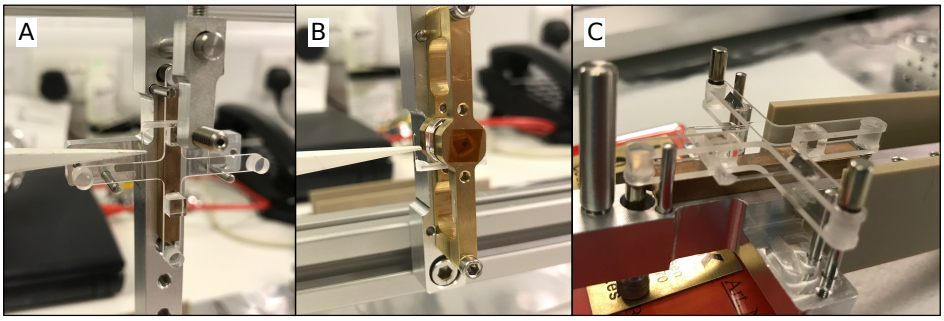

Figure 7.47: Pictures A and B show the gluing of the fibre to penultimate and test mass respectively. In Picture C the top cross is glued to the bottom cross to complete the penultimate mass.

to the cradle ears on the penultimate and test mass respectively. All glue joints are left for 24 h to settle before removing the tweezers. Picture C shows the completion of the penultimate mass where the top cross is glued to the bottom cross. The top cross is aligned to three alignment pins.

The glued monolithic assembly was used in a first dirty-build of the 1 g ITM suspension. In this build all mechanical parts could be tested and checked for any design errors before all parts were prepared for use in vacuum. Additionally, it was possible to test the procedures for introducing and releasing the monolithic assembly as well as the introduction of the ECD assembly that can be found in Appendix C.3.3. Some pictures of an initial hang test can be found in Figure 7.48. Picture A shows the weld jig and the cap removal tool mounted to the horizontal-vertical adjusters of the ECD assembly. As described in Section 7.11.1 the removal tool is interfaced with the top part of the mass cap. At this point the wire loops coming from the upper intermediate mass are fed around the horizontal arms of the penultimate mass cross onto the break-off prisms. In Picture B the cap is opened and the weld jig as well as cap removal tool slightly retracted. The whole platform with the jig and removal tool still attached can be removed once they are fully retracted. Picture C depicts the re-introduced ECD assembly with the glued monolithic assembly and Picture D

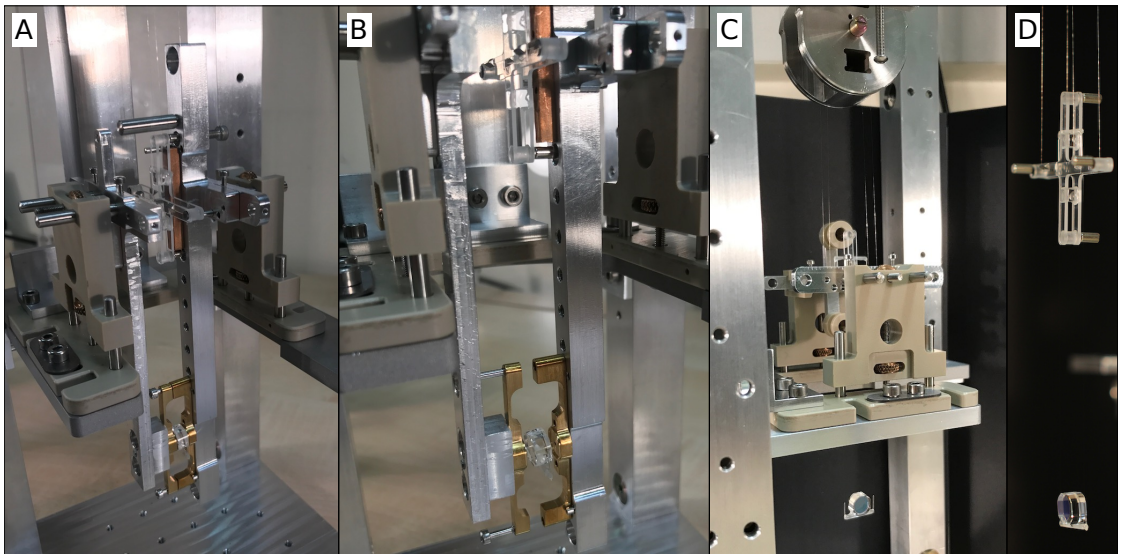

Figure 7.48: Picture A shows the weld jig and the cap removal tool mounted to the horizontal-vertical adjusters of the ECD assembly. The removal tool is interfaced with the top cap. In Picture B the cap is opened and the weld jig as well as cap removal tool slightly retracted. Picture C depicts the re-introduced ECD assembly with the glued monolithic assembly and Picture D presents a side view of the glued monolithic assembly.

presents a side view of the glued monolithic assembly.

7.11.4 Weld plan and required precision

The welding of the fibres to the cradle ears on test and penultimate mass is planned to be done with a similar weld tool as used for the initial gluing test. The initial changes to be made are the size of the frame to give more clearance for the tweezer assembly and the 10 µm fibres. In contrast to the welding procedure of the 100 g monolithic assemblies in which stock material is fed vertically into the weld, the fibres for the 1 g monolithic assemblies will be welded to the cradle ears from the side. This is the same way in which the fibres were glued for the test of the welding equipment and the first hang test. A schematic of the proposed welding procedure is depicted in Figure 7.49. In Image 1 the stock is held in

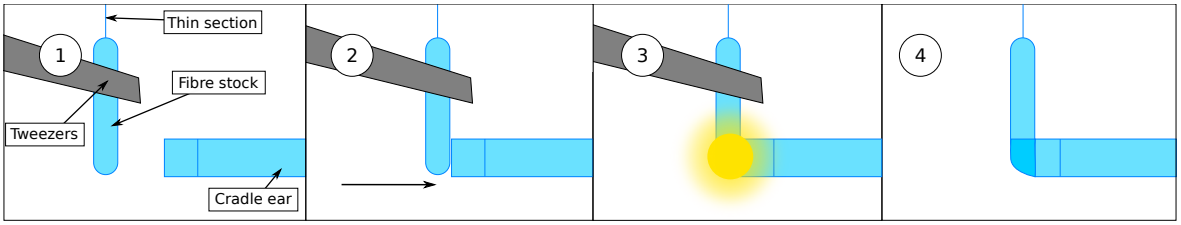

Figure 7.49: Schematic of a 1 g weld. Image 1 shows the 400 µm stock held in tweezers and the cradle ear. Note that the thin section of the fibre is under tension at all times. In Image 2 the stock is brought close to the ear. Image 3 shows the heating of the ear tip and stock. Image 4 depicts the finished weld.

the tweezer assembly. Image 2 shows how the fibre is moved close to the ear tip until they touch. The stock of the fibre and the ear are then heated to their melting point in Image 3. Image 4 depicts the final weld between 400 µm stock and cradle ear. The fibre stays under tension for the whole weld procedure.

One estimation to be made is to what accuracy the welding of the fibres and thus the definition of the break-off points has to be done to allow operation of the Sagnac speed meter experiment. Having only one fibre on either side of the 1 g test mass does not allow pitch adjustments to be made with any of the coil magnet actuators on the upper stages. The initial plan for the 1 g ITM suspension was to compensate for any pitch misalignment of the 1 g mirror with the two 100 g ETM suspensions in each cavity, however the only possibility of pitch alignment in a 1 g ITM suspension would be to use thick fibres or ribbons, which cause high vertical mode frequencies as well as very strong longitudinal to pitch coupling due to their stiffness. In case of the 10 µm fibres for the 1 g ITM suspension the bending point of the thin section of the fibre is of the order of 1 mm which does not allow pitch alignment from an upper pendulum stage. The 1 g substrate will be always suspended in such a way that the break-off point and centre of mass are aligned vertically, meaning that lateral shifts in direction of the main surfaces inevitably cause rotations of the mass itself. As a requirement, the beam spot on the 100 g ETM substrate is allowed to vary by ± 10 mm. With the cavity length of about 1.3 m, this shift of ± 10 mm is equivalent to an angle of ± 3.8 mrad at the location of the 1 g ITM substrate. Together with the break-off point 2 mm above centre of mass of the bonded 1 g ITM substrate, the angle can be used to determine the required lateral position of the break-off point to ± 7.7 µm. In the small angle approximation, the numbers scale linearly with break-off point distance above centre of mass, so even a break off point 10 mm above centre of mass will require a precision of ± 38.5 µm. One way to overcome this challenge is an optical lever set-up and in-situ modification of the fibre location. This approach, together with a four fibre design, will be discussed in Chapter 9.

7.12 Conclusion

In this chapter the design of the 1 g ITM suspension for the Sagnac speed meter experiment was presented. The suspension is designed as a quadruple pendulum to allow damping of the 1 g test mass while making use of the same vertical blade springs that are implemented in the 100 g ETM suspension. All masses and the general design of the suspension cage with all its features were explained in detail. The modelling of the suspension dynamics showed that the estimated displacement noise due to seismic noise is well below requirement. The creation of the 1 g monolithic assembly was discussed in depth and all necessary

tools and auxiliary parts were presented. The fibres for the 1 g ITM suspension were pulled in the same way as the fibres for the 100 g suspension and their design considerations were elaborated upon. Thermal noise modelling settled the final diameter and length of the thin section of these fibres. The plan for welding the monolithic assemblies was highlighted with an example in which the first monolithic assembly was produced with glue in order to test procedures and functionality of the designed parts and suspension cage. The desired weld-precision for placement of the break-off point in order to not be limited by pitch-rotation of the 1 g test mass was quantified to be $\pm 7.7\,\mu$m for a break-off point of the fibre 2 mm above centre of mass. This accuracy coupled with the desire for pitch adjustment presents a future challenge for the experiment. However, a brief discussion of these challenges and possible solutions can be found in Chapter 9.

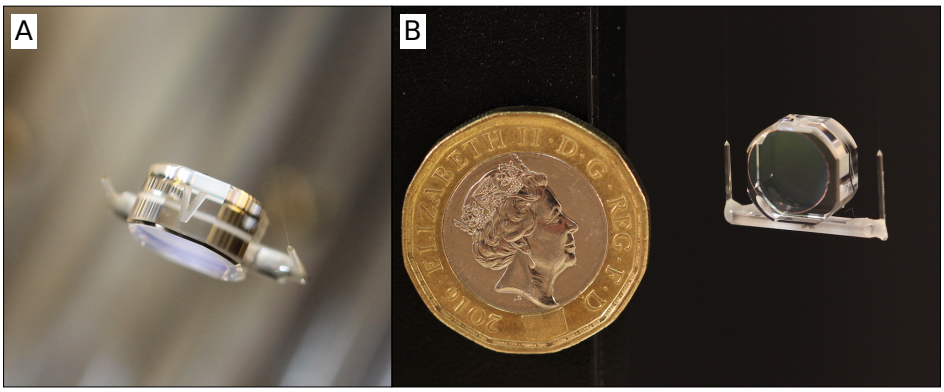

Figure 7.50: Picures A and B show close-up photographs of the first suspended glued 1 g ITM substrate. In Picture B a one pound coin served as a reference for the size of the 1 g mirror.

Chapter 8

Switchable eddy current damping

The content of this chapter has been published as *Demonstration of a switchable damping system to allow low-noise operation of high-Q low-mass suspension systems* in [134]. The author of this thesis led the writing of that paper and contributed to all aspects of the study, and the results published in the paper are explained in greater detail in this chapter in order to provide a broader base of understanding and application. The results and conclusions shown here are the same as in [134].

8.1 High-Q pendulum systems

In order to achieve the sensitivities required in gravitational wave detectors, the mirrors are suspended as multistage pendulums. As shown in Chapter 4, every pendulum stage acts as a harmonic oscillator with a $1/f^2$ response above its highest mode frequency. Adding multiple pendulum stages increases this effect, and a triple pendulum suspension such as the 100 g ETM suspension (see Chapter 6) has a $1/f^6$ response above its highest rigid body mode. Using multiple pendulum stages attenuates noise introduced at higher pendulum stages, but does not attenuate intrinsic noise of the lowest pendulum stage such as thermal noise in the suspension materials. In the Sagnac speed meter experiment the lowest pendulum stages of the 100 g ETM and 1 g ITM suspensions is made fully monolithic using fused silica; a material with low mechanical loss ϕ. Creating a high-Q systems ($Q = 1/\phi$), a trade-off has to be made between low suspension thermal noise is and high ring-down times of resonances once they are excited. The ring-down of a pendulum mode can be described by

$$A(t) = A(0) \exp\left[-\frac{\omega_{\mathrm{res}}}{2Q}t\right], \tag{8.1}$$

where $A(0)$ denotes an arbitrary initial amplitude, t is time and ω_{res} denotes the angular resonance frequency of the excited mode. It is obvious from this equation that a higher quality factor Q means longer ring-down times of the excited mode. In order to allow practical implementation the high-Q resonances need to be damped.

8.2 Active and passive damping

In general there are two approaches to damping that could be used: active damping [95] and passive damping [96]. Active damping, as described in Reference [95], is achieved by using a sensor to measure distortions or motion and an actuator that is used to counteract this motion. In Advanced LIGO so-called BOSEMs [94] are used. These consist of a coil-magnet actuator and a shadow sensor. The coil is wound around an aluminium coil former and the magnet, together with a little flag, is directly glued to the mass of the pendulum. When the mass moves, the flag is used to obscure a photodiode onto which a diode is pointed. Depending on the amount of light sensed by the photodiode, it is possible to tell the motion of the flag and thus the motion of the mass. By generating a current and sending it through the coil, the actuator is used to counteract the sensed motion, resulting in active damping of the system. Depending on the location of the BOSEMs, different degrees of freedom of the pendulum (ideally all of them) can be damped. Passive damping, as described in Reference [96], can be realised by using a magnet and a conductive material such as copper. These are arranged in a way that, whenever either the material moves relative to the magnet or vice versa, eddy-currents are induced in the conductor. Due to the residual resistance of the material these currents create Joule heating, which represents a velocity dependent power loss and thus viscous damping of the system. Eliminating the need of a sensor comes at the expense of additional force noise due to thermal noise from the damping system as can be seen in the following section.

8.3 Viscous damping and related force noise

In the Sagnac speed meter experiment passive damping is implemented in the design of all suspensions at the top stage. It has been previously and is currently also implemented in 100 g suspensions that were designed for optical spring experiments in the 10 m prototype in Glasgow [135]. In all these suspensions a coil is wound around a copper former, allowing actuation in addition to passive damping. In the case where a sensor is present it would even be possible to implement active damping. However, in the previously mentioned suspensions only passive damping is used and the coils are reserved for the application of static forces to adjust the alignment of the suspended optic. As shown in Reference [96] and as a

direct consequence of the fluctuation dissipation theorem [46] the amplitude spectral density of force noise of a coil-magnet actuator due to thermal noise in the conductive material is given by

$$\tilde{f} = \sqrt{4k_B T\gamma}, \tag{8.2}$$

where γ is the the (eddy-current) damping constant of the system, k_B is the Boltzmann constant, and T is temperature. The force noise can be related to displacement noise by multiplication with the force transfer function from the stage of the actuator to the test mass.

8.4 1 g ITM as a low-mass high-Q suspension

As a direct consequence of Equation 8.2, low force noise can only be achieved with a low damping constant. Whenever passive damping is facilitated, it is implemented in the top suspension stage using the pendulum stage(s) below for filtering of the force noise. In order to damp motion of the test mass at a higher pendulum stage the masses need to be matched in weight and moments of inertia as well as possible. This is the only way in which energy can be transferred efficiently between pendulum stages, allowing motion of the test mass to be damped at a higher pendulum stage. The 1 g ITM suspension is designed as a quadruple suspension in order to allow damping of test mass motion, as described in Section 7.2 and depicted in Figure 8.1. The quadruple pendulum can be de-coupled into a two-stage heavy pre-isolator and a low-mass high-Q double pendulum. Due to this de-coupling, the same

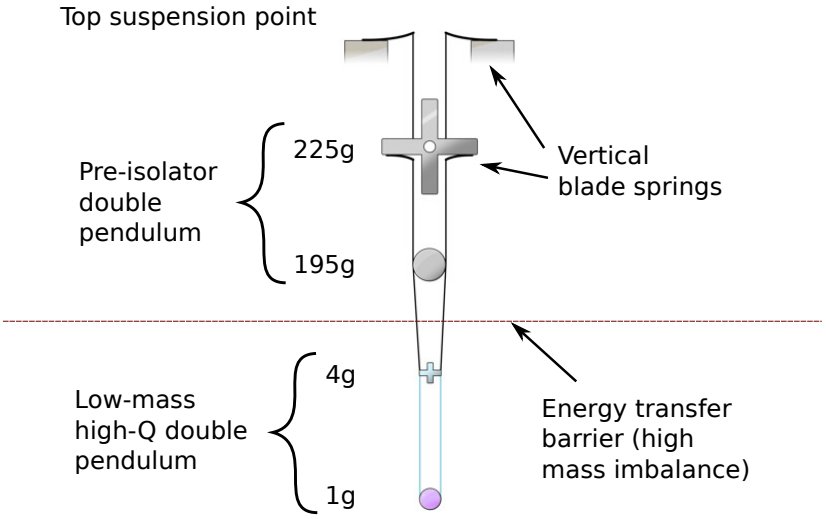

Figure 8.1: Schematic of the 1 g ITM suspension. The small vertical blade springs dictate the use of a fourth pendulum stage above the 1 g test mass to allow sufficient energy transfer for damping resonance mode frequencies of the low-mass high-Q double pendulum. For further details see Figure 7.1.

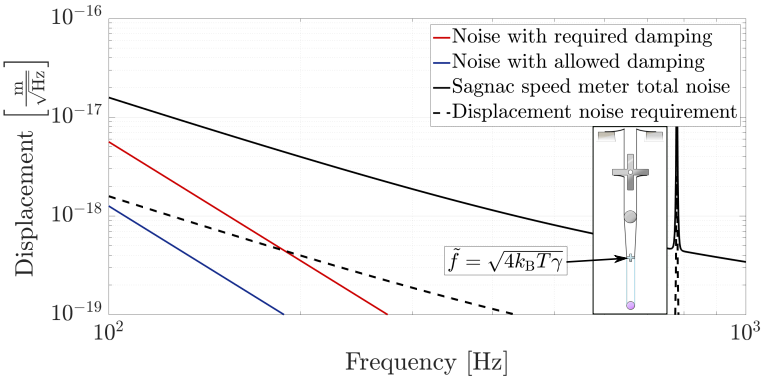

Figure 8.2: Comparison of noise with allowable to required damping for a 1 g suspension used in the SSM. The noise with required damping is derived from ring-down times of the longitudinal mode frequency where times above 10 s are considered impractical. The noise with allowable damping considers a safety factor of 10 below design sensitivity for one double pendulum and this safety factor is shown as the dashed black trace.

Simulink® model as for the auxiliary suspension (Section 5.3) could be used for simulations of the decay times in the high-Q state. It is expected that every time the triangular cavities of the Sagnac speed meter experiment lose lock, there will be a large excitation of the mirror, that will take a long time to settle. Damping of test mass motion is thus essential for practical implementation of the 1 g ITM suspension.

8.5 Force noise in low-mass high-Q suspensions

The longitudinal force-displacement transfer function of the low-mass high-Q double pendulum can be used to simulate the displacement noise spectral density due to force noise arising from damping in the system. Figure 8.2 depicts the displacement noise due to force noise on the penultimate stage of the 1 g ITM suspension. The red trace uses a high damping constant which is required to reduce ring-down times of the longitudinal mode to, of order 10 s. It is easy to see that at 100 Hz the design sensitivity of the Sagnac speed meter experiment is only a factor of five above the noise with required damping. In general it is desired to always keep a safety factor of 10 below design sensitivity, as marked by the dashed black trace. The blue trace is generated using a low damping constant to fulfil the requirements of this safety factor, however in this case the ring-down times of the longitudinal mode frequency is of order hundreds of seconds, which is impractical for implementation in the experiment. A solution to this problem is to make the passive damping switchable in the system, allowing low-noise operation in science mode and reducing ring-down times in damping mode.

8.6 Measurement of switchable ECD

In order to implement a switchable passive damping system, a coil-magnet actuator can be used. The damping of this actuator solely depends on its response and the residual resistance of the coil:

$$\gamma \approx \frac{C_{\mathrm{resp}}^2}{R}, \tag{8.3}$$

where γ is the damping factor in $\mathrm{kg\,s^{-1}}$, C_{resp} is the response of the coil-magnet actuator in $\mathrm{N\,A^{-1}}$ and R is the residual resistance in Ω. Adding a resistor between the coil ends with a high resistance, or leaving the coil open, minimises damping and short-circuiting the coil maximises damping.

To demonstrate the increase in damping for a closed coil compared to an open one, an auxiliary suspension was used and the copper cups and coil former were replaced by four coil formers made from polyether ether ketone (PEEK), a non-conductive material. Figure 8.3 shows a picture of the auxiliary suspension on the right and the coil former in the top left. The coils for this experiment were made from 200 µm nylon enamelled copper wire with 150 turns. The residual resistance of each coil was measured to be 3.6 Ω at the switch terminals to which they are connected. The magnets are the same as used in the regular auxiliary suspension, 3 mm × 6 mm (diameter×length) nickel-plated neodymium magnets. A silver-coated one inch mirror was used as a test mass for the measurement. Measurements were taken in an optical lever set-up as previously described in Section 5.5. Again, a QPD was used for readout of both rotational mode frequencies yaw and pitch. For each measurement a combination of coil-magnet actuators was used to excite the pendulum modes with an impulse. To take a measurement with high damping the coils were short-circuited with a mechanical switch and for the measurement of reduced damping this switch remained open. All data was recorded in CDS and the analysis was done in MATLAB®.

8.6.1 Yaw measurement

One horizontal coil was excited to measure the yaw pendulum mode frequency. The ring-down times of both high and low damping were measured. In order to achieve a better fit only one coil was used to damp the yaw mode. The result of the measurement can be seen in Figure 8.4. The measured raw data is shown in light colours, red for high damping and blue for low damping. The yaw measurement was taken over 600 seconds. The fitted curves in solid red and blue were calculated from the maxima of the ring-down oscillation. The Q-factor of both cases can be calculated using the relation from Equation 8.1. For high damping the Q-factor can be derived to be 1302 when the ECD is on and 10314 when

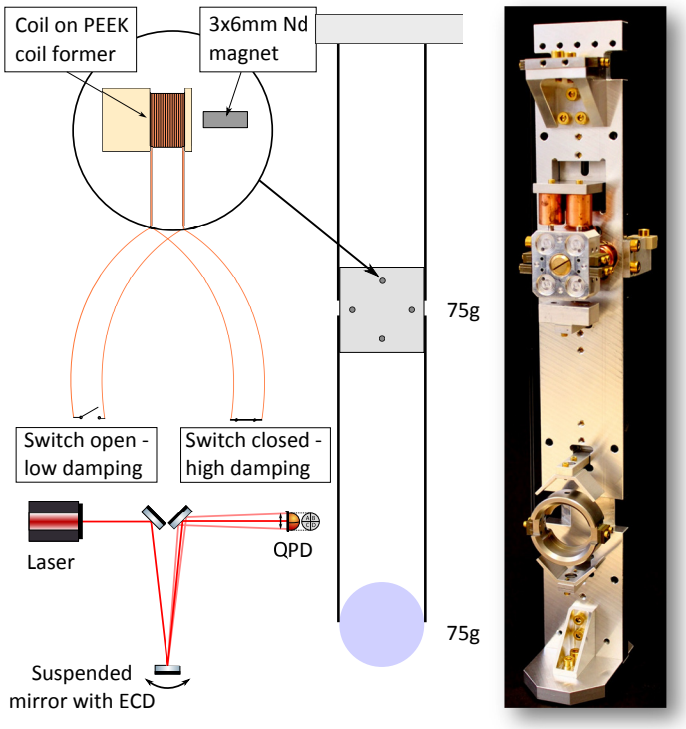

Figure 8.3: Experimental realisation of switchable ECD. Top left: The coils are wound around non-inductive PEEK coil formers. Short-circuiting the coils results in damping (dependent on residual resistance of coil) and opening the coils results in low damping but allows for actuation. Bottom left: Measurements are performed in an optical lever set up. Right: Picture of the an ordinary auxiliary suspension with copper coil formers.

the ECD is off. For both calculations the lower of the two yaw mode frequencies is used, corresponding to the common yaw mode. In general the double pendulum has two yaw modes, one common mode (lower frequency) and one differential mode (higher frequency), which can be also seen in Table 5.2 in Chapter 5. Using

$$\zeta = \frac{1}{2Q} = \frac{\gamma}{\gamma_c}, \tag{8.4}$$

where ζ is the damping ratio, γ is the damping constant and γ_c is the critical damping of the system ($\gamma_c = 2m\omega_n$, with ω_n being its natural frequency), it is possible to calculate the corresponding damping factors for either case. For the ECD switched on the damping factor can be calculated to be $1.26\,\mathrm{g\,s^{-1}}$ and $0.16\,\mathrm{g\,s^{-1}}$ for the ECD off. If it is assumed that the residual damping of the coil-magnet actuator is negligible for the low damping case, $1.10\,\mathrm{g\,s^{-1}}$ can be attributed to the damping factor of one coil in high damping mode. The simulated damping factor for the coil-magnet actuator was $3.0625\,\mathrm{g\,s^{-1}}$, using a simulated value for the actuators response of $0.105\,\mathrm{N\,A^{-1}}$ and a measured residual coil resistance of $3.6\,\Omega$. The difference between the measured and simulated damping factor can be explained by the alignment of the damping system. The PEEK coil former were originally designed

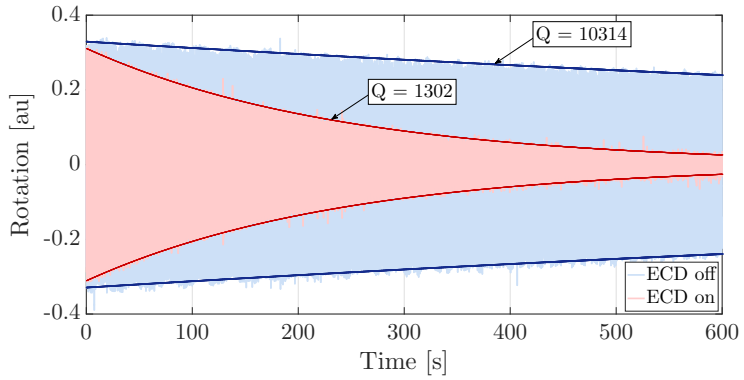

Figure 8.4: Measurement of switchable ECD on a test suspension in yaw. Light blue shows the ring-down measurement in ECD off (switches open) mode and light red shows the ring-down measurement in ECD on mode. The solid blue and solid red curves are fitted to the maxima of the corresponding ring-down measurement. A reduction of the damping factor by 1.10 g s^{-1} is achieved in this test experiment.

to be used in the 100 g ETM suspensions at the penultimate stage. As described previously in Chapter 6 the control assembly at this stage uses smaller 2 mm × 2 mm neodymium magnets. The clearance for the magnet in the former was designed accordingly to fit this type of magnet. However, the 3 mm × 6 mm magnets used in this experiment could not be placed in the sweet-spot of the actuator, that is the optimal distance between centre of coil and centre of magnet. Instead the position of the magnet is about 2.5 mm offset which leads to significantly reduced actuator response.

8.6.2 Pitch measurement

The pitch measurement was performed with two vertical coils. This was required due to the higher restoring force of the mode. Both vertical coils were used to excite the pitch mode and measure the ring-down of the first pitch mode. The result is depicted in Figure 8.5. Again the low damping measurement is shown in blue. Light blue shows the raw measurement data and the solid blue line shows the fitted ring-down of the lower pitch mode. The high damping measurement is shown in red, where light red shows the raw measurement data and solid red shows the fitted ring-down. From this measurement it is again possible to calculate the Q-factors for both cases, giving 8039 for the low damping and 1730 for the high damping case. From the Q-factors the damping constant can be calculated to be 1.18 g s^{-1} for the ECD switched on and 0.25 g s^{-1} for the ECD switched off. Note that these values are for one coil-magnet actuator and thus in good agreement with the results for the yaw measurement.

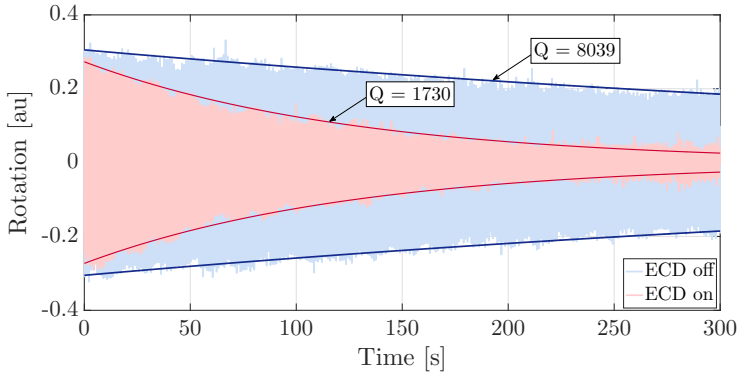

Figure 8.5: Measurement of switchable ECD on a test suspension in pitch. Light blue shows the ring-down measurement in ECD off (switches open) mode and light red shows the ring-down measurement in ECD on mode. The solid blue and solid red curves are fitted to the maxima of the corresponding ring-down measurement. A reduction of the damping factor by 0.97 g s^{-1} is achieved in this test experiment.

8.7 Optimisation of damping

The approximation for the damping factor that was used in Equation 8.3 in Section 8.6 is frequency independent. In order to account for significant coil inductance and/or resonant mode frequencies of the pendulum, the damping factor is considered to be frequency dependent and can be optimised. The optimisation can be achieved by impedance matching of the coils resistance to the RL-circuit that is defined by the coil itself. In general the coil can be described as an RL-circuit when it is short-circuited. Following the basics of induction, the motion of the magnet in the coil creates an electromotive force (EMF). This force creates the current inside the coil which itself generates a counter EMF. This force opposes the flow of current. This effect can be minimised by impedance matching of the coils resistance to the RL-circuit. In case of high resonance mode frequencies and/or high inductances of the coil it is not necessarily optimal to aim for lowest possible resistance, but to choose the resistance accordingly to the coil parameters. For a given coil inductance L the optimal resistance R can be calculated for the frequency of the resonance to be damped, from

$$\omega_{\text{res}} = \frac{R}{L}. \tag{8.5}$$

In this experiment each coil has a calculated inductance of 355 µH. In the case where the relative permeability of a neodymium magnet (1.05) is taken into account, the inductance of the coil is calculated to be 372.75 µH which represents an upper bound for the inductance as the magnet would need to entirely fill the inside of the coil. For Figure 8.6 the coil inductance was taken to be 355 µH. In this figure the dependence of the optimal coil resistance R for the resonance mode frequency of the mode to be damped is shown. It can be seen that for frequencies below 20 Hz the optimal coil resistance is 450 mΩ. A threshold at 20 Hz was

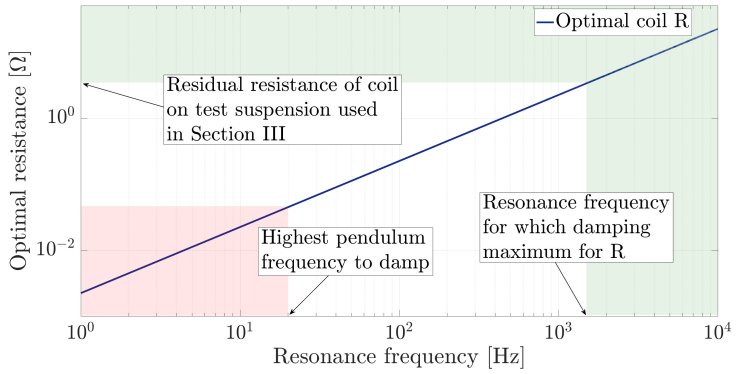

Figure 8.6: Optimal residual coil resistance in dependence of resonant mode frequency assuming a certain coil design with an inductance of 355 µH. The red shaded area represents the area in which resonant frequencies of a pendulum suspension typically lie. The optimal resistance is far below the 3.6 Ω coil resistance. The green shaded area shows the area above the coil resistance and thus the area in which optimisations could be achieved.

chosen due to the fact that the mode frequencies for which this damping system is planned to be used all lie at lower values. Comparing this to the residual resistance of the coil used in the experiment (3.6 Ω) is becomes clear that for this application the optimisation does not play a big role. However, it is to be noted that in applications with high resonance mode frequencies and similar coil parameters this damping system could be optimised.

8.8 Conclusion

This chapter summarises the investigation of a switchable passive damping system for the 1 g input test masses in the Sagnac speed meter experiment. In order to avoid limitation due to force noise from thermal noise of the damping system, the passive eddy-current damping needs to be switchable with the capability of being switched off in science mode. Whenever the demand for damping arises, the switchable system allows for an immediate increase of the damping factor. An increase in damping factor by about 1.10 g s^{-1} could be measured for the yaw mode and by about 0.97 g s^{-1} for the pitch mode on a double stage demonstration pendulum (a modified auxiliary suspension). The switchable damping system can in general be optimised for resistance of the coil. However, due to low pendulum frequencies and low coil impedances this optimisation cannot be applied here.

In the final Sagnac speed meter experiment it is planned to implement four coil-magnet actuators around the penultimate mass of the 1 g ITM suspension. Together with a 3 mm×6 mm neodymium magnet the coils will each deliver a damping factor of 2.4 g s^{-1}. In this case the coils are made from 160 µm Kapton enamelled copper wire with 250 turns. The coils are mounted on vertical horizontal adjusters in the switchable ECD assembly.

Chapter 9

Future developments for the 1 g ITM suspension

The estimation of the required precision for fibre break-off points above the centre of mass of the 1 g mirror revealed a significant challenge. Keeping the break-off location 2 mm above the centre of mass requires a precision in positioning of the break-off point of ± 7.7 µm in order to prevent pitch of the test mass and to keep the spot position within the allowable ± 10 mm on the 100 g ETM mirror. This chapter will briefly highlight an optical lever set-up with which this precision could be reached in an iterative measurement. In addition, a four fibre design with the available bonded cradle ear/ITM combination and with a slight and simple modification is presented. In the four fibre design the fibres will be attached to the sides of the cradle ear rather than its tips, or to an additional part that will be introduced.

9.1 Iterative process to achieve weld precision

As mentioned in Chapter 7 an optical lever set-up could be employed in an iterative process to achieve the desired weld precision. The necessary procedure would start from a welded assembly with welds as planned in Section 7.11.4. Instead of transferring the monolithic assembly to the lab and installing it in the suspension cage, it would be used in an optical lever set up to measure pitch rotation of the 1 g test mass. In this set-up the weld jig is mounted in the ECD assembly as presented in Figure 7.43. The platform would be mounted on a frame made from Bosch extrusion. In this configuration the top mass cap can be removed with the removal tool analogous to the installation in the suspension cage and once it has been retracted the removal tool can be taken away. The penultimate mass remains clamped to the weld jig at all times and is never to be loosened or removed. With a set of washers or an additional set of Bosch legs the platform can be ever so slightly tilted towards the side on which the removal tool was hosted. An angle of 20 mrad would separate

the bottom mass cap and the 1 g test mass by 2 mm which is sufficient to see the mass freely suspended.

The optical lever set-up would be built in the same lab in which the welding takes place. A schematic of a potential set-up can be seen in Figure 9.1. The light from a HeNe-laser

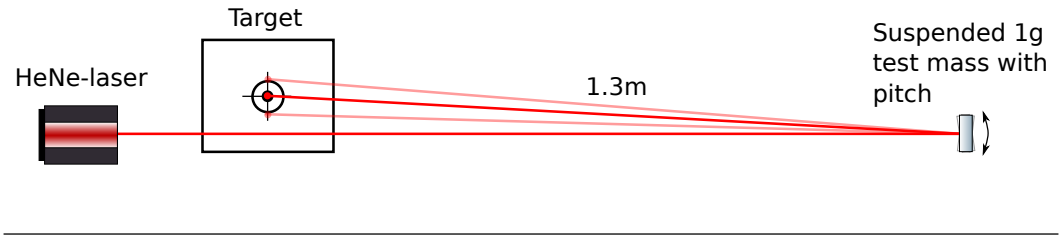

Figure 9.1: A HeNe-laser is used to reflect light off the freely suspended 1 g test mass. The reflected light from the AR surface is measured on a target at a distance of about 1.3 m.

is to be made horizontal and then reflected off the 1 g test mass. For this test the flat AR surface of the test mass would be used and placed at a distance of 1.3 m from the laser which is equivalent to the triangular cavities of the Sagnac speed meter experiment the reflected beam is measured on a target for pitch misalignment.

The platform with the weld jig is carefully made horizontal again so that the 1 g test mass touches the bottom mass cap concentric, then the cap removal tool with the top mass cap is re-introduced and re-aligned to re-attach the top mass cap. The procedure of re-attaching the top mass cap was tested during the first hang test. Once the 1 g test mass is held again in the mass caps the weld jig can be transferred to either the suspension cage or back to the weld tool depending on the outcome of the optical lever measurement. In the case the test mass was not hanging straight enough the weld jig would be re-installed in the weld tool. The tips of the tweezers can then be used to alter the position of the fibre stock to the precision of the micrometer stages on which they are mounted. The CO_2-laser can be used to heat the stock until it can be plastically deformed and push into a slightly different position with the tweezers. In this new configuration the optical lever measurement is repeated. This iterative process can be continued until the break-off point is positioned within the required tolerance.

9.2 Modelling of suspension dynamics

In order to verify the feasibility and to check different implementation options for the 4-fibre design the suspension dynamics were modelled. The 1 g ITM suspension as a quadruple pendulum can be de-coupled into a heavy-mass pre-isolator with vertical blade springs from which a low-mass high-Q double pendulum is suspended. To save computation time

and simplify the simulation, only the low-mass double pendulum is modelled. This approximation is valid as can be seen in Figure 9.2. The dashed blue curve represents the modelled

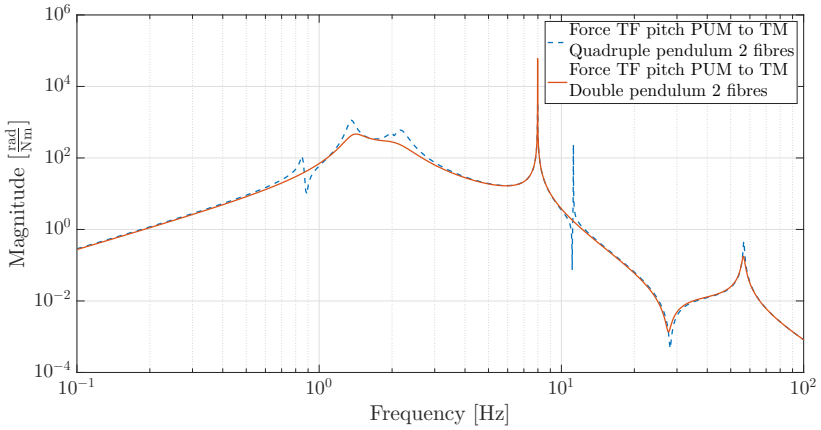

Figure 9.2: The dashed curve in blue shows the simulated force transfer function from pitch excitation at the penultimate stage to test mass motion for the complete quadruple pendulum with two fibres. The same force transfer function for the simplified lowest stage double pendulum is plotted in solid red. Both are in great agreement which makes the double pendulum a good approximation for investigations in this chapter.

force transfer function from pitch excitation at the penultimate stage to pitch motion of the test mass for the quadruple pendulum with two fibres. The same force transfer function for the double pendulum is plotted in solid red. It can be seen that the highest pitch frequencies, which could be attributed to test and penultimate mass, are at identical values. Furthermore the overall shape and level of the force transfer function is almost identical, meaning that the reduced double pendulum can be used as a valid approximation. For all following investigations the low-mass double pendulum is used as a basis.

9.3 4-fibre design

The 2-fibre design does not allow any static pitch adjustment of the test mass from the penultimate stage above. Manifestation of this fact can be seen in Figure 9.2 where the response vanishes with $1/f^2$ for small frequencies. The test mass orientation is always determined by the vertical line through break-off point and centre of mass. Any lateral shifts of the break-off point will cause a rotation of the test mass. In order to fulfil the requirement for static pitch of the test mass the break-off location needs to be accurate to sub $\pm 10\,\mu$m. One solution to overcome this challenge with an optical lever is presented above. However, it might be useful to gain access to static pitch alignment over the course of the experiment.

Static pitch adjustment of the 1 g ITM from the penultimate stage can be achieved by implementing a 4-fibre design for the monolithic assembly. In this case two fibres are attached

to either side of the test mass similar to the auxiliary suspension and the 100 g ETM suspension. For the 1 g ITM suspension this poses another small challenge. In the case of the penultimate mass the separation between the two cross pieces was chosen to be 3 mm (compare Section 7.2.3) and with the cradle ear width of 2 mm this leaves 500 µm space on either side of the ear to attach a fibre. With a stock diameter of 400 µm these welds could be challenging but will not be impossible. No interference between the thin section of the fibre and the penultimate mass cross can occur, as the fibre neck position was chosen to be 2 mm below centre of mass of the penultimate mass. A computer-aided-design model of two possible fibre configurations at the penultimate mass can be seen in Figure 9.3 Image

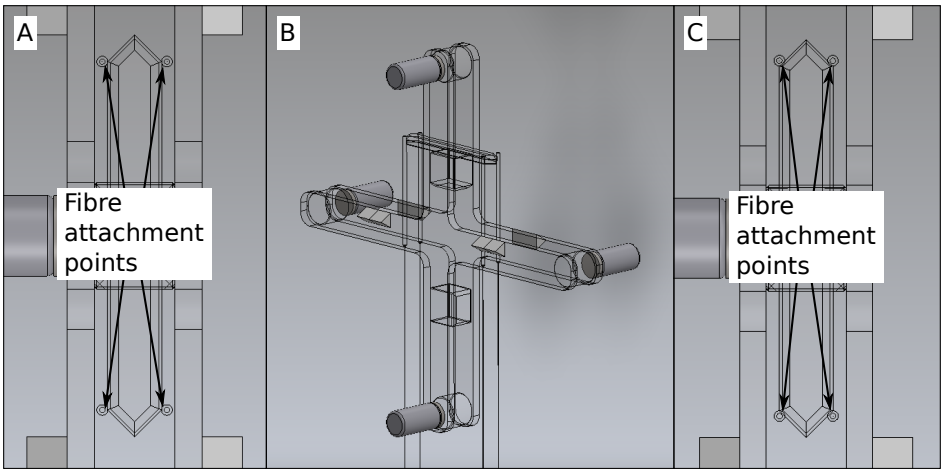

Figure 9.3: Images A and C show two possible 4-fibre configurations in which the fibres are directly welded to the sides of the cradle ear. The fibres are 2.4 mm and 2 mm apart respectively. Image B depicts an isometric view of the penultimate mass in this configuration.

A shows the configuration in which four fibres are welded to the sides of the cradle ear in a top view. The fibres will be separated by 2.4 mm. Allowing for the fibre stock diameter and the ear width, this leaves 100 µm space on either side between stock and cross piece. Image B presents an isometric view of the 4-fibre configuration. Image C depicts a second possible 4-fibre configuration in which the fibres are welded to the cradle ear side faces. For this second configuration the separation between the fibres is chosen to be 2 mm and the fibres are welded on the angled side towards the cradle ear tip leaving 300 µm space between stock and cross piece.

A separate solution involves a two-stage weld process. To further separate the fibres, an additional piece is welded orthogonal to the tip of the ear. This additional piece could be a 10 mm long stock or base material piece. For Figure 9.4 a piece of 2 mm diameter base material was used to create a hammer-head ear tip. Image A shows an isometric view of the penultimate mass in this configuration. Image B depicts a top view of the ear. In this the additional piece of base material can be seen. The resulting attachment points for the fibre are 10 mm apart and thus outside the penultimate mass cross.

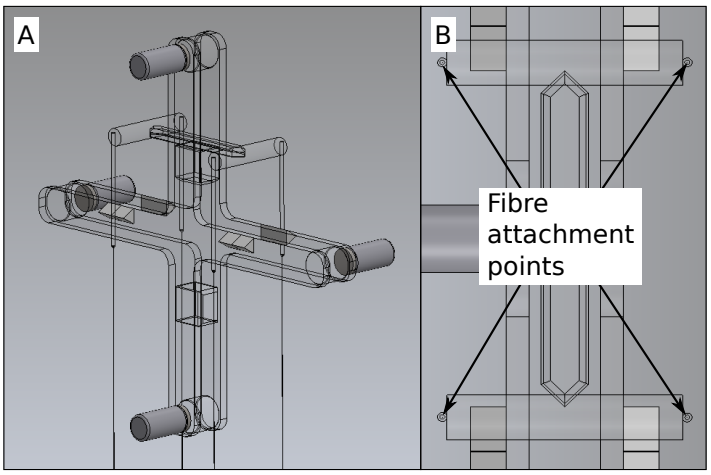

Figure 9.4: Image A shows a possible 4-fibre configuration in which the fibres are welded to an additional part which is welded to the cradle ear tip prior to the fibres. The fibres are 10 mm apart in this configuration. Image B depicts an isometric view of the penultimate mass in this configuration.

9.4 Comparison of 4-fibre configurations

In order to compare the potential candidates for 4-fibre configurations the resulting force transfer functions from penultimate stage excitation to test mass motion are modelled. The cases for 2.4 mm and 2 mm are considered to be closely matched, even though pitch resonances as well as yaw resonances are expected at slightly higher values for the larger separation. The modelling is based on the reduced double pendulum after this approximation was validated above. As the pitch resonance frequencies strongly depend on the fibre separation (set to 2 mm or 10 mm), a first comparison is done with the torque-angle transfer function from pitch excitation at the penultimate stage to test mass pitch motion. It is assumed that separation of the fibres will be the same at the cradle ears of penultimate mass and test mass. Figure 9.5 shows the corresponding transfer functions for the two separations. The blue trace shows the force transfer function of pitch excitation at the penultimate stage to test mass pitch motion for 2 mm separation of the fibres. The highest pitch resonance at about 55 Hz is pitch motion of the penultimate mass. The resonance at about 32 Hz can be associated with pitch of the 1 g test mass. The same transfer function for 10 mm fibre separation is plotted in red. Pitch motion of the penultimate mass can again be observed in the resonance at about 55 Hz. In this case the highest pitch resonance at about 161 Hz can be associated with pitch of the 1 g test mass.

Wire separations between 2.4 mm and 10 mm are not considered as the cross pieces would interfere with the fibre stock. The low frequency (and also static) response for both cases is similar which means both configurations result in equal alignment range. With a lever arm of 21 mm and a simulated response of $0.14\,\mathrm{N\,A^{-1}}$ per coil-magnet actuator a torque of about 194 µN m can be exerted on the penultimate mass. With the simulated force transfer

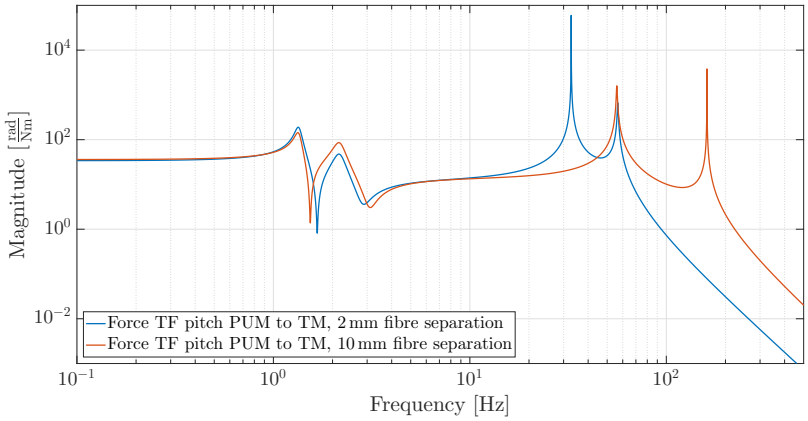

Figure 9.5: The blue trace depicts the force transfer function of pitch excitation at the penultimate stage to test mass pitch motion for 2 mm separation of the fibres. The highest pitch resonance is the pitch of the penultimate mass at about 55 Hz. The same transfer function for 10 mm fibre separation is plotted in red. In this case the highest pitch resonance at about 161 Hz can be associated with pitch of the test mass.

function a range of about ±6.8 mrad can be achieved for both configurations. From the resulting pitch mode frequencies for the cases of 2 mm and 10 mm fibre separation only the 2 mm case fulfils the requirement to not contaminate the measurement band of the Sagnac speed meter experiment.

9.5 4 vs 2 fibres

The impact of this change in the design for the 1 g ITM suspension on the suspension dynamics is summarised in Figure 9.6 where the corresponding force transfer functions from penultimate mass excitation to test mass motion are plotted for both the 2-fibre and 4-fibre cases. In all plots blue depicts the 4-fibre case and red the 2-fibre case. The top left plot shows the vertical displacement transfer function from top suspension point of the double pendulum (which would be equivalent with the upper intermediate mass for the quadruple pendulum) to vertical test mass motion. The bounce mode of the lowest stage is a little higher for the 4-fibre case due to lower stress in the fibres. The higher bounce mode of the penultimate mass is not influenced. The top right plot depicts the force transfer function from longitudinal excitation at the penultimate stage to test mass motion. The highest mode frequency can be associated with longitudinal to pitch coupling and is naturally at a higher frequency for the 4-fibre case. In the bottom left plot it can be seen that the yaw modes are not strongly influenced. The bottom right plot shows the force transfer function from pitch excitation at the penultimate stage to test mass pitch motion. As demonstrated above the 4-fibre case has constant response at towards low frequencies, where the 2-fibre case has decaying response, resulting in no static pitch adjustment from

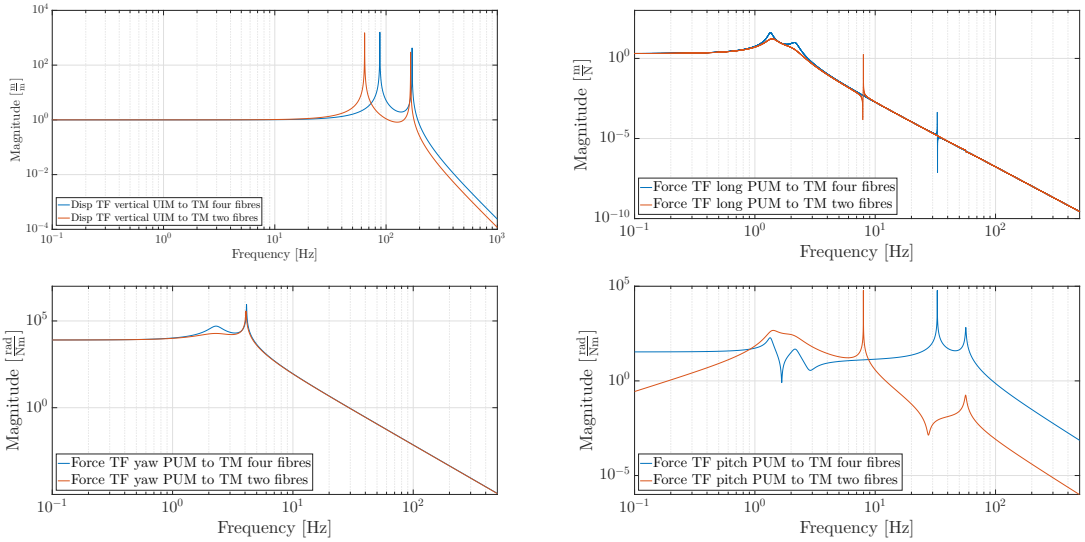

Figure 9.6: The blue trace in all plots depicts the 4-fibre case and the red trace the 2-fibre case. Top left shows the vertical displacement transfer function from upper intermediate mass, or in case of the simulated double pendulum the top suspension point, to test mass motion. In the top right graph the force transfer function from longitudinal excitation of the penultimate mass to longitudinal test mass motion can be seen. The bottom left plot presents the force transfer function for the yaw mode and the in the bottom right plot the same force transfer function for the pitch mode can be seen.

the penultimate stage.

Increasing the number of fibres from which the 1 g test mass is suspended has a negative effect on suspension thermal noise. In Figure 9.7 the suspension thermal noise for the 2-fibre and the 4-fibre case is plotted. In the 4-fibre case more fibre-material is used to suspend the 1 g mirror, resulting in lower stress in the fibre. The effect is twofold with a lower fundamental violin mode and a higher vertical bounce mode of the suspension. It can be seen in the figure that the vertical bounce mode increases by about 25 Hz to about 90 Hz and the fundamental violin mode decreases by about 200 Hz to about 500 Hz compared to the 2-fibre case. In both cases the requirement of a factor 10 below total noise of the Sagnac speed meter is fulfilled for suspension thermal noise.

9.6 Conclusion

In this chapter future developments for the 1 g ITM suspension were presented. The required weld precision in order to place the fibre break-off points poses a significant challenge for the production of the monolithic assembly. Utilising two fibres requires a precision of $\pm 7.7\,\mu m$. As outlined above this precision can be reached in an iterative weld process in which an optical lever is used to verify and measure the static pitch of the test mass. A 4-fibre solution was presented as well and simulations show that this design is within the requirements for the Sagnac speed meter experiment and gives rise to static pitch align-

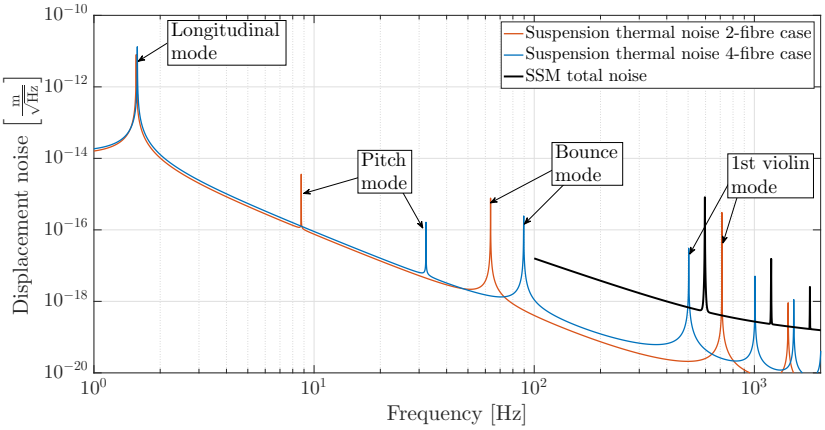

Figure 9.7: Comparison of suspension thermal noise for the 2-fibre and 4-fibre cases. In both cases suspension thermal noise is a factor 10 below design sensitivity of the Sagnac speed meter. In the 4-fibre case the gap between vertical bounce mode and fundamental violin mode is reduced due to lower stress in the fibres.

ment of the 1 g test mass. Suspension thermal noise was estimated for both cases, and it was found that the gap between vertical and first violin mode is reduced for the 4-fibre case.

Chapter 10

Conclusions and future work

Gravitational wave detectors of the 2nd generation will ultimately be limited in their sensitivity by quantum and thermal noise, with quantum radiation pressure noise dominating the low frequency end of the detectors' bandwidth. Research is being conducted in order to further reduce noise sources and improve the detectors' sensitivity. *Speed meters* are proposed to be capable to reduce quantum radiation pressure noise by measuring the velocity of the test masses—equivalent to the momentum, a quantum non-demolition variable—instead of continuously measuring their position [72]. The Glasgow Sagnac speed meter experiment aims to show the reduction of quantum radiation pressure noise in a Sagnac topology compared to Michelson topology with equivalent parameters at audio-band frequencies [76]. The main focus in this thesis was on the development of the optical layout for a bespoke Sagnac speed meter, which included the implementation of a suitable local oscillator for the balanced homodyne detector that is used as readout for the experiment, as well as the development, design, commissioning, and testing of suitable mirror suspensions in order to attenuate seismic ground motion to the desired level.

In Chapter 4 all necessary tools, as well as the foundations of suspension modelling, were highlighted. Due to the $1/f^2$ response above the fundamental resonance frequency, pendulums are used to suspend the test masses in order to attenuate seismic ground motion. Two approaches can be used to derive state space matrices of the pendulum to fully describe the suspension dynamics and allow modelling of displacement transfer functions as well as the force-displacement and torque-angle transfer functions from selected inputs to selected outputs of the model. The displacement transfer functions can be used for an estimation of displacement noise due to seismic ground motion and force-displacement, as well as the torque-angle transfer functions which can be used to characterise the suspension dynamics in measurements of test mass motion due to applied forces on the suspension.

Chapter 5 introduced the *auxiliary suspension*, a double pendulum from which auxiliary mirrors and beam splitters are suspended. These auxiliary suspensions are used to guide

the laser beam through the Sagnac speed meter experiment. As these suspensions are not part of the triangular cavities their displacement requirement was relaxed by the cavity factor to $<8 \times 10^{-15}\,\mathrm{m}/\sqrt{\mathrm{Hz}}$ at 100 Hz taking a safety factor of 10 into account. The multitude of assemblies and the limited space in the vacuum system required a compact design of this type of suspension which was achieved with a single back-plane mount. For further rigidity, auxiliary suspension back-planes can be connected to create a bigger cage with multiple feet. The modelled suspension dynamics were verified in transfer function measurements for the force-displacement and torque-rotation transfer functions in which white noise was injected to the top mass and the motion of the test mass measured with a vibrometer for the longitudinal displacement and in an optical lever setup for the rotational degrees of freedom, yaw and pitch. The model was further investigated in a parameter study as the initial model did not represent the measurement of the suspension dynamics. With the altered model, the longitudinal displacement noise due to seismic ground motion was estimated to about $1 \times 10^{-21}\,\mathrm{m}/\sqrt{\mathrm{Hz}}$ at 100 Hz for coupling from horizontal and $1.5 \times 10^{-17}\,\mathrm{m}/\sqrt{\mathrm{Hz}}$ at 100 Hz for coupling from vertical ground displacement and thus well below the initial requirement.

In Chapter 6 the end test mass suspensions for the triangular cavity, the *100 g ETM suspensions*, are presented. Originally based on a design that was developed in Glasgow for the AEI 10 m prototype, this suspension is a triple pendulum with two stages of vertical blade springs to reduce the fundamental vertical resonance frequencies. The design was altered to accommodate these suspensions in the vacuum system for the Sagnac speed meter experiment. These efforts included re-writing the model to reflect these changes. The final development steps were derived as part of this thesis, including the creation of the monolithic assembly, the production of bonded masses, and the production of the fused silica fibres. Due to the size of the ears, which are the interface between masses and fibres, and the flat surfaces on the 100 g substrates, all cleaning was performed in an ozone atmosphere before the ears were template-bonded to the masses with hydroxide catalysis bonding to create a strong quasi-monolithic connection. All fibres were re-defined in length due to elastic stretch of the fibre and were pulled in a horizontally orientated fibre puller into dedicated fibre-cartridges and roughly characterised to allow choosing of matching sets in terms of average diameter and shape of the thin fibre section, before they were welded to the ears on the masses with a CO_2-laser.

All five monolithic assemblies were built and the first assembly integrated in one 100 g ETM suspension in order to measure the suspension dynamics and validate the model. Due to the triangular cage of the suspension, only torque-angle transfer functions for the rotational degrees of freedom, pitch and yaw, were measured by injecting band limited white noise to the coil-magnet actuators at the top and penultimate mass and sensing the transferred test mass motion with a quadrant photo detector. It was found that the model

had to be further altered and re-defined in order to allow lateral and rotational motion of the vertical blade springs in order to match pitch mode frequencies of the model to the measurement. Additionally it was shown that the 100 g ETM suspension fulfils the requirement on displacement noise due to seismic ground motion as well as requirements for suspension thermal noise of the monolithic lowest stage.

Chapter 7 introduced the input test mass suspension for the triangular cavity in the Sagnac speed meter experiment; the *1 g ITM suspension* that build the core of this experiment as they allow limitation by radiation pressure noise. Starting from the demand of utilising the same top mass as well as vertical blade springs at the top suspension point and top mass[1], it was found that a fourth pendulum stage was required in order to allow damping of motion from the 1 g test mass. A 4 g penultimate mass was developed that allowed introduction of coil-magnet actuators that are used in a switchable passive damping system and as actuators around the penultimate mass.

The investigations on this system were published [134] and can be found as Chapter 8 in this thesis. The design for all four masses was explained and ANSYS simulations on structural mode frequencies undertaken and the viability of the designs was shown for the test and penultimate mass. In all cases the required tooling was developed for the creation of test and penultimate mass as well as for the creation of the monolithic assembly and was ultimately used to build a first prototype with glue joints (Masterbond EP30-2) between the ears and fibres. The 1 g ears were bonded to test and penultimate mass with hydroxide catalysis bonding. Similar to the fibres for the 100 g ETM suspensions the fibres for the 1 g ITM suspension had to be re-defined, were pulled into similar fibre-cartridges in the same fibre puller and characterised to allow selection of fibre sets based on average diameter and general shape of the fibres thin section.

A procedure for welding of the fibres to the ears of test and penultimate mass was developed and tested together with initial weld tooling. This approach was used for the first glued 'monolithic' assembly. To protect the masses during welding and to prevent damage to the 1 g substrates, sophisticated all-metal mass caps were developed and determined their parameters in ANSYS® simulations.

Initially designed with two fibres, the monolithic assembly requires a demanding precision on the fibre break-off points on the test mass of ± 7.7 µm. In the initial design considerations it was assumed that misalignments could be compensated by the dynamic range of the 100 g ETM suspension, however, recently the demand for control of the 1 g ITM arose and a two fibre design does not allow static adjustments of the test mass. The torque-angle and force-displacement transfer functions were presented and the longitudinal displacement noise

[1] These blade springs are at the threshold for manufacturing and cannot be made smaller or thinner to support smaller masses.

due to seismic ground motion estimated which showed the fulfilment of the set requirement of $<1.5 \times 10^{-18}\,\mathrm{m}/\sqrt{\mathrm{Hz}}$ at 100 Hz.

Chapter 8, published as Reference [134], summarises the investigations on a switchable passive damping system for the 1 g input test mass suspensions in the Sagnac speed meter experiment. The demand for passive damping of the test mass introduces a limiting noise source in form of thermal noise due to viscous damping. In order to overcome this limitation a switchable passive damping system was developed and tested on a modified auxiliary suspension. Instead of copper, the non-conductive material polyether ether ketone is used for the formers on which the coils of coil-magnet actuators are wound. In case of a closed coil loop around the magnets damping arises from induced eddy currents in the conductive copper wire material when the magnet moves inside the coil. Introducing a big resistance between the coil ends or leaving them open reduced the damping constant significantly. In ring-down measurements of the yaw and pitch mode on an auxiliary suspension it was shown that reductions in the damping factor of 8 and 5, respectively, are possible which is in agreement with theoretical calculations. Additionally, a possible optimisation of damping dependent on frequency was presented which does not find application in the scope of this thesis or more general suspension design.

In Chapter 9 a possible iterative welding procedure for the two-fibre design is highlighted with which the required weld precision could be achieved. In this procedure the precision of the welds can be inferred by measuring the pitch of the mass in an optical level setup and modifications can be done by re-heating and shifting fibre stock after the mass is caught again in its weld tool. An alternative four-fibre design for the monolithic 1 g assembly of the 1 g ITM suspension is presented and compared to the initial two-fibre design. It was shown that the introduction of four fibres is in general possible, even though challenging from a mechanical point of view due to limited space around the penultimate mass ear. It was further presented that with the simulated torque-angle transfer function and simulated response of the coil-magnet actuators at the penultimate mass, a four fibre design allows static rotational adjustments in pitch of the test mass of ± 6.8 mrad. In addition it was verified that a four fibre design does not impose limitation due to either suspension thermal noise or longitudinal displacement noise due to seismic ground motion on the 1 g ITM suspension.

The work presented in this thesis is essential for the success of the Sagnac speed meter experiment as well as the AEI 10 m prototype. The development of the different types of suspensions for the Sagnac speed meter experiment will ultimately enable a measurement in a Sagnac speed meter topology to show the reduction of quantum radiation pressure noise at audio-band frequencies. The technology developments on the 100 g monolithic assembly will find application in the 100 g suspensions for the AEI 10 m prototype and help to achieve a sub-SQL measurement. The 1 g ITM suspension and the 100 g ETM suspen-

sion could also find application in other opto-mechanical experiments in the mass regime between 1 g and 100 g.

For the Sagnac speed meter experiment it is planned to to implement all monolithic assemblies in the 100 g suspension cages and to characterise their dynamics in the way presented in this thesis in the near future. In parallel the 1 g welding procedure will be further developed in a slightly modified weld tooling that allows introduction of the CO_2-laser at the correct height and accommodates additional fume extractors to prevent silica vapours settling on the sides of the 1 g substrate. Once the 1 g monolithic assemblies are built they will be implemented in the 1 g ITM suspension cages and characterised similar to the 100 g ETM suspensions in an optical lever set up to measure the suspension dynamics. The first triangular cavity will be commissioned shortly after in which the control schemes essential for the operation of the Sagnac speed meter experiment, developed in Reference [117], will be tested. The developed suspensions will ultimately allow a measurement of reduced quantum radiation pressure noise in a Sagnac speed meter topology.

Appendix A

Phase representation

In order to present the phases in the measurements shown in Chapter 5 and Chapter 6 in a clear way, the phase data was shifted by -90 deg, unwrapped and shifted by +180 deg, and re-wrapped. The effective shift in phase is in this case +90 deg and the unwrapping and re-wrapping of the phase allows to eliminate noise features. The procedure is here shown in an example for the torque-angle transfer function from penultimate mass excitation to test mass motion for the 100 g ETM suspension as depicted in Figure 6.38 and here plotted again without the simulated curves in Figure A.1.

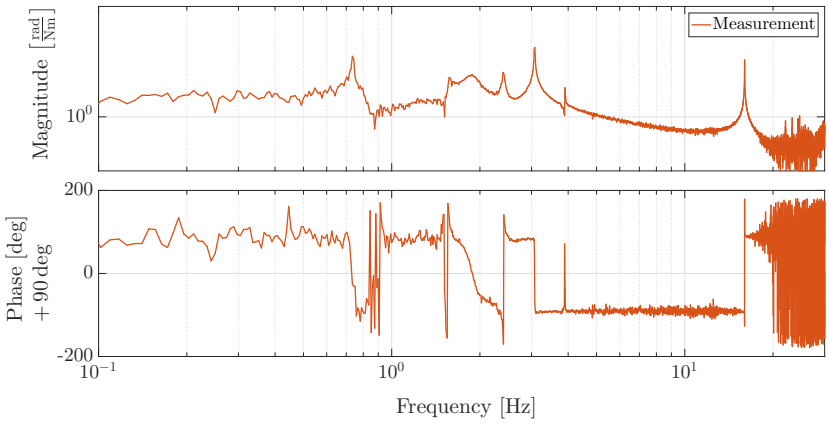

Figure A.1: The emphasis in the figure is on the phase. It can be seen that the phase is represented in a clean way, though it it shifted by 90 deg and thus does not show the "real" phase. The phase shift is done in order to avoid phase jumps due to noise on the phase data.

The original measurement data is shown in Figure A.2, where it is possible to see that the measured raw data is contaminated by noise at low frequencies, where the phase jumps from +180 deg to -180 deg and vice versa. These jumps are due to phase changes (noise in the measured data) around the levels +180 deg and -180 deg, where +180 deg equals -180 deg and whenever 180 deg is exceeded in either limit a jump to the inverted part is made to stay within the boundaries. The way to get around these phase jumps, is to shift the phase

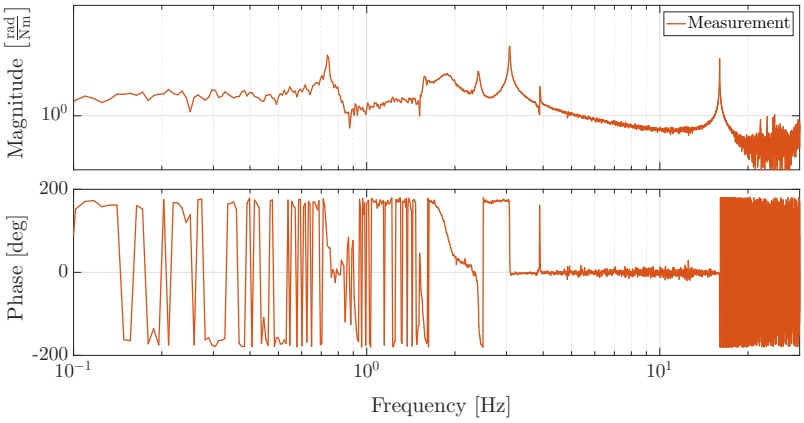

Figure A.2: The phase in this figure is shown as it was measured. At lower frequencies the phase is jumping a lot between +180 deg and -180 deg and it seems impossible to identify the real behaviour.

data by 90 deg, thus shifting the level at which jumps are to be made. Then the noisy data lies centrally in between +180 deg or -180 deg and 0 deg and phase jumps are avoided. The phase is unwrapped in order to unfold and clean it and re-wrapped to push it back into the boundaries. For the re-wrapping the same holds as before. If the data is not shifted by 90 deg, phase jumps occur again due to noise on the data near +180 deg or -180 deg. An example can be seen in Figure A.3, where the phase was not shifted during re-wrapping.

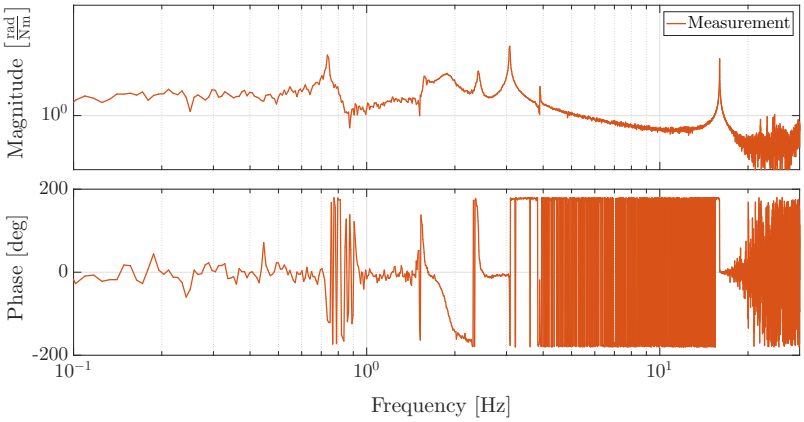

Figure A.3: For this figure the phase was not shifted prior to re-wrapping it. As the area between the resonances is meant to be at +180 deg, but shows a lot of noise, the phase is constantly jumping between +180 deg and -180 deg.

Comparing the region between the two main pitch modes from about 3 Hz to 15 Hz, it can be seen from Figure A.1 and Figure A.2 that some noise is visible on the phase. Re-wrapping that area without a phase shift results in the multitude of phase jumps, observable in Figure A.3. This is the reason why, throughout this theses, phases are represented with an offset as “phase+90 deg”.

Appendix B

Suspension modelling and parameters

B.1 Example of the Lagrangian approach

This short example will illustrate the way from the Lagrangian formulation of a suspended mass towards a state space model. The more detailed version of this example can be found in [101]. For the initial Lagrangian calculations it was assumed to have an independent set of generalised coordinates (here called x) to describe the motion of the pendulum. In a more practical view two different classes of coordinates become interesting. On the one hand there are position/orientation coordinates from the connection of the pendulum to the supporting structure s (which are fixed, but can be treated movable for transfer function calculations), and on the other hand so called floating coordinates that describe the movement of connections between elastic elements, such as wires q. Now consider a mass suspended by two connected springs with spring constants k_1 and k_2 as can be seen in Figure B.1. The new set of coordinates can be seen from the figure where s is the connection

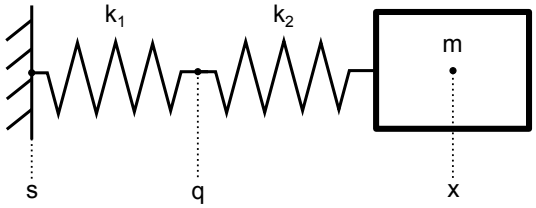

Figure B.1: A mass suspended by two coupled springs k_1 and k_2. Additional coordinates s and q are introduced to describe the system.

point towards mechanical ground, q is the coordinate of the movement of the connection point of the two springs and x is the movement of the COM of the mass. The potential energy of this system is

$$E_{\text{pot}} = \frac{1}{2}k_1(q-s)^2 + \frac{1}{2}k_2(x-q)^2. \tag{B.1}$$

From this we can deduce the potential master matrix

$$\mathbf{P} = \begin{pmatrix} \mathbf{K} & \mathbf{C}_{\mathrm{XQ}} & \mathbf{C}_{\mathrm{XS}} \\ \mathbf{C}_{\mathrm{QX}} & \mathbf{Q} & \mathbf{C}_{\mathrm{QS}} \\ \mathbf{C}_{\mathrm{SX}} & \mathbf{C}_{\mathrm{SQ}} & \mathbf{S} \end{pmatrix} = \begin{pmatrix} k_2 & -k_2 & 0 \\ -k_2 & k_1 + k_2 & -k_1 \\ 0 & -k_1 & k_1 \end{pmatrix}, \tag{B.2}$$

where $\mathbf{C}_{\mathrm{QX}} = \mathbf{C}_{\mathrm{XQ}}^{\mathrm{T}}$ etc. describe the cross coupling from one class of coordinates to the other and $\mathbf{K}$, $\mathbf{Q}$ and $\mathbf{S}$ describe the interactions in one class of coordinates while fixing the other two. In this the raw stiffness (mass) matrix $\mathbf{K}$ is only equal to the second spring, since all other coordinated (s and q) were assumed to be fixed. The according effective stiffness matrix, in which q is allowed to "float", can be calculated by

$$\mathbf{K}_{\mathrm{eff}} = \mathbf{K} - \mathbf{C}_{\mathrm{XQ}}\mathbf{Q}^{-1}\mathbf{C}_{\mathrm{QX}} = (k_2) - \left(\frac{k_2^2}{k_1 + k_2}\right) = \left(\frac{k_1 k_2}{k_1 + k_2}\right). \tag{B.3}$$

The coupling between support structure and the mass, $\mathbf{C}_{\mathrm{XS}}$, is zero, which indeed is not the case. The action of the two springs can be implemented and the effective matrix is

$$\mathbf{C}_{\mathrm{XS(eff)}} = \mathbf{C}_{\mathrm{XS}} - \mathbf{C}_{\mathrm{XQ}}\mathbf{Q}^{-1}\mathbf{C}_{\mathrm{QS}} = (0) - \left(\frac{(-k_2)(-k_1)}{k_1 + k_2}\right) = \left(\frac{-k_1 k_2}{k_1 + k_2}\right). \tag{B.4}$$

Similarly to the mass stiffness matrix the support structure stiffness matrix needs correction, since it is only dependent on the first spring. The effective value is found by

$$\mathbf{S}_{\mathrm{eff}} = \mathbf{S} - \mathbf{C}_{\mathrm{SQ}}\mathbf{Q}^{-1}\mathbf{C}_{\mathrm{QS}} = (k_1) - \left(\frac{k_1^2}{k_1 + k_2}\right) = \left(\frac{k_1 k_2}{k_1 + k_2}\right). \tag{B.5}$$

The kinetic energy in the system is

$$E_{\mathrm{kin}} = \frac{1}{2} m v^2 \tag{B.6}$$

and thus the mass matrix becomes

$$\mathbf{M} = (m) \tag{B.7}$$

The state space matrices can be calculated from

$$\mathbf{A} = \begin{pmatrix} \mathbf{0} & \mathbf{I} \\ \mathrm{Re}(-\mathbf{M}^{-1}\mathbf{K}_{\mathrm{eff}}) & \frac{\mathrm{Im}(-\mathbf{M}^{-1}\mathbf{K}_{\mathrm{eff}})}{2\pi f} \end{pmatrix}, \tag{B.8}$$

$$\mathbf{B} = \begin{pmatrix} \mathbf{0} & \mathbf{0} \\ \mathrm{Re}(-\mathbf{M}^{-1}\mathbf{C}_{\mathrm{XS(eff)}}) & \mathbf{M}^{-1} \end{pmatrix}, \tag{B.9}$$

$$\mathbf{C} = \begin{pmatrix} \mathbf{I} & \mathbf{0} \\ \mathrm{Re}(-\mathbf{C}_{\mathrm{SX(eff)}}) & \mathbf{0} \end{pmatrix}, \tag{B.10}$$

$$\mathbf{D} = \begin{pmatrix} \mathbf{0} & \mathbf{0} \\ \mathbf{S}_{\mathrm{eff}} & \mathbf{0} \end{pmatrix}. \tag{B.11}$$

For chosen inputs $(s, f_\mathrm{x})^\mathrm{T}$ (displacement s of the structure and force f_x on mass) and outputs $(x, f_\mathrm{s})^\mathrm{T}$ (displacement x of mass and force f_s back on structure) the state space equations become

$$\begin{pmatrix} \dot{x} \\ \ddot{x} \end{pmatrix} = \begin{pmatrix} 0 & 1 \\ \frac{-k_1 k_2}{m(k_1+k_2)} & 0 \end{pmatrix} \begin{pmatrix} x \\ \dot{x} \end{pmatrix} + \begin{pmatrix} 0 & 0 \\ \frac{-k_1 k_2}{m(k_1+k_2)} & \frac{1}{m} \end{pmatrix} \begin{pmatrix} s \\ f_\mathrm{x} \end{pmatrix}, \tag{B.12}$$

$$\begin{pmatrix} x \\ f_\mathrm{s} \end{pmatrix} = \begin{pmatrix} 1 & 0 \\ \frac{k_1 k_2}{k_1+k_2} & 0 \end{pmatrix} \begin{pmatrix} x \\ \dot{x} \end{pmatrix} + \begin{pmatrix} 0 & 0 \\ \frac{-k_1 k_2}{k_1+k_2} & 0 \end{pmatrix} \begin{pmatrix} s \\ f_\mathrm{x} \end{pmatrix}. \tag{B.13}$$

The method of defining a master potential matrix, obtaining effective matrices and from these the equations of motion as well as state space equations is also valid for more complicated systems such as multi stage pendulums as used for suspensions.

B.2 Auxiliary suspension parameters

Part	Parameter	Value
Top Mass	Mass	75.4 g
	Material	Aluminium
	I_x	16 053.6 g mm^{-2}
	I_y	7338.8 g mm^{-2}
	I_z	12 080.2 g mm^{-2}
	Wire separation (y)	39 mm
	Break-off point upper	5.5 mm
	Break-off point lower	5.5 mm
	Number of suspension wires	2
Test Mass	Mass	75.9 g
	Material	Stainless steel
	I_x	23 551.2 g mm^{-2}
	I_y	12 590.9 g mm^{-2}
	I_z	13 173.0 g mm^{-2}
	Wire separation (x)	4 mm
	Wire separation (y)	43 mm
	Break-off point	2.5 mm
	Number of suspension wires	4
Suspension wire	Material	AISI302
	Diameter	50 µm
	Length upper	100 mm
	Length lower	150 mm
Mirror	Material	UV-FS
	Diameter	30 mm
	Thickness	6 mm
	HR-coating	T_s = 1000 ppm

Table B.1: Design parameters of auxiliary suspensions.

Appendix C

Procedures

In this appendix all procedures for the creation of the 100 g and 1 g monolithic assemblies can be found. Section C.1 describes the pulling procedure for the fibres used in both monolithic assemblies. In Section C.2

C.1 Fibre pulling procedure

Both fibre geometries for either 100 g or 1 g monolithic assembly, were pulled in the same fibre puller. The procedure here can be applied for either with the difference in the 2nd stage pull.

1. Switch on computer
2. Switch on power supply for laser cooling
3. Switch on power supply for laser
4. Switch on power socket for LabView® equipment
5. Start LabView® program on computer
   "0Short Fibre Puller_acceleration & Time File_Summer2014.vi"
6. Load velocity profile for 1st-stage-pull — XX = version number
   "Desktop\Velocity Profiles\Two Stage\AEI_100g\Stage1\2stage1\vXX"
7. Set TL max vel to 0.8 for first stage pull
8. Move weld mirror +19 mm (TL Target Absolute Position)
9. If cartridge was removed, move weld mirror stage with left stage controller into place -> move until corner of stage and mark line up

10. Wear clean gloves and keep them clean
11. Cut 7.5 cm stock material
12. Wipe with Isopropanol/Methanol
13. Introduce stock to right collet and move in until 2-3 cm stock stick out
14. In program set “Newport Absolute Position” to -180 mm
15. Using both index fingers pull stock out of right collet and introduce to left collet -> Stock in both collets and ends not visible is the goal
16. Softly tighten the two nuts on the chucks
17. Only as far as you can feel a resistance
18. Using both hands tighten both nuts simultaneously
19. Tighten only hand-tight and do not use too much force
20. Switch on hoover, move hoover to next door and place exhaust close to stock 2 cm
21. Make sure correct velocity profile is loaded in program
22. Start at 50% laser power and slowly ramp up power
23. Do not rush things, power sometimes need to settle (thermodynamics)
24. When stock lights up bright keep power constant and start pull in program
25. Switch off laser when finished - lamp on stage controller off
26. Move exhaust out of way
27. Set “TL relative displacement” to -19 mm
28. Set “TL max vel” to 0.5
29. Load velocity profile for 2nd stage pull
30. Re-introduce exhaust 3-4 cm away
31. Start at 20% laser power and slowly ramp power up
32. When stock lights up again start pull in program
33. Turn off laser immediately after stage active light is off

34. Set “TL relative displacement” to 40 mm
35. Move weld mirror further with left stage controller on bench
36. Move as far as blue and silver parts become visible on right side of that stage (see picture next slide)
37. Introduce side rails
38. Far side first only hand tight
39. Near side second and watch for de-stress fibre
40. Use green marked Allen key to tighten rails
41. STOP program
42. Loose screws/chucks
43. Hold cartridge tight and move to left -> this shifts the stage but is ok
44. Take out cartridge and transfer to profiler
45. Switch off laser
46. Switch off hoover
47. Switch off all power

C.2 100 g procedures

In this section the necessary procedures for preparation, cleaning, bonding and welding of the parts for the 100 g monolithic assemblies are listed. These can be taken as a rough guideline, but should be revisited before blindly followed.

C.2.1 Mass cap procedure 100 g

1. Unpack substrate and inspect for dust and other contaminations under high power light (if no contamination or dust proceed to step 4)
2. Drag-wipe contaminated surface and watch for methanol residue and remove with second drag-wipe if necessary
3. Clean barrel of substrate and remove any marks left for indication of surface (remember which surface is which)

4. Screw rods onto mass cap (use pliers for final bit)
5. Screw adapter plates on both mass caps
6. Carefully check mass cap with rods for dust with high power light (wipe with methanol if necessary)
7. Carefully check mass (coatings etc.) again for dust particles under high power light
   (a) In case of dust use drag-wipe method to remove
   (b) Ideally use lens tissue for cleaning with methanol
8. Place mass down with HR surface down to cap (without hole)
   (a) Make sure the flats line up with edges of adapter plate
   (b) ... and are parallel (easiest to put against one adapter plate)
9. Check other mass cap and AR surface of mass for dust with high power light
10. Place other cap onto mass and reference to adapter plate same side
11. Tighten up M3 screws in rods (make sure cap does not slide)
12. Remove all adapter plates and put them to the side

C.2.2 Ozone cleaning procedure 100 g

1. Make sure ozone meter was continuously running for at least 2 h prior to cleaning
2. Set up ozone chamber in flow-bench
3. Attach ozone bulb to fitting
4. Connect power supplies (switched off) for ozone creation and termination UV bulb
5. Check inside of chamber for dust and exchange aluminium foil layer
6. Arrange double shield and check metal fan
7. Place 100 g substrates in mass caps with PEEK screw-cap on the aluminium foil
8. Place 100 g ears in small foil pouches with bonding surface pointing upwards
9. TAKE NOTE OF POSITION AND SERIAL-NUMBERS FOR EARS AND MASSES
10. Place lid on double shield

11. Close chamber and attach drill with full battery to metal fan
12. Switch on ozone-creating UV bulb, check bulb is 'on', and run drill on highest power for 11 min
13. Switch off ozone-creating bulb and switch on ozone-terminating bulb
14. WAIT 15 min
15. Switch off ozone-terminating bulb
16. Use ozone meter to verify safe ozone level in box using BNC connector opening on chamber
17. Open box, remove lid and take out parts, wrapping and labelling correspondingly before transfer to SRDG-lab

C.2.3 Bonding procedure 100 g

1. Prepare bonding solution and set pipette (0.2ul)
2. Put mass on V-block and make sure both aluminium caps rest on V-block (NOT THE MASS ITSELF!)
3. Final wipe with methanol bonding side and check for dust with high power light
4. Final wipe of bonding template with methanol and check for dust with high power light
5. Place bonding reference plate - spacer first, then actual bonding template
    (a) Reference to legs and edge furthest away from the ear
6. Final wipe tweezers with methanol and check for dust with high power light
7. Pour methanol on gold wipe
8. Pick up ear with tweezers and carefully drag across wipe with methanol
9. Check for dust with high power light
10. 2nd person in parallel:
11. pipette 0.2ul of bonding solution
12. Person 1 has ear ready near mass with tweezers

13. Person 2 applies bonding solution to mass
14. Person 1 puts down ear and gently touches in position on horn furthest away from reference corner
15. !!! DO NOT BREATH ON IT !!!
16. !!! WAIT FOR 1 HOUR !!!
17. Touch ear with tweezers to see if it is fixed

For test mass:

1. Unscrew reference plate
2. Slide to other side and remove template

For penultimate mass:

1. Tilt mass until mass cap hits V-block
2. Prepare glue (mix on scale 10:1 mass ratio - avoid incorporating bubbles)
3. Wipe prism and tweezers with methanol and check for dust with high power light
4. Pick up prism with tweezers on end faces
5. Apply glue to prism with pointy tool (to be re-defined)
6. Put prism down in template
7. Shift prism in position and press down for a couple of seconds
8. Leave over night to cure or place in oven at 40 °C and bake for 2 hours

C.2.4 Weld procedure 100 g

The weld procedure is kept in a separate document and is edited during the weld-procedure to add notes and go through the procedure step-by-step. Pictures taken are noted corresponding to their number on the DSLR. The "??" in the procedure are to be filled with corresponding positions and mass and fibre serial numbers that are used for the corresponding assembly.

Preparations

1. Bring test mass jack up by 1.5 mm
2. Turn welding bench by 180°, so that fan sits on the left
3. Get top piece out and connect it top plate at welding jig
4. Install top plate of welding jig
5. Install test mass. HR coating (NO screw cap) in direction of the bigger hole of top plate. Clamp it. MASS NUMBER USED = ??
6. Re-install bridge holder for upper mass
7. Insert upper/penultimate mass and clamp it. UPPER MASS NUMBER USED = ??
8. Measure horn to horn separation. (should be 204.3 mm)
9. Install 4 weld mirror at test mass level
10. Check for all weld mirrors that they do not touch the ear
11. Install 4 weld mirror at upper mass level
12. Check for all weld mirrors that they do not touch the ear

Fibre 1

1. Set up tweezer-setup for cutting fibre (setup A)
2. Bring up fibre cartridge holding jack to upper position = 104 mm
3. Set vapour extraction tubes to correct height
4. Take fibre out of fridge. USED FIBRE NUMBER = ??
5. Install fibre so that good end (short one) is down and fix it
6. Connect vapour extraction hoses to cutting jig
7. Check that lower neck is at 8 mm on ruler
8. Check that upper neck is at 200 mm
9. Bring tweezers in and clamp fibre at top and bottom
10. Cut fibre at ??mm to give 7-8 mm of stock.

11. Cut fibre at ??mm to give 7-8 mm of stock at top.
12. Take photographs to determine actual length of fibre and calculate how many turns we should have
13. Fully retract tweezers.
14. Slide tweezers with fibre into welding setup, position A. using guide rods and fix with wing nuts.
15. Install weld camera at top
16. Connect vapour extraction hoses to weld structure top and bottom
17. Weld 1: Top left
18. Install weld camera and laser head at bottom
19. Weld 2: Bottom left
20. Open tweezer at top and remove
21. Open tweezer at bottom and remove

Fibre 2

1. Setup tweezer setup for cutting, setup A
2. Take fibre out of fridge. USED FIBRE NUMBER = ??
3. Install fibre so that good end (short one) is down and fix it.
4. Bring tweezers in and clamp fibre at top and bottom.
5. Connect vapour extraction hoses to cutting jig.
6. Check that lower neck is at 8 mm on ruler.
7. Check that upper neck is at 200 mm.
8. Cut fibre at ??mm to give 7-8 mm of stock.
9. Cut fibre at ??mm to give 7-8 mm of stock at top.
10. Take photographs to determine actual length of fibre and calculate how many turns we should have
11. Fully retract tweezers

12. Connect vapour extraction hoses to weld structure top and bottom
13. Install weld camera and laser head at top
14. Switch on the fan.
15. Slide tweezers with fibre into welding setup, position A. using guide rods and fix with wing nuts.
16. Weld 1: Top left
17. Install weld camera and laser head at bottom
18. Weld 2: Bottom left
19. Fan off.
20. Open tweezer at top and remove
21. Open tweezer at bottom and remove

Fibre 3

1. Disconnect fan, remove weld camera, disconnect vapour extraction hoses
2. Unclamp weld structure and turn Welding setup by 180 (so that fan is on the right)
3. Check welding mirrors at top and bottom do not touch the ears.
4. Setup tweezer setup for cutting, position A
5. Bring down fibre cartridge holding jack to lower position = 62 mm
6. Take fibre out of fridge. USED FIBRE NUMBER = ??
7. Install fibre so that good end (short one) is on top and fix it.
8. Bring tweezers in and clamp fibre at top and bottom.
9. Connect vapour extraction hoses to cutting jig
10. Cut fibre at ??mm to give 7-8 mm of stock
11. Cut fibre at ??mm to give 7-8 mm of stock at top
12. Take photographs to determine actual length of fibre and calculate how many turns we should have

13. Fully retract tweezers
14. Bring fibre from cutting setup to welding setup, position B, which involves an inversion of the tweezers.
15. Connect vapour extraction hoses to weld structure top and bottom
16. Install weld camera and laser head at top
17. Weld 1: Top right
18. Install weld camera and laser head at bottom
19. Weld 2: Bottom right
20. Open tweezer at top and remove
21. Open tweezer at bottom and remove

Fibre 4

1. Setup tweezer setup for cutting, setup A
2. Take fibre out of fridge. USED FIBRE NUMBER = ??
3. Install fibre so that good end (short one) is on the top and fix it.
4. Bring tweezers in and clamp fibre at top and bottom.
5. Connect vapour extraction hoses to cutting jig
6. Cut fibre at ??mm to give 7-8 mm of stock
7. Cut fibre at ??mm to give 7-8 mm of stock at top
8. Take photographs to determine actual length of fibre and calculate how many turns we should have.
9. Fully retract tweezers
10. Connect vapour extraction hoses to weld structure top and bottom
11. Install weld camera and laser head at top
12. Switch on the fan.
13. Bring fibre from cutting setup to welding setup, position B, which involves inversion of the tweezers

14. Weld 1: Top left
15. Install weld camera and laser head at bottom
16. Weld 2: Bottom left
17. Fan off.
18. Open tweezer at top and remove
19. Open tweezer at bottom and remove
20. Remove tweezer setup and also suction tubes to get as much space as possible around the assembly.

Fibre guards + Extraction

1. Retract 4 welding mirrors at upper mass
2. Retract 4 welding mirror at test mass
3. Bring test mass jack down by 1.5 mm
4. Everyone cleans gloves and makes sure facemasks are well fitted.
5. Open fibre guard storage box under flow box
6. Bring in both fibre guards from the sides. Best down by two people so the they slot in well on top rail and the gap at test mass holder.
7. Install middle fibre guard opener at HR side and tighten it.
8. Loosen top plate to give more play and ensure fibreguards really hold the masses.
9. Install fibre guard lock at AR side.
10. Retract mass clamps at top and bottom of welding structure to free TM and PUM.
11. Drop bridge holding PUM (by undoing single screw)
12. Lift out monolithic assembly as straight and vertical as possible.
13. Install top fibre guard openers on AR side.
14. Remove top plate from assembly.
15. Carry assembly over to flow box and screw into transport box.
16. Inspect welding mirrors and get them clean or re-coated for next assembly.

C.3 1 g procedures

C.3.1 Bonding procedure 1 g

Bonding:

1. Check bonding template base for dust
2. Inspect ear for dust (side with smaller chamfers is bonding surface — marked with pencil)
3. Lay down on PEEK base
4. Use PEEK clamp to push in position and align
5. Fix PEEK clamp with screw
6. Check alignment of ear (any tilt?)
7. Final wipe of bonding surface with high grade Methanol
8. Inspect for dust once more
9. Take appropriate Perspex template and check for dust
10. Place Perspex template and push through dowel pins from top (Take care not to hover over ear)
11. Check for dust
12. Take PUM mass with tweezers / TM with fingers
13. Final wipe with methanol and inspect for dust
14. Pipette 0.2uL bonding solution on ear as central as possible
15. Pick up mass with tweezers / fingers
16. Drop mass onto ear and push into top left corner by pushing on bottom right (Careful with TM as only two small alignment points — check for rotation)

WAIT FOR 1H AND DO NOT MOVE OR TOUCH BONDING TEMPLATES

Removal and Storage:

1. Remove PEEK clamp
2. Slide out bonded assembly

For penultimate mass square:

1. Leave to cure

For test mass:

1. Inspect mass caps for dust
2. Inspect mass cap template for dust
3. On clean wipe: Drag wipe (high grade methanol) both TM surfaces and inspect for dust
4. Place lower mass cap on template and align to dowel pins
5. Place bonded TM on template and slide towards mass cap
6. Place top mass cap on template (screws attached) and slide towards TM
7. Push all three together against dowel pins and tighten screws
8. Attach final assembly to L-clamp with screws
9. Leave to cure

C.3.2 Assembly procedure 1 g PUM

Bottom and top cross are assembled independently. The final assembly step in which the top cross will be glued to the bottom cross with EP30-2 is performed post-welding in the weld jig and will be described in the weld procedure that yet has to be fully defined.

Bottom cross assembly:

1. Inspect baseplate and templates for dust under high power light
2. Final wipe of recesses and templates with high-grade Methanol
3. Insert M6 dowel pins to attach cross template
4. Insert square block, bonded square block and spacer rods in recesses
5. Attach cross template
6. Use pipette-tip to attach small glue dots (EP30-2) to surfaces of spacer rods and square blocks

7. Introduce cross piece and align to template
8. Gently push on centre of cross piece and watch for bubbles in glue
   (in case of bubbles push on glue joint to push out bubbles)
9. Leave for initial cure for at least 12 h, preferably 24 h
10. Remove cross template
11. Attach spacer and prism template (ear is **not** covered by template)
12. Use tweezers to hold prism and attach small dot of EP30-2 with pipette tip to surface on prism
13. Place prism in recess and align to bottom left corner
14. Gently push down with tweezers
15. Leave for initial cure for at least 12 h, preferably 24 h
16. Carefully remove metal template and spacer template
17. Attach magnet template to glue magnets vertically (on cross ends that host square blocks)
18. Prepare magnets by attaching a stand-off disc (3 mm × 0.5 mm) to a 3 mm × 6 mm magnet and making the disc concentric
19. Attach small dot of EP30-2 to the stand-off disc
20. Place magnet assembly on cross piece and align to template
21. Leave for initial cure for at least 12 h, preferably 24 h
22. Carefully remove magnet template
23. Remove assembled bottom cross and store with cross piece/magnets on wipe

Top cross assembly:

1. Inspect baseplate, cross reference plate, and templates for dust under high power light
2. Final wipe of recesses and templates with high-grade Methanol
3. Insert M6 dowel pins to attach cross template
4. Attach cross reference (same size as baseplate) onto baseplate

5. Align cross piece to cross reference plate
6. Attach spacer and prism template (opposite side to cross alignment reference)
7. Use tweezers to hold prism and attach small dot of EP30-2 with pipette tip to surface on prism
8. Place prism in recess and align to top left corner
9. Gently push down with tweezers
10. Leave for initial cure for at least 12 h, preferably 24 h
11. Carefully remove metal template and spacer template
12. Attach magnet template to glue magnets horizontally (on cross ends that host prisms)
13. Prepare magnets by attaching a stand-off disc (3 mm × 0.5 mm) to a 3 mm × 6 mm magnet and making the disc concentric
14. Attach small dot of EP30-2 to the stand-off disc
15. Place magnet assembly on cross piece and align to template
16. Leave for initial cure for at least 12 h, preferably 24 h
17. Carefully remove magnet template
18. Remove assembled bottom cross and store with cross piece on wipe

C.3.3 Integration of 1 g monolithic assembly

1. Remove ECD assembly with lower bar from suspension cage
2. Remove horizontal/vertical adjusters from ECD assembly
3. Attach cap removal tool to cross holder on one horizontal/vertical adjuster
4. Retract fully in horizontal direction
5. Introduce this horizontal/vertical adjuster with cap removal tool back into ECD assembly on short side
6. Attach weld jig with welded 1 g monolithic assembly to bar holder on second horizontal/vertical adjuster
7. Remove fibre guard

8. Retract fully in horizontal direction
9. Introduce weld jig with adjuster back in ECD assembly to long side
10. Introduce populated ECD assembly into suspension cage — beware of wire loops
11. Adjust horizontal position of weld jig until in nominal position
12. Adjust height of weld jig to allow wire loops around the cross arms
    !!!CAREFUL WITH WIRES AS FIBRES EXPOSED!!!
13. Store wires blocked by break-off prisms
14. Carefully lower weld jig further
15. Place wire on prisms and align into grooves
16. Lower weld jig carefully until wires are pulling straight and are just under tension
17. Adjust height of cap removal tool to interface with top cap
18. Check screw position for magnetic mounting and adjust if necessary
19. Remove spring plunger clamp and clamp pole
20. Carefully adjust horizontal position of cap removal tool until interfacing with top cap
21. Attach top cap to removal tool with two M2.5 screws
22. Loosen the two M2.5 captive screws, pull them out of bottom cap and screw in top cap
23. Retract cap removal tool fully in horizontal direction
24. Carefully unscrew magnetic mounting screws
25. Carefully retract weld jig, masses should free
26. Retract fully in horizontal direction
27. Remove ECD assembly to the side of the suspension cage !!!CAREFUL AS MASSES FREE AND FIBRES NOT VISIBLE!!!
28. Remove populated horizontal/vertical adjusters from ECD assembly
29. Remove weld jig and cap removal tool from horizontal/vertical adjusters
30. Attach coils to horizontal bar and cross holder

31. Re-attach horizontal/vertical adjusters to ECD assembly (opposite previous configuration - bar short end, cross long end)
32. Retract both fully in horizontal direction
33. Carefully introduce populated ECD assembly to suspension cage
    !!!CAREFUL AS 1 g MONOLITHIC FREELY HANGING!!!
34. Fix ECD assembly to cage
35. Align coils to magnets on PUM

Bibliography

[1] A. Einstein. “Die Grundlage der allgemeinen Relativitätstheorie”. In: *Ann. Phys.* 354.7 (1916), pp. 769–822.

[2] P. R. Saulson. *Fundamentals of Interferometric Gravitational Wave Detectors*. 2nd Edition. World Scientific, 2017.

[3] K. Danzmann and the LISA study team. “LISA: laser interferometer space antenna for gravitational wave measurements”. In: *Class. Quant. Grav* 13.11A (1996), A247.

[4] P. Amaro-Seoane et al. “Low-frequency gravitational-wave science with eLISA/NGO”. In: *Class. Quant. Grav* 29.12 (2012), p. 124016.

[5] C. Cutler and K. S. Thorne. “An overview of gravitational-wave sources”. In: *Gen. Rel. Gravit.* World Scientific, 2011, pp. 72–111.

[6] A. Hewish, S. J. Bell, J. D. H. Pilkington, P. F. Scott, and R. A. Collins. “Observation of a Rapidly Pulsating Radio Source”. In: *Nat. Phys.* 217 (1968), pp. 709–713.

[7] G. S. Davies, M. Pitkin, and G. Woan. “A targeted spectral interpolation algorithm for the detection of continuous gravitational waves”. In: *Class. Quant. Grav* 34.1 (2017), p. 015010.

[8] B. P. Abbott et al. “First low-frequency Einstein@Home all-sky search for continuous gravitational waves in Advanced LIGO data”. In: *Phys. Rev. D* 96 (12 2017), p. 122004.

[9] A. W. Alsabti and P. Murdin. *Handbook of Supernovae*. 1st Edition. Springer International Publishing, 2017.

[10] C. D. Ott. “Probing the core-collapse supernova mechanism with gravitational waves”. In: *Class. Quant. Grav* 26.20 (2009), p. 204015.

[11] A. Einstein. “Über Gravitationswellen”. In: *Sitzungsberichte der Königlich Preußischen Akademie der Wissenschaften (Berlin), Seite 154-167.* (1918).

[12] B. P. Abbott et al. “Observation of Gravitational Waves from a Binary Black Hole Merger”. In: *Phys. Rev. Lett.* 116 (6 2016), p. 061102.

[13] B. P. Abbott et al. “GW151226: Observation of Gravitational Waves from a 22-Solar-Mass Binary Black Hole Coalescence”. In: *Phys. Rev. Lett.* 116.24 (2016).

[14] B. P. Abbott et al. “GW170104: Observation of a 50-Solar-Mass Binary Black Hole Coalescence at Redshift 0.2”. In: *Phys. Rev. Lett.* 118.22 (2017), p. 221101.

[15] B. P. Abbott et al. “GW170608: Observation of a 19 Solar-mass Binary Black Hole Coalescence”. In: *Astrophys. J. Lett.* 851.2 (2017), p. L35.

[16] B. P. Abbott et al. “GW170814: A Three-Detector Observation of Gravitational Waves from a Binary Black Hole Coalescence”. In: *Phys. Rev. Lett.* 119 (14 2017), p. 141101.

[17] B. P. Abbott et al. “Astrophysical Implications of the Binary Black-hole Merger GW150914”. In: *Astrophys. J.* 818.2 (2016), p. L22.

[18] B. P. Abbott et al. “Tests of General Relativity with GW150914”. In: *Phys. Rev. Lett.* 116 (22 2016), p. 221101.

[19] B. P. Abbott et al. “GW170817: Observation of Gravitational Waves from a Binary Neutron Star Inspiral”. In: *Phys. Rev. Lett.* 119 (16 2017), p. 161101.

[20] B. P. Abbott et al. “Gravitational Waves and Gamma-Rays from a Binary Neutron Star Merger: GW170817 and GRB 170817A”. In: *Astrophys. J.* 848.2 (2017), p. L13.

[21] V. Savchenko et al. “INTEGRAL Detection of the First Prompt Gamma-Ray Signal Coincident with the Gravitational-wave Event GW170817”. In: *Astrophys. J. Lett.* 848 (2017), p. L15.

[22] B. P. Abbott et al. “A gravitational-wave standard siren measurement of the Hubble constant”. In: *Nature* 551.7678 (2017), p. 85.

[23] M. R. Drout et al. “Light curves of the neutron star merger GW170817/SSS17a: Implications for r-process nucleosynthesis.” In: *Science* 358.6370 (2017), pp. 1570–1574.

[24] B. P. Abbott et al. “Estimating the Contribution of Dynamical Ejecta in the Kilonova Associated with GW170817”. In: *Astrophys. J. Lett.* 850 (2017), p. L39.

[25] J. Weber. “Detection and Generation of Gravitational Waves”. In: *Phys. Rev.* 117 (1960), pp. 306–313.

[26] P. Astone. “Resonant mass detectors: present status”. In: *Class. Quant. Grav* 19.7 (2002), p. 1227.

[27] M. Pitkin, S. Reid, S. Rowan, and J. Hough. “Gravitational Wave Detection by Interferometry (Ground and Space)”. In: *Living Rev. Relat.* 5 (2011).

[28] G. M. Harry, J. L. Houser, and K. A. Strain. “Comparison of advanced gravitational-wave detectors”. In: *Phys. Rev. D* 65 (8 2002), p. 082001.

[29] B. Willke et al. “The GEO 600 gravitational wave detector”. In: *Class. Quant. Grav.* 19.7 (2002), p. 1377.

[30] B. P. Abbott et al. “LIGO: the laser interferometer gravitationalwave observatory”. In: *Rep. Prog. Phys.* 72.7 (2009), p. 076901.

[31] F. Acernese et al. “Advanced Virgo: a second-generation interferometric gravitational wave detector”. In: *Class. Quant. Grav* 32.2 (2015), p. 024001.

[32] J. Aasi et al. “Advanced LIGO”. In: *Class. Quant. Grav* 32.7 (2015), p. 074001.

[33] K. Somiya. “Detector configuration of KAGRA - the Japanese cryogenic gravitational-wave detector”. In: *Class. Quant. Grav.* 29.12 (2012), p. 124007.

[34] M. Punturo et al. “The Einstein Telescope: a third-generation gravitational wave observatory”. In: *Class. Quant. Grav* 27.19 (2010), p. 194002.

[35] B. P. Abbott et al. “Exploring the sensitivity of next generation gravitational wave detectors”. In: *Class. Quant. Grav* 34.4 (2017), p. 044001.

[36] J. Mizuno et al. “Resonant sideband extraction: a new configuration for interferometric gravitational wave detectors”. In: *Phys. Lett. A* 175.5 (1993), pp. 273 –276.

[37] J. E. Mason and P. A. Willems. “Signal extraction and optical design for an advanced gravitational-wave interferometer”. In: *Appl. Opt.* 42.7 (2003), pp. 1269–1282.

[38] S. M. Aston et al. “Update on quadruple suspension design for Advanced LIGO”. In: *Class. Quant. Grav.* 29.23 (2012), p. 235004.

[39] F. Matichard et al. “Seismic isolation of Advanced LIGO: Review of strategy, instrumentation and performance”. In: *Class. Quant. Grav* 32.18 (2015).

[40] F. Acernese et al. “Measurements of Superattenuator seismic isolation by Virgo interferometer”. In: *Astropart. Phys.* 33.3 (2010), pp. 182 –189.

[41] E. Hirose, T. Sekiguchi, R. Kumar, and R. Takahashi. “Update on the development of cryogenic sapphire mirrors and their seismic attenuation system for KAGRA”. In: *Class. Quant. Grav* 31.22 (2014), p. 224004.

[42] Y. Michimura et al. “Mirror actuation design for the interferometer control of the KAGRA gravitational wave telescope”. In: *Class. Quant. Grav* 34.22 (2017), p. 225001.

[43] R. Kumar et al. “Status of the cryogenic payload system for the KAGRA detector”. In: *J. Phys. Conf. Ser.* 716.1 (2016), p. 012017.

[44] J. Harms. “Terrestrial Gravity Fluctuations”. In: *Living Rev. Relat.* 18.3 (2015).

[45] J. Harms and S. Hild. “Passive Newtonian noise suppression for gravitational-wave observatories based on shaping of the local topography”. In: *Class. Quant. Grav.* 31.18 (2014), p. 185011.

[46] H. B. Callen and T. A. Welton. “Irreversibility and Generalized Noise”. In: *Phys. Rev.* 83 (1 1951), pp. 34–40.

[47] R. F. Greene and H. B. Callen. “On the Formalism of Thermodynamic Fluctuation Theory”. In: *Phys. Rev.* 83 (6 1951), pp. 1231–1235.

[48] H. B. Callen and R. F. Greene. “On a Theorem of Irreversible Thermodynamics”. In: *Phys. Rev.* 86 (5 1952), pp. 702–710.

[49] P. R. Saulson. “Thermal noise in mechanical experiments”. In: *Phys. Rev. D* 42 (8 1990), pp. 2437–2445.

[50] G. D. Hammond et al. “Reducing the suspension thermal noise of advanced gravitational wave detectors”. In: *Class. Quant. Grav* 29.12 (2012), p. 124009.

[51] A. Gillespie and F. Raab. “Thermal noise in the test mass suspensions of a laser interferometer gravitational-wave detector prototype”. In: *Phys. Lett. A* 178.5-6 (1993), pp. 357 –363.

[52] G. M. Harry et al. “Thermal noise in interferometric gravitational wave detectors due to dielectric optical coatings”. In: *Class. Quant. Grav.* 19.5 (2002), p. 897.

[53] Y. Levin. “Internal thermal noise in the LIGO test masses: A direct approach”. In: *Phys. Rev. D* 57 (2 1998), pp. 659–663.

[54] Y. T. Liu and K. S. Thorne. “Thermoelastic noise and homogeneous thermal noise in finite sized gravitational-wave test masses”. In: *Phys. Rev. D* 62 (12 2000), p. 122002.

[55] S. Reid and I. W. Martin. “Development of Mirror Coatings for Gravitational Wave Detectors”. In: *Coatings* 6.4 (2016).

[56] S. L. Danilishin and F. Y. Khalili. “Quantum Measurement Theory in Gravitational-Wave Detectors”. In: *Living Rev. Relat.* 15.5 (2012).

[57] V. B. Braginsky and F. Y. Khalili. *Quantum Measurement*. Ed. by K. Thorne. Cambridge University Press, 1995.

[58] C. M. Caves. “Quantum-mechanical noise in an interferometer”. In: *Phys. Rev. D* 23 (8 1981), pp. 1693–1708.

[59] S. P. Vyatchanin and E. A. Zubova. “Quantum variation measurement of force”. In: *Phys. Lett. A* 201 (1995), pp. 269–274.

[60] S. P. Vyatchanin and A. B. Matsko. “Quantum variation scheme of measurement of force and compensation of back action in intereferometric meter of position”. In: *J. Exp. Theor. Phys.* 83.4 (1996), pp. 690–697.

[61] V. B. Braginsky and F. Y. Khalili. “Low noise rigidity in quantum measurements”. In: *Phys. Lett. A* 257 (1999), pp. 241–246.

[62] A. Buonanno and Y. Chen. "Signal recycled laser-interferometer gravitational-wave detectors as optical springs". In: *Phys. Rev. D* 65 (4 2002), p. 042001.

[63] T. Corbitt et al. "An All-Optical Trap for a Gram-Scale Mirror". In: *Phys. Rev. Lett.* 98 (15 2007), p. 150802.

[64] H. Rehbein et al. "Double optical spring enhancement for gravitational-wave detectors". In: *Phys. Rev. D* 78 (6 2008), p. 062003.

[65] N. Gordon. "Characterisation and control of coupled optical springs for future gravitational wave detectors". PhD thesis. University of Glasgow, 2015.

[66] V. B. Braginsky and F. Y. Khalili. "Gravitational wave antenna with QND speed meter". In: *Phys. Lett. A* 147.5 (1990), pp. 251–256.

[67] B. P. Abbott et al. "Prospects for Observing and Localizing Gravitational-Wave Transients with Advanced LIGO, Advanced Virgo and KAGRA". In: *Living Rev. Relativ.* 19.1 (2013), p. 1.

[68] *Gravitational wave interferometer noise calculator, v3.1.* 2016.

[69] The Einstein Telescope Collaboration. *Einstein gravitational wave telescope conceptual design study.* Tech. rep. European Gravitational Observatory, 2011.

[70] S. Dwyer et al. "Gravitational wave detector with cosmological reach". In: *Phys. Rev. D* 91 (8 2015), p. 082001.

[71] V. B. Braginsky. "Classical and quantum restrictions on the detection of weak disturbances of a macroscopic oscillator." In: *J. Exp. Theor. Phys.* 26 (1967), pp. 831–834.

[72] V. B. Braginsky, M. L. Gorodetsky, F. Y. Khalili, and K. S. Thorne. "Dual-resonator speed meter for a free test mass". In: *Phys. Rev. D* 61 (2000), p. 044002.

[73] P. Purdue and Y. Chen. "Practical speed meter designs for quantum nondemolition gravitational-wave interferometers". In: *Phys. Rev. D* 66 (12 2002), p. 122004.

[74] A. R. Wade et al. "Polarization speed meter for gravitational-wave detection". In: *Phys. Rev. D* 86 (6 2012), p. 062001.

[75] M. Wang et al. "Realistic polarizing Sagnac topology with DC readout for the Einstein Telescope". In: *Phys. Rev. D* 87 (9 2013), p. 096008.

[76] C. Gräf et al. "Design of a speed meter interferometer proof-of-principle experiment". In: *Class. Quant. Grav.* 31.21 (2014), p. 215009.

[77] S. H. Huttner et al. "Candidates for a possible third-generation gravitational wave detector: comparison of ring-Sagnac and sloshing-Sagnac speedmeter interferometers". In: *Class. Quant. Grav* 34.2 (2017), p. 024001.

[78] S. L. Danilishin. "Sensitivity limitations in optical speed meter topology of gravitational wave antennas". In: *Phys. Rev. D* 69 (10 2004), p. 102003.

[79] G. Sagnac. "On the proof of the reality of the luminiferous aether by the experiment with a rotating interferometer". In: *Comptes rendus* 157 (1913), pp. 1410–1413.

[80] K.-X. Sun, M. M. Fejer, E. Gustafson, and R. L. Byer. "Sagnac interferometer for gravitational-wave detection". In: *Physical review letters* 76.17 (1996), p. 3053.

[81] Y. Chen. "Sagnac interferometer as a speed-meter-type, quantum-nondemolition gravitational-wave detector". In: *Phys. Rev. D* 67 (12 2003), p. 122004.

[82] S. L. Danilishin et al. "Quantum noise of non-ideal Sagnac speed meter interferometer with asymmetries". In: *New J. Phys.* 17.4 (2015), p. 043031.

[83] Y. Chen. "Sagnac interferometer as a speed-meter-type, quantum-nondemolition gravitational-wave detector". In: *Phys. Rev. D* 67.12 (2003), p. 122004.

[84] C. M. Caves and B. L. Schumaker. "New formalism for two-photon quantum optics. I. Quadrature phases and squeezed states". In: *Phys. Rev. A* 31 (5 1985), pp. 3068–3092.

[85] B. L. Schumaker and C. M. Caves. "New formalism for two-photon quantum optics. II. Mathematical foundation and compact notation". In: *Phys. Rev. A* 31 (5 1985), pp. 3093–3111.

[86] H. J. Kimble, Y. Levin, A. B. Matsko, K. S. Thorne, and S. P. Vyatchanin. "Conversion of conventional gravitational-wave interferometers into quantum nondemolition interferometers by modifying their input and/or output optics". In: *Phys. Rev. D* 65 (2 2001), p. 022002.

[87] D. A. Shaddock, M. B. Gray, and D. E. McClelland. "Experimental demonstration of resonant sideband extraction in a Sagnac interferometer". In: *Appl. Opt.* 37.34 (1998), pp. 7995–8001.

[88] P. T. Beyersdorf, R. L. Byer, and M. M. Fejer. "Results from the Stanford 10 m Sagnac interferometer". In: *Class. Quant. Grav.* 19.7 (2002), p. 1585.

[89] T. Eberle et al. "Quantum Enhancement of the Zero-Area Sagnac Interferometer Topology for Gravitational Wave Detection". In: *Phys. Rev. Lett.* 104 (25 2010).

[90] S. Steinlechner et al. "Local-oscillator noise coupling in balanced homodyne readout for advanced gravitational wave detectors". In: *Phys. Rev. D* 92 (7 2015), p. 072009.

[91] R Schilling. "OptoCad, A Fortran 95 module for tracing Gaussian beams through an optical set-up". In: (2002). Internal note.

[92] S. L. Danilishin et al. "Quantum noise cancellation in asymmetric speed meters with balanced homodyne readout". In preparation. 2018.

[93] C. Gräf. "Optical Design and Numerical Modeling of the AEI 10 m Prototype sub-SQL Interferometer". PhD thesis. Leibniz Universität Hannover, 2013.

[94] L. Carbone et al. "Sensors and actuators for the Advanced LIGO mirror suspensions". In: *Class. Quant. Grav* 29.11 (2012), p. 115005.

[95] M. V. Plissi et al. "GEO 600 triple pendulum suspension system: Seismic isolation and control". In: *Rev. Sci. Instrum.* (2000).

[96] M. V. Plissi et al. "An investigation of eddy-current damping of multi-stage pendulum suspensions for use in interferometric gravitational wave detectors". In: *Rev. Sci. Instrum.* 75.11 (2004), pp. 4516–4522.

[97] C. Torrie. "Development of Suspensions for the GEO 600 Gravitational Wave Detector". PhD thesis. University of Glasgow, 2001.

[98] B. Willke et al. "The GEO 600 gravitational wave detector". In: *Class. Quant. Grav* 19.7 (2002), p. 1377.

[99] L. Landau and E. Lifshitz. *Mechanics - Course of Theoretical Physics*. Vol. Volume 1. Pergamon Press, 1976.

[100] M. Husman. "Suspension and Control for Interferometric Gravitational Wave Detectors". PhD thesis. University of Glasgow, 2000.

[101] M. Barton. *Models of the Advanced LIGO Suspensions in Mathematica*. Tech. rep. T020205-v2. LIGO Laboratory / LIGO Scientific Collaboration, 2014.

[102] MATLAB. *R2016a*. Natick, Massachusetts: MathWorks, Inc., 2016.

[103] Mathematica. *version 11.0.0.0*. Champaign, IL: Wolfram Research, Inc., 2016.

[104] ANSYS. *ANSYS®: Academic Research Mechanical, Release 18.1*. ANSYS, Inc., 2017.

[105] ANSYS. *ANSYS® Maxwell®: Low Frequency Electromagnetic Fields, Version 13*. 2017.

[106] *Short-period Seismometer (Model S-13)*.

[107] *OFV-505 Sensor Head OFV-505 Sensor Head Ultimate Performance Vibrometer Datasheet*. Polytec.

[108] J. Batch. *Diaggui (DTT) User Interface Reference*. Tech. rep. 2017.

[109] C. Gräf. "Optical Design and Numerical Modeling of the AEI 10m Prototype sub-SQL Interferometer". PhD thesis. Leibniz Universität Hannover, 2013.

[110] E. J. Elliffe et al. "Hydroxide-catalysis bonding for stable optical systems for space". In: *Class. Quant. Grav* 22.10 (2005), S257–S267.

[111] F. Wayne. *SLT® wire*. Accessed 24/01/2018. http://www.fwmetals.com/products/slt/. 2018.

[112] J. Greenhalgh. “Investigation of blade spring design parameters”. (LIGO internal document).

[113] R. Weiss. *Collection of Reports on Barkhausen Noise*. Tech. rep. LIGO, 2008.

[114] H. Wittel, S. Hild, G. Bergmann, K. Danzmann, and K. A. Strain. “New design of electrostatic mirror actuators for application in high-precision interferometry”. In: *Class. Quant. Grav* 32.17 (2015), p. 175021.

[115] S. M. Aston et al. “Update on quadruple suspension design for Advanced LIGO”. In: *Class. Quant. Grav* 29.23 (2012), p. 235004.

[116] S. Margulies. “Force on a dielectric slab inserted into a parallel-plate capacitor”. In: *Am. J. Phys.* 52.6 (1984), pp. 515–518.

[117] S. Leavey. “Enhancing the sensitivity of future laser-interferometric gravitational wave detectors”. PhD thesis. University of Glasgow, 2017.

[118] D. Pascucci. “On optics surface imperfections and their effects on the sensitivity of sub-SQL interferometers”. In preparation. PhD thesis. University of Glasgow, 2018.

[119] K. Green, J. Burke, and B. F. Oreb. “Chemical bonding for precision optical assemblies”. In: *Opt. Eng.* 50.2 (2011), p. 023401.

[120] J. R. Vig. “UV/ozone cleaning of surfaces”. In: *J. Vac. Sci. Technol. A: Vacuum, Surfaces, and Films* 3.3 (1985), pp. 1027–1034.

[121] B. Willke et al. “The geo-hf project”. In: *Class. Quant. Grav* 23.8 (2006), S207.

[122] T. Accadia et al. “Status of the Virgo project”. In: *Class. Quant. Grav* 28.11 (2011), p. 114002.

[123] R. K. Iler. *The Chemistry of Silica: Solubility, Polymerization, Colloid and Surface Properties and Biochemistry of Silica*. John Wiley Sons Inc, 1979.

[124] K. W. Toland. “Development and characterisation of a pulling machine to produce small diameter silica fibres for use in prototype advanced gravitational wave detectors”. MA thesis. 2015.

[125] A. Heptonstall et al. “Enhanced characteristics of fused silica fibers using laser polishing”. In: *Class. Quant. Grav* 31.10 (2014), p. 105006.

[126] A. Cumming et al. “Apparatus for dimensional characterization of fused silica fibers for the suspensions of advanced gravitational wave detectors”. In: *Rev. Sci. Instrum.* 82.4 (2011), p. 044502.

[127] M. De Rosa, L. Conti, M. Cerdonio, M. Pinard, and F. Marin. “Experimental Measurement of the Dynamic Photothermal Effect in Fabry-Perot Cavities for Gravitational Wave Detectors”. In: *Phys. Rev. Lett.* 89 (23 2002), p. 237402.

[128] D. Kelley, J. Lough, F. Mangaña Sandoval, A. Perreca, and S. Ballmer. "Observation of photo-thermal feed-back in a stable dual-carrier optical spring". In: *Phys. Rev. D* 92 (July 2015).

[129] *MIT optomechanics research.* `https://www.ligo.caltech.edu/mit/page/research-development#Optomechanics%20Research`. Last accessed on 25/01/2018. Massachusetts Institute of Technology.

[130] Y. Enomoto, K. Nagano, M. Nakano, A. Furusawa, and S. Kawamura. "Observation of reduction of radiation-pressure-induced rotational anti-spring effect on a 23 mg mirror in a Fabry-Perot cavity". In: *Class. Quant. Grav* 33.14 (2016), p. 145002.

[131] T. T.-H. Nguyen et al. "Frequency dependence of thermal noise in gram-scale cantilever flexures". In: *Phys. Rev. D* 92 (11 2015), p. 112004.

[132] *Properties of fused silica.* `https://www.heraeus.com/en/hqs/fused_silica_quartz_knowledge_base/properties/properties.aspx`. Last accessed on 25/01/2018. Heraeus.

[133] *Free-Cutting Brass.* `http://www.matweb.com/search/DataSheet.aspx?MatGUID=bae961d2d6ed497a9096986641162def&ckck=1`. Last accessed on 25/01/2018. MatWeb.

[134] J.-S. Hennig et al. "Demonstration of a switchable damping system to allow low-noise operation of high-Q low-mass suspension systems". In: *Phys. Rev. D* 96 (12 2017), p. 122005.

[135] M. P. Edgar. "Experimental investigations into diffractive optics and optomechanical systems for future gravitational wave detectors". PhD thesis. University of Glasgow, 2011.